BULGARIAN CHEMICAL COMMUNICATIONS

2018 Volume 50 / Special Issue K

Selected papers presented on the International Symposium "Power and Chemical Engineering", June 29 – July 2, 2018, Sofia, Bulgaria

Journal of the Chemical Institutes
of the Bulgarian Academy of Sciences
and of the Union of Chemists in Bulgari

Preface

This special issue of the Bulgarian Chemical Communications contains the papers based on oral presentations from the International Symposium „Power and Chemical Engineering“, SOFIA’2018, 29.06.2018-02.07.2018, organized in honor of the Bulgarian Presidency of the Council of Europe by the International Scientific Center for Power and Chemical Engineering Problems (http://www.int-sci-center.bas.bg).

Co-organizers are Institute of Chemical Engineering, Bulgarian Academy of Sciences, Sofia; Research Center for Power Engineering Problems, Russian Academy of Sciences, Kazan; Institute of Catalysis, Russian Academy of Sciences, Novosibirsk.

Chairman of the Organizing Committee: Prof. Boyadjiev Chr., Inst. Chem. Eng., Bulgarian Acad. Sci.

At the Symposium were presented 17 reports of 45 co-authors from Ukraine, Russia, Germany, and Bulgaria.

This Symposium has provided a common platform for scientists and experts from various institutions to share knowledge, ideas, and achievements, to discuss the problems in a friendly environment. The symposium was dedicated to recent developments in the field of power and chemical engineering.

I would like to express my sincere gratitude to all the authors and to the editorial team of the Bulgarian Chemical Communications, all of whom have critically evaluated and improved the content.

Visiting Editor: Prof. Christo Boyadjiev

Bulgarian Chemical Communications, Volume 50, Special Issue K (pp. 07 - 23) 2018

New approach to modelling and simulation of chemical and mass transfer processes in column apparatuses

Chr. Boyadjiev, B. Boyadjiev

Institute of Chemical Engineering, Bulgarian Academy of Sciences, Acad. St. Angelov Str., Bl. 103, 1113 Sofia, Bulgaria

Received March 20, 2018, Accepted June 26, 2018

The classical mass transfer theory is not applicable for the modeling the mass transfer of chemical, absorption, adsorption and catalytic processes in column apparatuses, where the velocity distributions and interphase boundaries are unknown. The modeling of these processes is related with the creation of new type of convection-diffusion models (for qualitative analysis) and average-concentration models (for quantitative analysis), where the surface reactions are replaced by equivalent volume reaction, while the velocity and concentration distributions are replaced by average velocity and concentrations. The effect of the radial non-uniformity of the velocity in the average-concentration models is introduced by model parameters, which must be obtained experimentally. The new convection-diffusion and average-concentration models are obtained in the cases of different processes in column apparatuses: simple and complicated chemical reactions, physical and chemical absorption, physical and chemical adsorption, heterogeneous catalytic processes (physical and chemical adsorption mechanism). These models are presented in the monograph Chr. Boyadjiev, M. Doichinova, B. Boyadjiev, P. Popova-Krumova, *"Modelling of Column Apparatus Processes"* (Second edition), Springer-Verlag, Berlin Heidelberg, 2018. Two hydrodynamic situations are considered, when the radial velocity component is equal to zero, in the cases of an axial modification of the radial non-uniformity of the axial velocity component and when the radial velocity component is not equal to zero. The use of experimental data, for the average concentrations at the column end, for a concrete process and column, permits to be obtained the model parameters, related with the radial non-uniformity of the velocity. These parameter values permit to be used the average-concentration models for modeling of different processes.

Keywords: industrial mass transfer processes, convection-diffusion model, average-concentration model, velocity radial non-uniformity, parameters identification.

INTRODUCTION

The classical mass transfer theory is not applicable for the modeling the mass transfer of chemical, absorption, adsorption and catalytic processes in column apparatuses, where the velocity distributions and interphase boundaries are unknown. The modeling of these processes is related with the creation of new type of convection-diffusion and average-concentration models, where the surface reactions are replaced by equivalent volume reactions, while the velocity and concentration distributions are replaced by average velocity and concentrations.

In the general case a multicomponent ($i=1,2,...,i_0$) and multiphase ($j=1,2,3$ for gas, liquid and solid phases) flow, in a cylindrical column with radius r_0 [m] and active zone height l [m], will be considered. If F_0 is the fluid flow rate in the column and F_j, $j=1,2,3$ are the phase flow rates [$m^3.s^{-1}$], the parts of the column volume occupied by the gas, liquid and solid phase are respectively:

$$\varepsilon_j=\frac{F_j}{F_0},\quad j=1,2,3,\quad \sum_j^3 \varepsilon_j=1, \tag{1}$$

i.e., the phase volumes [m^3] in 1 m^3 of the column volume (hold-up coefficients of the phases).

The input velocities of the phases in the column u_j^0 [$m.s^{-1}$], $j=1,2,3$ may be defined as:

$$u_j^0=\frac{F_j}{\varepsilon_j \pi r_0^2},\quad j=1,2,3;\quad F_0=\sum_{j=1}^3 F_j. \tag{2}$$

The column apparatuses are possible to be modelled using a new approach [1-3] on the basis of the physical approximations of the mechanics of continua, where the mathematical point (in the phase volume or on the surface between the phases) is equivalent to a small (elementary) physical volume, which is sufficiently small with respect to the apparatus volume, but at the same time sufficiently large with respect to the intermolecular volumes in the medium. On this base convection-diffusion models for qualitative analysis of the processes are proposed [1, 2].

Convection-diffusion models

The physical elementary column volumes contain the elementary phase volumes and will be

* To whom all correspondence should be sent:
E-mail: chr.boyadjiev@gmail.com

presented as mathematical points *M* in a cylindrical coordinate system (r,z), where r and z [m] are radial and axial coordinates. As a result, the mathematical point $M(r,z)$ is equivalent to the elementary phase volumes, too.

The concentrations [kg-mol.m^{-3}] of the reagents (components of the phases) are $c_{ij}, i=1,2,...,i_0, j=1,2,3$, i.e. the quantities of the reagents (kg-mol) in 1 m^3 of the phase volumes in the column.

In the cases of a stationary motion of fluids in cylindrical column apparatus $u_j(r,z), v_j(r,z), j=1,2,3$ [m.s^{-1}] are the axial and radial velocity components of the phases in the elementary phase volumes.

In the column apparatuses the phase boundaries are unknown, and therefore the heterogeneous reactions (absorption, adsorption, catalytic reactions) are introduced as a volume sources (sinks) in the elementary phase volumes.

The volume reactions [kg-mol.m^{-3}.s^{-1}] in the phases (homogeneous chemical reaction and interphase mass transfer, as a volume source or sink in the phase volume in the column) are $Q_{ij}(c_{ij}), j=1,2,3, i=1,2,...,i_0$. The reagent (substance) concentrations in the elementary phase volumes can be created or disappear and the reaction rates Q_{ij} are determined by these concentrations $c_{ij}(t,r,z)$ $\left[\text{kg-mol.m}^{-3}\right]$, where t (*s*) is the time.

The volume reactions lead to different values of the reagent (substance) concentrations in the elementary phase volumes and as a result, two mass transfer effects exist - convective transfer (caused by the fluid motion) and diffusion transfer (caused by the concentration gradient).

The convective transfer in column apparatus is caused by a laminar or turbulent (as a result of large-scale turbulent pulsations) flow. In a small (elementary) phase volume around the point *M* (*r*, *z*) in the column, the mass transfer in this volume, as a result of the convection, is $u_j\frac{\partial c_{ij}}{\partial z}+v_j\frac{\partial c_{ij}}{\partial r}$ $\left[\text{kg-mol.m}^{-3}.\text{s}^{-1}\right]$, $j=1,2,3$, $i=1,2,\ldots,i_0$, i.e. convective transfer rate (kg-mol.s^{-1}) in 1 m^3 of the phase volume.

The molecular (or turbulent, caused by small-scale turbulent pulsations) diffusive mass transfer is $D_{ij}\left(\frac{\partial^2 c_{ij}}{\partial z^2}+\frac{1}{r}\frac{\partial c_{ij}}{\partial r}+\frac{\partial^2 c_{ij}}{\partial r^2}\right)$ [kg-mol.m^{-3}.s^{-1}], i.e. diffusive transfer rate (kg-mol.s^{-1}) in 1 m^3 of the phase volume and D_{ij} [m^2.s^{-1}] are the diffusivities of the reagents $(i=1,2,...,i_0)$ in the phases (j =1,2,3).

The mathematical models of the processes in the column apparatuses, in the physical approximations of the mechanics of continua, represent the mass balances in the phase volumes (phase parts in the elementary column volume) between the convective transfer, the diffusive transfer and the volume mass sources (sinks) (as a result of the chemical reactions and interphase mass transfer). The sum total of these three effects is equal to $\partial c_{ij}/\partial t$, $j=1,2,3$, $i=1,2,\ldots,i_0$. In the case of balance between these three effects, the mass transfer process is stationary $(\partial c_{ij}/\partial t=0)$.

In the stationary case, the convection-diffusion equations in the phases (as a mathematical structures of the mass transfer process models in the column apparatuses) are:

$$u_j\frac{\partial c_{ij}}{\partial z}+v_j\frac{\partial c_{ij}}{\partial r}=D_{ij}\left(\frac{\partial^2 c_{ij}}{\partial z^2}+\frac{1}{r}\frac{\partial c_{ij}}{\partial r}+\frac{\partial^2 c_{ij}}{\partial r^2}\right)+ Q_{ij}(c_{ij}),\quad j=1,2,3,\quad i=1,2,\ldots,i_0. \tag{3}$$

The axial and radial velocity components $u_j(r,z)$ and $v_j(r,z)$, $j=1,2,3$ satisfy the continuity equations in the phases:

$$\frac{\partial u_j}{\partial z}+\frac{\partial v_j}{\partial r}+\frac{v_j}{r}=0;$$
$$z=0,\quad u_j\equiv u_j(r,0),\quad j=1,2,3;$$
$$r=r_0,\quad v_j(r_0,z)\equiv 0,\quad j=1,2,3. \tag{4}$$

The models of the mass transfer processes in the column apparatuses (3) include boundary conditions, which express symmetric concentration distributions $(r=0)$, impenetrability of the column wall $(r=r_0)$, constant input concentrations c_{ij}^0 and mass balances at the column input $(z=0)$ of the phases:

$$r=0,\quad \frac{\partial c_{ij}}{\partial r}\equiv 0;\quad r=r_0,\quad \frac{\partial c_{ij}}{\partial r}\equiv 0;$$
$$z=0,\quad c_{ij}\equiv c_{ij}^0,\quad u_j^0 c_{ij}^0\equiv u_j c_{ij}^0-D_{ij}\left(\frac{\partial c_{ij}}{\partial z}\right)_{Z_j=0};$$
$$j=1,2,3,\quad i=1,2,\ldots,i_0. \tag{5}$$

In this paper two hydrodynamic situations will be considered, when the radial velocity component is equal to zero, in the cases of an axial modification of the radial non-uniformity of the

axial velocity component and when the radial velocity component is not equal to zero.

RADIAL VELOCITY COMPONENT IS EQUAL TO ZERO

Chemical reaction in column apparatus

Convection-diffusion model

Let's consider one-component chemical reaction in one-phase column, where $u_j = u(r), v_j = v = 0, c_{ij} = c(r,z), D_{ij} = D, Q_{ij} = kc$. In this case the model (3, 5) has the form:

$$u(r)\frac{\partial c}{\partial z} = D\left(\frac{\partial^2 c}{\partial z^2} + \frac{1}{r}\frac{\partial c}{\partial r} + \frac{\partial^2 c}{\partial r^2}\right) + kc;$$

$$r = 0, \quad \frac{\partial c}{\partial r} \equiv 0; \quad r = r_0, \quad \frac{\partial c}{\partial r} \equiv 0;$$

$$z = 0, \quad c \equiv c^0, \quad u^0 c^0 \equiv uc^0 - D\left(\frac{\partial c}{\partial z}\right)_{z=0}. \tag{6}$$

The qualitative analysis of the model (6) will be made, using generalized variables [1]:

$$r = r_0 R, \quad z = lZ, \quad u(r) = u(r_0 R) = u^0 U(R),$$

$$c(r,z) = c(r_0 R, lZ) = c^0 C(R,Z), \quad \varepsilon = \left(\frac{r_0}{l}\right)^2, \tag{7}$$

where r_0, l, u^0, c^0 are the characteristic (inherent) scales (maximal or average values) of the variables. The introduction of the generalized variables (7) in (6) leads to:

$$U(R)\frac{\partial C}{\partial Z} = \mathrm{Fo}\left(\varepsilon\frac{\partial^2 C}{\partial Z^2} + \frac{1}{R}\frac{\partial C}{\partial R} + \frac{\partial^2 C}{\partial R^2}\right) - \mathrm{Da}\,C;$$

$$R = 0, \quad \frac{\partial C}{\partial R} \equiv 0; \quad R = 1, \quad \frac{\partial C}{\partial R} \equiv 0;$$

$$Z = 0, \quad \mathrm{C} \equiv 1, \quad 1 \equiv U - \mathrm{Pe}^{-1}\frac{\partial C}{\partial Z};$$

$$\mathrm{Fo} = \frac{Dl}{u_0 r_0^2}, \quad \mathrm{Da} = \frac{kl}{u_0}, \quad \mathrm{Pe} = \frac{u_0 l}{D}, \tag{8}$$

where Fo, Da and Pe are the Fourier, Damkohler and Peclet numbers, respectively.

In industrial conditions the parameters $\mathrm{Fo} < 10^{-2}, \mathrm{Pe}^{-1} < 10^{-2}$ are small and model (8) has a convective form:

$$U(R)\frac{\partial C}{\partial Z} = -\mathrm{Da}\,C; \quad Z = 0, \quad \mathrm{C} \equiv 1. \tag{9}$$

Average-concentration model

Let us consider the model of the stationary simple chemical reaction case (6). The average values of the velocity and concentration at the column cross-sectional area are:

$$\bar{u} = \frac{2}{r_0^2}\int_0^{r_0} ru(r)dr, \quad \bar{c}(z) = \frac{2}{r_0^2}\int_0^{r_0} rc(r,z)dr. \tag{10}$$

The functions $u(r), c(r,z)$ in (6) can be presented with the average functions (10):

$$u(r) = \bar{u}\tilde{u}(r), \quad c(r,z) = \bar{c}(z)\tilde{c}(r,z), \tag{11}$$

where $\tilde{u}(r)$ and $\tilde{c}(r,z)$ represent the radial non-uniformity of the velocity and concentration.

The average concentration model may be obtained if (11) is put into (6), multiplied by *r* and integrated over *r* in the interval $[0, r_0]$. As a result, the average-concentration model has the form:

$$\alpha\bar{u}\frac{d\bar{c}}{dz} + \frac{d\alpha}{dz}\bar{u}\bar{c} = D\frac{d^2\bar{c}}{dz^2} - k\bar{c};$$

$$z = 0, \quad \bar{c}(0) = c^0, \quad \frac{d\bar{c}}{dz} = 0, \tag{12}$$

where

$$\alpha(z) = \frac{2}{r_0^2}\int_0^{r_0} r\tilde{u}(r)\tilde{c}(r,z)dr; \tag{13}$$

represents effect of the radial non-uniformity of the velocity.

The use of the generalized variables

$$r = r_0 R, \quad z = lZ, \quad u(r) = \bar{u}U(R),$$

$$\tilde{u}(r) = \frac{u(r)}{\bar{u}} = U(R), \quad c(r,z) = c^0 C(R,Z),$$

$$\bar{c}(z) = c^0\bar{C}(Z), \quad \tilde{c}(r,z) = \frac{c(r,z)}{\bar{c}(z)} = \frac{C(R,Z)}{\bar{C}(Z)},$$

$$\bar{C}(Z) = 2\int_0^1 RC(R,Z)dR,$$

$$\alpha(z) = A(Z) = 2\int_0^1 RU(R)\frac{C(R,Z)}{\bar{C}(Z)}dR, \tag{14}$$

leads to:

$$A(Z)\frac{d\bar{C}}{dZ} + \frac{dA}{dZ}\bar{C} = \mathrm{Pe}^{-1}\frac{d^2\bar{C}}{dZ^2} - \mathrm{Da}\,\bar{C};$$

$$Z = 0, \quad \bar{C} = 1, \quad \frac{d\bar{C}}{dZ} = 0. \tag{15}$$

In industrial conditions the parameter $\mathrm{Pe}^{-1} < 10^{-2}$ is small and model (15) has a convective form:

$$A(Z)\frac{d\bar{C}}{dZ}+\frac{dA}{dZ}\bar{C}=-\mathrm{Da}\,\bar{C};\quad Z=0,\quad \bar{C}=1. \tag{16}$$

Axial modification of the radial non-uniformity of the axial velocity component

Very often in the industrial conditions an axial modification of the radial non-uniformity of the velocity is realized. This radial non-uniformity is caused by the fluid hydrodynamics at the column inlet, where it has as maximum and decreases along the column height as a result of the fluid viscosity. The theoretical determination of the change in the radial non-uniformity of the axial velocity component in a column is difficult in one-phase processes and practical impossible in two-phase and three-phase processes. For a theoretical analysis of the effect of the axial modification of the radial non-uniformity of the velocity, this difficulty can be circumvented by appropriate hydrodynamic model, where the average velocity at the cross section of the column is a constant, while the maximal velocity (and as a result the radial non-uniformity of the axial velocity component too) decreases along the column height.

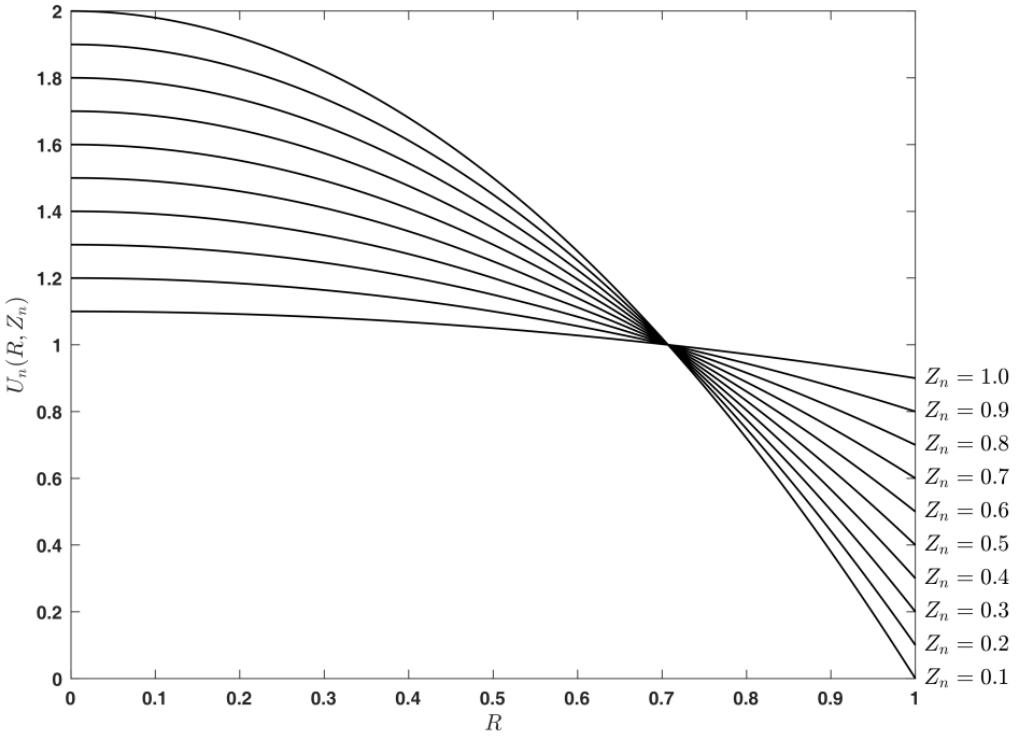

Fig. 1. Velocity distributions $U_n\left(R,Z_n\right), Z_n=0.1(n+1), n=0,1,...,9$.

Let's consider [4] the velocity distribution:

$$u_n\left(r,z_n\right)=u^0U_n\left(R,\mathrm{Z}_n\right),\quad n=0,1,...,9, \tag{17}$$

where $u^0=const$ is the inlet velocity, and an axial step change of the radial non-uniformity of the axial velocity component in a column (Fig. 1):

$$U_n\left(R,Z_n\right)=a_n-b_nR^2,$$
$$a_n=2-0.1n,\quad b_n=2\left(1-0.1n\right),$$
$$0.1n\le Z_n\le 0.1\left(n+1\right),\ n=0,1,...,9,\quad 0\le R\le 1. \tag{18}$$

If we put (17, 18) in (9), the model has the form:

$$U_n\frac{\partial C_n}{\partial Z_n}=-\mathrm{Da}\,C_n;$$
$$0.1n\le Z_n\le 0.1\left(n+1\right);$$
$$Z_n=0.1n,\quad \mathrm{C}_n\left(R,Z_n\right)=C_{n-1}\left(R,Z_n\right);$$
$$n=0,1,...,9;\quad Z_0=0,\quad \mathrm{C}_0\left(R,Z_0\right)\equiv 1. \tag{19}$$

The solution of (19) $C\left(R,Z\right)=C_n\left(R,Z_n\right), Z_n=0.1\left(n+1\right), n=0,1,...,9$ in the case $\mathrm{Da}=1$ is presented on the Fig. 2. This solution $C\left(R,Z\right)$ permits to be obtained in (14) the average ("theoretical") concentration distribution $\bar{C}\left(Z\right)=\bar{C}_n\left(Z_n\right), Z_n=0.1\left(n+1\right),$ in the column (the points on the Fig. 3) and function $A\left(Z\right)=A_n\left(Z_n\right),$

(the points on the Fig. 4) on every step $n = 0,1,...,9$.

From Fig. 4 is seen, that the function $A(Z)$ is possible to be presented as a quadratic approximation:

$$A(Z) = a_0 + a_1 Z + a_2 Z^2 \tag{20}$$

As a result, in the case of axial modification of the radial non-uniformity of the velocity, the model (16) has the form:

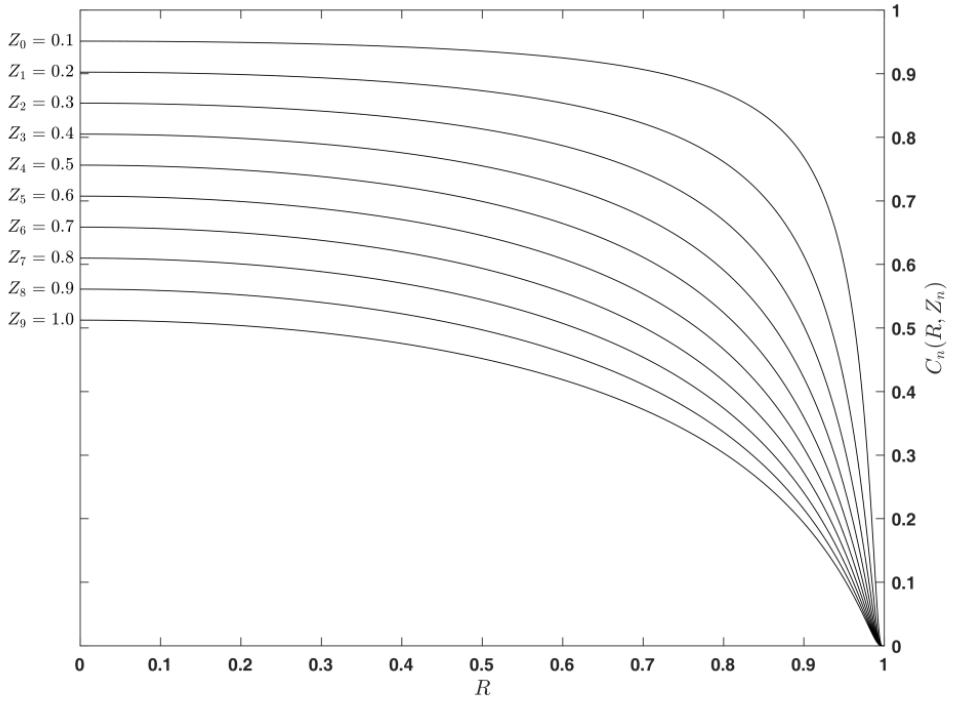

Fig. 2 Concentration distributions $C(Z) = C_n(Z_n)$, $Z_n = 0.1(n+1)$, $n = 0,1,...,9$

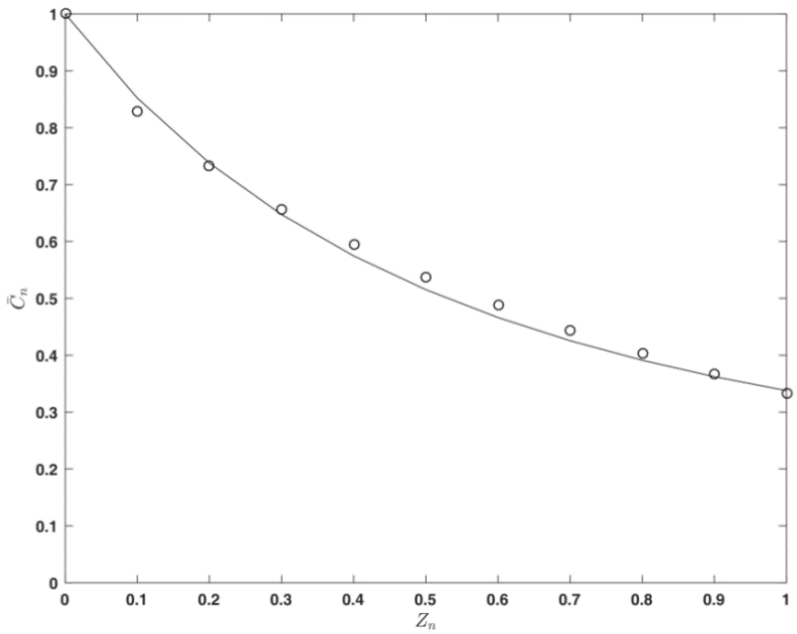

Fig. 3. Average concentration distribution: "theoretical" values (as solution of(10.1.4) and (10.1.5)) $\bar{C}(Z) = \bar{C}_n(Z_n)$, $Z_n = 0.1(n+1)$, $n = 0,1,...,9$ (points); $\bar{C}(Z)$ as a solution of (10.1.7) for "experimental" values of a_0, a_1, a_2 (line).

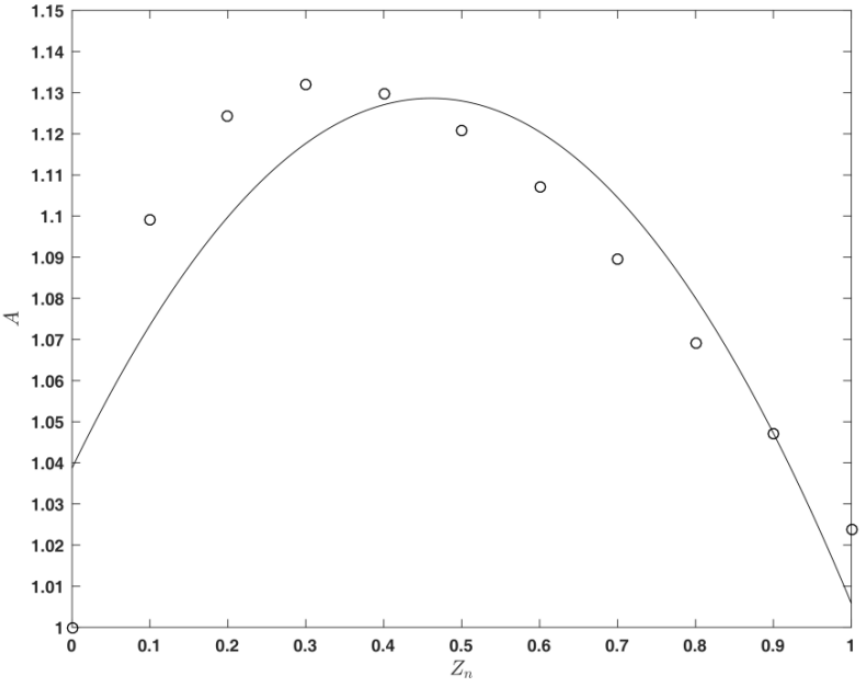

Fig. 4. Function $A(Z)=A_n(Z_n),\ Z_n=0.1(n+1),\ n=0,1,...,9$ (14) (points); $A(Z)$ as a quadratic approximation (20) (line)

$$\left(a_0+a_1Z+a_2Z^2\right)\frac{d\bar{C}}{dZ}+\left(a_1+2a_2Z\right)\bar{C}=-\mathrm{Da}\,\bar{C};$$
$$Z=0,\quad \bar{C}=1, \tag{21}$$

where the parameters a_0, a_1, a_2 must be obtained, using experimental data.

The obtained value of the function $\bar{C}(1)$ (Fig. 3) permit to be obtained the artificial experimental data $\bar{C}^m_{\exp}(1)$ for the column end ($Z=1$):

$$\bar{C}^m_{\exp}(1)=(0.95+0.1B_m)\bar{C}(1),\quad m=1,...,10, \tag{22}$$

where $0\le B_m\le 1, m=0,1,...,10$ are obtained by a generator of random numbers. The obtained artificial experimental data (22) are used for the illustration of the parameters (a_0,a_1,a_2) identification in the average concentrations model (21) by the minimization of the least-squares function:

$$Q(a_0,a_1,a_2)=\sum_{m=1}^{10}\left[\bar{C}(1,a_0,a_1,a_2)-\bar{C}^m_{\exp}(1)\right]^2, \tag{23}$$

where the value of $\bar{C}(1,a_0,a_1,a_2)$ is obtained after the solution of (21) for $Z=1$. The parameters (a_0,a_1,a_2) are used for the solution of (21) and the result (the line) is compared with the average ("theoretical") concentration values $\bar{C}(Z)=\bar{C}_n(Z_n), Z_n=0.1(n+1), n=0,1,...,9.$ (points) (as solution of (19) and (14)) on the Fig. 3.

Gas absorption in column apparatus

Convection-diffusion and average-concentration models

The new approach for the modelling of the processes in column apparatuses [1-3] will be used in the cases of the physical absorption processes in a co-current column [5], where the convection-diffusion and average-concentration models have the forms:

$$u_1\frac{\partial c_1}{\partial z}=D_1\left(\frac{\partial^2 c_1}{\partial z^2}+\frac{1}{r}\frac{\partial c_1}{\partial r}+\frac{\partial^2 c_1}{\partial r^2}\right)-k\left(c_1-\chi c_2\right);$$
$$u_2\frac{\partial c_2}{\partial z}=D_2\left(\frac{\partial^2 c_2}{\partial z^2}+\frac{1}{r}\frac{\partial c_2}{\partial r}+\frac{\partial^2 c_2}{\partial r^2}\right)+k\left(c_1-\chi c_2\right);$$
$$r=0,\quad \frac{\partial c_j}{\partial r}\equiv 0; \tag{24}$$
$$r=r_0,\quad \frac{\partial c_j}{\partial r}\equiv 0;\quad j=1,2;$$
$$z=0,\quad c_1\equiv c_1^0,\quad c_2\equiv 0,$$
$$u_1^0c_1^0\equiv u_1c_1^0-D_1\left(\frac{\partial c_1}{\partial z}\right)_{z=0},\quad \left(\frac{\partial c_2}{\partial z}\right)_{z=0}=0.$$

$$\alpha_1(z)\bar{u}_1\frac{d\bar{c}_1}{dz}+\frac{d\alpha_1}{dz}\bar{u}_1\bar{c}_1=D_1\frac{d^2\bar{c}_1}{dz^2}-k\left(\bar{c}_1-\chi\bar{c}_2\right);$$

$$\alpha_2(z)\bar{u}_2\frac{d\bar{c}_2}{dz}+\frac{d\alpha_2}{dz}\bar{u}_2\bar{c}_2=D_2\frac{d^2\bar{c}_2}{dz^2}+k\left(\bar{c}_1-\chi\bar{c}_2\right);$$

$$z=0,\quad \bar{c}_1(0)\equiv c_1^0,\quad \bar{c}_2(0)\equiv 0, \tag{25}$$

$$\frac{d\bar{c}_1}{dz}\equiv 0,\quad \frac{d\bar{c}_2}{dz}\equiv 0;$$

$$\alpha_j(z)=\frac{2}{r_0^2}\int_0^{r_0} r\tilde{u}_j\tilde{c}_j\,dr,\quad \tilde{u}_j(r)=\frac{u_j(r)}{\bar{u}_j},$$

$$\tilde{c}_j(r,z)=\frac{c_j(r,z)}{\bar{c}_j(z)},\quad j=1,2.$$

In (24, 25) χ is the Henry's number, k - volume interphase mass transfer coefficient [s^{-1}], k_0 - chemical reaction rate constant [s^{-1}], $u_j^0, c_j^0,\ j=1,2$ - input $(z=0)$ velocities and concentrations, $\bar{u}_j, \bar{c}_j(z),\ j=1,2$ - the average velocities and concentrations at the column cross-sectional area, $\tilde{u}_j(r), \tilde{c}_j(r,z),\ j=1,2$ - the radial non-uniformities of the velocities and concentrations.

In (24, 25) the generalized variables can be introduced:

$$r=r_0R,\quad z=lZ,\quad u_j(r)=\bar{u}_jU_j(R),\quad j=1,2,$$

$$c_1(r,z)=c_1^0C_1(R,Z),\quad c_2(r,z)=\frac{c_1^0}{\chi}C_2(R,Z),$$

$$\bar{c}_1(z)=c_1^0\bar{C}_1(Z),\quad \bar{c}_2(z)=\frac{c_1^0}{\chi}\bar{C}_2(Z), \tag{26}$$

and as a result is obtained:

$$U_1\frac{\partial C_1}{\partial Z}=\mathrm{Fo}_1\left(\varepsilon^2\frac{\partial^2C_1}{\partial Z^2}+\frac{1}{R}\frac{\partial C_1}{\partial R}+\frac{\partial^2C_1}{\partial R^2}\right)-$$

$$-K_1(C_1-C_2);$$

$$U_2\frac{\partial C_2}{\partial Z}=\mathrm{Fo}_2\left(\varepsilon^2\frac{\partial^2C_2}{\partial Z^2}+\frac{1}{R}\frac{\partial C_2}{\partial R}+\frac{\partial^2C_2}{\partial R^2}\right)+$$

$$+K_2(C_1-C_2);$$

$$R=0,\quad \frac{\partial C_j}{\partial R}\equiv 0;\quad R=1,\quad \frac{\partial C_j}{\partial R}\equiv 0;\quad j=1,2;$$

$$Z=0,\quad C_1\equiv 1,\quad C_2=0, \tag{27}$$

$$1\equiv U_1-\mathrm{Pe}_1^{-1}\frac{\partial C_1}{\partial Z},\quad \frac{\partial C_2}{\partial Z}\equiv 0.$$

$$A_1(Z)\frac{d\bar{C}_1}{dZ}+\frac{dA_1}{dZ}\bar{C}_1=\mathrm{Pe}_1^{-1}\frac{d^2\bar{C}_1}{dZ^2}-K_1\left(\bar{C}_1-\bar{C}_2\right);$$

$$A_2(Z)\frac{d\bar{C}_2}{dZ}+\frac{dA_2}{dZ}\bar{C}_2=\mathrm{Pe}_2^{-1}\frac{d^2\bar{C}_2}{dZ^2}+K_2\left(\bar{C}_1-\bar{C}_2\right);$$

$$Z=0,\quad \bar{C}_1=1,\quad \bar{C}_2=0,\quad \frac{d\bar{C}_1}{dZ}=0,\quad \frac{d\bar{C}_2}{dZ}=0.$$

In (27) are used the expressions:

$$\bar{C}_j(Z)=2\int_0^1 RC_j(R,\mathrm{Z})\,dR,$$

$$\tilde{c}_j(r,z)=\frac{c_j(r,z)}{\bar{c}_j(z)}=\frac{C_j(R,Z)}{\bar{C}_j(Z)},$$

$$\alpha_j(z)=A_j(Z)=2\int_0^1 RU_j(R)\frac{C_j(R,Z)}{\bar{C}_j(Z)}\,dR,$$

$$j=1,2. \tag{28}$$

In practical conditions the models (26, 27) have convective forms:

$$U_1\frac{dC_1}{dZ}=-K_1(C_1-C_2);$$

$$U_2\frac{dC_2}{dZ}=\omega K_1(C_1-C_2);$$

$$Z=0,\quad C_1\equiv 1,\quad C_2=0. \tag{29}$$

$$A_1(Z)\frac{d\bar{C}_1}{dZ}+\frac{dA_1}{dZ}\bar{C}_1=-K_1\left(\bar{C}_1-\bar{C}_2\right);$$

$$A_2(Z)\frac{d\bar{C}_2}{dZ}+\frac{dA_2}{dZ}\bar{C}_2=\omega K_1\left(\bar{C}_1-\bar{C}_2\right);$$

$$Z=0,\quad \bar{C}_1=1,\quad \bar{C}_2=0. \tag{30}$$

Effect of the axial modification of the radial non-uniformity of the axial velocity components

Let's consider [5] the velocity distributions:

$$u_{jn}(r,z_n)=u_j^0U_{jn}(R,\mathrm{Z}_n),\quad j=1,2,\ n=0,1,..,9, \tag{31}$$

where

$$U_{jn}\left(R,Z_n\right)=a_{jn}-b_{jn}R^2,\quad a_{jn}=2-0.1n,$$
$$b_{jn}=2\left(1-0.1n\right),\quad 0.1n\le Z_n\le 0.1\left(n+1\right),$$
$$n=0,1,...,9,\quad j=1,2. \tag{32}$$

If we put (32) in (29), the model has the form:

$$U_{1n}\frac{dC_{1n}}{dZ_n}=-K_1\left(C_{1n}-C_{2n}\right),$$
$$U_{2n}\frac{dC_{2n}}{dZ_n}=\omega K_1\left(C_{1n}-C_{2n}\right);$$
$$Z_n=0.1n,\quad \mathrm{C}_{jn}\left(R,Z_n\right)=C_{j(n-1)}\left(R,Z_n\right),$$
$$n=0,1,...,9,\quad j=1,2;$$
$$Z_0=0,\quad \mathrm{C}_{10}\left(R,Z_0\right)\equiv 1,\quad C_{20}\left(R,Z_0\right)=0. \tag{33}$$

The parameter ω in (33) is known beforehand. The solution of (33), for a concrete absorption process ($\omega=1$) of an average soluble gas and "theoretical" value of $K_1=1$, permits to be obtained the concentration distributions $C_{jn}\left(R,Z_n\right)$, $j=1,2$ for different $Z_n=0.1\left(n+1\right), n=0,1,...,9$ (Fig. 5). The solution of (33) (Fig. 5) and (28) permit to obtain the "theoretical" average concentration distributions

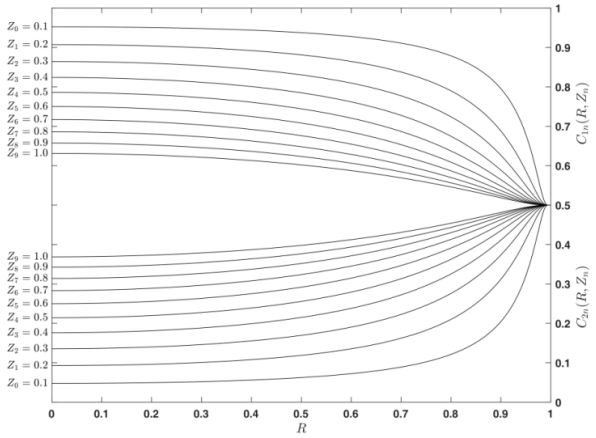

Fig. 5. Concentration distributions $C_{jn}\left(R,Z_n\right)$, $j=1,2$ in the case $\omega=K_1=1$ for different $Z_n=0.1\left(n+1\right), n=0,1,...,9$.

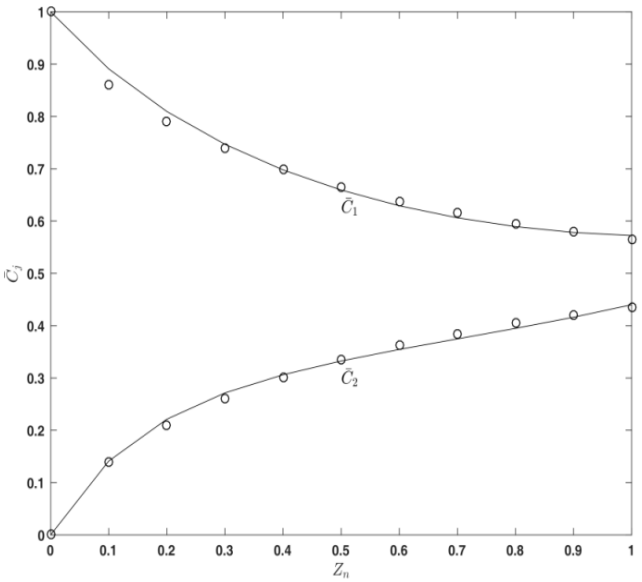

Fig. 6. Average concentration $\bar{C}_j\left(Z\right)$, $j=1,2$ in the case $\omega=K_1=1$: "theoretical" values $\bar{C}_j\left(Z\right)=\bar{C}_{jn}\left(Z_n\right)$, $j=1,2$ as solutions of (33) and (28) for different $Z_n=0.1\left(n+1\right), n=0,1,...,9$ (points); $\bar{C}_j\left(Z\right)$, $j=1,2$ as a solution of (35), using the "experimental" parameter values a_{j0}, a_{j1}, a_{j2}, $j=1,2, K_1$ (lines)

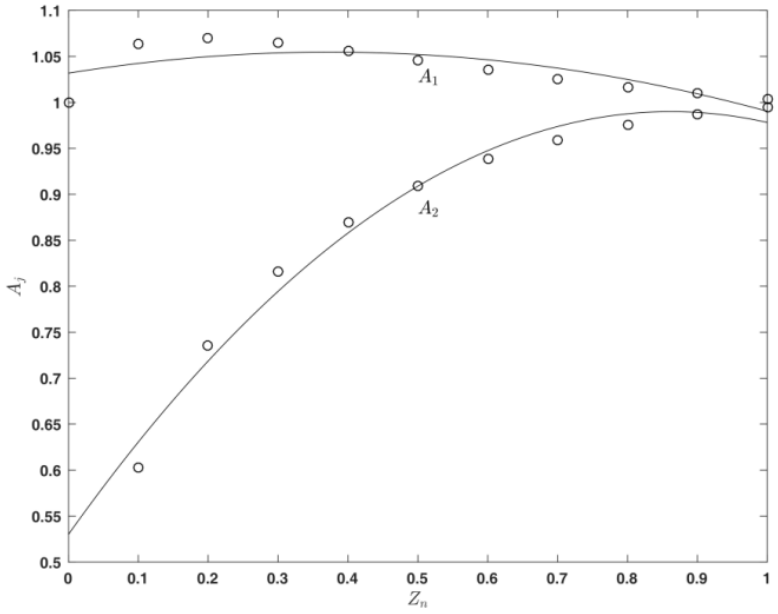

Fig. 7. Function $A_{jn}(Z_n)$, $j=1,2$ in the case $\omega = K_1 = 1$: as a solution of (29) and (28) for different $Z_n = 0.1(n+1)$, $n = 0,1,...,9$ (points); $A_j(Z)$, $j=1,2$ as a quadratic approximation (34) (line).

$\bar{C}_{jn}(Z_n)$, $j=1,2$ (the points in Fig. 6) and the functions $A_{jn}(Z_n)$, $j=1,2$ (the points in Fig. 7) for different $Z_n = 0.1(n+1)$, $n = 0,1,...,9$.

From Fig. 7 it is seen that the functions $A_{jn}(Z_n)$, $n = 0,1,...,4$, $j=1,2$ may be presented as quadratic approximations:

$$A_1(Z) = a_{10} + a_{11}Z + a_{12}Z^2,$$
$$A_2(Z) = a_{20} + a_{21}Z + a_{22}Z^2. \qquad (34)$$

As a result, in the case of axial modification of the radial non-uniformity of the velocity, the model (30) has the form:

$$\left(a_{10} + a_{11}Z + a_{12}Z^2\right)\frac{d\bar{C}_1}{dZ} + \left(a_{11} + 2a_{12}Z\right)\bar{C}_1 =$$
$$= -K_1\left(\bar{C}_1 - \bar{C}_2\right);$$
$$\left(a_{20} + a_{21}Z + a_{22}Z^2\right)\frac{d\bar{C}_2}{dZ} + \left(a_{21} + 2a_{22}Z\right)\bar{C}_2 =$$
$$= \omega K_1\left(\bar{C}_1 - \bar{C}_2\right);$$
$$Z = 0, \quad \bar{C}_1 = 1, \quad \bar{C}_2 = 0, \qquad (35)$$

where (at unknown velocity distributions in the two phases) ω is known beforehand for a concrete process, while the parameters a_{j0}, a_{j1}, a_{j2}, $j=1,2, K_1$ must be obtained using experimental data.

The obtained values of the functions $\bar{C}_{jn}(Z_n)$, $j=1,2$, for a concrete process $(\omega = 1)$, "theoretical" value of $K_1 = 1$ and different $Z_n = 0.1(n+1)$, $n = 0,1,...,9$ (Fig. 6), permit to be obtained the values of $\bar{C}_j(1)$, $j=1,2$ and the artificial experimental data:

$$\bar{C}^m_{j\exp}(1) = (0.95 + 0.1B_m)\bar{C}_j(1), \quad j=1,2,$$
$$m = 1,...,10, \qquad (36)$$

where $0 \le B_m \le 1$, $m = 1,...,10$ are obtained by a generator of random numbers. The obtained artificial experimental data (36) are used for the illustration of the parameters $P = (a_{j0}, a_{j1}, a_{j2}, j=1,2, K_1)$ identification in the average concentrations model (35) by the minimization of the least-squares function with respect to $P = (a_{j0}, a_{j1}, a_{j2}, j=1,2, K_1)$:

$$Q(P) = \sum_{m=1}^{10}\left[\bar{C}_1(1,P) - \bar{C}^m_{1\exp}(1)\right]^2 +$$
$$+\sum_{m=1}^{10}\left[\bar{C}_2(1,P) - \bar{C}^m_{2\exp}(1)\right]^2, \qquad (37)$$

where the values of $\bar{C}_j(1,P)$, $j=1,2$ are obtained as solutions of (35). The obtained ("experimental") parameter values a_{j0}, a_{j1}, a_{j2}, $j=1,2, K_1$ are used for the solution of (35) and the results (the lines) are compared with the "theoretical" average concentration values on Fig.6.

RADIAL VELOCITY COMPONENT IS NOT EQUAL TO ZERO

Chemical reaction in column apparatus

Convection-diffusion model

A theoretical analysis of the effect of the radial velocity components in the industrial column chemical reactors will be presented in the case, when the radial velocity component is not equal to zero for pseudo-first order chemical reactions. In the stationary case, the convection-diffusion model (3-5) has the form:

$$u\frac{\partial c}{\partial z}+v\frac{\partial c}{\partial r}=D\left(\frac{\partial^2 c}{\partial z^2}+\frac{1}{r}\frac{\partial c}{\partial r}+\frac{\partial^2 c}{\partial r^2}\right)-kc;$$
$$r=0,\quad \frac{\partial c}{\partial r}\equiv 0;\quad r=r_0,\quad \frac{\partial c}{\partial r}\equiv 0;$$
$$z=0,\quad c\equiv c^0,\quad u^0c^0\equiv uc^0-D\frac{\partial c}{\partial z}. \tag{38}$$

$$\frac{\partial u}{\partial z}+\frac{\partial v}{\partial r}+\frac{v}{r}=0;$$
$$r=r_0,\quad v(r_0,z)\equiv 0;\quad z=0,\quad u=u(r,0). \tag{39}$$

The theoretical analysis of the model (38, 39) will be made, using generalized variables (7) and

$$v(r,z)=v(r_0R,lZ)=u^0\varepsilon V(R,Z). \tag{40}$$

As a result from (7, 38-40) the following may be obtained:

$$U\frac{\partial C}{\partial Z}+V\frac{\partial C}{\partial R}=\mathrm{Fo}\left(\varepsilon^2\frac{\partial^2 C}{\partial Z^2}+\frac{1}{R}\frac{\partial C}{\partial R}+\frac{\partial^2 C}{\partial R^2}\right)-\mathrm{Da}\,C;$$
$$R=0,\quad \frac{\partial C}{\partial R}\equiv 0;\quad R=1,\quad \frac{\partial C}{\partial R}\equiv 0; \tag{41}$$
$$Z=0,\quad C\equiv 1,\quad 1\equiv U-\mathrm{Pe}^{-1}\frac{\partial C}{\partial Z}.$$

$$\frac{\partial U}{\partial Z}+\frac{\partial V}{\partial R}+\frac{V}{R}=0;$$
$$R=1,\quad V(1,Z)\equiv 0;\quad Z=0,\quad U=U(R,0). \tag{42}$$

In industrial conditions the parameters $\mathrm{Fo}<10^{-2}$, $\mathrm{Pe}^{-1}<10^{-2}$ are small and the model (41) has a convective form:

$$U\frac{\partial C}{\partial Z}+V\frac{\partial C}{\partial R}=-\mathrm{Da}\,C;$$
$$R=1,\quad C\equiv 0;\quad Z=0,\quad C\equiv 1. \tag{43}$$

Average-concentration model

The functions $u(r,z), v(r,z), c(r,z)$ in (38) can be presented with the help of the average functions (10):

$$u(r,z)=\bar{u}\,U(R,Z),\quad v(r,z)=\varepsilon\bar{u}V(R),$$
$$c(r,z)=\bar{c}(z)\,\tilde{c}(r,z). \tag{44}$$

As a result, the following is obtained:

$$\alpha(z)\bar{u}\frac{d\bar{c}}{dz}+\left[\beta(z)+\gamma(z)\right]\bar{u}\bar{c}_i=D\frac{d^2\bar{c}}{dz^2}-k\bar{c};$$
$$z=0,\quad \bar{c}\equiv c^0,\quad \frac{d\bar{c}}{dz}\equiv 0, \tag{45}$$

where

$$\alpha(z)=\frac{2}{r_0^2}\int_0^{r_0} rU\tilde{c}\,dr,\quad \beta(z)=\frac{2}{r_0^2}\int_0^{r_0} rU\frac{\partial\tilde{c}}{\partial z}dr,$$
$$\gamma(z)=\frac{2}{r_0^2}\int_0^{r_0} rV\frac{\partial\tilde{c}}{\partial r}dr,\quad \tilde{c}(r,z)=\tilde{C}(R,Z),$$
$$U=U(R,Z),\quad V=V(R). \tag{46}$$

The theoretical analysis of the model (45) will be made, using the next generalized variables and functions:

$$z=lZ,\quad r=r_0R,\quad \bar{c}(z)=c^0\bar{C}(Z),$$
$$\bar{C}(Z)=2\int_0^1 RC(R,Z)\,dR,$$
$$\tilde{c}(r,z)=\frac{c(r,z)}{\bar{c}(z)}=\frac{C(R,Z)}{\bar{C}(Z)}=\tilde{C}(R,Z),$$
$$\alpha(z)=A(Z)=2\int_0^1 RU(R,Z)\tilde{C}(R,Z)\,dR,$$
$$\beta(z)=\beta(lZ)=B(Z)=2\int_0^1 RU(R,Z)\frac{\partial\tilde{C}}{\partial Z}dR,$$
$$\gamma(z)=\gamma(lZ)=G(Z)=2\int_0^1 RV(R)\frac{\partial\tilde{C}}{\partial R}dR, \tag{47}$$

and as a result:

$$A(Z)\frac{d\bar{C}}{dZ}+\left[B(Z)+G(Z)\right]\bar{C}=\mathrm{Pe}^{-1}\frac{d^2\bar{C}}{dZ^2}-\mathrm{Da}\,\bar{C};$$
$$Z=0,\quad \bar{C}=1,\quad \frac{d\bar{C}}{dZ}=0. \tag{48}$$

In industrial conditions $\mathrm{Pe}>10^2$ and the model (48) has the convective form:

$$A(Z)\frac{d\bar{C}}{dZ}+\left[B(Z)+G(Z)\right]\bar{C}=-\mathrm{Da}\,\bar{C};$$
$$Z=0,\quad \bar{C}=1. \tag{49}$$

Axial and radial velocity components

The theoretical analysis of the change in the radial non-uniformity of the axial velocity component (effect of the radial velocity component) in a column can be made by an appropriate hydrodynamic model, where the average velocity at the cross section of the column is a constant (inlet average axial velocity component), while the radial non-uniformity of the axial velocity component decreases along the column height and as a result a radial velocity

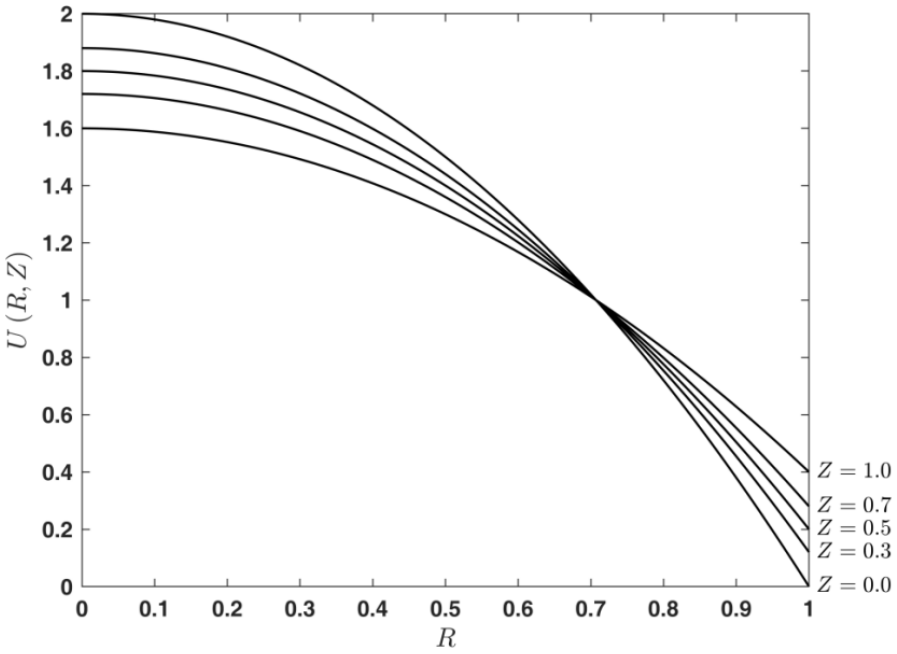

Fig. 8. Axial velocity component $U(R,Z)$ for different $Z=0,\,0.3,\,0.5,\,0.7,1.0$

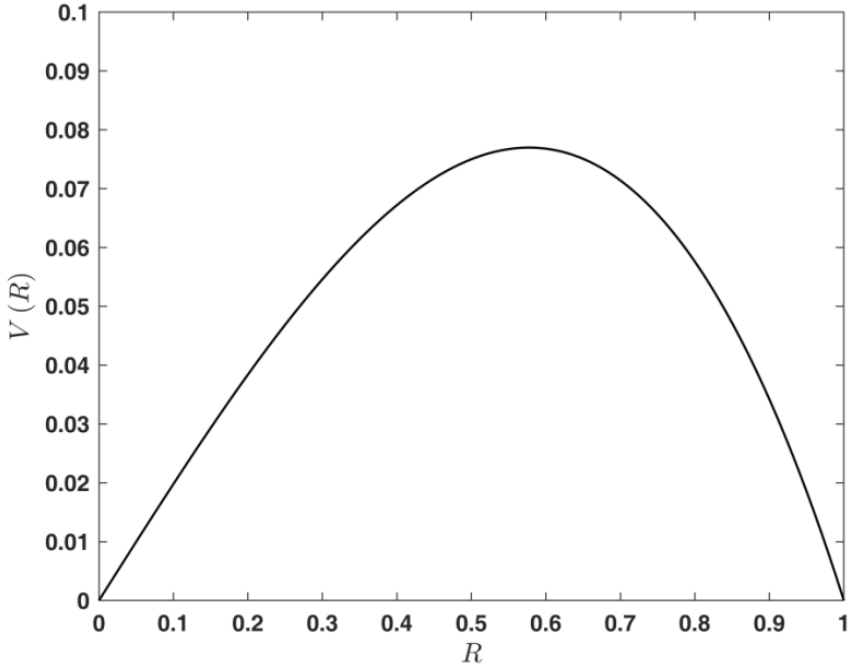

Fig. 9. Radial velocity component $V(R)$

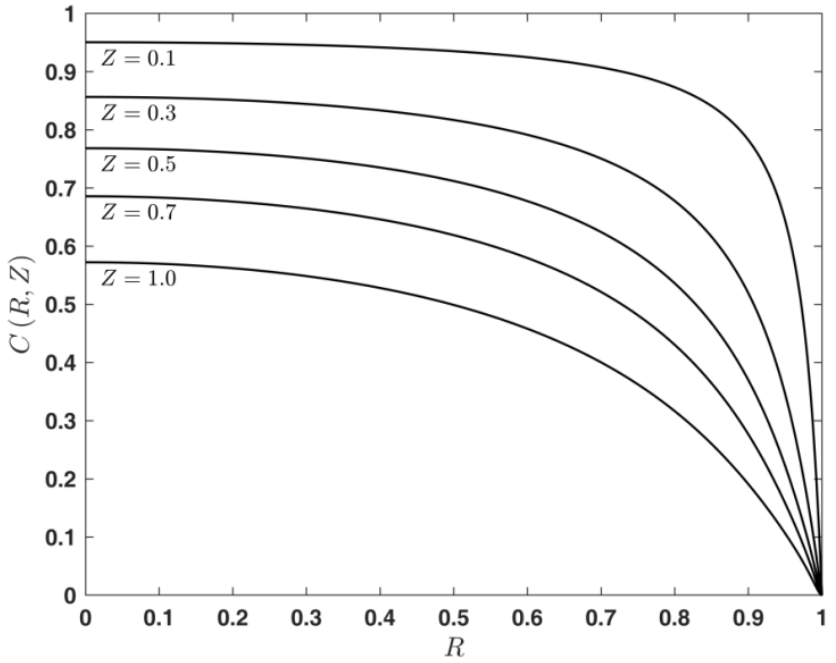

Fig. 10. Concentration distributions $C(R,Z)$ for different $Z = 0.1, 0.3, 0.5, 0.7, 1.0$

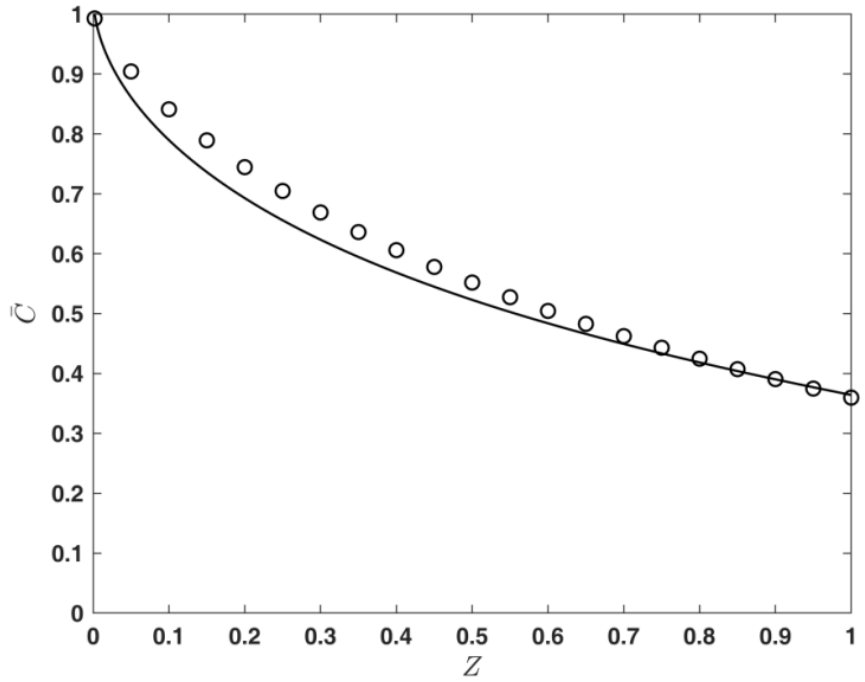

Fig. 11. Average concentrations $\bar{C}(Z)$: "theoretical" values $\bar{C}(Z_n)$, $Z_n = 0.1(n+1)$, $n = 0,1,...,9$ (points); solution of (49) (lines)

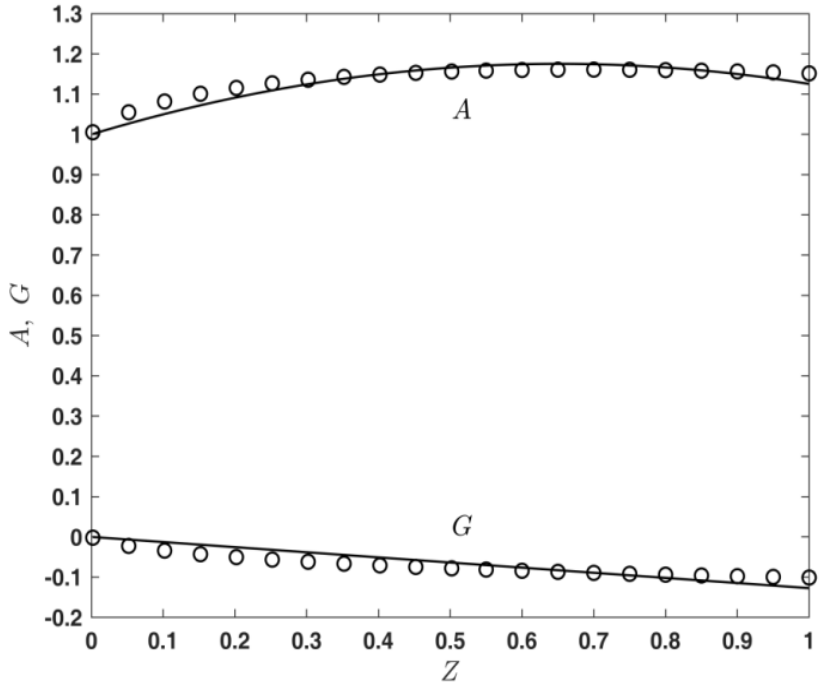

Fig. 12. Functions $A(Z_n), G(Z_n), Z_n = 0.1(n+1), n = 0,1,...,9$ (points) and theirs quadratic and linear approximations (53) (lines)

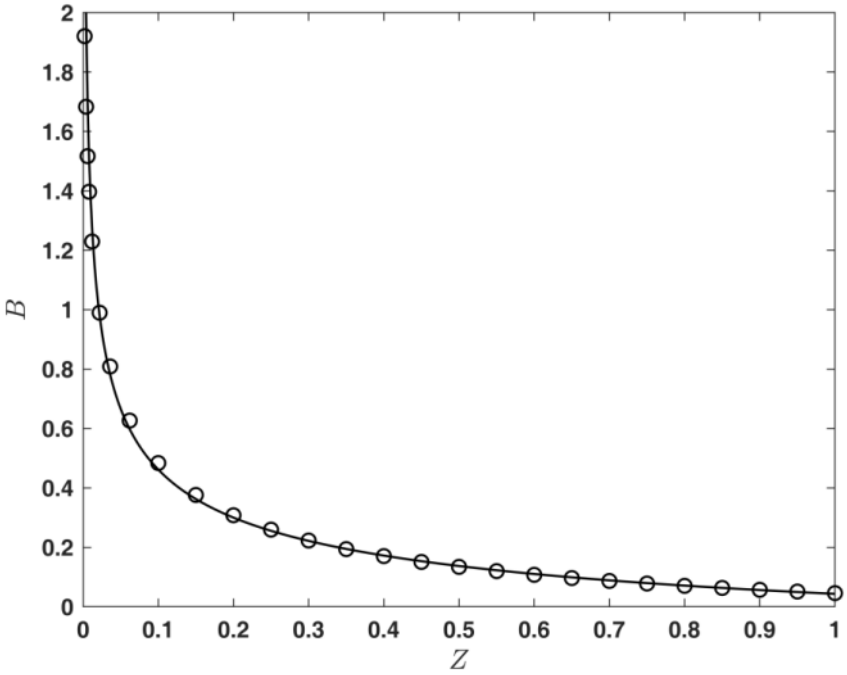

Fig. 13. Functions $B(Z_n), Z_n = 0.1(n+1), n = 0,1,...,9$ (points) and its parabolic approximation (53) (line).

component is initiated. In generalized variables (7) is possible to be used the model:

$$U=(2-0.4Z)-2(1-0.4Z)R^2,$$
$$V=0.2\left(R-R^3\right), \tag{50}$$

where the velocity components satisfy the equation (42). The velocity components (50) are presented on the Figs. 8, 9. From Fig. 9 is seen, that $V<0.1$ and must be presented with the help of a small parameter $0.1=\alpha\ll 1$, i.e.

$$V=\alpha V_0,\quad V_0=0.2\left(R-R^3\right)\alpha^{-1} \tag{51}$$

As a result, the problem (43) has the form:

$$U\frac{\partial C}{\partial Z}+\alpha V_0\frac{\partial C}{\partial R}=-\mathrm{Da}\,C;\quad R=1,\quad \frac{\partial C}{\partial R}\equiv 0;$$
$$Z=0,\quad C\equiv 1, \tag{52}$$

where $0.1=\alpha\ll 1$ is a small parameter and (52) must be solved by the perturbation method [1, 9].

The solutions of (52) in the case $\mathrm{Da}=1$, and $0.1=\alpha\ll 1$, lead to $C(R,Z)$ which is presented on Fig. 10.

The solution of (51, 52) and (47) permits to be obtained the average concentrations ("theoretical" values) $\bar{C}(Z_n)$ and functions $A(Z_n),\ B(Z_n),\ G(Z_n),\ Z_n=0.1(n+1),$ $n=0,1,...,9$, which are presented (points) on Figs. 11-13.

From Figs. 12, 13 is seen, that the functions $A(Z), B(Z), G(Z)$ are possible to be presented as the next approximations:

$$A(Z)=1+a_1Z+a_2Z^2,\quad B(Z)=b_0+b_1Z^{b_2},$$
$$G(Z)=gZ \tag{53}$$

As a result, the model (49) has the form:

$$\left(1+a_1Z+a_2Z^2\right)\frac{d\bar{C}}{dZ}+\left(b_0+b_1Z^{b_2}+gZ\right)\bar{C}=-\mathrm{Da}\,\bar{C};$$
$$Z=0,\quad \bar{C}=1, \tag{54}$$

where the parameters $P(a_1, a_2, b_0, b_1, b_2, g)$ must be obtained using experimental data.

The value of the function $\bar{C}(1)$ obtained from (51, 52) and (47) permits to be obtained the artificial experimental data $\bar{C}^m_{\exp}(1)$ for the column end ($Z=1$):

$$\bar{C}^m_{\exp}(1)=(0.95+0.1B_m)\bar{C}(1),\quad m=1,...,10, \tag{55}$$

where $0\le B_m\le 1, m=0,1,...,10$ are obtained by a generator of random numbers.

The obtained artificial experimental data (55) is possible to be used for the illustration of the parameters P identification in the average concentrations model (54) by the minimization of the least-squares function:

$$Q(P)=\sum_{m=1}^{10}\left[\bar{C}(1,P)-\bar{C}^m_{\exp}(1)\right]^2, \tag{56}$$

where the values of $\bar{C}(1,P)$ are obtained after the solution of (54) for $Z=1$.

The obtained ("experimental") parameter values are used for the solution of (54) and the results (the lines) are compared with the average ("theoretical") concentration values $\bar{C}(Z_n), Z_n=0.1(n+1), n=0,1,...,9$ (points) on Fig. 11.

GAS ABSORPTION IN COLUMN APPARATUS

Convection-diffusion model

The new approach of the processes modeling in the column apparatuses [1-3] permits to be created the convection-diffusion model of the co-current physical absorption process in the case, when the radial velocity component is not equal to zero:

$$u_j\frac{\partial c_j}{\partial z}+v_j\frac{\partial c_j}{\partial r}=D_j\left(\frac{\partial^2 c_j}{\partial z^2}+\frac{1}{r}\frac{\partial c_j}{\partial r}+\frac{\partial^2 c_j}{\partial r^2}\right)+$$
$$+(-1)^{(2-j)}k(c_1-\chi c_2);$$
$$r=0,\quad \frac{\partial c_j}{\partial r}\equiv 0;\quad r=r_0,\quad \frac{\partial c_j}{\partial r}\equiv 0;\quad j=1,2;$$
$$z=0,\quad c_1\equiv c_1^0,\quad c_2\equiv 0,$$
$$u_1^0c_1^0\equiv u_1c_1^0-D_1\left(\frac{\partial c_1}{\partial z}\right)_{z=0},\quad \left(\frac{\partial c_2}{\partial z}\right)_{z=0}=0. \tag{57}$$

$$\frac{\partial u_j}{\partial z}+\frac{\partial v_j}{\partial r}+\frac{v_j}{r}=0;$$
$$r=r_0,\quad v_j(r_0,z)\equiv 0;$$
$$z=0,\quad u_j=u_j(r,0);\quad j=1,2. \tag{58}$$

In (57, 58) the generalized variables can be introduced:

$$r=r_0R,\quad z=lZ,$$
$$u_j(r,z)=u_j(r_0R,lZ)=u_j^0U_j(R,Z),$$
$$v_j(r,z)=v_j(r_0R,lZ)=u_j^0\varepsilon V_j(R,Z),\quad j=1,2,$$
$$c_1(r,z)=c_1(r_0R,lZ)=c_1^0C_1(R,Z),$$
$$c_2(r,z)=c_2(r_0R,lZ)=\frac{c_1^0}{\chi}C_2(R,Z) \tag{59}$$

and as a result is obtained:

$$U_j\frac{\partial C_j}{\partial Z}+V_j\frac{\partial C_j}{\partial R}=\mathrm{Fo}_j\left(\varepsilon^2\frac{\partial^2 C_j}{\partial Z^2}+\frac{1}{R}\frac{\partial C_j}{\partial R}+\right.$$
$$\left.+\frac{\partial^2 C_j}{\partial R^2}\right)+(-1)^{(2-j)}K_j(C_1-C_2);$$
$$R=0,\quad \frac{\partial C_j}{\partial R}\equiv 0,\quad j=1,2;$$
$$R=1,\quad \frac{\partial C_j}{\partial R}\equiv 0,\quad j=1,2;$$
$$Z=0,\quad C_1\equiv 1,\quad C_2\equiv 0,$$
$$1\equiv U_1-\mathrm{Pe}_1^{-1}\frac{\partial C_1}{\partial Z},\quad \frac{\partial C_2}{\partial Z}\equiv 0.$$
$$\frac{\partial U_j}{\partial Z}+\frac{\partial V_j}{\partial R}+\frac{V_j}{R}=0;$$
$$R=1,\quad V_j(1,Z)\equiv 0;\quad Z=0,\quad U_j=U_j(R,0). \tag{60}$$

In industrial conditions the model (60) has a convective form:

$$U_j\frac{\partial C_j}{\partial Z}+V_j\frac{\partial C_j}{\partial R}=(-1)^{(2-j)}K_j(C_1-C_2);$$
$$R=1,\quad \frac{\partial C_j}{\partial R}\equiv 0;\quad j=1,2; \tag{61}$$
$$Z=0,\quad C_1\equiv 1,\quad C_2=0.$$

Average-concentration model

The functions $u_j(r,z),\ v_j(r,z),\ c_j(r,z),\ j=1,2$ in (57) can be presented with the help of the average functions:

$$u_j(r,z)=\bar{u}_jU_j(R,Z),\ v_j(r,z)=\varepsilon\bar{u}_jV_j(R,Z),$$
$$c_j(r,z)=\bar{c}_j(z)\ \tilde{c}_j(r,z),\quad j=1,2. \tag{62}$$

As a result, the following is obtained:

$$\alpha_j(z)\bar{u}_j\frac{d\bar{c}_j}{dz}+\left[\beta_j(z)+\gamma_j(z)\right]\bar{u}_j\bar{c}_j=$$
$$=D_j\frac{d^2\bar{c}_j}{dz^2}+(-1)^{(2-j)}k(\bar{c}_1-\chi\bar{c}_2);$$
$$z=0,\quad \bar{c}_j(0)\equiv(2-j)c_j^0,\quad \frac{d\bar{c}_j}{dz}\equiv 0;\quad j=1,2. \tag{63}$$

where

$$\alpha_j(z)=\frac{2}{r_0^2}\int_0^{r_0}rU_j\tilde{c}_j\,dr,$$
$$\beta_j(z)=\frac{2}{r_0^2}\int_0^{r_0}rU_j\frac{\partial\tilde{c}_j}{\partial z}\,dr,$$
$$\gamma_j(z)=\frac{2}{r_0^2}\int_0^{r_0}rV_j\frac{\partial\tilde{c}_j}{\partial r}\,dr,$$
$$U_j=U_j(R,Z),\quad V_j=V_j(R),$$
$$\tilde{c}_j(r,z)=\tilde{C}_j(R,Z),\quad j=1,2. \tag{64}$$

The theoretical analysis of the model (63) will be made, using the next generalized variables and functions:

$$r=r_0R,\quad z=lZ,\quad \bar{c}_j(z)=c_j^0\bar{C}_j(Z),\quad c_2^0=\frac{c_1^0}{\chi},$$
$$\bar{C}_j(Z)=2\int_0^1RC_j(R,Z)\,dR,$$
$$\tilde{c}_j(r,z)=\frac{c_j(r,z)}{\bar{c}_j(z)}=\frac{C_j(R,Z)}{\bar{C}_j(Z)}=\tilde{C}_j(R,Z),$$
$$\alpha_j(z)=A_j(Z)=2\int_0^1RU_j(R,Z)\tilde{C}_j(R,Z)\,dR,$$
$$\beta_j(z)=B_j(Z)=2\int_0^1RU_j(R,Z)\frac{\partial\tilde{C}_j}{\partial Z}\,dR,$$
$$\gamma_j(z)=G_j(Z)=2\int_0^1RV_j(R)\frac{\partial\tilde{C}_j}{\partial R}\,dR,\quad j=1,2, \tag{65}$$

and as a result the model (63) has the form:

$$A_j(Z)\frac{d\bar{C}_j}{dZ}+\left[B_j(Z)+G_j(Z)\right]\bar{C}_j=$$
$$=\mathrm{Pe}_j^{-1}\frac{d^2\bar{C}_j}{dZ^2}+(-1)^{(2-j)}K_j(\bar{C}_1-\bar{C}_2);$$
$$Z=0,\quad \bar{C}_1=1,\quad \bar{C}_2=0,$$
$$\frac{d\bar{C}_1}{dZ}=0,\quad \frac{d\bar{C}_2}{dZ}=0;\quad j=1,2. \tag{66}$$

In industrial conditions the model (66) has the convective form:

$$A_j(Z)\frac{d\bar{C}_j}{dZ}+\left[B_j(Z)+G_j(Z)\right]\bar{C}_j=$$
$$=(-1)^{(2-j)}K_1\omega^{(j-1)}(\bar{C}_1-\bar{C}_2);$$
$$Z=0,\quad \bar{C}_1=1,\quad \bar{C}_2=0;\quad j=1,2. \tag{67}$$

Axial and radial velocity components

The theoretical analysis of the effect of the radial velocity components in a column can be made by an appropriate hydrodynamic model. In generalized

variables, as an example, is possible to be used the next velocity distributions, where the difference between the gas and liquid flows is in the average (inlet) velocities, only:

$$U_j = (2-0.4Z) - 2(1-0.4Z)R^2,$$
$$V_j = 0.2\left(R - R^3\right), \quad j = 1.2, \tag{68}$$

where $V_j < 0.1$, $j = 1,2$ and must be presented with the help of a small parameter $0.1 = \alpha$ 1, i.e.

$$V_j = \alpha V_{j0}, \quad V_{j0} = 0.2\left(R - R^3\right)\alpha^{-1}, \quad j = 1,2. \tag{69}$$

In the cases of physical absorption) of an average soluble gas (ω 1) in an industrial absorption column, the convection-diffusion and average-concentration models (61, 67) have the forms:

$$\begin{aligned}
&U_1 \frac{dC_1}{dZ} + \alpha V_{10} \frac{dC_1}{dR} = -K_1 (C_1 - C_2);\\
&U_2 \frac{dC_2}{dZ} + \alpha V_{20} \frac{dC_2}{dR} = \omega K_1 (C_1 - C_2);\\
&R = 1, \quad \frac{\partial C_j}{\partial R} \equiv 0, \quad j = 1,2;\\
&Z = 0, \quad C_1 \equiv 1, \quad C_2 = 0.
\end{aligned} \tag{70}$$

$$\begin{aligned}
&\left(1 + a_{11}Z + a_{12}Z^2\right)\frac{d\bar{C}_1}{dZ} +\\
&+\left(b_{10} + b_{11}Z^{b_{12}} + g_1 Z\right)\bar{C}_1 = -K_1\left(\bar{C}_1 - \bar{C}_2\right);\\
&Z = 0, \quad \bar{C}_1 \equiv 1;\\
&\left(a_{20} + a_{21}Z + a_{22}Z^2\right)\frac{d\bar{C}_2}{dZ} + \left(b_{20} + b_{21}Z^{b_{22}} +\right.\\
&\left.+ g_{20} + g_{21}Z\right)\bar{C}_2 = \omega K_1\left(\bar{C}_1 - \bar{C}_2\right);\\
&Z = 0, \quad \bar{C}_2 \equiv 0;
\end{aligned} \tag{71}$$

where the parameters a_{j0}, a_{j1}, a_{j2}, b_{j0}, b_{j1}, b_{j2}, g_{j0}, g_{j1}, $j = 1,2$, K_1 must be obtained using experimental data.

The solution of (70), in the case $K_1 = 1, \omega = 1$, is obtained with the help of the perturbation method [10]. The solution of (70) and (65) permits to be obtained the average concentrations in the phases $\bar{C}_j(Z), i = 1,2$ ("theoretical" values, the points in Fig. 14).

The values of the functions $\bar{C}_j(Z)$, $j = 1,2$ permit to be obtained the values of $\bar{C}_j(1)$, $j = 1,2$ and the artificial experimental data (36), which are used for the parameters $P\left(a_{j0}, a_{j1}, a_{j2}, b_{j0}, b_{j1}, b_{j2}, g_{j0}, g_{j1}, K_1\right)$, $j = 1,2$ identification in the average concentrations model (71), by the minimization of the least-squares function (37) with respect to P, where the values of $\bar{C}_j(1, P)$, $j = 1,2$ are obtained as solution of (71).

The ("experimental") values of the parameters a_{j0}, a_{j1}, a_{j2}, b_{j0}, b_{j1}, b_{j2}, g_{j0}, g_{j1}, K_1, $j = 1,2$ are obtained for the solution of (71) and the results (lines) are compared (Fig 14) with the solution (points) of (70) and (65).

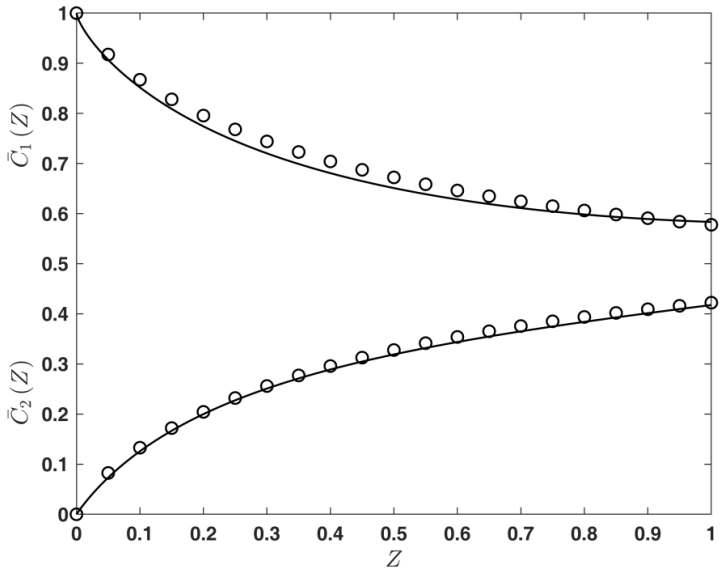

Fig. 14. Concentration distributions $\bar{C}_j(Z)$, $j = 1,2$: solution of (71) (lines); solution (points) of (70) and (65).

REFERENCES

1. Chr. Boyadjiev, Theoretical Chemical Engineering. Modeling and Simulation, Springer-Verlag, Berlin Heidelberg, 2010.
2. Chr. Boyadjiev, M. Doichinova, B. Boyadjiev, P. Popova-Krumova, Modeling of Column Apparatus Processes, Springer-Verlag, Berlin Heidelberg, 2016.
3. Chr. Boyadjiev, M. Doichinova, B. Boyadjiev, P. Popova-Krumova, Modeling of Column Apparatus Processes, 2nd edn., Springer-Verlag, Berlin Heidelberg, 2018.
4. B. Boyadjiev, Chr. Boyadjiev, New models of industrial column chemical reactors, *Bul. Chem. Commun.*, **49**, 706, 2017.
5. B. Boyadjiev, Chr. Boyadjiev, New models of industrial column absorbers. 1. Co-current absorption processes, *Bul. Chem. Commun.*, **49**, 711, 2017.
6. B. Boyadjiev, Chr. Boyadjiev, New models of industrial column absorbers. 2. Counter-current absorption processes, *Bul. Chem. Commun.*, **49**, 720, 2017.
7. B. Boyadjiev, Chr. Boyadjiev, A new approach for modeling of industrial adsorption column, *J. Eng. Thermophysics*, **27**, 1, 2018.
8. B. Boyadjiev, Chr. Boyadjiev, A new approach for modeling of industrial catalytic column, *J. Eng. Thermophysics*, 2018, (in press).
9. B. Boyadjiev, Chr. Boyadjiev, A new approach to modeling of chemical processes in industrial column apparatuses, *Chem. Eng. Techn*., 2018, (in press).
10. B. Boyadjiev, Chr. Boyadjiev, A new approach to modeling of chemical processes in industrial column apparatuses, *Chem. Eng. Techn*., 2018, (in press).

НОВ ПОДХОД ЗА МОДЕЛИРАНЕ И СИМУЛАЦИЯ НА ХИМИЧНИ И МАСОПРЕНОСНИ ПРОЦЕСИ В КОЛОННИ АПАРАТИ

Хр. Бояджиев, Б. Бояджиев

Институт по инженерна химия, Българска академия на науките, ул. Акад. Ст. Ангелов, бл. 103, 1113 София, България

Постъпила на 20 март, 2018 г.; приета на 26 юни, 2018 г.

(Резюме)

Класическата теория на масопренасяне не е приложима за моделиране на масопренасянето при химически, абсорбционни, адсорбционни и каталитични процеси в колонни апарати, където разпределението на скоростите и междуфазовите граници са неизвестни. Моделирането на тези процеси е свързано със създаването на нов тип конвективно-дифузионни модели (за качествен анализ) и модели на средната концентрация (за количествен анализ), където повърхностните реакции са заменени с еквивалентна обемна реакция, а скоростта и разпределението на концентрациите са заменени със средна скорост и концентрации. Влиянието на радиалната неравномерност на скоростта в моделите на средната концентрация се въвежда чрез модели параметри, които трябва да се определят експериментално. Новите конвекционно-дифузионни модели и тези на средната концентрация са получени в случаи на различни процеси в колонните апарати: прости и сложни химични реакции, физична и химична абсорбция, физична и химична адсорбция, хетерогенни каталитични процеси (физичен и химичен адсорбционен механизъм). Тези модели са представени в монографията на Хр. Бояджиев, М. Дойчинова, Б. Бояджиев, П. Попова-Крумова „Моделиране на процеси в колонни апарати”, второ издание, изд. Springer, Берлин-Хайделберг, 2018 г. Разгледани са две хидродинамични ситуации, когато радиалният скоростен компонент е равен на нула в случаите на аксиално модифициране на радиалната неравномерност на аксиалния скоростен компонент и когато радиалният скоростен компонент е различен от нула. Използването на експериментални данни за средните концентрации в края на колоната, за конкретен процес и колона, позволява да се получат параметрите на модела, свързани с радиалната неравномерност на скоростта. Стойностите на тези параметри позволяват да се използват модели на средната концентрация за моделиране на различни процеси.

Bulgarian Chemical Communications, Volume 50, Special Issue K (pp. 24 – 35) 2018

Multi-period deterministic model of sustainable integrated of hybrid first and second generation bioethanol supply chains for synthesis and renovation

B. Ivanov

Institute of Chemical Engineering, Bulgarian Academy of Sciences, Sofia, Bulgaria

Received March 20, 2018, Accepted June 20, 2018

This paper focuses on designing mathematical model ofan integrated bioethanol supply chain (IBSC) that will account for economic and environmental aspects of sustainability. A mixed integer linear programming model is proposed to design an optimal IBSC. Bioethanol production from renewable biomass has experienced increased interest in order to reduce Bulgarian dependence on imported oil and reduce carbon emissions. Concerns regarding cost efficiency and environmental problems result in significant challenges that hinder the increased bioethanol production from renewable biomass. The model considers key supply chain activities including biomass harvesting/processing and transportation. The model uses the delivered feedstock cost, energy consumption, and GHG emissions as system performance criteria. The utility of the supply chain simulation model is demonstrated by considering a biomass supply chain for a biofuel facility in Bulgarian scale. The results show that the model is a useful tool for supply chain management, including selection of the optimal bioethanol facility location, logistics design, inventory management, and information exchange.

Keywords: Bioethanol supply chain, Mathematical model, Economic and environmental aspects.

1. INTRODUCTION

Production and use of biofuels are promoted worldwide. Their use could potentially reduce emissions of greenhouse gases and the need for fossil fuels [1]. Accordingly, the European Union imposes a mandatory target of 10% biofuels by 2020 [2]. These fuels are produced from biomass. Their use for energy purposes has the potential to provide important benefits. Burning them releases such amount of CO_2 as was absorbed by the biomass in its formation [3]. Another advantage of biomass is its availability in the world due to its variety of sources. Despite the advantages of biomass with increasing quantities of biofuels to achieve the objectives of the European Union, this is accompanied by growing quantities of waste products. These wastes are related to the lifecycle of biofuels from crop cultivation, transportation, production to distribution and use. The main liquid biofuels are bioethanol and biodiesel. Depending on the raw material used, production is considered in three generations.

The first generation uses as feedstock crops containing sugar and starch to produce bioethanol, and oilseed crops to produce biodiesel [4]. In the production of biodiesel, the advantage of these materials is that they can be grown on contaminated and saline soils, as the process does not affect the fuel production. The drawback is that they raise issues related to their competitiveness in the food sector. These materials also have a negative impact in terms of the quantity of water consumed. This is related to their cultivation that requires significant amounts of water resources. Excessive use of fertilizers, pesticides and chemicals to grow them also leads to accumulation of pollutants in groundwater that can penetrate into water sources and thus degrade water quality.

According to the second generation, bioethanol is produced by using waste biomass (agricultural and forest waste) as raw material [5], i.e. lignocellulose which is transformed into a valuable resource as bioethanol. Biofuel production of second generation is an excellent way to deal with increasingly restrictive national and European regulations in this area and the use of organic waste for energy production and fertilizer as a byproduct. Logistics and use of these materials can be challenging due to the fact that they are usually dispersed. Another disadvantage from an environmental perspective is the need for further purification and processing.

The third generation comprises production from microalgae which occur as a promising feedstock for biofuel production. The advantage of this biomass is that it is a year-round production and does not compete with the food industry.

The main technologies for production of bioethanol are fermentation, distillation and dehydration [6]. The wastes of biofuels are divided into production and performance. The technological waste is produced mainly in the creation of products that occur as waste production. The management of these wastes is related to their

* To whom all correspondence should be sent:
E-mail: bivanov1946@gmail.com

reduction, recovery and disposal. These guidelines are united in the idea of acquiring more sophisticated production processes. Efforts are focused on the use of new sources of raw materials, new processes, and new ways of realization of the side products. The use of by-products as raw materials for other production closes the cycle in the supply chain, reducing the price of the obtained fuel. Operational waste is associated with gases and emissions released during operation and burning of biofuels.

2. AIM

The present study deals with the issue of designing optimal integrated bioethanol supply chains (IBSC) for waste management in the process of biofuel production and usage. Tools were developed for formulation of a mathematical model for description of the parameters, the restrictions and the goal function.

3. PROBLEM STATEMENT

The problem addressed in this work can be formally stated as follows. Given are a set of biofuel crops that can be converted to bioethanol. These include agricultural feedstock, e.g. wheat, corn, etc. A planning horizon of one year for government regulations including manufacturing, construction and carbon tax is considered. An IBSC network superstructure including a set of harvesting sites and a set of demand zones, as well as the potential locations of a number of collection facilities and bio refineries are set. Data for biofuel crops production and harvesting are also given. For each demand zone, the biofuel demand is given, and the environmental burden associated with bioethanol distribution in the local region is known. For each transportation link, the transportation capacity, available transportation modes, distance, and emissions of each transportation type are known.

3.1. General formulation of the problem

The overall problem can be summarized as follows:

- Optimal locations of biofuel production centers,
- Demand for petroleum fuel for each of the demand centers,
- The minimum required ratio between petroleum fuel and biofuel for blending,
- Biomass feedstock types and their geographical availability,
- Specific green house gas(GHG) emission factors of the biofuel life cycle stages,
- Potential areas where systems for utilization of solid waste from production can be installed.

The objectives are to minimize the total cost of an IBSC by optimizing the following decision variables:

- Supply chain network structure,
- Locations and scales of bioethanol production facilities and biomass cultivation sites,
- Flows of each biomass type and bioethanol between regions,
- Modes of transport for delivery for biomass and bioethanol,
- The GHG emissions for each stage in the life cycle,
- Supply strategy for biomass to be delivered to facilities,
- Distribution processes for biofuel to be sent to demand zones.

4. MODEL FORMULATION

The role of the optimization model is to identify what combination of options is the most efficient approach to supply the facility. The problem for the optimal location of bioethanol production plants and the efficient use of the available land is formulated as a MILP model with the following notation:

4.1. Mathematical model description

To start with the description of the MILP model, we first introduce the parameters, that are constant and known a priori, and the variables that are subject to optimization. Then we describe step by step the mathematical model by presenting the objective function and all the constraints. First of all, we introduce the set of time intervals of the horizon of planning $t = \{1,2,...,T\}$.

In this article the mathematical model that is used in the network design is described. Before describing the mathematical model, the input parameters, the decision variables, and the sets, subsets and indices are listed below.

4.1.1. Sets, subsets and indices. The following sets and subsets are introduced:

Sets/indices:

I	Set of biomass types indexed by i;
LF	Set of transport modes indexed by lf ;
P	Set of plant size intervals indexed by p ;
S	Set of utilization plant size intervals indexed by $s = \overline{1, N_s}$;
GF	Set of regions of the territorial division indexed by gf ;
K	Set of proportion of bioethanol and gasoline indexed by k ;
T	Set of time intervals, indexed by t .

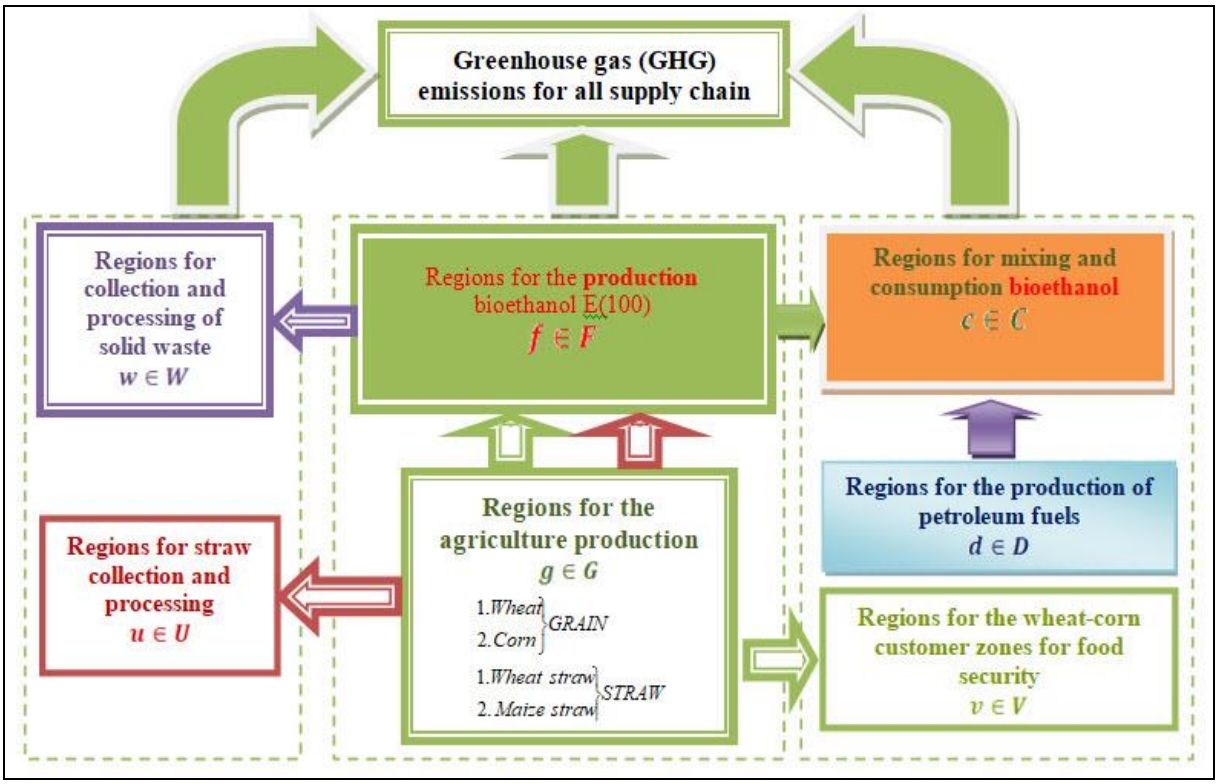

Fig.1. Superstructure of an integrated bioethanol supply chain (IBSC)

Subsets/indices:

B Set of transport modes for bioethanol and gasoline is a subset of LF ($B \subset FL$) indexed by b;

L Set of transport modes for biomass is a subset of LF ($L \subset LF$) indexed by l;

M Set of transport modes for solid wastes is a subset of LF ($M \subset LF$) indexed by m;

E Set of transport modes for straw is a subset of LF ($E \subset LF$) indexed by e;

Z Set of transport modes for wheat-corn for food security is a subset of LF ($Z \subset LF$) indexed by z;

F Set of candidate regions for bioethanol plants established, which is a subset of GF ($F \subset GF$) indexed by f;

C Set of bioethanol mixing and customer zones, which is a subset of GF ($C \subset GF$) indexed by c;

D Set for delivery and production of gasoline, which is a subset of GF ($D \subset GF$) indexed by d;

W Set for regions for collection and processing of solid waste, which is a subset of GF ($W \subset GF$) indexed by w;

U Set for regions for straw collection and processing, which is a subset of GF ($U \subset GF$) indexed by u;

V Set for regions for the wheat-corn customer zones, which is a subset of GF ($V \subset GF$) indexed by v;

4.1.2. Input parameters for the problem

Environmental parameters:

$EFBP_{ip}$ Emission factor for bioethanol production from biomass type $i \in I$ using technology $p \in P$, [$kgCO_2 - eq/tonbiofuel$];

ESW Emission factor of pollution caused by one ton of solid waste if not used, [$\frac{kgCO_2 - eq}{ton\,solid\,waste}$]

$EFDP_d$ Emission factor for gasoline production in the region $d \in D$, [$kgCO_2 - eq/tongasoline$];

$EFTRA_{il}$ Emission factor for biomass $i \in I$ supply *via* mode $l \in L$, [$kgCO_2 - eq/tonkm$];

$EFTRB_b$ Emission factor for bioethanol supply *via* mode $b \in B$, [$kgCO_2 - eq/tonkm$];

$EFTM_{il}$ Emission factor of transportation of biomass $i \in I$ for mode $l \in L$, [$kgCO_2 - eq/tonkm$];

$EFTB_b$ Emission factor of transportation of bioethanol and gasoline for mode $b \in B$, $kgCO_2 - eq/tonkm$];

$EFTRW_m$ Emission factor for transport of solid waste with transport $m \in M$, [$kgCO_2 - eq/tonkm$];

$EFTRU_e$ Emission factor for transport of straw with transport $e \in E$, [$kgCO_2 - eq/tonkm$];

$EFTRV_z$ Emission factor for transport of wheat-corn for food security with transport $z \in Z$, [$kgCO_2 - eq/tonkm$];

ECB, ECG Emissions during the combustion of CO_2 unit bioethanol and gasoline, $kgCO_2 - eq/tonbioethanol$] or [$kgCO_2 - eq/tongasoline$].

Monetary parameters:

$CosB_p$, $CosW_s$ Capital investment of bioethanol plant size $p \in P$ and capital investment of solid waste plant size $s \in S$, [$];

C_{CO_2} Carbon tax per unit of carbon emitted from the operation of the IBSC, [$/ $kgCO_2 - eq$];

PG Price of gasoline, [$/ton];

UTI_{il}, UTB_b, UTG_b, UTS_m, UTU_e, UTV_z, Unit transport cost for biomass $i \in I$, *via* mode $l \in L$, bioethanol *via* mode $b \in B$, gasoline*via* mode $b \in B$, solid wastes *via* mode $m \in M$, straw *via* mode $e \in E$, wheat-corn for food security *via* mode z, [$/tonkm];

Technical parameters:

PB_p^{MAX} / PB_p^{MIN} Maximum/Minimum annual plant capacity of size $p \in P$ for bioethanol production, [$ton/year$];

ENO, ENB Energy equivalent unit of gasoline&bioethanol, [GJ/ton];

ADD_{dcb}, ADG_{gfl}, ADF_{fcb}, ADU_{gue}, ADW_{fwm}, ADV_{gvz} Actual delivery distance between grids *via* model of transport ($b \in B$, $l \in L$, $e \in E$, $m \in M$, $z \in Z$), [km];

SW_{ip} The total amount of solid waste generated for production of bioethanol using biomass i for technology p, [$\frac{ton\ solid\ waste}{ton\ biofuel}$];

$JobB_p$, $JobO_p$ The number of jobs needed to build and operation a bio-refinery with size $p \in P$ for year;

$JobG_{ig}$ The number of jobs required to grow a unit of i biosource in the region $g \in G$ per year.

Environmental parameters depending on the time interval:

$EFBC_{igt}$ Emission factor for cultivation of biomass type $i \in I$ in region $g \in G$ for each time interval t, [$kgCO_2 - eq/tonbiomass$];

TEI_t^{MAX} Maximum total environmental impact, [$kgCO_2 - eqd^{-1}$].

Monetary parameters depending on the time interval:

ς_t Interest rate, %;

ε_t Discount factor;

M_{ft}^{const} Factor to the change of the base price, depending on the region $f \in F$ where the plant is installed, [$Dimensionless$];

$Cost_{pft}^F$ Capital investment of plant size p for bioethanol production in each zone f, [$];

INS_{ft} The government incentive includes construction incentive and volumetric from region $f \in F$, [$/ton];

UPC_{igt} Unit production costs for biomass type $i \in I$ in the region $g \in G$ for each time interval $t \in T$, [$/ton];

UPB_{ipft} Unit bioethanol production cost from biomass type $i \in I$ at a biorafinery of scale $p \in P$ installed in region $f \in F$, [$/ton];

UPD_{dt} Unit gasoline production cost at a rafinery d, [$/ton].

Technical parameters depending on the time interval:

K_{ct}^{mix} Proportion of bioethanol and gasoline subject of mixing for each of the customer zones, [$Dimensionless$];

A_{gt}^S Set-aside area available in region $g \in G$ for biomass production for each time interval $t \in T$, [ha];

A_{gt}^{Food} Set-aside area available in region $g \in G$ for food, [ha];

β_{igt} Production rate of biomass i in region $g \in G$, [ton/ha];

LT_t Duration of time intervals $t \in T$, [$year$];

α_t Operating period for IBSC in a year, [$d/year$];

γ_{ipt} Biomass to bioethanol conversion factor s pecific for biomass i using technology p, [$ton\_bioethanol\ /ton\_biomass$];

YO_{ct} Gasoline demand in customer zones $c \in C$, [$ton/year$];

PBI_{igt}^{MIN} / PBI_{igt}^{MAX} Minimum/ Maximum biomass of type $i \in I$ which can be produced in the region, $g \in G$ per year, [$ton/year$];

QI_{igt}^{MAX} Maximum flow rate of biomass i from region g, [ton/d];

QB_{ft}^{MAX} Maximum flow rate of bioethanol from region f, [ton/d];

QD_{dt}^{MAX} Maximum flow rate of gasoline from region d, [ton/d];

QW_{ft}^{MAX} Maximum flow rate of solid wastes from f, [ton/d];

QU_{gt}^{MAX} Maximum flow rate of straw from region $g \in G$, [ton/d];

QV_{gt}^{MAX} Maximum flow rate of wheat-corn for food security from region $g \in G$, [ton/d];

4.1.3. Decision variables for the problem X_t

To find the optimal configuration of the IBSC, the following decision variables are required:

A/ Positive continuous variables

PBB_{igt} Biomass i demand in region $g \in G$ at time interval $t \in T$;

QI_{igflt} Flow rate of biomass $i \in I$ via mode $l \in L$ from region $g \in G$ to $f \in F$, for each $t \in T$, [ton/d];

QB_{fcbt} Flow rate of bioethanol produced from all biomass $i \in I$ via mode $b \in B$ from region $f \in F$ to $c \in C$ for each $t \in T$, [ton/d];

QBP_{ifcbpt} Flow rate of bioethanol produced from biomass i *via* mode b from f to c using technology p for each $t \in T$, [ton/d];

QD_{dcbt} Flow rate of gasoline *via* mode $b \in B$ from region $d \in D$ to $c \in C$, for each time interval $t \in T$, [ton/d];

QW_{fwmt} Flow rate of solid waste *via* mode $m \in M$ from the region $f \in F$ to $w \in W$, for each $t \in T$, [ton/d];

QU_{guet} Flow rate of straw collection and processing *via* mode e from region g to u, for each $t \in T$, [ton/d];

QV_{gvzt} Flow rate of wheat-corn for food security *via* mode $z \in Z$ from region $g \in G$ to $v \in V$, for each $t \in T$, [ton/d];

QED_{ct} Quantity of gasoline to be supplied to meet the energy needs of the region $c \in C$, for each $t \in T$, [$ton/year$];

QEB_{ct} Quantity of bioethanol produced from biomass to be supplied to meet the energy needs of the region $c \in C$, [$ton/year$];

A_{igt} Land occupied by crop i in region g, [ha];

A_{igt}^{F} Land by crops needed for food security of the population in the region $g \in G$, for each $t \in T$,

B/ Binary variables

X_{igflt} 0-1 variable, equal to 1 if biomass type i is transported from region g to f using transport l, and 0 otherwise at $t \in T$;

Y_{fcbt} 0-1 variable, equal to 1 if bioethanol is transported from region f to c using transport b, l, and 0 otherwise at $t \in T$;

WS_{fwmt} 0-1 variable, equal to 1 if a solid waste is transported from region f to w using transport m and 0 otherwise for each $t \in T$;

WU_{guet} 0-1 variable, equal to 1 if straw is transported from region g to $u \in U$ using transport $e \in E$ and 0 otherwise for each $t \in T$;

WV_{gvzt} 0-1 variable, equal to 1 if wheat-corn is transported from region g to v using transport z and 0 otherwise for each $t \in T$;

ZW_{swt} 0-1 variable, equal to 1 if a solid waste utilization plant size s is installed in region w and 0 otherwise at time interval $t \in T$;

ZWF_{swt} 0-1 variable, equal to 1 if a solid waste utilization plant size s is to be working in region w and 0 otherwise at $t \in T$, which includes the plants installed in the previous time and the new ones built during this time which is calculated with equation $ZWF_{swt} = ZWF_{sw(t-1)} + ZW_{swt}$ for the first year ($t = 1$) configuration is set by initializing $ZWF_{sw'1'} = ZW_{sw'1'}$;

Z_{pft} 0-1 variable, equal to 1 if bioethanol production plant size p is to be established in region f and 0 otherwise for each $t \in T$;

ZF_{pft} 0-1 variable, equal to 1 if bioethanol production plant size $p \in P$ is to be working in region $f \in F$ and 0 otherwise at time interval $t \in T$, which includes the plants installed in the previous time interval and the new ones built during this time interval which is calculate with equation $ZF_{pft} = ZF_{pf(t-1)} + Z_{pft}$ for first year ($t = 1$) configuration is set by initializing $ZF_{sw'1'} = Z_{sw'1'}$;

PD_{dt} 0-1 variable, equal to 1 if gasoline is manufactured by the region $d \in D$ and 0, otherwise at time interval $t \in T$;

DT_{dcbt} 0-1 variable, equal to 1 if gasoline is transported from region d to c using transport b and 0 otherwise for each $t \in T$.

5.1. Basic relationships

As noted above, the assessment of IBSC production and distribution of bioethanol will be made by environmental and economic criteria.

5.1.1. Model of total environmental impact of IBSC

The environmental impact of the IBSC is measured in terms of total GHG emissions ($kg\,CO_2-eq$) stemming from supply chain activities and the total emissions are converted to carbon credits by multiplying them with the carbon price in the market.

The environmental objective is to minimize the total annual GHG emission resulting from the operations of the IBSC. The formulation of this objective is based on the field-to wheel life cycle analysis, which takes into account the following life cycle stages of biomass-based liquid transportation fuels:

- biomass cultivation, growth and acquisition,
- biomass transportation from source locations to facilities,
- transportation of bioethanol facilities to the demand zones,
- local distribution of liquid transportation fuels in demand zones,
- emissions from bioethanol and gasoline usage.

Ecological assessment criteria will represent the total environmental impact at work on IBSC through the resulting GHG emissions for each time interval t. These emissions are equal to the sum of the impact that each of the stages of life cycle has on the environment. The GHG emission rate is defined as follows for each $t \in T$:

$$TEI_t = ELS_t + ELB_t + ELD_t + ETT_t + ESW_t + ECAR_t, \forall t \quad (1)$$

where:

TEI_t Total GHG impact at work on IBSC [$kg\,CO_2-eq\,d^{-1}$];

$\{ELS_t, ELB_t, ELD_t, ETT_t\}$ GHG impact of life cycle stages;

$ECAR_t$ Emissions from bioethanol and gasoline usage in vehicle operations [$kg\,CO_2-eq\,d^{-1}$];

ESW_t Emissions from utilization solid waste for each $t \in T$.

Evaluation of environmental impact at every stage of life cycle is:

A. *Growing biomass* ELS_t;

B. *Production of bioethanol* ELB_t;

C. *Production of petroleum* gasoline ELD_t;

D. *Utilization of solid wastes* ESW_t

E. *Transportation biomass* ETA_t;

F. *Transportation bioethanol* ETE_t;

G. *Transportation gasoline* ETD_t;

H. *Transportation of solid waste* ETW_t;

I. *Transportation of straw* ETU_t;

J. *Transportation of wheat-corn for food security* ETV_t;

K. *Usage of bioethanol and gasoline* $ECAR_t$.

1/ Greenhouse gases to grow biomass ELS_t,

GHG emissions resulting from the production of biomass depend on the cultivation practice adopted as well as on the geographical region in which the biomass crop has been established [7]. In particular, the actual environmental performance is affected by fertilisers and pesticides usage, irrigation techniques and soil characteristics. The factor may differ strongly from one production region to another. Accordingly, the biomass production stage is defined as follows:

$$ELS_t = \sum_{i\in I}\sum_{g\in G}\left(EFBC_{igt}\frac{\beta_{igt}A_{igt}}{\alpha_t}\right), \ \forall t, \quad (2)$$

2/ Total GHG emissions from bioethanol production ELB_t

The environmental impact of the bioethanol production stage is related to raw materials and the technology employed for the production of bioethanol.

$$ELB_t = \sum_{i\in I}\sum_{f\in F}\sum_{c\in C}\sum_{b\in B}\sum_{p\in P}\left(EFBP_{ip}QBP_{ifcbpt}\right), \ \forall t \quad (3)$$

Since only one of the technologies $p \in P$ can be selected for a region $f \in F$ (which is guaranteed by the condition $\sum_{p\in P} ZF_{pft} \le 1.0 \ \ \forall t, f$), it QBP_{ifcbpt} is equal to "0" for all except $p \in P$ for the selected technology. This is ensured by implementing the inequality $G^{MAX}ZF_{pft} \ge QBP_{ifcbpt}, \ \forall i, f, c, b, p, t$ where G^{MAX} there is a large enough number.

3/ Total GHG emissions from gasoline production ELD_t

$$ELD_t = \sum_{d\in D}\sum_{c\in C}\sum_{b\in B} EDP_{dt}QD_{dcbt}, \ \forall t \quad (4)$$

4/ The environmental impact of transportation ETT_t

The global warming impact related to both biomass supply and fuel distribution depends on the use of different transport means fuelled with fossil energy, typically either conventional oil-based

fuels. The resulting GHG emissions of each transport option depend on both the distance run by the specific means and the freight load delivered. As a consequence, the emission factor represents the total carbon dioxide emissions equivalent accordingly:

$$ETT_t = ETA_t + ETB_t + ETD_t + ETW_t + ETU_t + ETV_t \qquad (5)$$

where,

$ETA_t = \sum_{i\in I}\sum_{g\in G}\sum_{f\in F}\sum_{l\in L}\left(EFTM_{il} ADG_{gfl} QI_{igftl}\right), \ \forall t$ is environmental impact of transportation of biomass $[kgCO_2 - eq\, d^{-1}]$;

$ETE_t = \sum_{f\in F}\sum_{c\in C}\sum_{b\in B}\left(EFTB_b ADF_{fcb} QB_{fcbt}\right), \ \forall t$ is environmental impact of transportation of bioethanol from zones $f \in F$ to $c \in C$ where $QB_{fcbt} = \sum_{i\in I}\sum_{p\in P} QBP_{ifcbpt}$ $[kgCO_2 - eq\, d^{-1}]$;

$ETD_t = \sum_{d\in D}\sum_{c\in C}\sum_{b\in B}\left(EFTB_b ADD_{dcb} QD_{dcbt}\right), \ \forall t$ is environmental impact of transportation of gasoline from zones $d \in D$ to $c \in C$;

$ETW_t = \sum_{f\in F}\sum_{w\in W}\sum_{m\in M}\left(EFTRW_m ADW_{fwm} QW_{fwmt}\right), \ \forall t$ is environmental impact of transportation of solid wastes from zones $f \in F$ to $w \in W$;

$ETU_t = \sum_{g\in G}\sum_{u\in U}\sum_{e\in E}\left(EFTRU_e ADU_{gue} QU_{guet}\right), \ \forall t$ is environmental impact of transportation of straw from zones $g \in G$ to $u \in U$;

$ETV_t = \sum_{g\in G}\sum_{v\in V}\sum_{z\in Z}\left(EFTRV_z ADV_{gvz} QV_{gvzt}\right), \ \forall t$ is environmental impact of transportation of wheat-corn from zones $g \in G$ to $v \in V$;

5/ Total GHG emissions from utilization of solid wastes ESW_t

$$ESW_t = \left(\sum_{i\in I}\sum_{f\in F}\sum_{c\in C}\sum_{b\in B}\sum_{p\in P} SW_{ip} QBP_{ifcbpt} - \sum_{f\in F}\sum_{w\in W}\sum_{m\in M} QW_{fwmt}\right) ESW, \quad \forall t, \qquad (6)$$

6/ GHG emissions from bioethanol and gasolineusage in vehicle operations $ECAR_t$

$$ECAR_t = ECB\sum_{f\in F}\sum_{c\in C}\sum_{b\in B} QB_{fcbt} + ECG\sum_{d\in D}\sum_{c\in C}\sum_{b\in B} QD_{dcbt}, \ \forall t, \ (7)$$

5.1.2. Model of total cost of a IBSC

The annual operational cost includes the biomass feedstock acquisition cost, the local distribution cost of final fuel product, the production costs of final products, and the transportation costs of biomass and final products. In the production cost, we consider both the fixed annual operating cost, which is given as a percentage of the corresponding total capital investment, and the net variable cost, which is proportional to the processing amount. In the transportation cost, both distance-fixed cost and distance-variable cost are considered. The economic criterion will be the cost of living expenses to include total investment cost of bioethanol production facilities and operation of the IBDS. This price is expressed through the dependence [8] for each time interval $t \in T$ **:**

$$TDC_t = TIC_t + TPC_t + TTC_t + TTAXB_t - TL_t, \ \forall t \qquad (8)$$

where:

TDC_t Total cost of a IBSC for year [$\$\, year^{-1}$];

TIC_t Total investment costs of production capacity of IBSC relative to the operational period per year [$\$\, year^{-1}$];

TPC_t Production cost for biorefineries [$\$\, year^{-1}$];

TTC_t Total transportation cost of an IBSC [$\$\, year^{-1}$];

$TTAXB_t$ A carbon tax levied according to the total amount of CO_2 generated in the work of IBSC [$\$\, year^{-1}$];

TL_t Government incentives for bioethanol production and use;

1/ Model investment costs for biorefineries by year TIC_t

A rational IBSC planning over the time is based upon the assumption that once a production facility has been built, it will be operating for the remaining time frame.

$$TIC_t = \varepsilon_t \sum_{f\in F}\sum_{p\in P}\left(Cost_{pf}^{F} Z_{pft}\right), \ \forall t \qquad (9)$$

where ε_t is calculated by equation (10):

$$\varepsilon_t = \frac{1}{(1+\varsigma_t)} \qquad (10)$$

Capital cost of biorefineryforeach regionis determined bythe equation:

$$Cost_{pf}^{F} = M_f^{cost} Cost_p, \forall p \in P, \forall f \in F, \qquad (11)$$

2/ Total production cost model of IBSC TPC_t [$\$\, year^{-1}$]

Total production cost term, TPC_t consists of biomass cultivation TPA_t, bioethanol production costs TPB_t and production cost for gasoline TPD_t as follows for each time interval t:

$$TPC_t = TPA_t + TPB_t + TPD_t, \forall t, \qquad (12)$$

where the components of (12) are defined according to the relations:

$$\left.\begin{aligned} TPA_t &= \sum_{i\in I}\sum_{g\in G}\left(UPC_{igt}A_{igt}\beta_{igt}\right) \\ TPB_t &= \sum_{i\in I}\sum_{f\in F}\sum_{c\in C}\sum_{b\in B}\sum_{p\in P}\left(\alpha_t UPB_{ipft}QBP_{ifcbpt}\right) \\ TPD_t &= \sum_{c\in C}\sum_{b\in B}\sum_{d\in D}\left(\alpha_t UPD_{dt}QD_{dcbt}\right) \end{aligned}\right\},\ \forall t$$

3/ Total transportation cost model TTC_t [$\$\ year^{-1}$]

With regard to transport, both the biomass delivery to conversion plants and the fuel distribution and transport of diesel to blending terminals are treated as an additional service provided by existing actors already operating within the industrial/transport infrastructure. As a consequence, TTC_t is evaluated as follows:

$$TTC_t = TTCA + TTCB_t + TTCD_t +, \forall t \qquad (13)$$

where, $TTCA_t = \sum_{l\in L}\sum_{i\in I}\sum_{f\in F}\sum_{g\in G}\left(\alpha_t UTC_{igfl}QI_{igflt}\right),\ \forall t$ is transportation cost for energy crops, $TTCB_t = \sum_{b\in B}\sum_{c\in C}\sum_{f\in F}\left(\alpha_t UTB_{fcb}QB_{fcbt}\right),\ \forall t$, for bioethanol, $TTCD_t = \sum_{b\in B}\sum_{c\in C}\sum_{d\in D}\left(\alpha_t UTD_{dcb}QD_{dcbt}\right),\ \forall t$ and for gasoline, where,

$$\left.\begin{aligned} UTC_{igfl} &= IA_{il} + \left(IB_{il}ADG_{gfl}\right) \\ UTB_{fcb} &= OA_b + \left(OB_b ADF_{fcb}\right) \\ UTD_{dcb} &= OAD_b + \left(OBD_b ADD_{dcb}\right) \end{aligned}\right\},$$

IA_{il} and IB_{il} is fixed and variable cost for transportation biomass type $i \in I$ and (OA_b, OB_b) is fixed and variable cost for transportation bioethanol.

The biomass transportation cost UTC_{igfl} is described by *Börjesson and Gustavsson* [9], for transportation by tractor, truck and train UTB_{fcb}. They are composed of a fixed cost (IA_{il}, OA_b) and a variable cost (IB_{il}, OB_b). Fixed costs include loading and unloading costs. They do not depend on the distance of transport. Variable costs include fuel cost, driver cost, maintenance cost, etc.

4/ Government incentives for bioethanol production cost model TL_t **,** [$\$\ year^{-1}$]

$$TL_t = \sum_{f\in F}\sum_{c\in C}\sum_{b\in B}\left(INS_{ft}\alpha_t QB_{fcbt}\right),\ \forall t \qquad (14)$$

5/ A carbon tax levied cost model $TTAXB_t$, [$\$\ year^{-1}$]

Many countries are implementing various mechanisms to reduce GHG emissions including incentives or mandatory targets to reduce carbon footprint. Carbon taxes and carbon markets (emissions trading) are recognized as the most cost-effective mechanisms. The basic idea is to put a price tag on carbon emissions and create new investment opportunities to generate a fund for green technology development. There are already a number of active carbon markets for GHG emissions [10].

$$TTAXB_t = \left(\alpha_t TEI_t\right)C_{CO_2},\ \forall t \qquad (15)$$

5.2. Restrictions

Plants capacity limited by upper and lower constrains

Plants capacity is limited by upper and lower bounds, where the minimal production level in each region is obtained by:

$$\sum_{p\in P}\left(PB_p^{MIN}ZF_{pft}\right) \le \alpha_t\sum_{c\in C}\sum_{b\in B}QB_{fcbt} \le \sum_{p\in P}\left(PB_p^{MAX}ZF_{pft}\right), \forall f,t \qquad (16)$$

$$\left.\begin{aligned} &\sum_{m\in M}\sum_{w\in W}QW_{fwmt} \le QW_{ft}^{MAX}, \forall f \\ &\sum_{e\in E}\sum_{u\in U}QU_{guet} \le QU_{gt}^{MAX},\ \forall g \\ &\sum_{z\in Z}\sum_{v\in V}QV_{gvzt} \le QV_{gt}^{MAX},\ \forall g \end{aligned}\right\},\ \forall t \qquad (17)$$

Constraints balance of bioethanol to be produced from biomass available in the regions

$$\alpha_t\sum_{i\in I}\sum_{f\in F}\sum_{c\in C}\sum_{b\in B}\sum_{p\in P}\left(\frac{QBP_{ifcbpt}}{\beta_{igt}\gamma_{ipt}}\right) = \sum_{i\in I}\sum_{g\in G}\left(A_{igt}\right),\ \forall t \qquad (18)$$

A condition that ensures that the total amount of solid waste generated by all bio-refineries can be processed in the plants built for this purpose

$$\sum_{w\in W}\sum_{m\in M}QW_{fwmt} \le \sum_{p\in P}\sum_{i\in I}\sum_{c\in C}\sum_{b\in B}\left(SW_{ip}QBP_{ifcbpt}\right),\ \forall f,t \qquad (19)$$

A restriction that ensures that the amount of solid waste processed at the plant is within its production capacity:

$$\left.\begin{aligned} &\sum_{s\in S}P_s^{MIN}ZWF_{swt} \le \alpha_t\sum_{f\in F}\sum_{m\in M}QW_{fwmt} \\ &\alpha_t\sum_{f\in F}\sum_{m\in M}QW_{fwmt} \le \sum_{s\in S}P_s^{MAX}ZWF_{swt} \end{aligned}\right\},\ \forall t,w \qquad (20)$$

Logical Constrains

- Restriction which guarantees that a given region $f \in F$ installed power plant with $p \in P$ for bioethanol production.

$$\left.\begin{aligned} &\sum_{p\in P}Z_{pft} \le 1 \\ &\sum_{p\in P}ZF_{pft} \le 1 \end{aligned}\right\},\ \forall f,t \qquad (21)$$

and for a utilization systems of solid wastes (21):

$$\left.\begin{array}{l}\sum_{s\in S} ZW_{swt} \le 1 \\ \sum_{s\in S} ZWF_{swt} \le 1\end{array}\right\}, \quad \forall w,t \qquad (22)$$

- Limitation ensuring the availability of at least one connection to a region of bioresources and region for biofuel:

$$\sum_{g\in G}\sum_{l\in L} X_{igflt} \ge \sum_{c\in C}\sum_{b\in B} Y_{fcbt} \ge \sum_{p\in P} ZF_{pft}, \quad \forall i, f, t \qquad (23)$$

- Limit which guarantees that each region will provide only one plant with a biomass type $i \in I$

$$\sum_{f\in F}\sum_{l\in L} X_{igflt} \le 1, \quad \forall i, g, t \qquad (24)$$

- Limitation of assurance that at least one region $f \in F$ producing bioethanol is connected to a costumer zones $c \in C$

$$\sum_{b\in B}\sum_{f\in F} Y_{fcbt} \le 1, \quad \forall c, t \qquad (25)$$

- Limitation of assurance that at least one region f is connected to a solid waste utilization plant located in region $w \in W$

$$\sum_{w\in W}\sum_{m\in M} WS_{fwmt} \le 1, \quad \forall f, t \qquad (26)$$

Condition ensuring that the solid waste produced from a given bio-refinery will be processed in only one of the plants for use

$$\sum_{m\in M}\sum_{w\in W} WS_{fwmt} = \sum_{p\in P} ZF_{pft}, \ \forall f, t \qquad (27)$$

- Condition ensuring that a plant used in a given region will be connected to at least one plant in which solid waste is generated:

$$\sum_{m\in M}\sum_{f\in F} WS_{fwmt} \ge \sum_{s\in S} ZWF_{swt}, \quad \forall w, t \qquad (28)$$

Transport Links

Restrictions on transportation of biomass are:

$$PBI_{ig}^{MIN}\sum_{l\in L} X_{igflt} \le \alpha_t \sum_{l\in L} QI_{igflt} \le PBI_{ig}^{MAX}\sum_{l\in L} X_{igflt}, \forall i, g, f, t \qquad (29)$$

Mass balances between bioethanol plants and biomass regions

The connections between bioethanol plants and biomass regions:

$$\sum_{l\in L}\sum_{g\in G}\sum_{i\in I}\left(QI_{igflt}\right) \le \sum_{p\in P}\left(\frac{PB_p^{MAX} ZF_{pft}}{\gamma_{ipt}}\right), \ \forall f, t \qquad (30)$$

Mass balances between bioethanol plants and customer zones

$$\sum_{b\in B}\sum_{f\in F}\left(\alpha_t QB_{fcbt}\right) = QEB_{ct}, \ \forall c, t \qquad (31)$$

Energy Restriction

- limitation ensuring that the overall energy balance in the region is provided:

$$ENO\sum_{c\in C} QEO_{ct} + ENB\sum_{c\in C} QEB_{ct} = ENO\sum_{c\in C} YO_{ct}, \forall t \qquad (32)$$

- limitation ensuring that each region will be provided in the desired proportions with fuels

$$ENB\, QEB_{ct} = K_{ct}^{mix} ENO\, YO_{ct}, \ \forall c, t \qquad (33)$$

5.3. Economic objective function

Objective function associated with the minimization of the economic costs includes all the operating costs of the supply chain, from the purchase of biomass feedstock to transportation of the final product, as well as the investment cost of biorefineries [11]. The costs of the supply chain are: the cost of raw material, the transport of raw material to the facilities, the cost of transport to the biorefineries, the cost of transformation into bioethanol and the cost of final transport to the blending facilities. The economic objective is to minimize the total annual costs. The terms of the cost objective corresponding to the annual operation costs of the IBSC are described in the following equation:

$$COST = \sum_{t\in T}\left(LT_t TDC_t\right) \qquad (34)$$

Environmental objective function

The environmental objective function corresponds to the minimization of the entire environmental impact measured through the Eco indicator 99 method. The cumulative environmental impact of system performance defined as the amount of carbon dioxide equivalent generated over the whole life cycle and during its operation, is expressed by means of the equation:

$$ENV = \sum_{t\in T}\left(LT_t TEI_t\right) \qquad (35)$$

Social objective function

As an estimate of the social impact of the system work, the exact coefficients that account for indirect jobs in the local economy are used. Then, the social impact (in terms of jobs) is determined according to the relationship [$Number of\ Jobs$]:

$$JOB = \sum_{t\in T}\left(LT_t Job_t\right) \qquad (36)$$

6. OPTIMIZATION PROBLEM FORMULATION

The problem for the optimal design of a IBSC is formulated as a MILP model for the objective function of Minimizing cost.

The task of determining the optimal location of facilities in the regions and their parameters is formulated as follows:

$$\left\{\begin{array}{l} Find: X_t\left[\text{Decision variables}\right]^T \\ MINIMIZE\left\{COST\right\} \rightarrow (Eq.34) \\ s.t.: \left\{Eq.16 - Eq.33\right\} \end{array}\right\} \quad (37)$$

The problem is an ordinary MILP and can thus be solved using MILP techniques. The present model was developed in the commercial software GAMS [12]. The model chooses the less costly pathways from one set of biomass supply points to a specific plant and further to a set of biofuel demand points. The final result of the optimisation problem would then be a set of plants together with their corresponding biomass and biofuel demand points.

7. CASE STUDY: POTENTIAL BIOETHANOL PRODUCTION IN BULGARIA FOR 2016-2020

Two major types of biomass resources, wheat and corn for production of first generation and wheat straw and corncobs for production of second generation bioethanol are used.

Model input data

Bulgaria has 27 regions. In this case study, each region is considered to be a feedstock production region, a potential location of a biorefinery facility and a demand zone. In other words, the biofuel supply chain network consists of 27 areas for feedstock production, 27 potential biorefinery locations, 27 demand zones, 4 potential solid waste utilization zones and 3 regions for the production of petroleum fuels. For the purposes of this study, data on population, cultivated area, as well as the free cultivated area, which in principle can be used for the production of energy crops for bioethanol production are taken from (Ivanov, Stoyanov,2016). For 2016, the consumption of petroleum gasoline for transportation in the country is 572,000 tons and for the next years it is: 2017→762,000t,2018→980,000t,2019→1,220,000t 2020→1,640,000t. For the purposes of this study, it is assumed that the consumption of gasoline for each region is approximately proportional to its size.

8. DISCUSSION AND CONCLUSION

This paper studies the interactions among biofuel supply chain design, agricultural land use and local food market equilibrium. The study was focused on the eco compatible behavior of the stakeholders in the biofuel supply chain incorporating them into the supply chain design model. The model includes the problem of crop rotation and solid waste utilization. The model is believed to be important for practical application and can be used for design and management of similar supply chains.

Table 1. Flow rate of biomass from growing region to bioethanol plants (Plant-R-XX) and solid waste from Plant-R-XX to solid waste plants (SW-R-XX) for 2020.

Transport → TRACTOR							
	Energy crops	Wheat	Corn	Straw Wheat	Straw Corn	Flow path	Solid Waste
Plant-R-9	R-26 to R-9	1.00	1.00	500.72	1.00	Plant-R-9 to SW-R-26	258.24
Plant-R-8	R-12 to R-8	1.00	1.00	500.72	1.00	Plant-R-8 to SW-R-12	258.24
Plant-R-26	R-9 to R-26			500.72		Plant-R-26 to SW-R-26	258.24
	R-26 to R-26	1.00	1.00		1.00		
Plant-R-12	R-8 to R-12			364.03		Plant-R-12 to SW-R-12	258.24
	R-12 to R-12	1.00	1.00	136.68			
	R-22 to R-12				1.00		
Plant-R-27	R-4 to R-27			47.34		Plant-R-27 to SW-R-18	219.51
	R-27 to R-27			78.11			
	R-18 to R-27	1.00	1.00	298.48	1.00		
	R-2 to R-27				1.00		
Plant-R-18	R-27 to R-18	1.00		374.40		Plant-R-18 to SW-R-18	193.68
	R-22 to R-18				1.00		
	R-18 to R-18		1.00				
Plant-R-22	R-14 to R-22	1.00	1.00	393.66	38.02	Plant-R-22 to SW-R-14	258.24
	R-16 to R-22			70.04			

Table 2. Summary of computational results in case - Minimum Annualized Total Cost

Years	2016	2017	2018	2019	2020
Investment cost ($/year)$10^6$	1.862	2.793	3.531	4.462	6.248
Production cost ($/year)$10^6$	4.326	6.740	9.907	13.871	20.756
Transportation cost ($/year)$10^6$	3.165	4.457	6.086	8.317	12.854
Carbon tax levied in the work of IBSC ($/year)$10^6$	1.743	2.727	4.014	5.661	12.952
Government incentives for bioethanol production	-2.800	-4.371	-6.453	-9.079	-13.622
TOTAL COST ($/year)$10^6$	8.297	12.346	17.086	23.232	34.778
GHG emission to grow biomass	1422	1413	1978	1792	1792
GHG emission for production bioethanol and waste	64.220	100.238	147.930	208.018	312.033
GHG emission from transportation	228.289	211.298	311.615	266.253	277.120
GHG emission from biofuel usage	37.866	59.113	87.276	122.781	184.219
Total GHG emission for IBSC (kgCO2-eq./year)10^6	1752.468	1783.808	2525.148	2389.185	2565.732
Bioethanol produced from grain (ton/Year)	337	505	674	842	1179
Bioethanol produced from Straw and Maize cobs	32221	50323	74370	104730	157220
TOTAL BIOETHANOL PRODUCTION (ton/year)	32558	50828	75044	105573	158400
TOTAL GAZOLINE NEED (ton/year)	552015	730801	933938	1155199	1542775
Proportion Bioethanol/Gasoline (%)	6%	7%	8%	9%	10%
Social function Job_t ($Number of\ Jobs$)	200	100	90	100	200

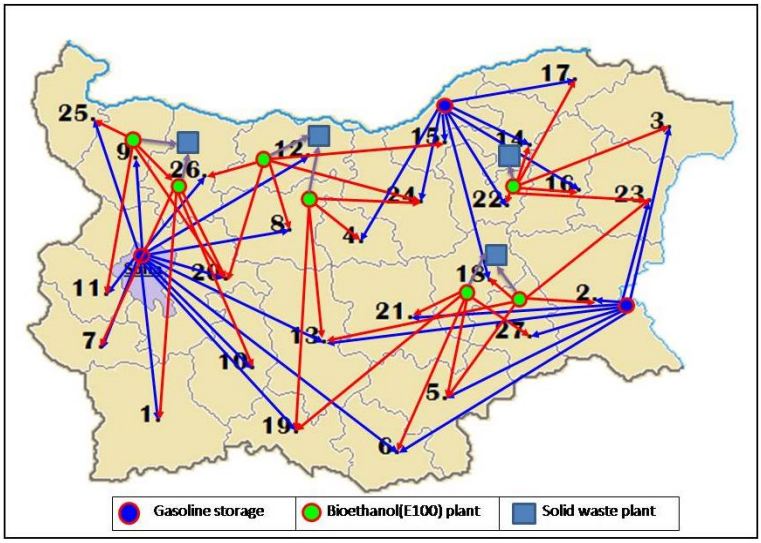

***Fig. 2**. Optimal BG IBSC configuration for 2020*

***Acknowledgements**: The author would like to thank the Bulgarian National Science Fund for the financial support obtained under contract DN 07-14/15.12.2016.*

REFERENCES

1. IEA, World energy outlook 2007, Paris, France, International Energy Agency, 2007.
2. European Commission, Directive 2009/28/EC of the European Parliament and of the Council of 23 April 2009 on the Promotion of the use of energy from renewable sources and Amending and Subsequently Repealing Directives 2001/77/EC and 2003/30/EC. *Official J. Eur. Parliam.*, Brussels.
3. O. Kitani, H.W. Carl, The state of food and agriculture. New York: Food and Agriculture Organization, Rome, Italy: FAO, 2008, vol. 5.
4. C. Mireta, Ph. Chazara, L. Montastruc, S. Negny, S. Domenech,Design of bioethanol green supply chain: Comparison between first and second generation biomass concerning economic, environmental and social criteria. *Computers and Chemical Engineering*,**85,**16 (2016).
5. S. Banerjee, S. Mudliar, R. Sen, L. Giri, D. Satpute, T. Chakrabarti, R.A. Pandey,. Commercializing lignocellulosic bioethanol: technology bottlenecks and possible remedies, *Biofuels, Bioproducts and Biorefining*,**4**, 77 (2010).
6. O. Akgul, A. Zamboni, F. Bezzo, N. Shah, L. Papageorgiou, Optimization-Based Approaches for Bioethanol Supply Chains, *Ind. Eng. Chem. Res*., **50**, 4927 (2011).
7. A. Zamboni, F. Bezzo, N.Shah,Spatially explicit static model for the strategic design of future bioethanol production systems, 2. Multi-objective environmental optimization. *Energy and Fuels*, **23**, 5134 (2009).

8. A. Ozlem, N. Shah, L. Papageorgiou, Economic optimisation of a UK advanced biofuel supply chain, *Biomass and Bioenergy*,**41**,57 (2012).
9. P. Börjesson, L. Gustavsson, Regional Production and Utilization of Biomass in Sweden. *Energy*,**21**, 747(1996).
10. E. Johnson, R. Heinen, Carbon trading: time for industry involvement. *Environment International*, **30**, 279 (2004).
11. A. Osmani, J. Zhan, Multi-period stochastic optimization of a sustainable multi-feedstock second generation bioethanol supply chain − A logistic case study in Midwestern United States,*Land Use Policy*,**61,**420 (2017).
12. B. McCarl, A. Meeraus, Pvd. Eijk, M. Bussieck, S. Dirkse, P. Steacy, McCarl Expanded GAMS user Guide,Version 22.9. GAMS Development Corporation, 2008.

МУЛТИПЕРИОДИЧЕН ДЕТЕРМИНИСТИЧЕН МОДЕЛ НА УСТОЙЧИВИ ИНТЕГРИРАНИ ХИБРИДНИ ВЕРИГИ ЗА ДОСТАВКА НА БИОЕТАНОЛ ОТ ПЪРВА И ВТОРА ГЕНЕРАЦИЯ ЗА СИНТЕЗ И РЕНОВАЦИЯ

Б. Иванов

Институт по инженерна химия, Българска академия на науките, София, България

Постъпила на 20 март, 2018 г.;приета на20 юни, 2018 г.

(Резюме)

В статията се предлага математичен модел на интегрирана ресурсно-осигурителна верига (РОС) която да отчита икономическите, екологичните и социалните аспекти на устойчивостта. За проектиране на оптимална РОС се предлага модел на смесено линейно програмиране. Производството на биоетанол от възобновяема биомаса е предмет на засилен интерес с оглед намаляване на зависимостта на България от вноса на петрол и намаляване на въглеродните емисии. Ефективността на разходите и опазването на околната среда водят до значителни проблеми, които възпрепятстват увеличеното производство на биоетанол от възобновяема биомаса. Моделът разглежда ключовите дейности по захранващата верига, включително прибирането / преработката и транспортирането на биомаса. Моделът взема пред вид разходите за доставка на суровината, потреблението на енергия и емисиите на парникови газове като критерии за ефективност на системата. Полезността на симулационния модел на захранващата верига се демонстрира чрез разглеждането на захранващата верига за биомаса в съоръжение за биогорива в български мащаб. Резултатите показват, че моделът е полезен инструмент за управление на захранващата верига, включително избор на оптимално местоположение на съоръжението за биоетанол, логистичен дизайн, управление на инвентара и обмен на информация.

Bulgarian Chemical Communications, Volume 50, Special Issue K (pp. 36 – 44) 2018

Characteristics of boiling heat transfer on hydrophilic surface with SiO_2 coating

A. S. Surtaev[1,2*], V. S. Serdyukov[1,2], A. N. Pavlenko[1], D. V. Kozlov[2,3], D. S. Selishchev[2,3]

[1] Kutateladze Institute of Thermophysics, Siberian Branch of Russian Academy of Science, Novosibirsk, 630090, Russia; [2] Novosibirsk State University, Novosibirsk, 630090, Russia;
[3] Boreskov Institute of Catalysis, Siberian Branch of Russian Academy of Science, Novosibirsk, 630090, Russia

Received May 17, 2018, Accepted June 26, 2018

The paper presents the results of an experimental study of the effect of wetting properties on the local and integral characteristics of heat transfer at water boiling on the saturation line under atmospheric pressure. To control the wetting characteristics, the nanocoatings of SiO_2 were synthesized on the sapphire substrate surface using various chemical methods including dip coating and spin coating. New experimental data on dynamics of vapor bubble growth and detachment, evolution of microlayer and dry spot regions, nucleation site density and bubble emission frequency, heat transfer, etc., were obtained using the high-speed imaging techniques, including infrared thermography and video recording from the bottom side of transparent heater. The analysis of experimental data on the local and integral characteristics of the boiling process made it possible to determine the mechanisms of the influence of deposited hydrophilic coatings on the heat transfer intensity.

Keywords: Boiling, Hydrophilic coating, IR thermography, Heat transfer, Bubble dynamics

INTRODUCTION

It is well-known that the properties of heat exchange surfaces, especially wettability, significantly affect the dynamics of phase transition at boiling and condensation. Thus, for instance, the use of hydrophobic coatings allows to significantly increase the heat transfer coefficient at vapor condensation due to implementation of the dropwise condensation mode [1, 2]. The wetting properties also have a significant effect on the bubble dynamics, heat transfer and critical heat fluxes (CHF) at liquid boiling [1, 3-11]. For example, a theoretical expression for describing the effect of the contact angle on the CHF at liquid boiling is obtained by Kandlikar [5] based on the balance of forces acting on the individual bubble. Here, it is worth noting that this pioneering work is often cited when analyzing data on the crisis phenomena at boiling of nanofluids. This relates to the fact that when nanofluids (i.e. liquids with added nanoparticles of Al_2O_3, TiO_2, SiO_2, etc.) are boiling, a significant increase in the critical heat flux is observed [12-16]. For the first time a reasonable explanation for such influence was given by Kim *et al*. [13]. The authors showed that an increase in CHF is primarily caused by the fact that during nanofluid boiling, nanoparticles are deposited on the surface resulting in the formation of a nanocoating. This was confirmed by the results of experiments carried out with pure water boiling on a surface, pre-boiled in a nanofluid, which also showed an increase in CHF. The formed nanoparticle coatings significantly improve the wetting characteristics; as a result, the heat transfer surfaces become superhydrophilic. However, as it was noted in many papers devoted to nanofluid boiling, including [17, 18], improvement of wettability or decrease in the contact angle is associated not only with changes in the free surface energy of the heat exchange surface, but also with a change in its morphology and porosity, which has also an additional effect on the increase in CHF. The influence of the coatings, formed by nanofluid boiling, on heat transfer remains unclear, and this is caused by contradictory experimental information. For example, in some works, an increase in HTC (heat transfer coefficient) was registered, in others there was heat transfer deterioration; in some works it was shown that the formed coatings have no noticeable effect on heat transfer intensity, but they increase the threshold value for the development of crisis phenomena. The detailed review and analysis of papers dealt with various aspects of nanofluid boiling with a history of development of this problem are presented in [19-21].

The hydrophobic coatings present a certain practical interest in the problems of increasing the efficiency of some heat exchangers, including those for the chemical industry, operating by thermodynamic cycles with coolant boiling. The fact is that the hydrophobic coatings cause a significant reduction in the boiling onset [7, 10-11, 22] with a decrease in the temperature drop of boiling-up and increase in the nucleation site

* To whom all correspondence should be sent:
E-mail: surtaevas@gmail.com

density, and this is important for a number of practical problems. Also, as it is shown in [23], slightly hydrophobic coatings cause fouling inhibition at boiling of water-salt solutions, which is also an actual problem for many types of heat exchangers. However, according to [7, 11], with an increase in hydrophobicity, the heat transfer rate can worsen significantly. Despite the fact that when boiling on a hydrophobic surface, the onset of boiling usually occurs during the first power step, at about 1-2K of wall superheat, the heat transfer data are in qualitative agreement with a film boiling heat transfer trend [7]. Interesting results were obtained by Phan and co-workers [11], where the authors investigated the local and integral characteristics of heat transfer at water boiling (ΔT_{sub} ~ 15 K) on a thin-walled foil (20 μm) by using coatings with different free surface energies and changing contact angle in the range of 22-112°, deposited by using various surface nanomodification techniques, including MOCVD, PECVD and nanofluid boiling. In this work, it is shown that the heat transfer coefficient behaves in a strange way, depending on the contact angle. In particular, in the range θ ~ 30-90° the heat transfer coefficient decreases as contact angle decreases. At the same time, when the contact angle is varied in the range of θ ~ 22-31°, improvement of wettability leads to an increase in HTC. The latter trend is also confirmed by the experiments of Takata [9]. In this work, the authors used TiO_2 films as a superhydrophilic coating (θ ~ 4 - 13°). The fact is that under UV irradiation, the TiO_2 films become superhydrophilic for a sufficiently long period. This allows an exclusion of the influence of surface morphology on the boiling process, and investigation of only the influence of wettability. It was found in [9] that the heat transfer coefficient of superhydrophilic TiO_2 increases by 20-30% compared to the surface without coating.

Despite the fact that the wetting properties have a significant effect on the local characteristics of the process and heat transfer intensity at boiling, now there are no reliable theoretical models for describing the observed phenomena. Insufficient understanding of the physics of the process is connected, among other things, with a limited array of experimental information. For example, in [9], the effect of wetting properties in the contact angle range θ ~ 0-30° on the integral characteristics of the process, namely the heat transfer coefficient and critical heat flux, is analyzed without further theoretical analysis of the experimental results. In more recent works [7, 11], in addition to measuring the heat transfer coefficient, the authors use a high-speed video of the process from the side of the heating surface, which allows them to visualize evolution of vapor bubbles, measure bubble departure diameter and bubble emission frequency. Nevertheless, this format of recording has several drawbacks, including inability to visualize the dynamics of microlayer and evolution of dry spots under individual vapor bubbles, as well as a high error in determining the nucleation site density, especially in the range of high heat fluxes using hydrophobic coatings.

Recently, the development of modern experimental methods, including high-speed infrared thermography, video recording, laser interferometry, etc., for visualization of the process from the bottom side of a transparent substrate with a thin film heater, allows us to obtain fundamentally new information on nucleation dynamics and heat transfer characteristics at liquid boiling [24-27]. The use of the above spectrum of methods makes it possible to investigate in detail the evolution of vapor bubbles, region and structure of liquid microlayer and dry spots under the different sites, to measure the nucleation site density and frequency of bubble emission over a wide range of heat fluxes, and visualize evolution of the temperature field in various local areas of the surface. Despite the prospects of the above-described high-speed measurement techniques, there are practically no studies in the literature that would allow one to study the effect of nanocoatings with different wetting characteristics on the local and integral characteristics of heat transfer at liquid boiling using these methods. This would make it possible to achieve a significant progress in understanding the fundamental laws governing the influence of wetting properties on the most important parameters characterizing the process of liquid boiling.

In this paper we will present the results of the investigation of the effect of hydrophilic SiO_2 coatings on the internal characteristics of the process (density of nucleation sites, dynamics of vapor bubble growth and departure, evolution of heat under the active nucleation sites, etc.) and heat transfer at water boiling on a transparent heater obtained using modern experimental methods with high temporal and spatial resolution, including video and infrared thermography.

EXPERIMENTAL SETUP

A schematic diagram of the setup for pool boiling experiments is shown in Fig. 1. The detailed description of the experimental facility, heating element and measurement techniques is presented in [27,28]. Deionized water produced by Direct-Q 3 UV water purification system was used as the working liquid. In the experiments 1-μm-thick

films of indium-tin oxide (ITO), vacuum-deposited onto 400-μm-thick sapphire substrates, were used as the heaters. Fabricated samples had an electrical resistance of 2-3 Ohms and a heating area of 20×20 mm^2. The surface roughness (R_a) of the sapphire substrate was less than 1 nm according to the manufacturer (Hong Yuan Wafer Tech Co). The main advantage of ITO as a heater material in the experiments on investigation of integral and local characteristics of heat transfer at nucleate boiling is its transparency in the visible region (380-750 nm) and opacity in the mid-IR region (3-5 μm) of the spectrum. At the same time, sapphire transmission in the wavelength range of 0.3-5 μm exceeds 80 %. The combination of these properties makes it possible to measure the non-stationary temperature field on the ITO film surface by infrared camera and visually record vapor bubbles dynamics and liquid-vapor system structure directly on the sapphire substrate by high-speed video camera. Therefore, such construction of the heating element was recently widely used for pool boiling experiments [24, 27-29].

Samples were resistively heated (Joule heating) by a DC power supply Elektro Automatik PS 8080-60 DT *via* thin silver electrodes vacuum deposited onto the ITO film. To determine the heat release rate for a given current I, voltage V was measured on the heater with the use of APPA 109N digital multimeter. The heat flux density was calculated as $q = V \cdot I/A$, where A is the area of heater surface. The error in measuring the heat flux density consists of the errors in measuring the voltage in the working section, current and surface area, and does not exceed 3 %.

Video and infrared high-speed visualizations

To visualize the boiling process with high spatial and temporal resolutions, a digital video camera Vision Research Phantom v.7.0 with frame rate up to $20 \cdot 10^3$ FPS was used. Visualization was performed from the bottom side of the transparent heater, as shown in Fig. 1. To study in detail the evolution of the microlayer and dry spot regions, Nikon 105mm f/2,8G macro lens was used in the work. The maximum spatial resolution of video recording in the experiments was 33 μm/pix. As it will be shown below, this format of visualization allowed us not only to measure the outer diameter of the vapor bubbles, but also to study in detail the evolution of the regions of microlayer and dry spots.

In the experiments the high-speed thermographic camera FLIR Titanium was used to measure the non-stationary temperature field of the heating surface. As configured for this study, the thermographic camera had a frame rate of 1000 FPS and maximum resolution of 150 μm/pix. The total uncertainty of the temperature measurements in the experiments did not exceed 1 K. Due to high thermal conductivity (k = 25 W/m·K) and small thickness of the sapphire substrate, the temperature on its surface was assumed to be equal to the temperature of the ITO film recorded by thermographic camera. The use of IR camera made it possible not only to investigate integral heat transfer at boiling, but also to estimate the nucleation site density, activation temperature and nucleation frequency.

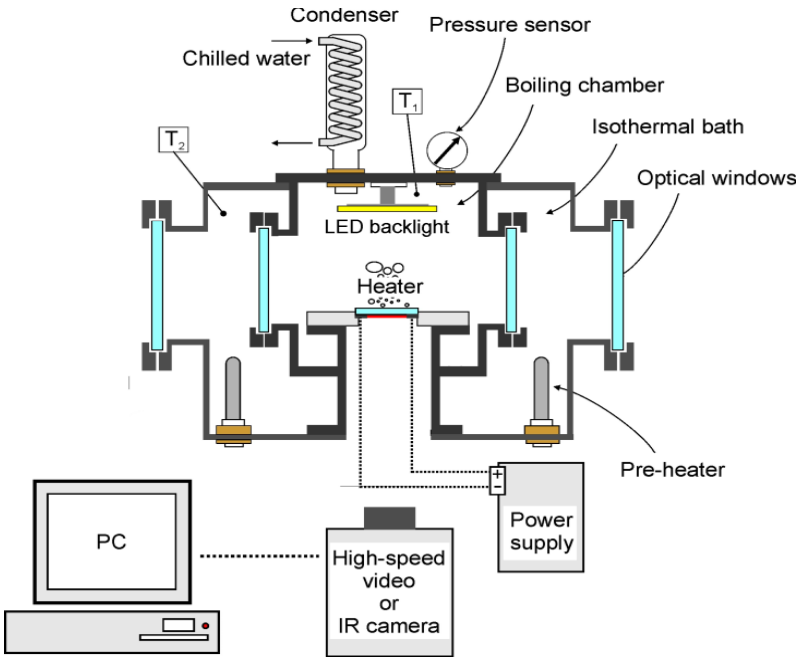

Fig. 1. Scheme of experimental setup.

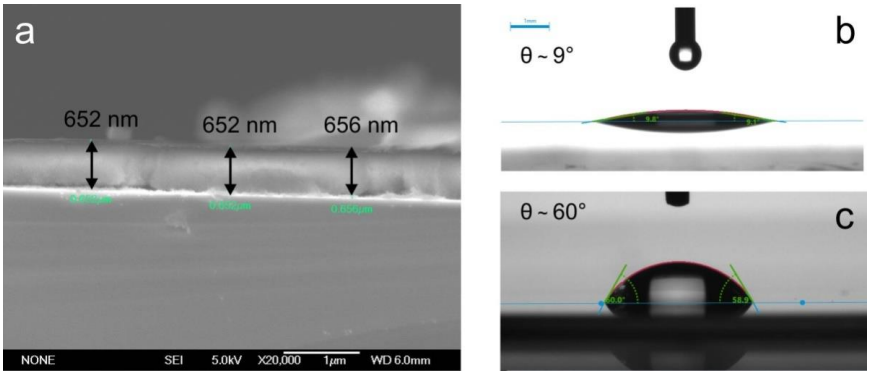

Fig. 2. a – cross-sectional view of the substrate with SiO_2 coating by SEM; b – contact angle measurement with water droplet (V = 5 μl) on the SiO_2 coated surface; c – contact angle measurement on the pure sapphire substrate.

Surface modification

The SiO_2 coating was deposited on the sapphire substrate with a view to change the wetting properties of the heat transfer surface *via* dip-coating and spin-coating techniques using a commercial colloidal solution of SiO_2 Ludox AS-30 (30 wt.% SiO_2 in water, pH 9.1), produced by Sigma-Aldrich (USA). After the synthesis, the physico-chemical properties of each sample were analyzed using a complex of modern methods, including nanoprofilometry, electronic spectroscopy and microscopy (EDX, SEM), and KRUSS setup for measuring free surface energy and contact angle. The photograph of a typical SiO_2 coating in cross-sectional view is shown in Fig. 2a. The thickness of the coating was 650 nm. According to the analysis of the water droplet shape on the substrate (Fig. 2b), the SiO_2 coating has hydrophilic properties. Its contact angle reached 9°, which is much less than the value measured on the surface of pure glass and sapphire (θ ~ 60°, Fig. 2c). The analysis of coating morphology also showed that the roughness value R_a does not exceed 3 nm, which is higher than the R_a value for the surface of polished sapphire, but it is significantly smaller than the characteristic value of the critical vapor nucleus for observed superheating of liquid at water boiling.

RESULTS OF EXPERIMENTS

Results of the first series of experiments obtained for the SiO_2 coatings are presented in the paper. To construct boiling curves, experimental data about the heating surface temperature obtained by IR thermography were averaged over the recording time of 10 s and surface area at different heat flux densities. Corresponding boiling curves for water on the heating surfaces with hydrophilic SiO_2 coating and without it are presented in Fig. 3. Analysis of data shows that the coefficients of heat transfer during water boiling on the coated hydrophilic surface are higher by 20-30% than on the uncoated sapphire surface. This result agrees well with experimental observations of the authors in experiments with water boiling on hydrophilic and superhydrophilic coatings [9, 11].

To determine the possible causes of the influence of SiO_2 coatings on heat transfer, we measured the following local boiling characteristics: growth rate of vapor bubbles, departure diameters, density of nucleation sites (NSD), etc. The latter was measured using synchronized IR thermography and video data. It should be noted that for the analysis of this value by thermograms, the temperature field was averaged over 10 s, and this guaranteed consideration of only constantly active nucleation sites [27]. Analysis shows that the NSD for water boiling on the surface with a hydrophilic coating is lower for the given heat fluxes than that for boiling on the surface of uncoated sapphire (Fig. 4), and this agrees with the theoretical concepts. This result shows that an increase in heat transfer intensity with improvement of wetting properties in the region of low heat fluxes is not associated with an increase in the density of nucleation sites, but it rather is observed on a surface relatively depleted of active sites.

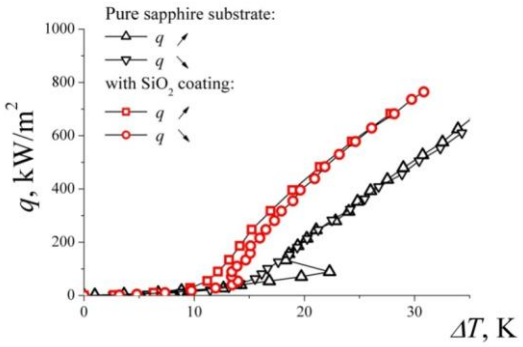

Fig. 3. Boiling curves for saturated water on the pure sapphire surface and surface with SiO_2 coating. The data are presented at both cases – with gradual increase and decrease of heat flux.

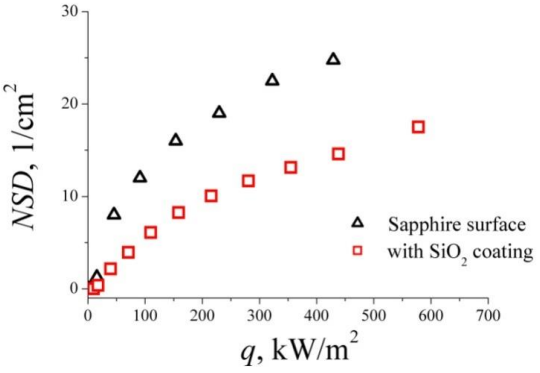

Fig. 4. Dependence of nucleation site density (NSD) on heat flux at water pool boiling on surface with different wettability.

The next step was the analysis of high-speed visualization of the growth dynamics and departure of vapor bubbles, as well as evolution of the microlayer and dry spots under individual bubbles at boiling on a SiO_2 coated surface. Typical video frames of vapor bubble evolution are shown in Fig. 5. In these frames, we can clearly see the outer diameter of the bubble base, microlayer and dry spot regions. In parallel with the analysis, we compared these data with our earlier results obtained for water boiling on a sapphire surface, described in [28, 30]. Histograms of distributions of separated bubble dimensions at boiling on the sapphire substrate and surface with SiO_2 coating at similar heat fluxes are shown in Fig. 6. It can be seen from the figure that the average dimensions of separated bubbles increase noticeably with improvement of the wetting properties. This result agrees with experimental data of [11]. In that work, water boiling on surfaces with different wetting properties was visualized at the side of the heating surface, which made it impossible to analyze evolution of the microlayer region and dynamics of the contact line at the vapor bubble base. In the present study, such measurements were carried out; in particular, Fig. 7 presents time dependences of the diameter of vapor bubble base, size of microlayer and dry spot region for a single nucleation site. In general, the behavior of curves is similar to the results obtained for water boiling on the surface of pure sapphire without coating. However, as it was noted in [28, 30], when boiling on the sapphire surface, the beginning of bubble departure stage almost coincides with the time of complete liquid evaporation in the microlayer region. The results of measurements on the hydrophilic surface show that for the bubbles with high growth rate and relatively large departure diameter (D_{dep} > 5 mm), the stage of separation, when the contact line size decreases (while the outer diameter of the bubble base remains almost constant), begins much earlier than the time of complete evaporation of the liquid microlayer. The measurement results also show that the growth rates of dry spots at water boiling on the hydrophilic surface and surface without coating almost coincide with each other for similar heat fluxes. This suggests that the wetting properties (in the contact angle range θ ~ 10 - 60°) do not affect the dynamics of liquid evaporation in the microlayer region under vapor bubble.

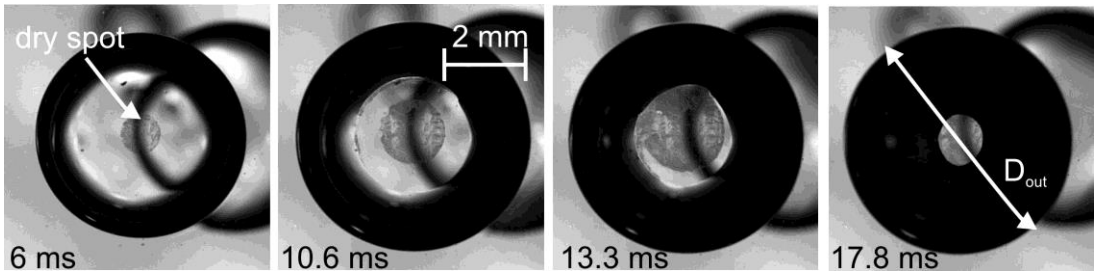

Fig. 5. Frames of high-speed macro visualization of single vapor bubble dynamics at water boiling on the sapphire surface with SiO_2 coating (q = 26.7 kW/m^2). The time is indicated from the moment of bubble appearance.

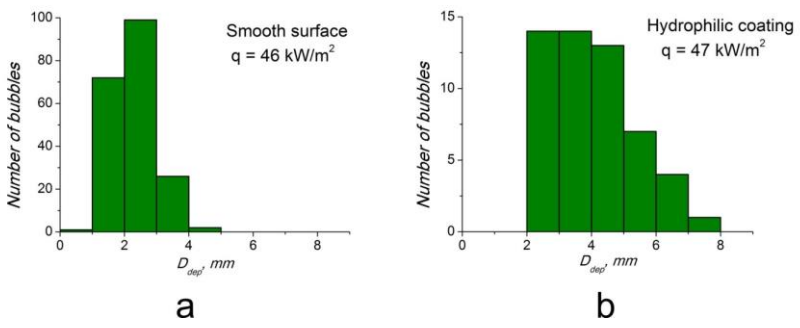

Fig. 6. Effect of surface wettability on the size distribution of separated vapor bubbles obtained at similar heat fluxes.

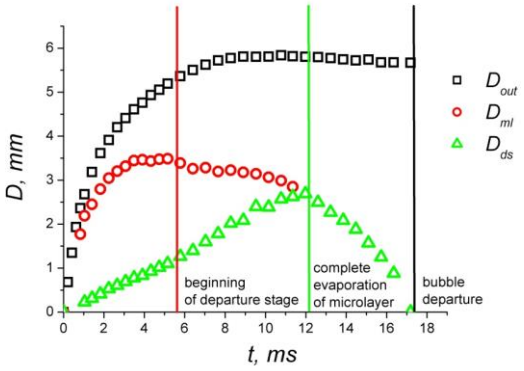

Fig. 7. Evolution of the outer diameter of a single bubble (D_{out}), the region of a microlayer (D_{ml}) and a dry spot (D_{ds}) at water boiling on the sapphire surface with SiO_2 coating (q = 52.2 kW/m^2).

One of the important local characteristics at boiling is bubble emission frequency. According to the analysis of experimental results on pure sapphire, the value of bubble emission frequency, as well as the value of bubble departure diameter vary in a wide range, for different sites at boiling with a given heat flux. Nevertheless, there is a regularity that bubble emission frequency decreases with an increase in the temperature threshold of site activation and increase in bubble departure diameter. To confirm the above, time dependence of local temperature of the ITO film surface is shown in Fig. 8 for different nucleation sites, where the dimensions of separated bubbles differ significantly, at boiling on the sapphire surface with SiO_2 coating. It can be seen from the figure that the higher the temperature of site activation, the greater is the value of bubble separation diameter and the lower is the bubble emission frequency. On the one hand, it is logical that lower nucleation frequency corresponds to a larger bubble diameter due to an increase in duration of the stage of bubble growth and departure. However, the main contribution to the reduction in nucleation frequency is related to an increase in time of thermal layer restoration and achievement of the threshold temperature of new nucleus activation in the region of low heat fluxes. Thus, it follows that the improvement of the wetting properties not only leads to an increase in bubble departure diameters, but also to a decrease in average nucleation frequency.

The following question arises from the analysis of local boiling characteristics on the sapphire surface with and without SiO_2 coating: what is the main reason for an increase in heat transfer intensity at boiling on a hydrophilic surface? For example, this may be caused by the fact that an increase in bubble departure diameter leads to an increase in the microlayer region and, consequently, to the volume of thin liquid layer near the heated wall, which means an increase in the heat removed from the heating surface due to intensive evaporation.

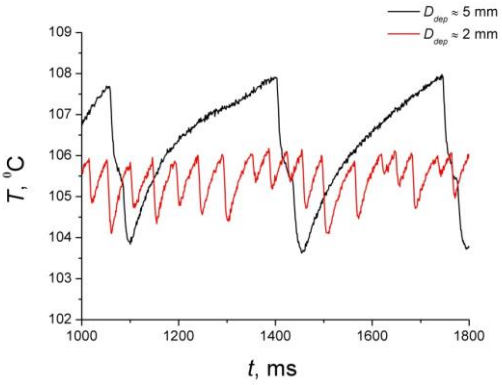

Fig. 8. Dependences of local temperature of the surface with coating on time measured in active nucleation sites with different bubble emission frequency (q = 52.2 kW/m^2).

In previous works [28, 30], as well as in the present study, it is shown that the size of microlayer region D_{ml} and bubble departure diameter D_{dep} are related by the ratio D_{ml}/D_{dep} ~ 0.5 - 0.6 before the beginning of bubble departure stage. In addition, separation of the larger vapor bubbles increases the volume of fresh liquid fed to the heat exchange surface by convection, which increases the amount of heat for thermal layer restoration.

To evaluate the effect of vapor bubbles with different departure diameters, growth rate and activation temperature on heat transfer rate at boiling, we use the mechanistic approach described in [31]. In this approach, it is assumed that the total heat flux removed from the heat exchange surface at liquid boiling is the sum of various components:

$$q_{total} = \frac{q_{ml} t_g + q_r t_w}{t_g + t_w} + q_{nc}, \qquad (1)$$

where q_{ml} is heat removed by evaporation of a liquid microlayer at the stage of vapor bubble growth (t_g); q_r is heat required for repeated formation of the destroyed boundary layer at the stage of expectation of bubble appearance after its departure (t_w); q_{nc} is heat transferred by convection on the surface free of bubbles.

To estimate the contribution to heat transfer, we compared two bubbles with significantly different sizes D_{dep} = 1.2 mm and D_{dep} = 5.7 mm from the data obtained at boiling on a surface with SiO_2 coating (q = 52.2 kW/m^2). The expressions for q_{ml} and q_r, referred to the unit cycle of a vapor bubble, take the following form:

$$q_{ml} = \rho_l h_{fg} nf \cdot V_{ml} \qquad (2)$$

$$q_r = \frac{2k_l}{\sqrt{\pi\alpha_l t_w}}(na)(T_w - T_{sat}), \quad (3)$$

where f – bubble emission frequency, n – nucleation site density. According to the expression for calculation of q_{ml}, it is necessary to define V_{ml}. In [31], using different approximations, the authors eventually obtain the following expression:

$$q_{ml} = \frac{\gamma\phi\sqrt{\pi}}{10} B^2 Ar^{0.27} Ja(\alpha_l)^{3/2} \sqrt{t_g}\rho_l h_{fg} n, \quad (4)$$

where γ, φ, B – empirical constants, Ar - Archimedes number, Ja – Jacob number. In our case, V_{ml} can be calculated directly based on the analysis of data obtained in the present work and data on the liquid microlayer thickness obtained using laser interferometry [26] through simple geometric representation:

$$V_{ml} = \frac{2\pi}{3}\delta_{ml}\frac{D_{dep}^2}{4}. \quad (5)$$

The experimental data on local boiling characteristics required for calculation by (2), (3) and calculation results for q_{ml} and q_r, are given in Table 1 below:

Table 1. Experimental data on local boiling characteristics

D_{dep}, mm	1.2	5.7
ΔT, °C	6	8
f, Hz	27	3.6
t_g, ms	8.8	50
t_w, ms	28.2	226
q_{ml}, kW/m^2	0.28	0.81
q_r, kW/m^2	0.78	7.9

It is seen from the presented results that the ratios q_{ml} and q_r for different nucleation sites are equal to 2.9 and 10, respectively. This suggests that the sites, where the larger vapor bubbles are formed, contribute more to heat transfer at boiling as compared to the sites that generate smaller vapor bubbles with higher nucleation rate. At that, the main contribution to heat transfer is made by the component associated with the non-stationary thermal conductivity and restoration of the thermal boundary layer after vapor bubble departure (q_r) in order to achieve the threshold of site activation temperature. The above estimates also show that the ratio of heat fluxes is so high that despite a decrease in nucleation site density at water boiling on the hydrophilic surface, the heat transfer rate increases in comparison with liquid boiling on a conventional surface.

To verify calculations, the total heat flux q_{total}, delivered to the liquid by all bubbles (1), was estimated using the experimental data of density of nucleation sites, which showed that the calculated value $q_{total} \approx 48$ kW/m^2 is in good agreement with the measured value of input heat flux (q = 52.3 kW/m^2). We should note that in these estimates, we did not take into account the convective component since, as it was shown earlier for pool boiling, q_{ml} and q_r components have the main contribution to q_{total}, and q_{nc} can be neglected [24].

CONCLUSIONS

New fundamental results on the effect of hydrophilic coating on the local and integral characteristics of heat transfer at liquid boiling are obtained in the current research. The use of modern high-speed experimental methods, including IR thermography and video recording, and transparent substrates with a thin film heater and SiO_2 nanocoating, made it possible to determine the following:

- The intensity of heat transfer at water boiling on the surface with hydrophilic SiO_2 coating increases in comparison with boiling on the uncoated sapphire surface, which agrees with the data of [9, 11]. At that, the density of nucleation sites for the given heat fluxes decreases noticeably with improvement of the surface wettability.

- Based on the statistical analysis, it is shown that the dimensions of separated bubbles increase and nucleation frequency decreases at boiling on a hydrophilic surface coated with SiO_2. Based on the visualization analysis, it is shown that a change in the wetting characteristics has no effect on the rate of dry spot growth under vapor bubbles in the region of low heat fluxes.

- Various components of heat transfer at boiling were estimated using the mechanistic approach suggested in [31] and experimental data on local boiling characteristics obtained in the current study for low heat fluxes. It is shown that the increase in quench heat flux q_r (i.e., the transient conduction heat transfer following bubble departure) is the dominant contribution to an increase in nucleate boiling heat transfer on the hydrophilic surface. This fact is associated with an increase in the volume of fresh liquid with increasing size of separated bubbles and increasing temperature threshold of site activation.

Certainly, in order to expand knowledge about influence of surface wettability on local and integral characteristics of the boiling, further investigations with the use of modern high-speed experimental techniques are required in a wide range of wetting properties of the heat exchange surface. According to the authors of this study, transparent photocatalytically active TiO_2

nanocoatings are promising. The fact is that under UV irradiation the surface of TiO_2 coating becomes superhydrophilic with a wetting angle of less than 10°. In addition, the contact angle of TiO_2 can be increased up to 130-140° *via* subsequent fluorination. Therefore an advantage of TiO_2 coatings for boiling experiments is the possibility to change its wetting properties in a wide range without changing the surface morphology.

Acknowledgement: *The reported study was funded by the Russian Foundation for Basic Research according to the research project № 17-08-01342 and Complex Program of Basic Research SB RAS "Interdisciplinary Joint Investigations" (project No. 23, theme AAAA-A18-118022090033-1). We express our gratitude to the Novosibirsk State University for giving us an access to the library*.

REFERENCES

1. I. C. Bang, J. H. Jeong, *Nuclear Eng. Technol.*, **43**, 217 (2011).
2. R. Wen, Q. Li, J. Wu, G. Wu, W. Wang, Y. Chen, X. Ma, *Nano Energy*, **33**, 177 (2017).
3. D. Attinger, C. Frankiewicz, A. R. Betz, T. M. Schutzius, R. Ganguly, A. Das, C.-J. Kim, C. M. Megaridis, *MRS Energy Sustainability*, **1**, E4 (2014).
4. C. H. Wang, V. K. Dhir, *J. Heat Transfer*, **115**, 659 (1993).
5. S. G. Kandlikar, *J. Heat Transfer*, **123**, 1071 (2001).
6. M. H. Kim, G. C. Lee, J. Y. Kang, K. Moriyama, H. S. Park, *Int. J. Heat Mass Transfer*, **108**, 1901 (2017).
7. E. Teodori, T. Valente, I. Malavasi, A. S. Moita, M. Marengo, A. L. .N. Moreira, *Appl. Therm. Eng.*, **115**, 1424 (2017).
8. H. O'Hanley, C. Coyle, J. Buongiorno, T. McKrell, L. W. Hu, M. Rubner, R. Cohen, *Appl. Phys. Lett.*, **103**, 024102 (2013).
9. Y. Takata, S. Hidaka, J. M. Cao, T. Nakamura, H. Yamamoto, M. Masuda, T. Ito, *Energy*, **30**, 209 (2005).
10. I. I. Gogonin, *Thermophys. Aeromech.*, **17**, 243 (2010).
11. H. T. Phan, N. Caney, P. Marty, S. Colasson, J. Gavillet, *Int. J. Heat Mass Transfer*, **52**, 5459 (2009).
12. S. M. You, J. H. Kim, K. H. Kim, *Appl. Phys. Lett.*, **83**, 3374 (2003).
13. S. J. Kim, I. C. Bang, J. Buongiorno, L. W. Hu, *Int. J. Heat Mass Transfer*, **50**, 4105 (2007).
14. J. S. Coursey, J. Kim, *Int. J. Heat Fluid Flow*, **29**, 1577 (2008).
15. C. Gerardi, J. Buongiorno, L. Hu, T. McKrell, *Nanoscale Res. Lett.*, **1**, 1 (2011).
16. A. R. Neto, J. L. G. Oliveira, J. C. Passos, *Appl. Therm. Eng.*, **111**, 1493 (2017).
17. B. P. Fokin, M. Y. Belenkiy, V. I. Almjashev, V. B. Khabensky, O. V. Almjasheva, V. V. Gusarov, *Tech. Phys. Lett.*, **35**, 440 (2009).
18. H. Kim, E. Kim, M. H. Kim, *Int. J. Heat Mass Transfer*, **69**, 164 (2014).
19. H. Kim, *Nanoscale Res. Lett.*, **6**, 1 (2011).
20. A. S. Surtaev, V. S. Serdyukov, A. N. Pavlenko, *Nanotechnologies in Russia*, **11**, 696 (2016).
21. G. Liang, I. Mudawar, *Int. J. Heat Mass Transfer*, **124**, 423 (2018).
22. B. Bourdon et al., *Int. Commun. Heat Mass Transfer*, **45**, 11 (2013).
23. L. L. Wang, M. Y. Liu, *AIChE J.*, 57, 1710 (2011).
24. C. Gerardi, J. Buongiorno, L. Hu, T. McKrell, *Int. J. Heat Mass Transfer*, **53**(19), 4185 (2010).
25. I. Golobic, J. Petkovsek, D.B.R. Kenning, *Int. J. Heat Mass Transfer*, **55**, 1385 (2012).
26. S. Jung, H. Kim, *Int. J. Heat Mass Transfer*, **73**, 365 (2014).
27. A. S. Surtaev, V. S. Serdyukov, M. I. Moiseev, *Instrum. Exper. Tech.*, **59**, 615 (2016).
28. A. Surtaev, V. Serdyukov, J. Zhou, A. Pavlenko, V. Tumanov, *Int. J. Heat Mass Transfer*, **126**, 297 (2018).
29. I. C. Chu, H. C. No, C. H. Song, *Int. J. Heat Mass Transfer*, **62**, 142 (2013).
30. A. S. Surtaev, V. S. Serdyukov, *Thermophysics and Aeromechanics*, **25**(1), 67 (2018).
31. R. J. Benjamin, A. R. Balakrishnan, *Int. J. Heat Mass Transfer*, **39**, 2495 (1996).

ХАРАКТЕРИСТИКИ НА ТОПЛОПРЕНАСЯНЕТО ПРИ КИПЕНЕ ВЪРХУ ХИДРОФИЛНА ПОВЪРХНОСТ С ПОКРИТИЕ ОТ SiO_2

А. С. Суртаев[1,2*], В.С. Сердюков[1,2], А. Н. Павленко[1], Д.В. Козлов[2,3], Д.С. Селищев[2,3]

[1] Институт по термофизика „Кутателадзе", Сибирски клон на Руската академия на науките, Новосибирск, 630090, Русия

[2] Новосибирски държавен университет, Новосибирск, 630090, Русия

[3] Институт по катализ „Боресков", Сибирски клон на Руската академия на науките, Новосибирск, 630090, Русия

Постъпила на 17 май, 2018 г.; приета на 26 юни, 2018 г.

(Резюме)

Представени са резултатите от експериментално изследване на влиянието на характеристиките на умокряне върху локалните и интегралните характеристики на топлопреноса при кипене на вода върху линията на насищане при атмосферно налягане. За контрол на характеристиките на умокряне са синтезирани нанопокрития от SiO_2 върху повърхността на сапфирен субстрат чрез различни химични методи, включително покритие чрез потапяне и покритие чрез въртене. С помощта на високоскоростни изобразителни техники като инфрачервена термография и видеи запис на дъното на прозрачен нагревател са получени нови експериментални данни относно динамиката на растеж и откъсване на мехурчета от пара, излъчване на микрослойни и сухи точки, плътност на зародишообразуване, честота на отделяне на мехурчета, топлообмен и др. Чрез анализ на експерименталните данни за локалните и интегралните характеристикип на процеса на кипене са установени механизмите на влиянието на хидрофилните покрития върху интензитета на топлопренос.

Bulgarian Chemical Communications, Volume 50, Special Issue K (pp. 45 – 48) 2018

Scaling of the mechano-chemical process of production of silicon chelates from plant raw materials

E. G. Trofimova[1], E. M. Podgorbunskikh[1], T. S. Skripkina[1*], A. L. Bychkov[1, 2], O. I. Lomovsky[1]

[1]*Institute of Solid State Chemistry and Mechanochemistry SB RAS, 18, Kutateladze str., 630128, Novosibirsk, Russia*
[2]*Novosibirsk State Technical University,630073, Novosibirsk, 20, Prospekt K. Marksa, Russia*

Received May 17, 2018, Accepted June 26, 2018

In order to scale up the mechanochemical process of production of biologically active silicon chelates from plant raw materials the transfer from laboratory mechanochemical reactors to industrial equipment with a productivity of 15-70 kg / h was carried out. The efficiency of raw material grinding (by size characteristics of the product) and activation effects (by solubility of silicon dioxide) were studied depending on the technological treatment regimes (processing intensity and feed rate). The characteristics of the product obtained at laboratory scale (equilibrium concentration of soluble silicon chelates of 28 mg / l) were improved with a rotor speed of 1500 rpm and a productivity of 15-20 kg / h. Taking into account the energy costs, the rotation speed of 1200 rpm and feed rate of 43 kg / h can be considered as the optimal mode, which provides the obtaining of product with an equilibrium concentration of soluble chelates of 24 mg / l.

Keywords: Scaling, Mechanochemistry, Mechanochemical reactor, Technology, Silicon chelate

INTRODUCTION

Silicon performs a number of important functions in the human body, animals and plants [1]. The highest biological activity is displayed by complexes of silicon with organic compounds [2]. Rice husk is a promising renewable source of biogenic silicon dioxide with a content of up to 20% by weight. The chemical form of silicon in the rice husk is hydroxylated amorphous silica. It concentrates at the outer surfaces of plant tissues, where it forms a cellulose-silica composite membrane [3]. Due to its unique composition and fibrillary ultrastructure rice husk has high-strength characteristics, chemical inertness, low density and high ash content. Thereby the tasks of efficient mechanical and mechanochemical processing of silicon dioxide in plant raw materials are closely related to the increase of the specific surface area, the production of chemically active surface centers, and the synthesis of soluble products. Thus, it was snown in [4, 5] on model systems (silica gel and pyrocatechol, silica gel and dihydroquercetin, silica gel and green tea catechins) at a laboratory scale that the interaction of silicon dioxide with polyphenolic compounds can be achieved using a solid-phase mechanochemical method. Hydroxyl groups of polyphenols interact with the silanol groups of silicon dioxide during the mechanochemical treatment of the reagents, which leads to the formation of surface complexes of silicon with polyphenols. With subsequent dissolution, the silicon chelates go into solution.

The introduction of developments in the industry requires scaling of the dependencies obtained on laboratory equipment and the establishment of optimal technological regimes [6].

Therefore, the goal of this work was to determine the optimum conditions for mechanochemical treatment of silicon-containing plant raw material in industrial mills, allowing achieving the effects obtained in laboratory mills for the production of biologically active products with an increased amount of water-soluble silicon.

MATERIALS AND METHODS

The following materials and chemicals were used: rice husk *Oryza sativa (L.)* (Liman sort, Krasnodar Krai, Russia), green tea *Camelia sinensis (L.)* (State standard # TU 9191-003-00570186-04, Krasnodar Krai, Russia)**,** $(NH_4)_2MoO_4$ (99.5 %, Russia), H_2SO_4 (99.9 %, Russia), Na_2SiO_3 (99 %, Russia), KBr (optical grade, Russia), pyrocatechol (99 %, Alfa Aesar), ammonium acetate (98 %, Russia), ascorbic acid (99 %, Russia), oxalic acid (99 %, Russia).

Moisture content of the samples of plant raw materials and products was measured according to [7] using an automatic moisture analyzer Radwag WPS 50SX (Poland) and was equal to 5.8-6.1 %. Granulometric analysis was carried out on a vibrating screen “Analysette-3 Pro”, equipped with a set of screens 20-1000 μm (FRITSCH, Germany). The specific surface area of the samples was determined from the thermal desorption of nitrogen on the “Sorbtometer M” instrument (Katakon, Russia) using Gregg and Singh approximation [8].

* To whom all correspondence should be sent:
E-mail: shapolova@solid.nsc.ru

Mechanochemical treatment of plant raw material

Mechanochemical treatment of plant raw material was carried out in an industrial mechanochemical reactor of centrifugal roller type mill "RM-50" (production of ISSC SB RAS, Novosibirsk), equipped with water cooling [9]. A mixture of 85% rice husk containing silica, and 15% green tea containing catechins was used as a raw material for the production of chelated silicon. The grinding bodies were steel rollers fixed on the drive shafts which treated mechanically the material with a controlled intensity. The technological regimes used in the work were: feed rate 15-70 kg / h, rotor speed 900-1500 rpm. The temperature in the treatment zone was controlled by a water-cooled jacket and did not exceed 65-70 ° C.

Determination of the equilibrium concentration of silicon chelates in solution

The equilibrium concentration of silicon chelates in solution was determined according to the following procedure. Samples were dissolved in 0.05 M acetate buffer under a hydromodule of 1000 at 25 ° C for 4 h with periodic mixing. After dissolution, the suspension was centrifuged to separate the supernatant (5000 rpm, 15 min. A 350 μl portion of supernatant was taken into a 5-ml test tube, then 150 μl of a solution of ammonium molybdate (0.5 M) was added and allowed to stay for 10 min at room temperature. Then, 300 μl of a reducing agent solution (0.4 M ascorbic acid and 0.7 M oxalic acid) and 3.25 ml of water were added. After 30 min, the optical density was mwasured at a wavelength of 810 nm. The concentration of silicon chelates was determined from a calibration curve plotted using a State Standard Sample of silica # 8934-2008) under similar conditions.

RESULTS AND DISCUSSION

Comparison of apparatuses with different types of mechanical action was conducted under laboratory conditions [10]. It was shown that the use of machines with shear type of action, such as centrifugal roller mill, is preferable for the solid-phase reaction between silicon dioxide of rice husk and polyphenols in the matrix of plant raw materials. Using this type of equipment provides reducing of the particle size and increasing the specific surface area from 0.5 to 2.3 m^2/g, disordering of the ultrastructure of cell walls, amorphization of cellulose and activation of silicon dioxide surface with formation of new active centers. For this reason, a centrifugal roller mill RM-50 was chosen for scaling. It can provide a capacity of up to 100 kg of product per hour, which is sufficient for the industrial production of silicon chelates.

The most important technological parameters that determine the efficiency of processing of raw materials in the mechanochemical reactor are the rotor speed and the fillability of the processing zone associated with the feed rate. Often with the same particle size of the raw material, the fineness of product grinding is proportional to the power consumption. The processing of the rice husk mixture with green tea was carried out with two variable parameters: the input frequency of the current and the feed rate. The input frequency of the current determines the rotor speed and reactor power consumption (Table 1).

Fig. 1 shows a typical particle size distribution of the processed product at a fixed rotor speed. It can be seen that a decrease in the feed rate of the raw material through the treatment zone causes a decrease of material passing per the unit of time. Thereby more energy is supplied to the raw material (per unit mass) and the grinding proceeds more efficiently.

Increasing of the efficiency of grinding can be achieved not only by reducing the feed rate, but also by increasing the energy input. Summary data on the influence of processing parameters on the average particle size of the rice husk are presented in Table 2. As can be seen from the results in Table 2, the most efficient grinding occurs with low raw material feed rate and high rotor speed, the feed rate being more important. Thus, acceptable regimes providing efficient grinding, high yields of the product at relatively low power consumption are as follows: rotor speed of 1200-1350 rpm and feed rate of 30-40 kg / h. In particular, for the sample obtained at 1200 rpm and 33 kg / h, the specific surface area was equal to 2.1 m^2 / g, which is comparable to the value for the sample obtained at laboratory scale [9].

Determination of the equilibrium concentration of soluble chelated forms of silicon and consideration of the data in Table 2 in graphic form (Fig. 2) allows determination of the maximum attainable concentration of chelated forms of silicon, as well as the specific change in concentration with increasing energy intensity (by how many units will the chelate concentration increase with an increase in the engine rotation speed by 1 rpm or a decrease in the feed rate by 1 kg / h).

The maximum attainable concentration of chelated forms of silicon, corresponding to a rotation speed of 1500 rpm and supply of raw

materials tending to zero, is 40.2 mg/l. For the rotation speeds of 1200 and 900 rpm, these values are 29.5 and 18.5 mg / l, respectively. It can also be noted that under intensive mechanical action (1500 rpm), the dependence of the concentration of monomeric forms of silicon on the feed rate, determined from the slope of the straight line, is stronger than under less impact (1200 and 900 rpm).

Table 1. Dependence of the rotor speed and power consumption of the mechanochemical reactor on the input current frequency.

Current frequency, Hz	Rotor speed, rpm	Energy consumption without raw materials, kW	Energy consumption with raw materials, kW
20	550	2.7	5.0
30	900	5.5	7.1
40	1200	9.5	10.3
50	1500	14.5	18.7

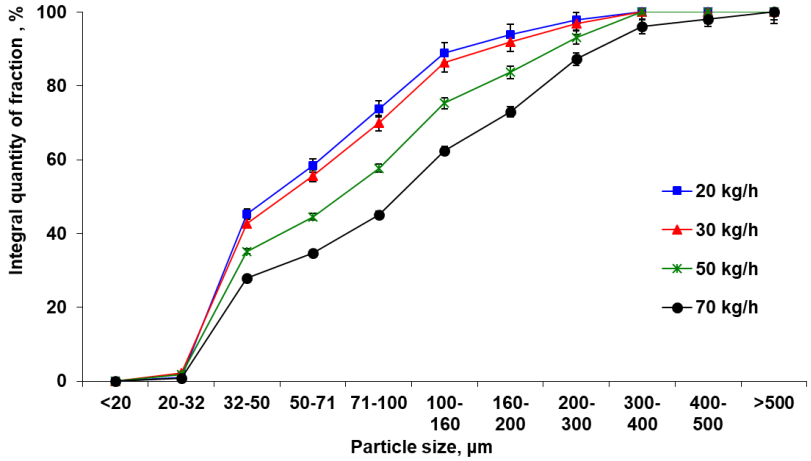

Figure 1. Influence of feed rate on the granulometric composition of mechanically activated rice husk (at a rotor speed of 1200 rpm)

Table 2. Dependence of the average particle size of the product on the rotor speed and feed rate

Rotor speed, rpm	Feed rate, kg / h	Average particle size of the product, μm
900	15	145 ± 2
	20	157 ± 1
	33	172 ± 3
	43	179 ± 4
	52	170± 3
	70	199 ± 3
1200	15	92 ± 5
	20	84 ± 1
	33	92 ± 2
	43	107 ± 6
	52	112 ± 6
	70	119 ± 3
1350	15	62 ± 2
	20	69 ± 4
	33	73 ± 3
	43	91 ± 2
	52	94 ± 2
	70	104 ± 3
1500	15	57 ± 3
	20	57 ± 2
	33	62 ± 2
	43	73 ± 2
	52	76 ± 1
	70	80 ± 3

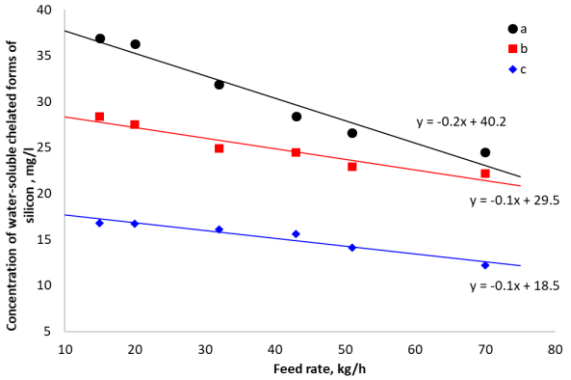

Figure 2. Dependence of the equilibrium concentration of water-soluble chelated forms of silicon on the conditions of mechanochemical treatment: a, b, c: 1500, 1200, 900 rpm, respectively.

Taking into account the energy costs and the minimum angle of slope (indicating a more stable mode of treatment) the optimum mode is as follows: rotor speed of 1200 rpm and feed rate of 43 kg / h, which leads to a product with an equilibrium concentration of soluble chelates of 24 mg / l.

CONCLUSIONS

On the basis of the presented results it can be concluded that the intensity of the mechanical action and the feed rate of raw materials play a significant role on the efficiency of mechanochemical interactions in the activation of the raw materials. Optimal technological regimes of mechanical treatment of plant raw materials in a semi-industrial centrifugal roller mill leading to the production of a product characterized by an increased concentration of chelated soluble forms of silicon were determined. The most rational modes from the point of view of chemical and economic efficiency are: rotor speed of 1200 rpm and feed rate of 43 kg / h. This mode provides an increase in the yield of chelated forms of silicon from 6 to 24 mg / l, which corresponds to the values reached at laboratory level.

Acknowledgements: *This research was carried out within the State Assignment to ISSCM SB RAS (project 0301-2018-0004).*

REFERENCES

1. M. A. Farooq, K. J. Dietz, *Front Plant Sci.*, **6**, 1 (2015).
2. C. Exley, *Prog. Mol. Subcell. Biol.*, **47**, 173 (2009).
3. B.D. Park, S.G. Wi, K.H. Lee, A.P. Singh, T.H. Yoon, Y.S. Kim, *Biomass Bioenergy*, **25**, 319 (2003).
4. E. G. Shapolova, O. I. Lomovsky, *Russ. J. Bioorg. Chem.*, **39** (7), 765 (2013).
5. E. G. Shapolova, O. I. Lomovsky *J. Int. Sci. Publications: Materials, Methods & Tech.*, **7**, 39 (2013).
6. G. G. D. Silva, M. Couturier, J.-G. Berrin, A. Buléon, X. Rouau, *Biores. Technol.*, **103**, 192 (2012).
7. ISO 18134-3:2015. Solid biofuels. Determination of moisture content. Oven dry method. Moisture in general analysis sample, 2015.
8. S.J. Gregg, K.S.W. Sing, Adsorption, surface area, and porosity, Academic Press: London, 1982
9. O. Lomovsky, A. Bychkov, I. Lomovsky, in: Biomass Fractionation Technologies for a Lignocellulosic Feedstock Based Biorefinery, S. I. Mussatto (ed.), Elsevier, 2016, p. 649.
10. E. G. Shapolova, O. I. Lomovskij, *Khimija Rastitel'nogo Syr'ja (Chemistry of Plant Raw Material)*, **2**, 69 (2015).

ОКРУПНЯВАНЕ НА МЕХАНОХИМИЧНИЯ ПРОЦЕС НА ПРОИЗВОДСТВО НА СИЛИЦИЕВИ ХЕЛАТИ ОТ РАСТИТЕЛНИ СУРОВИНИ

Е. Г. Трофимова[1], Е. М. Подгорбунских[1], Т. С. Скрипкина[1*], А. Л. Бичков[1, 2], О. И. Ломовский[1]

[1] *Институт по химия на твърдото тяло и механохимия, ул. Кутеладзе 18, 630128, Новосибирск, Русия*
[2] *Новосибирски държавен технически университет, проспект К. Маркс 20, 630073, Новосибирск, Русия*

Постъпила на 17 май, 2018 г.; приета на 26 юни, 2018 г.

(Резюме)

За укрупняване на механохимичния процес на производство на биологично-активни силициеви хелати от растителни суровини е направен преход от лабораторни механохимични реактори към промишлено оборудване с производителност от 15-70 kg / h. Ефективността на смилане на суровината (оценена от размерите на продукта) и на активиращите ефекти (оценени от разтворимостта на силициевия диоксид) са изследвани в зависимост от технологичните режими на обработка (интензивност на обработката и скорост на захранване). Характеристиките на лабораторно получения продукт (равновесна концентрация на разтворими силициеви хелати от 28 mg / l) са подобрени с използване на скорост на ротора от 1500 rpm и производителност от 15-20 kg / h. Вземайки под внимание енергийните разходи, като оптимални могат да се считат скоростта на въртене от 1200 rpm и скоростта на захранване от 43 kg / h, които осигуряват получаването на продукт с равновесна концентрация на разтворими хелати от 24 mg / l.

Bulgarian Chemical Communications, Volume 50, Special Issue K (pp. 49 – 57) 2018

Hydrodynamics and heat transfer in a centrifugal film evaporator

V. G. Rifert[1], P. A. Barabash[1], A. S. Solomakha[1*], V. Usenko[1], V.V. Sereda[2], V.G. Petrenko[1]

[1]*Department of theoretical and industrial heat engineering, Igor Sikorsky Kyiv Polytechnic Institute, Ukraine*
[2]*National university of water and environmental engineering, Rivne, Ukraine*

Received March 20, 2018, Accepted July 24, 2018

Evaporators with a rotating surface (a disk or a cone) are used for the concentration of liquids in the food, pharmaceutical industries and bioindustry. They are also relevant for water recovering from liquid waste in life support systems for spacecraft and space stations. The paper reviews the works on the study of characteristics of a liquid film (thickness, wave parameters) flowing under the action of a centrifugal force and heat transfer during film condensation and film evaporation. In most theoretical and experimental studies, the flow of a film on a rotating surface was investigated when R/R_i (the ratio of the radius of the entire surface to the radius of the jet irrigation) is less than 5, which is typical for installations with a small radius of the rotating surface. The authors of the paper give new data on the film characteristics at $R/R_i > 5$, which is relevant for the food and pharmaceutical industries.

Keywords: Centrifugal, Film, Condensation, Evaporation

INTRODUCTION

Most multicomponent liquids, sea water, juices, etc. contain heat-sensitive substances that can lead to deterioration of the quality of the useful product during evaporation. These processes are intensified with the temperature increase. Conducting the process of concentration in a solution film significantly improves the situation. In film devices, high speeds of a thin layer of liquid processed product are achieved, which drastically shortens the time of its contact with the heat exchange surface. The most effective method for concentrating heat-sensitive liquids is evaporation in a film on a rotating surface. Thus, in comparison with other evaporators, centrifugal ones allow the process to be realized with a minimum thermal load in the shortest possible time (see Fig.1).

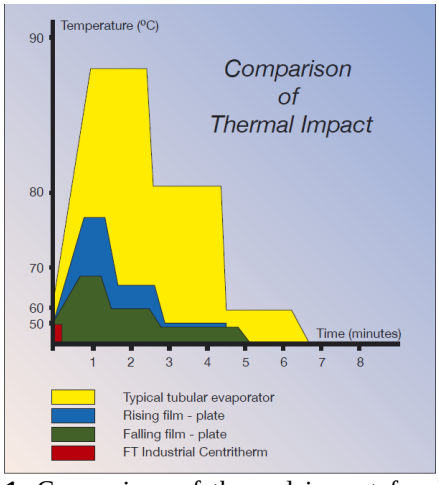

Fig. 1. Comparison of thermal impact for different types of evaporators [1]

In this paper we analyze the existing studies on the hydrodynamics of a film, the condensation of vapor, and the evaporation of a liquid in a film flowing on a rotating surface, including the data published by the authors.

Types of centrifugal evaporators and their applications

One of the first to describe and study the characteristics of a centrifugal evaporator for desalination of sea water was Hickman [2]. The rotating surface was in the form of a disk with a diameter of 1.27 and 2.8 m.

Bromley and co-workers [3, 4] describe and study a multistage evaporator for sea water with a rotating surface in the form of disks. The evaporator consists of a number of evaporator plates, up to 30, located directly above one another. When sea water was desalinated, the productivity of the 29-stage device was G_d = 1440 kg/h, the heat transfer coefficient was about h = 8500 W/m^{2}K.

Despite the very high heat transfer coefficients in centrifugal evaporators, they have not found wide application in the processes of sea water desalination. This is due to the fact that in the 1970-1980 the reverse osmosis method was used for desalination of sea water. In such desalination plants with relatively small dimensions, the energy consumption was 5-10 kWh/m^3, which was much more effective.

In 1962, a vacuum centrifugal steam compressor distiller was developed in the USA with a rotating surface of practically cylindrical shape, called VCD to be used in life support systems for space objects. Its characteristics are: G = 1.3...1.6 l/h, n = 150…250 rpm. From 1962 to 2008, about 10 prototypes were developed and tested. The last

* To whom all correspondence should be sent:
E-mail: a.solomakha@kpi.ua

VCD flight model was installed on the ISS in 2008 and is still operational [5].

In 1976-1990, multi-stage centrifugal distillers (CD) for water recovery systems for space missions were developed in the Kyiv Polytechnic Institute (Ukraine) [6-13]. The CD employs a variation of the thin-film vacuum rotary distillation concept. The system uses a multistage rotating distiller (n = 600 ... 1200 rpm) coupled with a thermoelectric heat pump (THP).

To concentrate various heat-sensitive liquids, Alfa Laval (Sweden) and Centrotherm (Australia) produce a centrifugal evaporator with a conical surface [14].

Characteristics of a liquid film on a rotating surface

To design and operate a centrifugal film evaporator, first of all, knowledge of the thickness of the film is required to calculate the heat transfer coefficient.

The motion of a fluid film on a rotating surface is described by the Navier-Stokes equation and the continuity equation [15]. For the case of laminar steady flow and assuming that the angular velocity of the fluid is equal to the speed of rotation of the disk, these equations are reduced to a simple balance of forces in the direction R:

$$-\omega^2 R = \frac{1}{\rho}\frac{d\tau_r}{dz} \qquad (1)$$

Integration of (1) gives the distribution of radial shear direction:

$$\tau_r = \rho R\omega^2\left(\delta - z\right) \qquad (2)$$

Re-integration gives a velocity profile:

$$u = \frac{R\omega^2\delta^2}{\nu}\left(\frac{z}{\delta} - \frac{1}{2}\frac{z^2}{\delta^2}\right) \qquad (3)$$

which is parabolic for a laminar flow.

The thickness of the film on the rotating disk can be obtained after calculating the volume flow.

$$Q = \int_0^{\delta} 2\pi R u dz = \frac{2\pi}{3}\frac{R^2\omega^2\delta^3}{\nu} \qquad (4)$$

From equation (4), the average thickness of the liquid film for the case of laminar flow was first obtained by Hinze and Milborn [16]:

$$\delta = \left(\frac{3}{2\pi}\frac{Q\nu}{R^2\omega^2}\right)^{1/3}. \qquad (5)$$

A similar solution was obtained in the study [17], taking into account the tangential component of the relative velocity of motion:

$$\delta^+ = \left(\frac{3}{2\pi}\frac{Q}{R\nu}\right)^{1/3}\left(\frac{\omega R^2}{\nu}\right)^{-1/6} \qquad (6)$$

where $\delta^+ = \delta\left(\omega/\nu\right)^{1/2}$ – the dimensionless thickness of the liquid film. In addition, it is indicated in [18] that the angular velocity of rotation of the liquid film is equal to the rotation speed of the disk, provided that $\delta^+ \le 0{,}5$. A similar result was also obtained in the study [19] when solving problems on the condensation of vapor on a rotating disk. The study [19] shows an insignificant effect of the surface tension on the film thickness and the shape of the free surface, which are mainly determined by the strength of the centrifugal forces. For calculations of the average thickness, equation (5) is recommended.

Aroesty *et al.* [20] obtained an approximate analytical solution, which extends to much larger radial distances. The final expression for the average film thickness according to [20] is similar to formula (5).

In the studies of Gasley and Charvat [21], the approximate solution by [20] was basically repeated and additional expression was obtained that allows one to determine the deviation of the circumferential velocity on the surface of the film u_c from the local velocity of the disk ωR:

$$\frac{\omega R - u_c}{\omega R} = 1{,}8\left(\frac{R}{L}\right)^{-8/3} \qquad (7)$$

Dependence (7) is more rigorous than that in study [20], which determines the length of the input section R_{in}, at which the circumferential velocity lags behind the surface of the film u_c from the local velocity of the disk ωR.

In the study [22], the dependence for δ was obtained by applying the Karman method for the solution of the Navier-Stokes equation for the axisymmetric flow of a laminar film over the surface of a rotating disc, and applying the assumptions similar to the ones used in the study [17]. Approximating the distribution of radial and circumferential velocities by a polynomial of the second degree, the authors in [22] obtained the equation:

$$Q^+ = \frac{1}{3}\left(\delta^+\right)^3 \qquad (8)$$

where Q^+ is the dimensionless flow, $Q^+ = Q/2\pi R^2\sqrt{\nu\omega}$. The transformation of the obtained dimensionless parameters gives the well-known formula (5).

A similar solution was presented in the study [23], however, in contrast to [22], polynomials of higher degree –third, fourth and fifth – were used to approximate the distribution of the axial, tangential, and radial velocities. It is shown (Fig. 2) [15] that for thin laminar films, when the dimensionless flow rate $Q^+ < 0{,}075$, and the dimensionless thickness coordinate $\delta^+ < 0{,}6$, all solutions for laminar flow give close values, which corresponds to the earlier conclusions of Sparrow [18] and Vachagin [17].

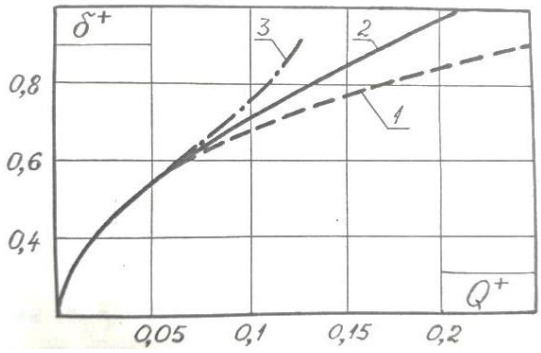

Fig. 2. Comparison of different theoretical dependencies for the thickness of a liquid film [15]: 1 - [16]; 2 - [24] and the approximation by a polynomial of the 4th, 5th degree according to [23]; 3 - approximation by a polynomial of the 3rd degree according to [23].

Thus, almost all theoretical studies on hydrodynamics of a fluid film on a rotating surface were conducted for the case of laminar flow. For thin laminar films, all solutions provide dependences for δ similar to Nusselt's solution [25] for a gravitational film, if g is replaced by $\omega^2 R$ in those solutions.

The experimental determination of the average film thickness at the time of the fluid flowing along the surface of a rotating disk is associated with certain technical difficulties due to the lack of reliable measurement methods and small measured thicknesses (up to $1 \cdot 10^{-6}$ m). Therefore, despite the widespread use of such film flows, at present there is a limited amount of studies describing the measurement of the average film thickness when the fluid moves in the field of centrifugal forces.

The contact method of measurements used in [23, 26-29] has a number of significant drawbacks - adhesion of liquid to the needle, presence of an extraneous element in the liquid flow, closure of the measuring circuit through the air layer which is saturated with water vapor, etc. Moreover, the method is not reliable in the case of rotation of the irrigation surface, since beating of the surface is possible, which, at small measured thicknesses (up to $1 \cdot 10^{-6}$ m), introduces significant errors in the measurements. As a result, essentially different results were obtained for approximately the same initial conditions in the different studies. In the study [26], a good agreement between the experimental data and formula (5) is noted. In [23, 29], there is a good coordination with the dependences that were obtained when the velocity distribution was approximated by polynomials of the fourth and fifth degree (see Fig. 2). An analysis of the results obtained in ref. [27] showed that the average film thickness is by 40% higher than the calculated one, and in ref. [28] the film thickness is 1.71 times higher than the calculated one.

Gasley and Charvat [21] measured the thickness of the film on a rotating disk by the optical method by absorbing infrared rays passing through the transparent disk. The results for the average thickness of the film are 2-3 times lower than those calculated using (5), with a greater deviation observed in the field of thin films. There is no proper explanation of this fact in ref. [21].

In the study [30], as our analysis showed, the average film thicknesses obtained are twice as high as the theoretical dependence.

In paper [15], experimental studies of the local parameters of a liquid film during its flow along a rotating disc were performed using the local electrical conductivity method. The experimental data on the average thickness of the liquid film (distillate, glycerin, surface-active substances) obtained in [15] are in qualitative agreement with the theoretical dependence (5) for a laminar film in the entire range of flow rate variation, disk rotation speed and its radius. The quantitatively obtained experimental data are by 18% lower than the theoretical ones. At the same time, the surface tension of the liquid did not affect the average film thickness. For the case $10^{-10} < Q\nu/\omega^2 R^5 < 10^{-8}$, a dependence is proposed for calculating the average film thickness:

$$\delta = 0,65R\left(\frac{Q\nu}{R^5\omega^2}\right)^{1/3} \qquad (9)$$

In Fig. 3 the dimensionless coordinates δ/R and $Q\nu/R^5\omega^2$ present all experimental data obtained on the average thickness of the fluid film on a rotating disk. The figure shows that the experimentally obtained character of the effect of the complex $Q\nu/R^5\omega^2$ on the dimensionless thickness δ/R corresponds to the theoretical dependence for the laminar flow (5) (curve 1) when $Q\nu/R^5\omega^2 > 10^{-10}$. At its lower values, the degree of influence of this complex increases, which can be explained by the turbulence of the liquid film.

Thus, as a result of an analysis of the actual data on the hydrodynamics of a film, it can be concluded that the calculation method to be used to determine the film thickness should be clarified.

Heat transfer during film condensation on the surface

One of the first fundamental works to deal with mathematical simulation on hydrodynamics and heat transfer during film condensation on a rotating surface was performed by Sparrow and Gregg in 1959 [31]. For the problem statement the authors used a system developed from five differential equations: three equations of a viscous fluid motion

written as Navier-Stokes equations, a differential equation of energy and an equation of mass conservation.

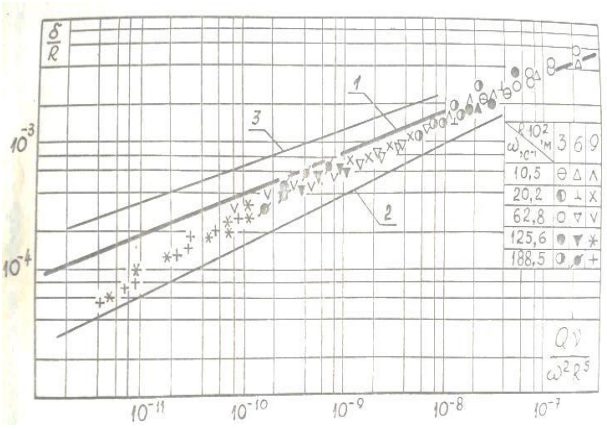

Fig. 3. Generalization of the experimental data on the average thickness of the liquid film on a rotating disk: points - experimental data [15]: 1 - calculation according to the theoretical dependence (5); 2 - calculation according to the empirical dependence of Gasley and Charvat [21]; 3 - experimental data of Povarov [30].

Sparrow and Gregg [31] have used a Karman's variable transformation which has been applied to the hydrodynamic problem solving for viscous liquid flow on the rotating disk in infinite space, simultaneous coordinates transformation with accepted assumptions have made it possible to reduce partial derivatives equations systems into a simple differential equation. For a number of Pr wide-band (from 10^{-3} up to 10) numerical solutions were obtained for the following dimensionless complexes:

$$Nu = \frac{h \cdot \left(\frac{\nu}{\omega}\right)^{0,5}}{\lambda} = 0,904 \left(\frac{\Pr}{c_p \Delta T / r} \right)^{0,25} \qquad (10)$$

The next step in theoretical analysis Sparrow and Gregg [18] made in 1960, performed theoretical analysis of the vapor braking effect on hydrodynamics and heat transfer of the rotating surface film condensation. The conclusion was drawn that the braking influence on heat transfer is restricted by several percent and can be neglected in the theoretical analysis.

In 1961 Sparrow and Hartnett [32] made a theoretical analysis of the heat transfer at film condensation on a rotating conic surface. When $\omega^2 R >> g \sin\varphi$ (φ is the taper angle), the hydrodynamics of the film and the heat transfer in case of condensation on both the inner and outer surfaces in the form of a cone will not differ from the case of flowing on a rotating disk.

One of the first experiments on the heat transfer at film condensation on the rotating surface was the report [33] published by Chernobylskiy and Schegolev in 1949. The device with a rotating surface was designed as a cylindrical steam camera with a rotating shaft placed coaxially to the camera's central axis. Taking into account the grounded assumption that the rotation radius *R* was considerably bigger than the tubes diameter and setting, thus for vertical parts the responsibility for film flow centrifugal forces and their density were approximately constant, the following equation was obtained:

$$h = const \frac{\lambda}{d} \cdot \sqrt[4]{\frac{d^3 R \omega r \rho}{\nu \lambda \Delta T}}. \qquad (11)$$

In 1960 Nandapurkar and Beatty [34] conducted experimentation on a horizontal water-cooled rotating disk. The experiments were performed at condensation of vapors of organic liquids such as spirits and refrigerants. The surface temperatures were measured at several points along the disk radius; the heat transfer coefficients for total surface were calculated on the base of these experimental temperatures. The experimental data demonstrated heat transfer coefficients values of 25-30% less in comparison with those predicted by the Sparrow and Greg [31] theory for laminar condensation on the rotation disk.

Heat transfer at steam film condensation experimentation and film flow parameters was also performed by Astafiev [28], Astafiev and Baklastov [35, 36]. Tests were performed on rotating horizontal disks with diameters of 80 and 105 mm. The shaft rotating velocity was varied from 0 up to 2500 rpm. It was assumed for flow patterns visualization in a special series of experiments a colouring substance in an amount not more than 7% of the condensate mass to be injected through the disks center. The fluid ring appearance on the disk edge was observed; detachment of the ring occurred at the moment when the centrifugal forces exceeded the surface forces.

The heat transfer coefficients data were generalized by the equation:

$$Nu = 1,38 \left(\Pr \cdot K \right)^{0,25} \left(Ga \right)^{0,215}. \qquad (12)$$

where: $Ga = \frac{\omega R^3}{\nu^2}$.

In dimensional form the authors [35] experimental data were generalized by the equation:

$$h = 1{,}18\left(\frac{\lambda^3 \rho r}{\nu \Delta T}\right)^{0{,}25} \omega^{0{,}43}. \qquad (13)$$

Butuzov and Rifert [37, 38] presented the experimental data on the inversed downwards condensing rotating surface. The steam condensation experimentation was performed on a horizontal rotating copper disk with a diameter of 0.3 m. The experimental measurements were performed for the disk angular velocity changes within 10 – 224 radian/s at heat flux densities from 20 up to 190 kW/m^2. The condensation had taken place in all experiments on the disks inversed downward surfaces.

The experiments demonstrated that at a constant disk angular velocity the average heat transfer coefficient at condensation decreased with both heat flux and temperature drop increasing, so for these conditions $h \sim \Delta T^{-0{,}25}$ which were typical for a condensate laminar film flow (fig. 4).

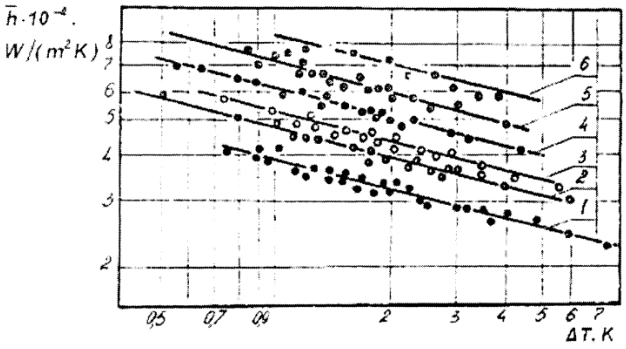

Fig. 4. The water steam condensation average heat transfer: T_s = 373K; R = 0.125 m; 1 – ω = 10.9 s^{-1}; 2 – 51.5 s^{-1}; 3 – 73.5 s^{-1}; 4 – 104 s^{-1}; 5 – 146 s^{-1}; 6 – 200 s^{-1}.

The dependence of h upon ω at ΔT = const in logarithmic coordinates (fig. 5) appears as a broken line with two zones: the first one extended from 10 to 40-52 radian/s. The second zone exceeded 52 radian/s. For the first one $h \sim \omega^{0{,}23}$, for the second $h \sim \omega^{0{,}5}$. The smaller influence of ω on heat transfer within the first zone was connected with the fact that at the slow rotation of the disk regions situated close to the rotation axis the gravitation forces influence on film flow was significant, so under these forces action, drops separation from a film took place. At ω > 52 radian/s a condensate film flow, as well as the heat transfer coefficients, were determined mainly by centrifugal forces and in this case the power index at ω was the same as in the Sparrow and Gregg equation (10).

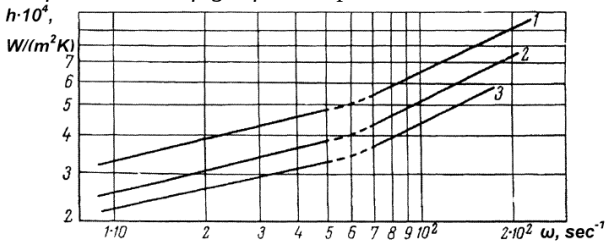

Fig. 5. The average heat transfer coefficient dependence from disks rotation velocity by the following different temperatures drops: 1 – ΔT = 1 K; 2 – ΔT = 2,5 K; 3 – ΔT = 4 K.

Yanniotis and Kolokotsa [39] experimentally studied heat transfer at film condensation of the steam on an aluminium disk inversed downwards with a smooth surface. The experiments were conducted on a disk with a diameter of 30 cm and thickness of 10 mm. The experiments were carried out at a saturated vapor temperature between 45 - 60°C.

The experimental results (fig. 6) show that the local heat transfer coefficient practically did not vary zonally on the disk surface. It agreed with the Sparrow and Gregg theory. The revolution rate in the experiments varied from 0 up to 1000 rpm.

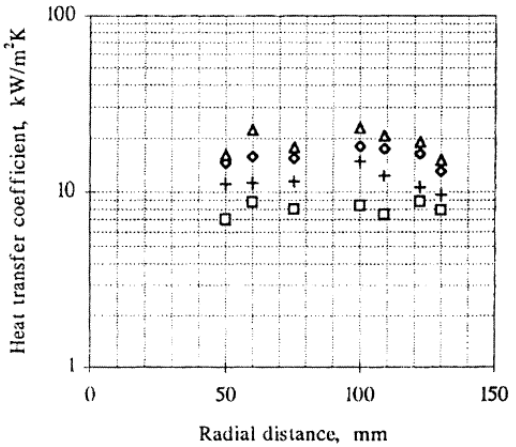

Fig. 6. Heat transfer coefficient for a temperature drop of 4 K between the steam and the disc wall.

It was established by authors experimentation, that the heat transfer coefficient increased with increasing angular velocity. So if the temperature drop (T_s – T_{wall}) was more than 20 K the heat transfer coefficient increase was approximately proportional to the angular velocity power of the $\omega^{0{,}25}$. When temperature drops decreased to 8 ºC by angular velocity, the influence increased and became proportional to $\omega^{0{,}42}$.

The temperature drops increase reduced the heat transfer coefficient in power ΔT^{-m} approximately, where m varied from 0.27 up to 0.18 with the rotation per minute increasing from 200 to 1000 rpm.

Heat transfer during evaporation of the liquid film on a rotating surface

The first studies that provided the formulas for calculating the heat transfer during evaporation of a liquid flow along a rotating surface, were conducted by Bromley [40]. The author accepts the laminar flow of a liquid film, which in those years and up to the present time is accepted (without proofs) when $\mathrm{Re} = 4G/P\mu < 200$ ($P = 2\pi R$).

For the evaporators studied in ref. [40], the authors believe that for the equation $\mathrm{Re} = 4G/2\pi R\mu = 2000$ there will be a laminar flow of the liquid film on the most part of the surface. Using the dependence (5) for determining the thickness for a laminar flow of a film, a well-known dependence is obtained in the dimensionless form:

$$Nu = 1,47\,\mathrm{Re}^{-1/3} \qquad (14)$$

Rahman and Faghri [41], using the well-known theoretical model of heat transfer for laminar condensation and evaporation of thin laminar films, obtained a dimensionless dependence:

$$Nu = Nu^{*} A\,\mathrm{Re}_{in}^{-1/3} E_{in}^{-2/3} \left(R/R_{in}\right)^{2/3} \qquad (15)$$

Substituting in (15) $Nu^{*} = h\delta/\lambda$, $A = \left(\nu^2/3gR_{in}^3\right)^{1/3}$, $\mathrm{Re}_{in} = u\delta/\nu$, $u = \omega^2 R\delta^2/3\nu$, $E_{in} = \nu/\omega R^2$ the dependence (14) is obtained.

Theoretical solutions on how to calculate the heat transfer and general heat transfer at the time of the evaporation of a liquid in a film on a rotating conical surface are presented in ref. [42-44]. The following dependencies are obtained:

$$h = \frac{1}{x - L_1}\int_{L_1}^{x} \frac{\lambda}{\left[3\left(Q_f - Q_e\right)\nu\right]^{1/3}} \qquad (16)$$
$$\left\{2\pi g x \sin\beta\cos\beta\left(\frac{\rho-\rho_v}{\rho}\right) + 2\pi x^2\omega^2\sin^3\beta\right\}^{1/3} dx$$

The novelty of the dependence (16) is in the presence of a term in the formula $2\pi g x \sin\beta\cos\beta\left(\frac{\rho-\rho_v}{\rho}\right)$. In real centrifugal evaporators, this term is smaller than the centrifugal acceleration term $2\pi x^2\omega^2\sin^3\beta$, even for small angles $\beta \approx 10^{\circ}$, which occur in ref. [42-44]. If we exclude the term $2\pi g x \sin\beta\cos\beta\left(\frac{\rho-\rho_v}{\rho}\right)$ from (16), we obtain (14).

The heat transfer coefficients measured at the experiments in [42-43] during evaporation and condensation for water, solutions of NaCl and sugar solution differed both in the values of h (by 15 ... 30%) and in the character of the effect of the fluid flow. The coefficient of heat transfer did not decrease with an increase in the fluid flow rate (Re_{in}), which follows from the authors' theory (formula (16)), but tended to increase (Fig.7).

In all studies presented [40, 42-44], as well as in [2, 3, 45, 46], the total heat transfer coefficient was measured.

The first measurements of the coefficients of heat transfer during the evaporation and boiling of water in NaCl solutions were performed in ref. [37, 47,48].

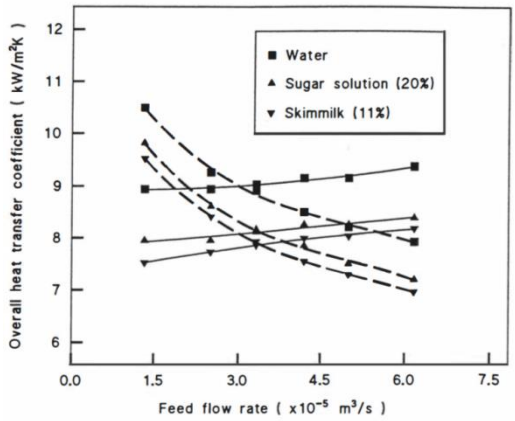

Fig.7. Effect of the feed flow rate on the overall heat transfer coefficient for water, 20% sugar solution and skimmilk in the Centritherm evaporator. Solid lines are experimental values while dashed lines are theoretical values. Evaporating temperature 60ºC, rotating speed 146.6 rad/s, temperature difference 10K.

In the experiments [47], the influence of the flow rate of liquid supplied to the center of the disk, the speed of rotation of the disk ω, the dimensions of the disk, the density of the heat flux and the evaporation temperature on the average coefficient of heat transfer during evaporation and boiling of liquids were studied. In our experiments, the temperature of the rotating surface was measured by thermocouples through a current collector. The temperature of the cold junctions was measured using a semiconductor thermistor fixed to the current collector rotor. Cold junctions together with the thermistor were qualitatively insulated. This ensured the possibility of obtaining reliable experimental data that are in good agreement with the theory for laminar and turbulent flows of a liquid film. Since only average heat flux could be measured in the experiments, it was not possible to evaluate experimentally the local (by the radius of the disk) heat transfer coefficient.

Figs. 8 and 9 [37] show the effect of ω, G and q on the average heat transfer coefficient. The main feature of these data is the absence of a laminar law of influence of G (Re) on h, which contradicts the models of a purely laminar film ($h \sim \mathrm{Re}^{-1/3}$), accepted in refs [40-42, 49]. This fact was noted in

the study [50], in which the author assumes that given the certain rates of fluid consumption and the small disk sizes Re can reach values at which the film will be turbulent. Using the two-layer model of a turbulent film described in the studies of Kutateladze [51], the author of [50] presented a dependence for the average heat transfer during evaporation of a liquid film, which takes into account the effect of turbulence on a disk with a radius of $R < R_{cr}$ and laminar flow with a radius of $R > R_{cr}$ (formula (14)).

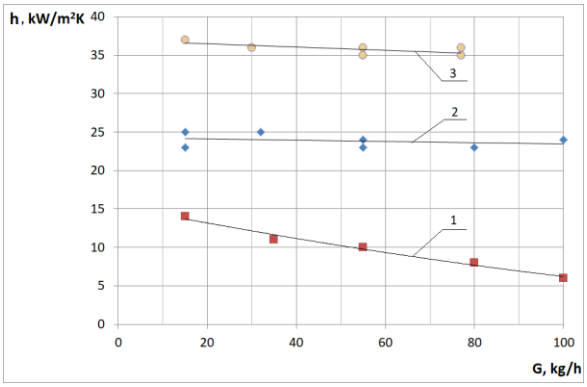

Fig. 8. Influence of the feedwater flow G on the heat transfer during the evaporation of the liquid film on a rotating disk at different rotation speeds ω: 1 - ω = 21 rad/s; 2 - ω = 52 rad/s; q = 6,6·10^4 W/m^2; 3 - ω = 105 rad/s; q = 9,6·10^4 W/m^2.

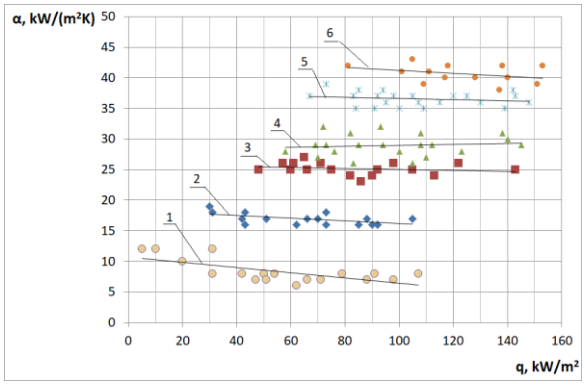

Fig. 9. The effect of the rotation speed of the disk and the heat flow on the average coefficient of heat transfer: 1 - ω = 21 rad/s; 2 - ω = 31 rad/s; 3 – ω = 52 rad/s; 4 - ω = 73 rad/s; 5 - ω = 105 rad/s; 6 - ω = 126 rad/s.

$$h = h_{lam}\frac{R^2 - R_{cr}^2}{R^2} + h_{turb}\frac{R_{cr}^2 - R_i^2}{R^2} \qquad (17)$$

Comparison of the experimental data from [48] with the calculations made using this formula showed satisfactory convergence.

However, our recent studies of the effect of turbulence in the film flow of a fluid [52] show a more accurate possibility to estimate the heat transfer coefficients for evaporation in a film on a rotating surface at high liquid flow rates (i.e. for large Re numbers).

CONCLUSIONS

A review and analysis of the state-of-the-art on the flow of a liquid film, its evaporation and condensation on a rotating surface of centrifugal evaporators is presented.

1. At present time, the characteristics of the liquid film in the field of a steady-state flow at $R >> R_i$ for laminar and wave flows have been well studied. It is necessary to pay attention to the question of justifying the criterion for the transition of a film on a rotating surface to a turbulent flow.

2. The flow of steam condensate on a rotating surface is well studied in the field of laminar flow and it also requires a refinement of heat transfer at low rotations of the rotating surface, when $\omega^2 R$ is close to g. Also the question of condensation on a liquid film, which, for example, takes place in centrifugal evaporators for space missions requires more research to be conducted.

3. The calculation of heat transfer during the evaporation of a liquid film on a rotating surface requires clarification, considering the real nature of the influence of the Re number on the processes of film condensation and evaporation.

REFERENCES

1. http://flavourtech.com/
2. K. C. D. Hickman, *Industrial and Engineering Chemistry*, **5**, 786 (1957).
3. R. L. Clark, L. A. Bromley, *Chemical Engineering Progress*, **1**, 64 (1961).
4. L. A. Bromley, *Desalination*, **1**, 367 (1966).
5. L. Carter, K. Takada, C. A. Browm, J. Bazley, D. Gazda, R. Schaezler, F. Thomas, 47th International Conference on Environmental Systems 17 – 20 July 2017, Charleston, South Carolina, ICES-2017-036.
6. N. Samsonov, L. Bobe, V. Novikov, N. Farafonov, B. Pinsky, G. Abramov, S. Berezkin, E. Grigorov, E. Zaitsev, N. Protasov, V. Komolov, A. Grigoriev, Ju. Sinjak, V. Rakov, V. Rifert, SAE Technical Paper 972559 (1997).
7. N. Samsonov, L. Bobe, V. Novikov, B. Pinsky, V. Rakov, N. Farafonov, V. Rifert, P. Barabash, N. Protasov, V. Komolov, SAE Technical Paper 951605 (1995).
8. N. Samsonov, L. Bobe, V. Novikov, N. Farafonov, B. Pinsky, G. Abramov, M. Amiragov, V. Astafyev, V. Rifert, V. Filonenko, N. Protasov, Ju. Sinjak, SAE Technical Paper 941536 (1994).
9. V. Rifert, P. Barabash, N. Goliyad, *SAE Technical Paper* 901249 (1990).
10. V. Rifert, V. Usenko, I. Zolotukhin, A. MacKnight, A. Lubman, *SAE Technical Papers*, 1999-01-1991 (1999).

11. V. Rifert, V. Usenko, I.Zolotukhin, A. Lubman, A. MacKnight, *Technical Papers* 2003-01-2625 (2003).
12. A. Lubman, A. MacKnight, V. Rifert, P. Barabash, *SAE Technical Papers* 2007-01-3177 (2007).
13. V. G. Rifert, P. A. Barabash, V. Usenko, A. S. Solomakha, L.I. Anatychuk , A.V. Prybyla, 68th International Astronautical Congress (IAC), Adelaide, Australia, 25-29 September 2017. IAC-17-A1.IP.25.
14. R. S. Jebson, Proceedings of Fifth International Conference on Enhanced, Compact and Ultra-Compact Heat Exchangers: Science, Engineering and Technology, Hoboken, NJ, USA, September 2005. CHE 2005 – 39.
15. A. A. Muzhilko, V. G. Rifert, P. A. Barabash, *Heat transfer. Soviet research*, **15**, 1 (1983).
16. I. O. Hinze, H. Milborn, *J. Appl. Mech.*, **2**, 145 (1950).
17. K. D. Vachagin, V. S. Nikolaev, *Khimiya i Khimicheskie Tekhnologii*, **6**, 71 (1960).
18. E. M. Sparrow, J. L. Gregg, *Trans., of ASME J, Heat Transfer*, **82**, 71 (1960).
19. R. H. Muhutdinov, *Journal of Engineering Physics and Thermophysics*, **4**, 80 (1961).
20. J. Aroesty, J. F. Gross, M.M. Illickal, J.V. Maloney, Digest Seventh Int. Conf. on Medical and Biological Eng., Stockholm, 527 (1967)
21. A.F. Charvat, R.E. Kelly, C.Gasley, *J. Fluid Mech.*, 2, 229 (1972).
22. Y. Oyama, K. Endou, *Chem. Eng., Japan*, 17, 256 (1953).
23. S. Matsumoto, K. Saito, Y. Takashima, *Chem. Eng., Japan*, **6**, 503 (1953).
24. S. Bruin, *Chem. Eng. Sc.*, **24**, 1475, (1970).
25. W. Nusselt, *Zeitschrift des Vereins Deutscher Ingenieure*, **60**, 541 (1916).
26. R. H. Muhutdinov, A. A. Trufanov, *Proceedings of the Kazan Chemical Technology Institute*, **2**, 134 (1957).
27. H. Espig, R. Hoyle, *J. Fluid Mech*, 22, 671, (1965).
28. V. B. Astafiev, PhD Thesis, Moscow, 1968.
29. G. I. Lepehin, G. V. Ryabchuk, N. V. Tyabin, E. R. Shulman, *Theor. Found. Chem. Eng.*, **15**, 391, (1981).
30. O. A. Povarov, E. G. Vasilchenko, P. G. Petrov, *Proceedings of Academy of Sciences. Power Engeneering and Transport*, **1**, 172 (1978).
31. E. M. Sparrow, J. L. Gregg, *Journal of Heat Transfer*, **5**, 113 (1959).
32. E. M. Sparrow, J. P. Hartnett, *J. Heat Transfer*, **1** (1961)
33. I. I. Chernobylskiy, G. M. Schegolev, *The Thermophysics Institute Works*, **1**, 118 (1949).
34. S. S. Nundupurkar, K. O. Beatty, *A.J.Ch.E. Chemical Eng. Prog.*, **30**, 129 (1960).
35. V. B. Astafiev, A. M. Baklastov, *Thermal Engineering*, **9**, 55 (1970).
36. V. B. Astafiev, A. M. Baklastov, *Thermal Engineering*, **10**, 74 (1970).
37. A. T. Butuzov, V. G. Rifert, *Heat Transfer Soviet Research*, **6**, 150 (1972).
38. A .I. Butuzov, V. G. Rifert, I.I. Puchovoy, *The Ukraine Chemical Industry*, **6**, 23 (1969).
39. S. Yanniotis, D. Kolokotsa, *Int. Comm. Heat Mass Transfer*, **5**, 721 (1996).
40. L. A. Bromley, *Ind. Eng. Chem.*, **50**, 233 (1958).
41. M. M. Rahman, A. Faghri. *Int. J. Heat Mass Transfer*, **10**, 2655 (1992).
42. H. Chen, PhD Thesis, 1997.
43. H. Chen, R. S. Jebson, O. H. Campanella, *Food Bioprod. Proc. Trans. Inst. Chem. Eng.*, **75**, 17 (1997).
44. H. Chen, R. S. Jebson, O. H. Campanella, *Food Bioprod. Proc. Trans. Chem Eng*., **81**, 293 (2003).
45. C. S.Wang, R. Greif, A. D. K. Laird, *Desalination*, **33**, 259 (1980).
46. B. W. Tleimat, ASME Publication, 71-HT-3. (1971).
47. A. I. Butuzov, V. G. Rifert, *Heat Transfer-Soviet Research*, 1 (1973).
48. V. G. Rifert, I. I. Pukhovoy, E. I. Nikitenko, Proc. of the 2nd European Thermal Sciences and the 14th UIT National Heat Transfer Conference (1996), **1**, p. 249.
49. Sh. Muhhamad, PhD Thesis, 2010.
50. V. G. Rifert. *Journal of Engineering Physics and Thermophysics*, **2**, 970 (1973).
51. S. S. Kutateladze, Fundamentals of heat transfer, 1964.
52. V. G. Rifert, V. V. Sereda, P. A. Barabash, V. V. Gorin, A. S. Solomakha, International symposium. Power and Chemical Engineering, Bulgaria, (2018), in press.

ХИДРОДИНАМИКА И ПРЕНОС НА ТОПЛИНА В ЦЕНТРОФУЖЕН ФИЛМОВ ИЗПАРИТЕЛ

В. Г. Риферт[1], П. А. Барабаш[1], А. С. Соломаха[1*], В. Узенко[1], В. В. Середа[2], В. Г. Петренко[1]

[1] *Департамент по теоретично и индустриално топлинно инженерство, Киевски политехнически институт „Игор Сикорски”, Киев, Украина*

[2] *Национален университет по водно стопанство и природно инженерство, Ривне, Украйна*

Постъпила на 20 март, 2018 г.; приета на 24 юли, 2018 г.

(Резюме)

Изпарители с въртяща се повърхност (диск или конус) се използват за концентриране на течности в хранителната, фармацевтичната индустрия и биоиндустрията. Намират приложение също за възстановяване на водата от течни отпадъци в системи за поддръжка на космически кораби и космически станции. В статията е направен преглед на работите върху изучаването на характеристиките на течен филм (дебелина, вълнови параметри), течащ под действието на центрофужна сила и пренос на топлина по време на кондензацията и изпаряването на филма. В повечето теоретични и експериментални изследвания филмовият поток е изследван при R/R_i (съотношение между радиуса на цялата повърхност и радиуса на струята) по-малко от 5, което е типично за инсталации с малък радиус на въртящата се повърхност. Авторите на статията представят нови данни за филмовите характеристики при $R/R_i > 5$, което е от значение в хранителната и фармацевтичната индустрия.

Bulgarian Chemical Communications, Volume 50, Special Issue K (pp. 58 – 69) 2018

Restoration of correctness and improvement of a model for film condensation inside tubes

V. G. Rifert[1*], V. V. Sereda[2], V. V. Gorin[1], P. A. Barabash[1], A. S. Solomakha[1]

[1]*National Technical University of Ukraine, Igor Sikorsky Kyiv Polytechnic Institute*
[2]*National University of Water and Environmental Engineering, Rivne, Ukraine*

Received March 20, 2018; Revised July 26, 2018

This work is devoted to the experimental studies aimed at increasing the efficiency of horizontal tube condensers by strictly accurate evaluation of heat transfer and regime parameters in various condensing refrigerants in the horizontal tubes of such devices. The unique measurements of heat fluxes and heat transfer coefficients local by circumference were carried out during condensation of Freon R-22 and steam which varies over a wide range of the main regime parameters (G, x, q, Re_l). The improved model of film condensation inside the horizontal tubes for prediction of heat transfer with application of the results of numerical solutions of Bae *et al.* is suggested. In this model more precise definition of the interphase friction coefficient as the main parameter crucial for condensation is given. This more precise definition contains experimental substantiation of β_q – prediction for calculation of pressure losses by friction and correction β_q that takes into account surface suction at the interphase. Heat exchange predicted by the improved method was compared with the experimental data of various authors for 13 fluids (steam, R-22, R-123, R-134a, R-245fa, carbon dioxide, propylene, propane, ether, isobutene, refrigerants FC-72, Novec®649, HFE-7000) in annular and intermediate modes. Good agreement of the experiments with calculations (divergence within 25%) proves the correctness of the proposed method for both laminar flow of condensate film and turbulent flow.

Keywords: Film condensation, Heat transfer, Plain tube, Friction coefficient

INTRODUCTION

In modern air conditioning systems, refrigeration and heat pump plants, in the technology of seawater evaporation and power systems heaters, the process of vapour condensation is carried out mainly inside the horizontal tubes and channels. Heat exchange processes occurring in condensers of this type have a significant effect on the overall energy efficiency of these systems. The difference in temperature between the condensing and the cooling fluids and the loss of pressure of these fluids affects the rate of entropy production in the condenser, and hence, the exergy efficiency factor (EEF) of the apparatus.

Currently, the results obtained by the available methods and models for calculating heat transfer for condensation of two-phase flows in horizontal tubes differ by 50-70%. This inaccuracy is due to the presence of a large number of parameters that affect the heat exchange, the wide range of changes in these parameters and the lack of understanding of their influence on the laws of heat exchange. For example, geometrical sizes (length and diameter of tubes), thermophysical properties (heat conductivity, density, surface tension and other) of condensing fluids and operating parameters (pressure, flow, heat fluxes), vary 10-100 times in different heat exchangers. Inaccurate estimation of heat transfer can lead to the unjustified change in the size of the apparatus and pressure differences, which either increase or decrease, resulting in an efficiency decrease. Also, the lack of accuracy of heat transfer calculation leads to the inaccurate evaluation of the effectiveness of various methods of intensifying the heat transfer process during condensation in horizontal tubes.

In view of this, it is urgent to carry out new studies on the influence of regime parameters of the two-phase current on the regularities of local and average heat transfer during the film condensation of moving vapour in a horizontal tube. These studies will open up a possibility of developing a new method for calculating heat transfer during condensation of various refrigerants in horizontal tubes of heat exchangers. More precisely, the estimation of heat exchange and regime parameters will make it possible to increase the efficiency of the work of horizontal tube condensers.

Literature review

Nusselt [1] described the basis of heat transfer during laminar film condensation on a flat vertical surface. The Nusselt theory is used in many studies on condensation within vertical and horizontal tubes. Dukler [2], Bae *et al.* [3] and Traviss *et al.* [4] developed a model of film condensation inside tubes for laminar and turbulent flow of condensate.

* To whom all correspondence should be sent:
E-mail: volodya.81.vs@gmail.com

The results of the theoretical solutions in [2-4] are presented in the form of graphs $Nu_f=f(\beta, Re_l, Pr_l)$. Rifert and Sereda [5,6] analyzed more than 20 theoretical methods and correlations for heat transfer prediction during different modes of condensate film flow. In [5,6] it is shown that all theoretical solutions give results close to the theory of Bae *et al*. [3], despite the use of different models of turbulence. Rifert and Sereda [5,6] recommended the method of Bae *et al.* [3] as the most correct theoretical method for heat transfer prediction in annular flow of the phases.

Different authors have proposed a large number (over 60) of empirical dependencies for calculating heat transfer when condensing in tubes. Reviews of such dependences are given in many papers, in particular in [6-10]. In [10] Rifert *et al*. compared the most commonly used formulae of Thome *et al.* [11] and Shah [12] with the formula of Ananiev *et al.* [13]. As shown in [10], the model of Ananiev *et al.* [13] is one of most successful relationships for a generalization of experimental data on vapor condensation inside horizontal and vertical tubes in a wide range of G, x and refrigerant physical properties.

In the experimental studies of condensation inside the tubes, beginning with the work of Tepe and Mueller [14] up to present time, the coefficients of heat transfer are averaged over a certain length of the tube. Providing in the experiments relatively small changes in the vapour content Δx, the authors assume that they measure local heat transfer coefficients. This is true for a vertical tube, but not always suitable for condensation inside a horizontal one. In most of the experimental work there is no comparison with theoretical calculations [1-4]. Comparison of experimental data of different authors with different empirical dependencies was carried out by Rifert *et al*. in [6,10]. The authors [6,10] showed that over 60 empirical correlations for heat transfer prediction reveal significant discrepancies with experimental heat-transfer coefficients. The best convergence with the experiments of different authors have the correlations by Thome *et al.* [11], Shah [12] and Cavallini *et al.* [15]. In these correlations all included complexes are selected by intuition, without any theoretical or experimental substantiation.

Experimental coefficients of heat transfer are compared with the theory of film condensation only in a small number of the considered works. In these works, there is a large discrepancy between experimental data and theory. The reasons for such discrepancies are due to the incorrect determination of the boundaries of the film flow regimes and the inaccurate estimation of the tangential stress (friction coefficient). In this regard, various authors have proposed dozens of different models and dependencies for calculating heat transfer during condensation. In these cases, there is often no justification for new dependencies, based on the physical nature of the condensation process. Also, there is a disagreement between different dependencies with different experiments, and lack of limits of the suggested methods application.

Based on the nature of the condensation process, and new experimental data of the local heat transfer coefficients, the methods for determining the tangential stress on the vapour and film boundary are substantiated. That made it possible to improve the film condensation model and calculate the heat transfer inside the tubes under the effect of vapour velocity in the laminar and turbulent regime of the condensate film flow.

Test facility

The detailed description of the experimental apparatus and method of heat transfer investigation during film condensation of moving vapour inside horizontal tube can be found in Rifert's previous publication [16]. The apparatus included evaporator, test section, condenser to condense vapor downstream, inspection sections, pressure and temperature gauges at the inlet and outlet of all condensation sections, and condensate flow meters. The test section (Fig. 1) consists of two defining sections 1 and 2, two working sections 3 and 4, as well as sites for visual observation 5, and is designed to study the local coefficients of heat transfer over the length and perimeter of the normal cross-section of the horizontal tube during the condensation of different refrigerants in the tubes by the thick-walled method.

Defining sections 1 and 3 are intended to change the vapour content in the working sections, which allows modelling the process of condensation in tubes of different lengths at different massive vapour velocities. Both defining sections are made in the form of a heat exchanger "pipe in a pipe" with the length of l = 0.8 m. All sections are located on the same axis and have the same internal diameter of 17 mm.

The basis of working sections 2 and 4 shown in Fig. 2 is a segment of thick-walled tube with internal and external diameter of 17 and 80 mm respectively. The material used for the sections is brass brand LS-59. The section length is 96 mm. On the outer perimeter, the sections are surrounded

by a ring cavity, in which water is supplied for cooling.

Changing the flow of cooling water allows getting different values of heat flows in the work areas. The condensation temperature at the input to the first defining section was measured using a thermocouple. The obtained value was controlled by a thermocouple installed in the second working section.

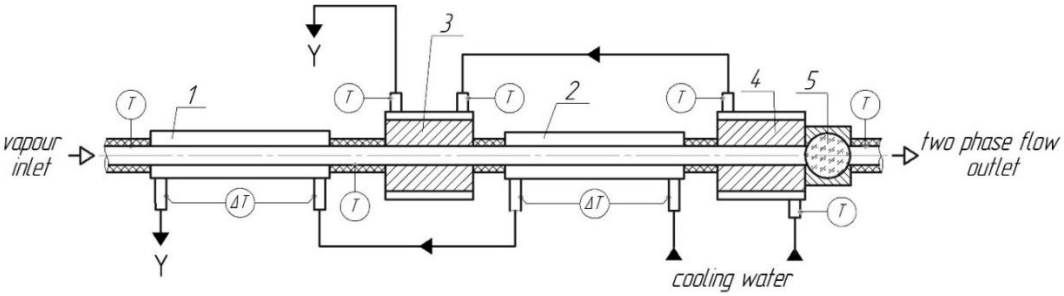

Fig. 1. Schematic view of the tested section: *1*, *2* – defining sections; *3*, *4* – brass working sections; *5* – inspection section; *T* – thermocouple

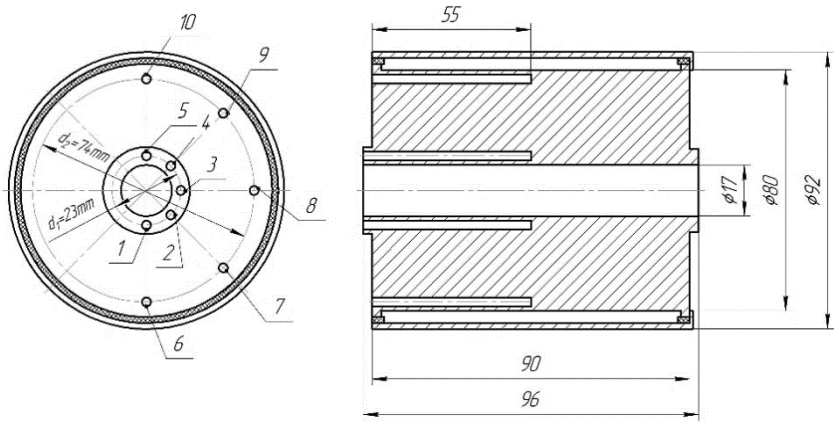

Fig. 2. Drawing of the brass working section: *1…10* – channels for locating thermocouples

To determine the temperature distribution in the wall of the work sections, chromel-collier thermocouples were used, which were placed inside the wall of the working sections at the diameters d_1 = 23 mm i d_2 = 74 mm in the axial channels with angular coordinates φ of 0, 45, 90, 135, 180 ° (Fig. 2).

The greater part of the experiments was carried out at local temperature differences in the wall and between the wall and the vapour above 8 ºC and 4 ºC, respectively. In this case, the temperature gradient in the wall in axial direction was much lower than that in adial direction. Such results indicate that the two-dimensionality does not affect the temperature distribution in the wall of the working sections. To calculate the local values of the coefficients of heat transfer α_φ local linear heat fluxes q_l, specific heat fluxes, assigned to the inner surface of the tube q_φ, and the temperature on the inner wall of the tube t_w were determined based on the dependencies:

$$q_l = \frac{2\lambda_b \pi \left(t_i - t_j\right)}{\ln\left(d_2/d_1\right)}; \quad q_\varphi = \frac{q_l}{\pi d};$$

$$t_w = t_i + \frac{q_l}{\pi}\frac{1}{2\lambda_b}\ln\frac{d_1}{d}; \quad \alpha_\varphi = \frac{q_\varphi}{\left(t_s - t_w\right)},$$

where λ_b – coefficient of thermal conductivity of the working section; *i*, *j* – numbers of thermocouples on the diameters d_1 and d_2 respectively (Fig. 2).

Average by the perimeter, but local by length of the tube, the values of thermal flows $\overline{q_\varphi}$ and heat transfer coefficients $\overline{\alpha_\varphi}$ were determined by the formulae:

$$\overline{q}_\varphi = \int_0^\varphi q_\varphi d\varphi, \quad \overline{\alpha}_\varphi = \int_0^\varphi \alpha_\varphi d\varphi.$$

The basic parameters of the two-phase current in all sections of the experimental area and in the condenser were determined by solving the equations of the material and thermal balance recorded for each section in which steam condensation took place, as well as for the

capacitor. The range of change of these parameters is shown in table 1.

Table 1. Main operating conditions during condensation tests.

Fluid	t_s, °C	G, kg/(m²·s)	Local vapor quality x	ΔT, °C	q, kW/m²
Steam	100	9–54	0.98–0.4	8–22	40–320
R-22	40	11–300	0.24–0.99	4–10	5–50

To prove the accuracy of measuring the local α_φ, the study was carried out for turbulent fluid flow inside a smooth tube provided that hydrodynamic and thermal stabilization were carried out in the adjacent layer. Under these conditions, the temperature of the walls of the working sections, the temperature fluctuations and local heat fluxes almost did not change along the perimeter of the tube, as it should be in the case of fluid flow through a complete section inside the tube.

The control and measuring equipment and the applied method of conducting experiments allowed determining the coefficients of heat transfer with a mean square error of ± 8%. The maximum imbalance of the material and thermal balance of the experimental setup for all conducted studies was 3 and 7%, respectively.

Substantiation of the choice of theoretical dependencies

For annular phase flow by Bae *et al.* [3] the, results of the calculations are represented in dimensionless terms as:

$$Nu_f = f\left(\beta, \mathrm{Re}_l, \mathrm{Pr}_l\right), \qquad (1)$$

where $Nu_f = \alpha\left(\nu_l^2/g\right)^{1/3}/\lambda_l$, $\beta = C_f Fr_l/2$ and $\mathrm{Re}_l = 4\mathrm{Re}_f$ are given in [3].

These correlations are plotted in [3] for numbers Pr_l from 1 to 5. In Figs. 3 and 4 such diagrams are plotted for Pr_l = 1 and Pr_l = 5, respectively. The analysis of correlation (1) makes it possible to note the following features of heat exchange that could be laid down in the improved calculation method. In the region of low values of Re_l heat transfer decreases with increasing Re_l, while the degree of β and Re_l impact corresponds to Nusselt's theory of laminar film condensation [1].

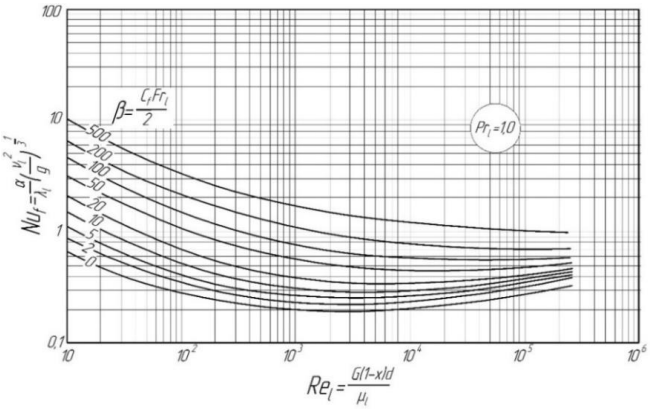

Fig. 3. Dimensionless local heat transfer coefficients from Bae *et al.* [3] at Pr_l=1.

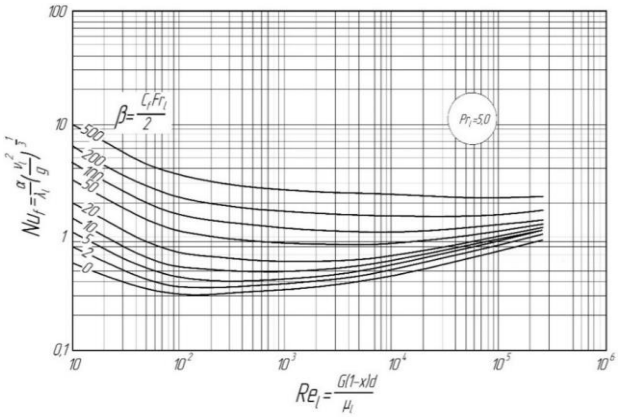

Fig. 4. Dimensionless local heat transfer coefficients from Bae *et al.* [3] at Pr_l=5.

As Re_l increases the heat transfer (Nu) decreases at the beginning and then depending on Pr_l value a wide (at low Pr_l numbers) or a narrow (at high Pr_l numbers) region of independence upon Re_l followed by increasing Nu is observed. In the region close to laminar flow of condensate film (Re_l < 100÷200) the effect of Pr_l is negligible and in some regimes (Re_l < 100 and β > 50÷100) is generally absent. It is true for a laminar flow. At turbulent condensate flow in accordance with the theory the heat transfer intensifies, as Pr_l grows.

The results of calculations by the formula (1) correctly reflect the nature of the condensation flow of the moving vapour inside tubes and channels, only when the influence of gravity on the film of condensation can be neglected. For horizontal tubes, these conditions correspond only to the annular mode of phase flow.

The conducted experimental studies showed that even minor asymmetry of the condensate flow in the upper part of the tube leads to a change in the wave and turbulent characteristics of the film and affects the distribution of local heat transfer

coefficients, therefore the accuracy of the obtained results depends on the correct evaluation of the area with the annular mode of phase flow. The method of Rifert *et al.* [17] was used to determine the boundary conditions and the boundary value of the correlation of friction forces τ_f and the gravitational forces τ_f based on the obtained experimental data was corrected. The following criteria for determining the limits of flow regimes were obtained:

at $\tau_f/\tau_g > 10$ – annular flow; (2)

at $1 \le \tau_f/\tau_g \le 10$ – intermediate flow; (3)

at $\tau_f/\tau_g < 1$ – stratified flow, (4)

where $\tau_f = C_f \rho_v w_v^2/2$; $\tau_g = \rho_l g \delta$.

The value of the film thickness δ was calculated by the equation:

$$\delta^+ = \delta/\nu_l \left(\tau_f/\rho_l\right)^{0.5}, \quad (5)$$

where the dimensionless thickness of the film δ^+ depends on the value of Re_l number:

$$Re_l < 50, \quad \delta^+ = 0{,}7071 Re_l^{0{,}5}; \quad (6)$$

.

$$50 < Re_l \le 1125, \quad \delta^+ = 0{,}4818 Re_l^{0{,}585}; \quad (7)$$

$$Re_l > 1125, \quad \delta^+ = 0{,}095 Re_l^{0{,}812}. \quad (8)$$

To compare the experimental values of the mean by the φ coefficients of heat transfer obtained in this paper on the basis of the theory of Bae *et al.* [3], sample points were selected which correspond only to the annular or intermediate phase flow modes according to (2)-(4).

The value of the theoretical number Nu_o was calculated on the basis of the interpolation of the graphs $Nu = f(\beta, Re_l, Pr_l)$ from the works [3] (in this work, spline interpolation was used by the values of Re_l, Pr_l i β_o in the Mathcad package). The parameter β_o was determined by the following formula for the single-phase flow:

$$\beta_o = C_{fo} Fr_l/2, \quad (9)$$

where $C_{fo} = 0{,}079/Re_v^{0{,}25}$ *at* $Re_v < 10^5$; $C_{fo} = 0{,}046/Re_v^{0{,}2}$ *at* $Re_v > 10^5$.

The results of this comparison are presented in Fig. 5.

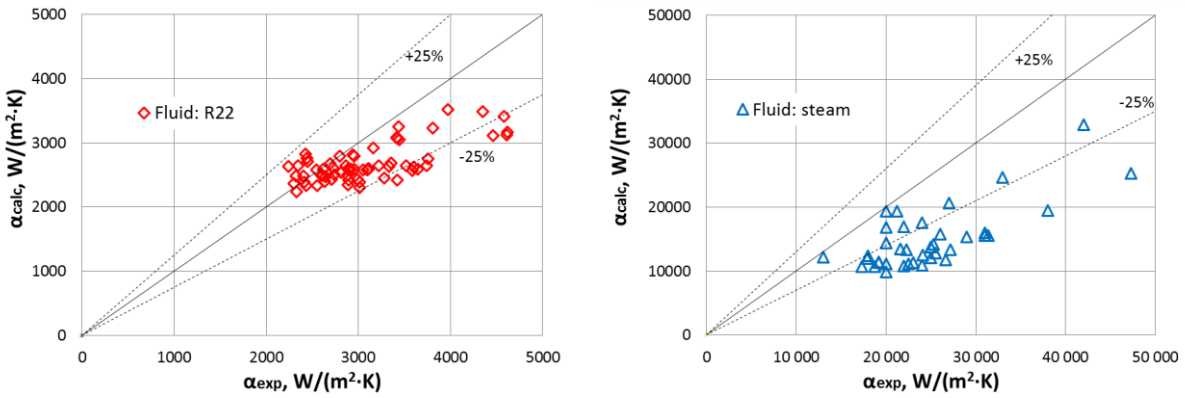

a) Fluid: R22 b) Fluid: steam

Fig. 5. Calculated *vs.* experimental heat transfer coefficients: predictions by Bae *et al.* [3] theoretical model.

Table 2. Statistical comparison of Bae *et al.* [3] theoretical model with experimental data (in %)

Statistical comparison	R22 G=300÷119 kg/(m²s) x=0.99÷0.56; q=50÷5 kW/m²	Steam G=54÷9 kg/(m²s) x=0.98÷0.4; q=320÷40 kW/m²
e_A	13.9	38.5
e_R	-11.3	-37.6
σ_N	12.2	14.2
Percentage of predicted points lying within ±25% error bars	77	18

The statistical comparison of the theoretical model of Bae *et al.* [3] with the experimental data is summarized in Table 2 which presents the mean absolute deviation e_A, the average deviation e_R, and the standard deviation, σ_N, given in Eqs. (10)–(12), respectively, along with the percentage of predicted points lying within ±20% error bars.

$$e_A = 1/n \sum 100 \left| \left(\alpha_{calc} - \alpha_{exp}\right)/\alpha_{exp} \right|, \quad (10)$$

$$e_R = 1/n \sum 100 \left[\left(\alpha_{calc} - \alpha_{exp}\right)/\alpha_{exp} \right], \quad (11)$$

$$\sigma_N = \left[1/(n-1)\sum (e-e_R)^2\right]^{0.5}. \quad (12)$$

where $e = 100\left[(\alpha_{calc} - \alpha_{exp})/\alpha_{exp}\right]$, n – number of calculation points.

Figure 5 and table 2 show that the greatest discrepancy is observed for the case of steam condensation. For freon R22, part of the data at Re_l=2300÷970 exactly matches the theory.

Such a deviation of the experimental data from theoretical calculations can be explained as follows. The calculations by the theory of film condensation essentially depend on the method of determining the loss of pressure on friction, and, accordingly, the friction coefficient C_f, which is included in the dependence (1) for the calculation of heat transfer. As noted in [6,18], none of the available scientific works have a sufficiently precise idea of the nature of the effect of friction force condensation on the boundary between phase separation. The determination of the friction coefficient C_f for a single-phase flow by the formula (9) is valid only if the value of the Lokart-Martinelli X_{tt} parameter is approximately zero. In this case, as follows from the numerous calculated dependences of works [19,20], the friction coefficients in single-phase and two-phase streams will be the same. However, in annular and intermediate flow modes, the value of the parameter X_{tt} can reach nonzero values. In particular, in this paper, when performing experimental studies, the value of the parameter X_{tt} varies from 0.005 to 0.24. As the experiments have shown, with these values of X_{tt}, the two-phase flow begins to affect the friction coefficient C_f, which leads to the increase in the parameter β, and local and medium heat transfer coefficients, respectively. In addition, as a result of experimental studies of local heat transfer coefficients, the growth of α_φ with the increase in the heat flux was noted, which is not taken into account in formula (1) and other well-known methods for calculating film condensation [11,12,15].

Therefore, in order to improve the coordination of the theory [3] with the experimental data obtained, in this paper it is proposed to take into account the influence of the heat flux and the parameters of the two-phase flow on the parameter β, which characterizes the effect of the interfacial friction force τ_f on the heat transfer.

Investigating the influence of the two-phase flow parameters on average heat transfer

The two-phase flow is characterized by such basic parameters as the mass velocity of the vapour *G*, the vapour content *x*, the vapour density ρ_v, and the density of the liquid ρ_l. In this paper, the influence of these parameters on heat transfer is recommended to be taken into account by the parameter β_v:

$$\beta_v = \Phi_v^2 \beta_o \quad (13)$$

where Φ_v^2 – correction complex for taking into account the influence of the two-phase flow.

The dependence for the calculation of Φ_v^2 was selected, based on the analysis of experimental data on average heat transfer obtained when condensing refrigerant R22 to the annular and intermediate regimes. In these studies, the input mass speed of the couple ranged from 119 to 305 kg/(m^{2}s), and of vapour content – 0.99 to 0.56. All experiments were performed for the same $\overline{q_\varphi}$, but for variable *G* and *x*. This procedure allows examining the specific impact on heat transfer of vapour velocity and vapour content at constant value or small changes of other characteristics.

To calculate the parameter Φ_v^2 four known formulae were used, which are presented in the works [21-24]:

from [21]: $\Phi_v^2 = 1 + 9{,}4X_{tt}^{0{,}62} + 0{,}564X_{tt}^{2{,}45}$; (14)

from [22]:

$$\Phi_v^2 = \left\{1 + 0{,}5\left[\frac{G}{gd\rho_v(\rho_l - \rho_v)^{0{,}5}}\right]^{0{,}75} X_{tt}^{0{,}36}\right\}^2; \quad (15)$$

from [23]: $\Phi_v^2 = \left(1 + 2{,}85X_{tt}^{0{,}523}\right)^2$; (16)

from [24]: $\Phi_v^2 = 1 + CX_{tt}^n + X_{tt}^2$, (17)

where

$$C = 21\left\{1 - e^{\left(1-0{,}28Bo^{0{,}5}\right)}\right\}\left\{1 - 0{,}9e^{-0{,}02Fr_l^{1{,}5}}\right\}, \quad n = 1 - 0{,}7e^{-0{,}08Fr_l},$$

$$Bo = \frac{gd^2(\rho_l - \rho_v)}{\sigma}, \quad Fr_l = \frac{Gx}{\sqrt{gd\rho_v(\rho_l - \rho_v)}}.$$

The results of calculating parameter Φ_v^2 from the experimental data using the formulae (14)-(17) are shown in Fig. 6. It shows that the value of the Φ_v^2 complex significantly changes depending on the formula for its calculation and it is impossible to choose the best among them. Therefore, the experimental values of the mean values by φ heat transfer coefficients with the theoretical calculation (1) are compared. The number Nu is determined by the values Re_l, Pr_l and β_v. The coefficient β_v is calculated by the formula (13) using the dependences (14)-(17) to determine the complex Φ_v^2. The results of the comparison are shown in Fig. 7.

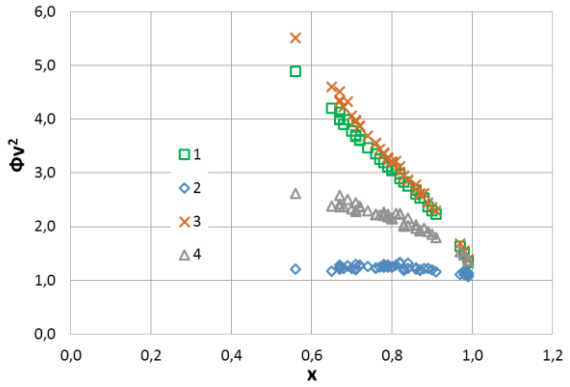

Fig. 6. Variation of Φ_v^2 with x: *1* – Φ_v^2 calculated by equation (14); *2* – by (15); *3* – by (16); *4* – by (17).

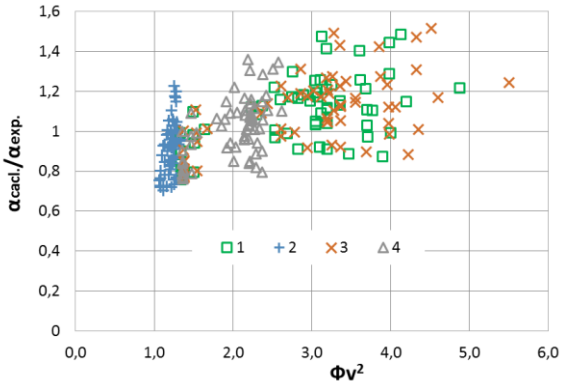

Fig. 7. Comparison of the experimental data for R22 condensation with calculations by (1): *1* – Φ_v^2 calculated by equation (14); *2* – by (15); *3* – by (16); *4* – by (17).

As it can be seen from Fig. 7, using the formulae (14) and (15), with the increase of parameter Φ_v^2 the values of heat transfer coefficients are overestimated by 50%. The calculation of Φ_v^2 by the formula (16) practically does not affect heat transfer. The best correlation between the experiment and the calculation is provided by the formula (17), which permits to summarize all data with an accuracy of ± 20%. Therefore, the dependence (17) is recommended to be used for determining the β_v coefficient by (13).

Consequently, the effect of the two-phase condensation current on the heat transfer is recommended to be taken into account by the correction of β_v by the formula (13), which makes it possible to use the theory (1) to calculate the heat transfer in the case of condensation of freon R22 not only for the annular, but also for the intermediate phase flow with sufficient accuracy (± 20 %).

Investigating the influence of heat flux on the average heat transfer

The effect of the heat flux on the hydraulic resistance and heat exchange in two-phase flows under phase transformations is theoretically justified in [25,**Error! Reference source not found.**] and is explained by the phenomenon of suction of the condensate mass into vapour in the adjacent layer. In [25] it is shown that at a relative rate of suction $j = q/rGx > 10^{-4}$, the hydraulic resistance of the friction coefficient C_f at the boundary of the phase separation increases in comparison with the resistance of the single-phase flow (C_{fo}) and is described by the formula:

$$C_f / C_{fo} = 1 + 17{,}5\,\mathrm{Re}_v^{0{,}25}\, j\,. \qquad (18)$$

In [**Error! Reference source not found.**] the dependence for the definition of C_f has the following form:

$$C_f / C_{fo} = (1 - 0.25b)^2 / (1 + 0.25b)^{0.2}, \qquad (19)$$

where $b = -2q/rGxC_{fo}$.

In this case, there is a limitation of the use of the formula (19) with b less than minus 4, when the phenomenon of suction of the condensate mass does not affect the C_f/C_{fo} ratio.

The authors of [27] suggested much earlier than in [25,**Error! Reference source not found.**] the dependence for taking into account the influence of the heat flux on the C_f/C_{fo} ratio:

$$C_f / C_{fo} = b / (e^b - 1)\,. \qquad (20)$$

In this paper, the effect of the heat flux on heat transfer is proposed to be taken into account by the correction β_q:

$$\beta_q = \Phi_q \beta_o\,, \qquad (21)$$

where $\Phi_q = C_f / C_{fo}$ – correction factor to take into account the influence of heat flux.

The formula for determining the C_f / C_{fo} value was selected by analyzing the experimental data obtained for the case of steam condensation by the following parameters: t_s=102 °C, G=54÷9 kg/(m²s), x=0,4÷0,98, q=320÷40 kWt/m², which correspond to the annular and intermediate phase flow modes. All experiments were performed for the same G and x, but for variable $\overline{q_\varphi}$. This allowed to show the special effect of the heat flux on the heat transfer at a constant value or at a slight change in the other characteristics.

The results of the calculation of the Φ_q parameter are shown in Fig. 8. It is seen that calculations by formulae (18)-(20) provide values

very close among themselves (difference within ± 10%), and to calculate the coefficient β_q for (21) one can use any of the formulae. In this work, the dependence (18) with the limitation of the suction effect on the boundary values of parameter b is used less than minus 4.

The analysis of the obtained experimental data showed that the effect of the heat flux on the heat transfer should be taken into account with β_q correction by the formula (21). This makes it possible to use the theory (1) to calculate the heat transfer in the case of steam condensation not only for the annular, but also for intermediate phase flow with adequate accuracy (± 25%).

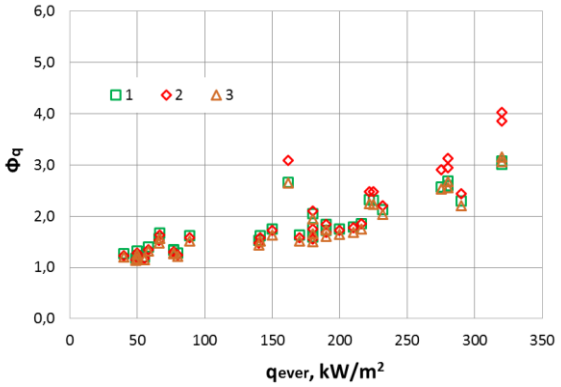

Fig. 8. Variation of Φ_q with average by φ heat flux: *1* – Φ_q calculated by equation (18); *2* – by (19); *3* – by (20).

Comparing the proposed method with the obtained experimental data

The practical application of the developed method for calculating heat transfer under various condensation parameters is complicated by the necessity of the solution of the dependence (1) given in an implicit form. Solving the equation (1) is possible in two ways. Graphically, using the interpolation of graphs in Figs. 3 and 4, or numerically. However, the numerical solution (1), presented in [3,4] has a very cumbersome and uncomfortable look for permanent use. Therefore, the proposed method for calculating heat transfer in this paper is presented in the form of a special program, which is developed in the package Mathcad. With the help of information technology of "cloud" functions, the principle of which is described in detail in [28], the developed program is available on the Internet by link: http://twt.mpei.ac.ru/MCS/Worksheets/Thermal/Heat-transfer-during-condensation-in-smooth-horizontal-tubes.xmcd and is available for all users.

The work of this program is based on the following algorithm:

1. Using the values of the Froude numbers Fr_l and the friction coefficient for the single-phase flow C_{fo}, the parameter β_o is determined by the formula (9).

2. The values of correction complexes Φ_v^2 and Φ_q are calculated from the relations (13) and (21), respectively.

3. The parameter β_{qv} which takes into account the influence of both the two-phase current and the heat flux on the frictional force τf is determined by the formula:

$$\beta_{qv} = \beta_o \Phi_v^2 \Phi_q . \qquad (22)$$

4. The values of the dimensionless Nu number are calculated on the basis of the interpolation of the graphs given in Figs. 3 and 4. To do this, the Mathcad package uses spline interpolation with values Re_l, Pr_l and β_{qv}.

5. The values of heat transfer coefficient are based on the formula $\alpha = Nu_f \lambda_l \left(v_l^2/g\right)^{-1/3}$.

Table 3 shows a part of the experimental data by average heat transfer coefficients obtained for three different cases. The first is with the complex $\Phi_v^2 \approx 1{,}0$, and Φ_q>1.6. The second, on the contrary, is Φ_q<1.2 and $\Phi_v^2 > 1{,}6$. And the third case, when the value of both complexes is more than 1.6. Theoretical values of Nusselt numbers Nu_o, Nu_v and Nu_{vq}, are obtained using the developed program by the following parameters: for Nu_o: Re_l, Pr_l and β_o; for Nu_v: Re_l, Pr_l and β_v; for Nu_{vq}: Re_l, Pr_l and β_{qv}. It can be seen that under the values $\Phi_q << \Phi_v^2$ it is possible not to take into account the influence of heat flux on the heat transfer and, accordingly, not to take into account the effect of Φ_v^2, when $\Phi_q >> \Phi_v^2$. Considering these two amendments makes it possible to obtain a fairly accurate (up to ± 25%) reconciliation of calculation and experimental data.

The comparison of all experimental data obtained with the proposed method for the annular and intermediate flow regimes is shown in Fig. 9. The statistical comparison of the suggested method with the experimental data is summarized in Table 4.

Table 3. Comparison of the experimental data for R22 and steam condensation with theoretical calculations

№	Fluid	$\frac{G,\ [kg/(m^2 s)]}{x}$	$\frac{\bar{q}\cdot 10^{-3}[W/m^2]}{\bar{\alpha}\cdot 10^{-3}[W/(m^2 K)]}$	$\overline{Nu}_{exp}$	$Fr_l\cdot 10^{-3}$	Re_l	$C_{fo}\cdot 10^3$	$\frac{\beta_o}{Nu_o}$	$\frac{\Phi_v^2}{Nu_v}$	$\frac{\Phi_q}{Nu_{vq}}$
1	Steam	36 0.975	180 42	1.26	10	59	5.25	26 0.99	1.02 1.0	1.6 1.3
2	Steam	26 0.97	190 33	0.99	5.08	57	5.72	15 0.74	1.02 0.75	1.82 1.06
3	R22	192 0.9	5 2,81	0.43	3.57	2287	3.91	7 0.38	1.85 0.43	1.04 0.44
4	R22	232 0.86	18,2 3.35	0.,5	4.33	4134	3.35	8 0.4	2.1 0.47	1.2 0.49
5	R22	139 0.67	37.3 2.89	0.44	1.11	5512	4.39	2 0.35	2.4 0.39	1.8 0.44
6	Steam	36 0.48	275 19.2	0.57	2.4	1209	6.28	8 0.34	1.82 0.41	2.57 0.55

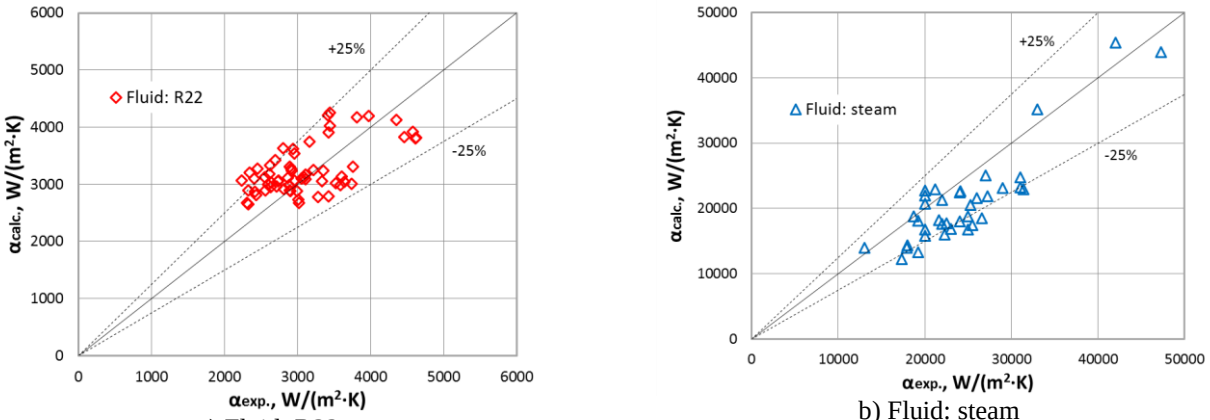

a) Fluid: R22

b) Fluid: steam

Fig. 9. Calculated *vs*. experimental heat transfer coefficients: predictions by the improved model

Table 4. Statistical comparison of the suggested method with experimental data (in %)

Statistical comparison	R22	Steam
	G=300÷119 kg/(m^{2}s); x=0.99÷0.56; q=50÷5 kW/m^2	G=54÷9 kg/(m^{2}s); x=0.98÷0.4; q=320÷40 kW/m^2
e_A	12.1	17.1
e_R	1.1	-10.9
σ_N	15	14.4
Percentage of predicted points lying with in ±25% error bars	92	95

It can be seen from Fig. 9 and Table 4 that the calculation for complexes Φ_v^2 and Φ_q to determine the correction β_{qv} by the formula (22) greatly improves the reconciliation of experimental data with the proposed method.

Comparing the proposed method for calculating heat transfer with other methods on the basis of experimental data of various authors

In order to confirm the accuracy of the developed method, its verification was performed with experimental data from the works of the following scientists: concerning the condensation of steam – Boyko [**Error! Reference source not found.**]; freons R-22, R-123 and R-134a – Yu *et al*. [30]; carbon dioxide –Kim and Jang [31]; propylene, propane, ether and isobutane – Park *et al*. [32]; refrigerant FC-72 –Lee *et al*. [33] and refrigerants R-245fa, Novec®649, HFE-7000 –

Ghim and Lee [34]. The results are shown in Figs. 10-15, which make it evident that the developed method of calculation with an accuracy of ± 25% generalizes all experimental data in the annular and intermediate modes of phase flow.

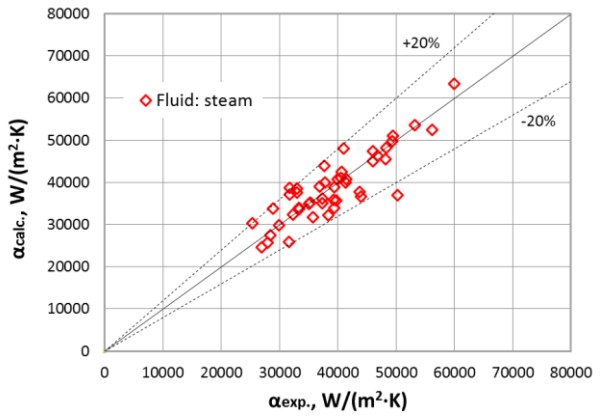

Fig. 10. Application of the improved model to Boyko [**Error! Reference source not found.**] data.

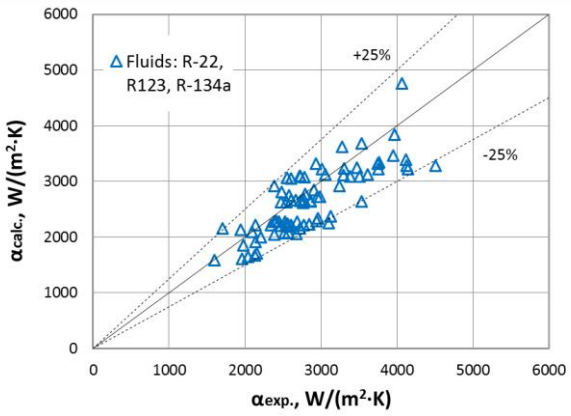

Fig. 11. Application of the improved model to Yu *et al*. [30] data.

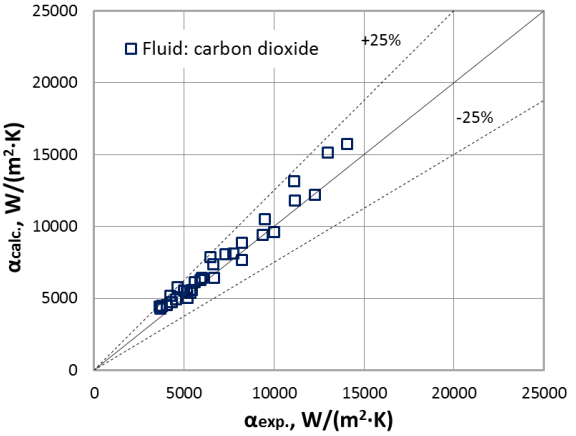

Fig. 12. Application of the improved model to Kim and Jang [31] data.

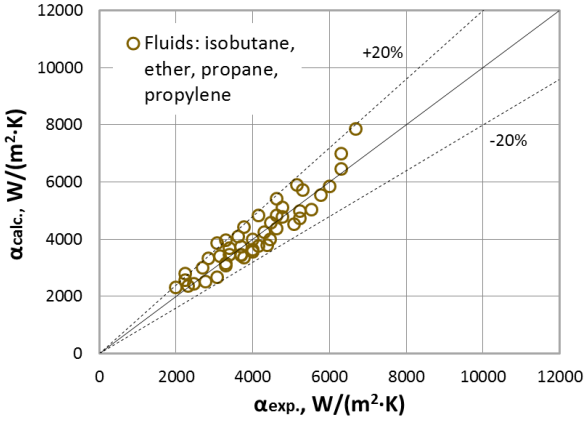

Fig. 13. Application of the improved model to Park *et al.* [32] data.

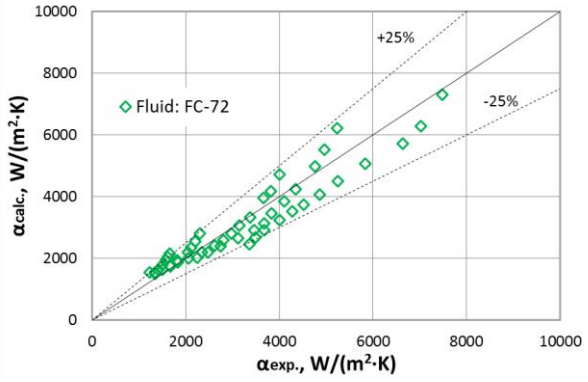

Fig. 14. Application of the improved model to Lee *et al.* [33] data.

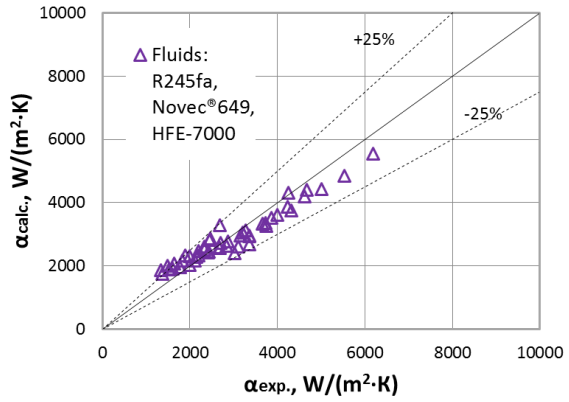

Fig. 15. Application of the improved model to Ghim and Lee [34] data.

CONCLUSIONS

As a result of the theoretical studies and the analysis of experimental values averaged by the perimeter of the tube of the heat transfer coefficients during the condensation of freon R22 and steam within the horizontal tube, we can formulate the following conclusions:

1. The application of the theory of film condensation [3] was proven to be correct when calculating the heat transfer during condensation in a horizontal tube for the annular phase flow regime. The necessity of more accurate estimation of influence, both of two-phase condensation current, and of heat flux on the laws of heat exchange is shown.

2. The influence of the two-phase condensation current on the heat transfer is recommended to be taken into account with the parameter $\beta_v = \Phi_v^2 \beta_o$. It is experimentally proven that the formula (17) for calculating the complex Φ_v^2 is correct.

3. The effect of heat flux on the heat transfer is expedient to be estimated by correction $\beta_q = \Phi_q \beta_o$. In this case, the application of formula (18) is used experimentally to calculate the parameter Φ_q.

4. The use of complexes β_v and β_q for the calculation of heat exchange by the theory of film condensation (1) allows to generalize with adequate accuracy (error ± 25%) both the experimental data obtained and the experimental data of other authors for the annular and intermediate modes of phase flow in a wide range of changes in regime parameters. Such calculation accuracy is not achievable for other, most commonly used methods [11,12,15].

5. The developed method for calculating heat transfer is presented as a program in the package Mathcad. With the help of information technology of "cloud" functions, this program is available on the Internet by the link: http://twt.mpei.ac.ru/MCS/Worksheets/Thermal/Heat-transfer-during-condensation-in-smoth-horizontal-tubes.xmcd and is available to all users.

Nomenclature

Bo – Bond number ($= gd^2(\rho_l - \rho_v)/\sigma$)
C_f – friction coefficient
d – inner diameter of tube, [m]
Fr_l – liquid Froude number ($= \dfrac{\rho_v(\rho_l - \rho_v)w_v^2}{\rho_l^2(\nu_l g)^{2/3}}$)
G – mass velocity, [kgm^{-2}s^{-1}]
g – gravitational acceleration, [ms^{-2}]
l – length of the tube, [m]
Nu_f – film Nusselt number, ($= \dfrac{\alpha}{\lambda_l}\left(\dfrac{\nu_l^2}{g}\right)^{1/3}$)
Pr – Prandtl number
q – heat flux, [W·m^{-2}]
r – heat of vaporization, [J·kg^{-1}]
Re_f – film Reynolds number ($= ql/(r\mu_l)$)
Re_l – liquid Reynolds number ($= G(1-x)d/\mu_l$)
Re_v – vapor Reynolds number ($= Gxd/\mu_v$)
t – temperature, [°C]
w – velocity, [ms^{-1}]
x – vapor quality
X_{tt} – Martinelli parameter
($= (\mu_l/\mu_v)^{0.1}(\rho_v/\rho_l)^{0.5}\left[(1-x)/x\right]^{0.9}$)

Greek symbols:
α – heat transfer coefficient, [Wm^{-2}K^{-1}]
β – parameter related to friction stress in the interphase
ΔT – temperature difference (=t_s-t_w), [K]
λ – thermal conductivity, [Wm^{-1}K^{-1}]
μ – dynamic viscosity, [Pas]
ν – kinematic viscosity, [m^{2}s^{-1}]
ρ – density, [kgm^{-3}]
σ – surface tension, [Nm^{-1}]
τ – shear stress, [Pa]
φ – angular coordinate, [°]
Φ_v^2 – parameter that takes into account influence of two-phase flow on shear stress
Φ_q – parameter that takes into account surface suction at the interphase

Sub- and superscripts
f – frictional factor
l – liquid
v – vapor/gas
exp – experimental
calc – calculated;
\+ – non-dimensional symbol

REFERENCES

1. W. Nusselt, *Zeitschrift VDI*, **60**, 541 (1916).
2. A. E. Dukler, *Chem. Eng. Progress Symposium Series*, **30**, 1 (1960).
3. S. Bae, J. S. Maulbetsch, W. M. Rohsenow, Refrigerant forced-convection condensation inside horizontal tubes. Report No. DSR-79760-64. Massachusetts Institute of Technology, Cambridge, MA, 1969, p. 120.
4. D. P. Traviss, A. B. Baron, W. M. Rohsenow, Forced-convection condensation inside tubes. Report No. DSR-72591-74. Massachusetts Institute of Technology, Cambridge, MA, 1971, p. 105.
5. V. G. Rifert, *J. Eng. Phys. Thermophys.*, **44**, 700 (1983).
6. V. G. Rifert, V. V. Sereda, *Sci. J. Thermal Sci.*, **19**, 1769 (2015).
7. A. Cavallini, G. Censi, D. Del Col, L. Doretti, G. A. Longo, L. Rossetto, C. Zilio, *.Int. J. Refrigeration*, **26,** 373 (2003).
8. O. Garcia-Valladares, *Heat Transfer Eng.*, **24**, 6 (2003).
9. A. S. Dalkilic, S. Wongwises, *Int. J. Heat Mass Transfer*, **52,** 3409 (2009).
10. V. G. Rifert, V. V. Gorin, V. V. Sereda, V. V. Treputnev, *Int. J.Mech. Aerospace, Industrial, Mechatronic Manufact. Eng.*, **11**, 1376 (2017).
11. J. R. Thome, J. Hajal, A. Cavallini, *Int. J. Heat Mass Transfer*, **46**, 3365 (2003).
12. M. Shah, *ASHRAE Trans.*, **15**, 889 (2009).

13. E. P. Ananiev, L. D. Boyko, G. N. Kruzhilin, *Int. Heat Transfer Conf.*, **2**, 290 (1961).
14. J. B. Tepe, A. C. Mueller, *Chem. Eng. Progr*. **43,** 267 (1947).
15. A. Cavallini, G. Censi, D. Del Col, L. Doretti, M. Matkovic, L. Rossetto, C. Zilio, Proc. 3rd International Conference on Heat Transfer, Fluid Mechanics and Thermodynamics, Cape Town, South Africa, 21-24 June 2004, p. 21.
16. V. G. Rifert, V. V. Sereda, P. A. Barabash, V. V. Gorin, *Thermal Sci.*, **21**, 1479 (2017).
17. V. G. Rifert, *Int. J. Heat Mass Transfer*, **31**, 517 (1988).
18. V. G. Rifert, V. V. Gorin, P. A. Barabash, V. V. Sereda, *Sci. J. Tranc Academenergo*, **4,** 57 (2011).
19. A.S. Dalkilic, O. Agra, I. Teke, S. Wongwises, *Int. J. Heat Mass Transfer*, **53**, 2052 (2010).
20. S. G. Kandlikar, S. Garimella, D. Li, S. Colin, M. R. King, Heat Transfer and Fluid Flow in Minichannels and Microchannels, Elsevier Ltd, Kidlington, Oxford, 2005, p. 450.
21. C. C. Wang, C. S. Chiang, D. C. Lu, *Exper. Thermal Fluid Sci*., **15**, 395 (1997).
22. S. Koyama, L. Gao, T. Fujii, Enhancement of in-tube condensation of non-azeotropic refrigerants mixtures with a micro-fin tube, Proc. XVIII International Congress of Refrigeration, Montreal, Quebec, Canada, 10-17 August 1991, p. 142.
23. M. Soliman, J. R. Schuster, P. J. Berenson, *J. Heat Transfer*, **90**, 267 (1968).
24. H. M. Afroz, A. Miyara, K. Tsubaki, *Int. J. Refrigeration*, **31**, 1458 (2008).
25. R. B. Kinney, E. M. Sparrow, *J. Heat Transfer*, **92**, 121 (1970).
26. S. S. Kutateladze, A. I. Leont'ev, Heat, mass transfer and friction in the turbulent boundary layer (in Russian), Moscow, Energiya, 1972.
27. H. S. Mickley, R. Ross, A. Squyers, W. E. Stewart, Heat, mass and moment transfer for flow over a flat plate with blowing and suction, Massachusetts Inst. of Tech., NASA TN № 3208, 1953, p. 315.
28. V. Ochkov, K. Orlov, V. Voloshchuk, Thermal Engineering Studies with Excel, Mathcad and Internet. Springer International Publishing, 2016. p. 432.
29. L. D. Boyko, Heat transfer during vapor condensation inside tubes (in Russian), in: Heat Transfer in the Elements of Power Plants, 1966, p. 197.
30. J. Yu, S. Koyama, H Haraguchi, S. Momoki, A. Ishibashi, *Reports Inst. Adv. Material Study Kyushu Univ.*, **9**, 137 (1995).
31. Y. J. Kim, J. Jang, P. S. Hrnjak, M. S. Kim, *J. Heat Transfer ASME*, **131**, 021501 (2009).
32. K. J. Park, D. Jung, T. Seo, *J. Multiphase Flow*, **34**, 628 (2008).
33. H. Lee, I. Mudawar, M. Hasan, *Int. J. Heat Mass Transfer*, **66**, 31 (2013).
34. G. Ghim, J. Lee, *Int. J. Heat Mass Transfer*, **1**, 718 (2017).

ВЪЗСТАНОВЯВАНЕ НА КОРЕКТНОСТТА И ПОДОБРЯВАНЕ НА МОДЕЛА ЗА ФИЛМОВА КОНДЕНЗАЦИЯ В ТРЪБИ

В. Г. Риферт[1], В. В. Середа[2], В.В . Горин[1], П. А. Барабаш[1], А. С. Соломаха[1]

[1] *Департамент по теоретично и индустриално топлинно инженерство, Киевски политехнически институт „Игор Сикорски”, Киев, Украина*

[2] *Национален университет по водно стопанство и природно инженерство, Ривне, Украйна*

Постъпила на 20 март, 2018 г.; коригирана на 26 юли, 2018 г.

(Резюме)

В статията са разгледани експерименталните изследвания, целящи увеличаване на ефективността на хоризонтални тръбни кондензатори чрез много точна оценка на топлопреноса и режимните параметри при кондензиране на различни охладители в хоризонталните тръби на устройствата. Уникалните измервания на топлинните потоци и коефициентите на топлопренос са проведени при кондензация на Freon R-22 и водна пара в широк интервал на режимните параметри (G, x, q, Re_l). Предложен е подобрен модел на филмова кондензация в хоризонталните тръби за предсказване на топлопреноса с използване на резултатите от цифровите решения на Bae *et al*. В този модел е дефиниран по-точно междуфазният фрикционен коефициент като основен параметър, определящ кондензацията. По-точната дефиниция включва експериментална обосновка на предсказването на β_q за изчисляване на загубите в налягането от триенето и корекцията на β_q, която взема пред вид повърхностното засмукване в междинната фаза. Топлообменът, предсказан от подобрения метод, е сравнен с експерименталните данни на различни автори за 13 течности (водна пара, R-22, R-123, R-134a, R-245fa, въглероден диоксид, пропилен, пропан, етер, изобутен, охладители FC-72, Novec®649, HFE-7000) в пръстеновидни и междинни режими. Доброто съвпадение между експериментите и изчисленията (различие в рамките на 25%) доказва коректността на предложения метод при ламинарни и турбулентни потоци на кондензатния филм.

Bulgarian Chemical Communications, Volume 50, Special Issue K (pp. 70 – 75) 2018

Mathematical modelling of heat and mass transfer processes in wastewater biological treatment systems

A. P. Safonyk*, O.O. Hrytsyna, V. A. Voloshchuk, V. V. Sereda

National University of Water and Environmental Engineering, Rivne, Ukraine

Received May 17, 2018, Accepted July 27, 2018

In this paper, a mathematical model is presented for wastewater biological treatment of multicomponent pollutants. The proposed model includes a simulation of the wastewater clarification in the clarifier; simulation of the wastewater aerobic treatment in the porous medium; numerical-asymptotic approximation for solutions of spatial model problems of the wastewater aerobic treatment; simulation of singularly perturbed processes of convective diffusion, taking into account mass transfer and temperature regime; computer modeling of the wastewater biological treatment process in the aerotank regenerator.

The idea of perturbation theory is used for constructing a mathematical model of an appropriate nonlinear problem (this theory is based on the consideration of new factors and effects, by perturbing the output, well-known backgrounds, but not by solving new appropriate intricate modeling problems). The relevant processes, such as "filtration-convection-diffusion-heat and mass transfer", are considered in the media (one connected areas, bounded by equipotential lines and flow lines), which can be deformed depending on the certain process characteristics. This, by turn, predetermine the process nature, i.e. there is a mutual influence of the medium characteristics and the process. Filtration flow is regarded as a certain background for the convective transport of soluble substances (pollutants), taking into account small diffusion effects.

Based on the above, a mathematical model of the wastewater aerobic treatment, taking into account the interaction of bacteria, organic and biologically non-oxidizing substances in conditions of diffuse and mass-transfer disturbances and the influence of temperature regimes, has been constructed.

Keywords: mathematical model, temperature regime, wastewater aerobic treatment

INTRODUCTION

Domestic wastewater contains pollutants of mineral and organic origin, while industrial one differs both in composition and concentration, depending on the region. Regardless of the type, the wastewater needs to be cleaned, because it contains pollutants that significantly exceed the permissible concentration levels. To prevent the harmful effects of impurities on the environment, the filter systems that provide acceptable contamination levels are used.

An effective tool for studying the operating modes of such systems and optimizing their parameters is mathematical modeling. In this regard, there is a problem of the creation and implementation of an adequate mathematical model that reflects the physics of phenomena occurring in the systems of biological wastewater treatment. The aim is to develop a mathematical model of the process of biological wastewater treatment, enabling to predict the manufacturing process wastewater treatment in more detail taking into account the temperature regimes, that further enables the implementation of automated control over the process of effective deposition of impurities in biological filters depending on the output data of the aquatic environment, the improvement of these systems in accordance with the accepted conditions and criteria, as well as the possibility of finding an effective combination of wastewater biological treatment schemes with the systems of energy recovery from wastewater treatment (e.g. heat pump installations).

LITERATURE REVIEW

In recent years, a large number of scientific researches on the issues of modeling and automation of biochemical wastewater treatment have been carried out. These studies have considerably expanded the concept of water purification, heat and mass transfer, influence of variable parameters necessary for automatic control over output information, and also defined certain principles for the construction of schemes and automation tools.

In some models, wastewater treatment is considered as a technological process with the features of mechanical structures without taking into account the dynamics of time changes of the filter effective operation, in others – interconnections of active sludge and impurities without taking into account the system of interacting parameters, or a set of equations that does not take into account the interconnection between parameters, which are

* To whom all correspondence should be sent:
Email: a.p.safonyk@nuwm.edu.ua

clearly expressed in experiments and play an important role.

However, most of these works do not take into account the influence of the environmental temperature, which is one of the main factors affecting the occurring of reactions.

The combination of the above shows the relevance of this work, which is to develop a mathematical model of the process of wastewater treatment from pollutants, which takes into account the interaction of bacteria, active sludge and impurities, as well as temperature regime. The next step is to study the model using computer simulation to calculate the optimal parameters of the technological process [1-9].

FORMULATION OF THE PROBLEM

It is necessary to consider the process of treating liquids of organic impurities. According to the literary sources, the following stages of wastewater treatment of pollutants are distinguished:

- decomposition of organic contamination by bacteria;
- growth and death of bacteria;
- production of "young" bacteria by active sludge;
- the transfer of impurities to a biologically non-oxidizing substance.

To describe the dynamics of changes in the concentration of pollution, taking into account the influence of activated sludge on the absorption of impurities, there is used the equation of the type [10]:

$$\frac{\partial C_i}{\partial \tau} = v_C \frac{\partial C_i}{\partial x} - \beta_i C_i B T + D_C \frac{\partial^2 C_i}{\partial x^2}, \quad (1)$$

where β_i is the coefficient, which takes into account the design features of the aerotank, the flow rate of the liquid and the absorption of the substrate in accordance with the bacteria activity;

C_i is the concentration of i-th contamination in water;

T is the temperature of the aerotank;

v_C is the velocity of the substrate movement;

D_C is the diffusion coefficient.

Given that the bacteria move along with the contaminated substance in the porous medium, and also settle down in the lower part of the aerotank in the form of active sludge, the following equation for the growth, death and transfer of bacteria taking into account the biological need of oxygen is arrived at:

$$\frac{\partial B}{\partial \tau} = v_B \frac{\partial B}{\partial x} + \beta B K T K_B + w_B + D_B \frac{\partial^2 B}{\partial x^2}, \quad (2)$$

where B is the concentration of activated sludge;

K_B is the coefficient of oxygen and bacteria absorption;

w_B is the rate of active sludge accumulation according to the adequacy of the model;

v_B is the velocity of activated sludge movement;

D_B is the diffusion coefficient.

In order to improve the efficiency of the process and ensure optimal living conditions of bacteria, oxygen is additionally introduced, and the equation describing the dynamics of this process has the following form:

$$\frac{\partial K}{\partial \tau} = v_K \frac{\partial K}{\partial x} + \beta K T + \\ + K_K \cdot C \cdot (K_0 - K) + w_K + D_K \frac{\partial^2 K}{\partial x^2}, \quad (3)$$

where K is the oxygen concentration, necessary to maintain the best bacterial absorption of contamination;

K_K is the coefficient of mass transfer of oxygen;

K_0 is the concentration of saturation of water with oxygen at given temperature and pressure;

w_K is the rate of absorption of the oxygen substrate;

v_K is the oxygen flow rate;

D_K is the diffusion coefficient.

The basis for the thermal calculation of a biofilter is the equation of the thermal balance of its water mass, which takes into account the following components of heat fluxes:

1. The inflow of heat in a biofilter with a circulation loss of heat input incident, with the outflow of heat supplied to the aerators.
2. The inflow of heat due to the absorption of total solar radiation.
3. The outflow of heat with water at the outlet of the biofilter.
4. The loss of heat due to evaporation.
5. The loss of heat due to convective heat exchange between water and air.
6. The loss of heat due to effective radiation of water surface.

Since the processes occurring in the aerotank (Fig. 1) occur with the release and absorption of energy, the law of thermodynamics is used:

$$Q_{in} + Q_{heat} - Q_w + Q_{bot} - \\ - Q_{air} - Q_{evap} - Q_{out} = 0, \quad (4)$$

where Q_{in} is the amount of heat coming from the input water;

Q_{heat} is the amount of heat given by the air;

Q_w is the amount of heat lost through the aerotank walls;

Q_{bot} is the amount of heat given to the heating of the earth through the bottom of the aerotank;

Q_{air} is the amount of heat given to the air on the surface of the water in the aerotank;

Q_{evap} is the energy of heat that will be emitted for evaporation;

Q_{out} is the residual heat that will be removed with the outflowing water.

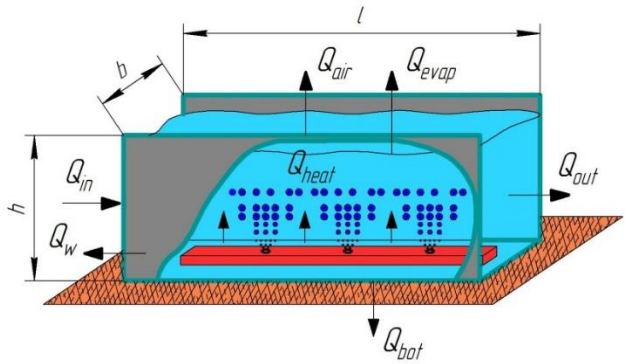

Fig. 1. Thermal balance of aerotank

To determine the energy supplied by the temperature of the incoming water, the formula is used (5):

$$Q_{in} = c_w \cdot m\left(T_{in} - T\right), \qquad (5)$$

where T, K is the water temperature in the aerotank;

$c_w, \frac{J}{kg \cdot K}$ is the specific heat of water;

m, kg is the mass of water in which heat transfer occurs;

$\rho, \frac{kg}{m^3}$ is water density;

$V = l \cdot h \cdot b, m^3$ is the volume of the aerotank;

l, m is the length of the aerotank;

h, m is the height of the aerotank;

b, m is the width of the aerotank;

T_{in}, K is the temperature of the water incoming into the aerotank.

The amount of heat transferred from the air is described by Fourier's law:

$$Q_{heat} = -\lambda_p \cdot grad\, T_{air} \cdot h \cdot b, \qquad (6)$$

where $\lambda_p, \frac{W}{m^2 \cdot K}$ is the coefficient of thermal conductivity of air;

T_{air}, K is the air temperature.

But since heat is supplied only in certain areas of the aerotank, the function that describes the amount of heat provided from the outside will look like (7), where we additionally multiply by 2 the area of interaction, because heat is absorbed by water, located on both sides of the point of heat supply:

$$\begin{cases} Q_{heat} = -\lambda_p \cdot grad\, T_{air} \cdot h \cdot b \cdot 2, x = 20 \cdot n; \\ Q_{heat} = 0, x \neq 20 \cdot n. \end{cases} \qquad (7)$$

where x, m is the coordinate along the aerotank in which the coolant is supplied;

$n = 1, 2, 3, ..., k$ are natural numbers.

The loss of heat through the walls of the aerotank is determined by the equation (8):

$$Q_w = \frac{\lambda_w}{\sigma}\left(T_{aver} - T\right) S_w, \qquad (8)$$

where $\lambda_w, \frac{W}{m \cdot K}$ is the coefficient of the wall thermal conductivity;

σ, m is the wall thickness;

T_{aver}, K is the average temperature of the air that surrounds the aerotank;

$S_w = 2 \cdot l \cdot h, m^2$ is the area of the aerotank's lateral surface through which the heat is lost.

The transfer of heat through the bottom of the aerotank to the soil is similar to the formula (8), given that the temperature of the earth is less than the air temperature.

$$Q_{bot} = \frac{\lambda_w}{\sigma} \cdot \left(T_{earth} - T\right) \cdot S_{bot}, \qquad (9)$$

where T_{earth}, K is the average temperature of the earth;

$S_{bot} = l \cdot b, m^2$ is the area of the bottom surface through which the heat is emitted to heat the earth.

The transfer of heat from water to air through the aerotank surface is described by Newton-Richman's law:

$$Q_{air} = \alpha \cdot \left(T_{aver} - T\right) \cdot F, \qquad (10)$$

where $\alpha, \frac{W}{m^2 \cdot K}$ is the heat transfer coefficient of air;

$F = l \cdot b, m^2$ is the surface area of the water through which the heat is emitted to heat the air.

The energy of heat that will be emitted for evaporation can be described with the equation (11) from the work [11]:

$$Q_{evap} = \alpha_e \cdot (e_s - e_2) \cdot S_{bot} + \frac{1}{\rho \cdot c_w} \frac{\partial I}{\partial x}, \qquad (11)$$

where $\alpha_e, \frac{W}{m^2 \cdot mbar}$ is the coefficient of heat transfer by evaporation;

$e_s, m^2 \cdot mbar$ is the maximum water vapor moisture, which corresponds to the average temperature of the water surface;

$e_2, m^2 \cdot mbar$ is the humidity of water vapor at the height of 2 m above the water surface;

I is the flow of solar energy;

ρ is water density.

The residual heat that will be removed with the outflowing water is determined by the ratio (12):

$$Q_{out} = c_w m\left(T_{out} - T\right), \qquad (12)$$

where T, K is the temperature of water in the aerotank;

T_{out}, K – the temperature of the water outflowing from the aerotank.

Also, a part of the energy will be transferred along the length of the aerotank due to the motion of water. To do this, in addition to equation (13), we introduce the convective and diffusive components of the mass transfer, as well as the function of the source, which has the following form:

$$k = \gamma \cdot \left(T_{aver} - T_{in}\right) \cdot x, \qquad (13)$$

where $\gamma, \frac{1}{m \cdot K}$ is the rate of heat transfer along the aerotank, depending on the environment.

Taking into account the mentioned components of heat fluxes, as well as the corresponding dependences (4)-(13), after carrying out corresponding generalizations, the following equation for the transfer of heat to the aerotank has been obtained:

$$\frac{\partial T}{\partial t} + v_T \frac{\partial T}{\partial x} = D_T \frac{\partial^2 T}{\partial x^2} + F_T + \frac{1}{\rho \cdot c_w} \frac{\partial I}{\partial x}, \qquad (14)$$

where v_T is the velocity of heat motion;

D_T is the diffusion coefficient;

F_T is heat transfer function.

The set of differential equations (1), (2), (3) and (14) gives complex description of the change in the concentration of bacteria, pollution, oxygen and temperature in the aerotank. Various interactions between the characteristics of the environment and the process should be taken into account by introducing the coefficients into the corresponding equation, which makes it possible to analyze the processes taking place in the aerotank as a set of interconnected influences. Proceeding from the above, the following model problem can be arrived at:

$$\begin{cases} \dfrac{\partial C_i}{\partial t} = v_C \dfrac{\partial C_i}{\partial x} - \beta_i C_i BT + D_C \dfrac{\partial^2 C_i}{\partial x^2}, \\ \dfrac{\partial B}{\partial t} = v_B \dfrac{\partial B}{\partial x} + \beta BKTK_B + w_B + D_B \dfrac{\partial^2 B}{\partial x^2}, \\ \dfrac{\partial K}{\partial t} = v_K \dfrac{\partial K}{\partial x} + \beta KT + K_K \cdot C \cdot \left(K_0 - K\right) + \\ + w_K + D_K \dfrac{\partial^2 K}{\partial x^2}, \\ \dfrac{\partial T}{\partial t} + v_T \dfrac{\partial T}{\partial x} = D_T \dfrac{\partial^2 T}{\partial x^2} + F_T + \dfrac{1}{\rho \cdot c_w} \dfrac{\partial I}{\partial x}; \end{cases} \qquad (15)$$

$$\begin{aligned} C_i\big|_{x=0} &= C_{i*}^*(t), \; B\big|_{x=0} = B_*^*(t), \\ K\big|_{x=0} &= K_*^*(t), \; T\big|_{x=0} = T_*^*(t), \\ \left.\frac{\partial C_i}{\partial x}\right|_{x=l} &= 0, \; \left.\frac{\partial B}{\partial x}\right|_{x=l} = 0, \\ \left.\frac{\partial K}{\partial x}\right|_{x=l} &= 0, \; \left.\frac{\partial T}{\partial x}\right|_{x=l} = 0; \end{aligned} \qquad (16)$$

$$\begin{aligned} C_i\big|_{t=0} &= C_i^*(x), \; B\big|_{t=0} = B^*(x), \\ K\big|_{t=0} &= K^*(x), \; T\big|_{t=0} = T^*(x), \end{aligned} \qquad (17)$$

where l is the aerotank length;

$C_{i*}^*(t)$, $B_*^*(t)$, $K_*^*(t)$, $T_*^*(t)$, $C_i^*(x)$, $B^*(x)$, $K^*(x)$, $T^*(x)$ given a sufficient number of times, are the numbers of differential functions, coordinated in the angular points of the area $G = \left\{(x,t): 0 < x < l, 0 < t < t_* < \infty\right\}$.

The solution of the problem (15)-(17) with accuracy $O\left(\varepsilon^{n+1}\right)$ are sought in the form of asymptotic series by the power of a small parameter ε [12]:

$$C(x,t) = C_0(x,t) + \sum_{i=1}^{n} \varepsilon^i C_i(x,t) + \\ + \sum_{i=0}^{n+1} \varepsilon^i \tilde{C}_i\left(\tilde{\xi},t\right) + R_C(x,t,\varepsilon), \qquad (18)$$

$$B(x,t) = B_0(x,t) + \sum_{i=1}^{n} \varepsilon^i B_i(x,t) + \\ + \sum_{i=0}^{n+1} \varepsilon^i \tilde{B}_i\left(\tilde{\xi},t\right) + R_B(x,t,\varepsilon), \qquad (19)$$

$$K(x,t)=K_0(x,t)+\sum_{i=1}^{n}\varepsilon^i K_i(x,t)+ \\ +\sum_{i=0}^{n+1}\varepsilon^i\tilde{K}_i\left(\tilde{\xi},t\right)+R_K(x,t,\varepsilon) \quad , (20)$$

$$T(x,t)=T_0(x,t)+\sum_{i=1}^{n}\varepsilon^i T_i(x,t)+ \\ +\sum_{i=0}^{n+1}\varepsilon^i\tilde{T}_i\left(\tilde{\xi},t\right)+R_T(x,t,\varepsilon) \quad , \quad (21)$$

where R_B, R_K, R_C, R_T – reminders;

$C_i(x,t)$, $B_i(x,t)$, $K_i(x,t)$, $T_i(x,t)$ $(i=\overline{0,n})$ – regular part of the asymptotics;

$\tilde{C}_i\left(\tilde{\xi},t\right)$, $\tilde{B}_i\left(\tilde{\xi},t\right)$, $\tilde{K}_i\left(\tilde{\xi},t\right)$, $\tilde{T}_i\left(\tilde{\xi},t\right)$ $(i=\overline{0,n+1})$ – function of the borderline type (correspondingly amendments at the output of purified substance);

$\tilde{\xi}=(L-x)\cdot\varepsilon^{-1}$ – corresponding transformations.

The solution to the corresponding model problem (15)-(17) has been found in the form of asymptotic series, analogous to [13]. The effectiveness of this approach in works [12-15] has been "worked out", in particular, with the consideration of "diffusion contributions" on strong convection and filtration backgrounds. The corresponding processes, such as "filtration-convection-diffusion-heat-mass-exchange", are considered in environments (single-connected domains bounded by equipotential lines and flow lines) that can undergo deformations depending on certain process characteristics, which in turn determines the nature of the process (that is, the interaction of the characteristics of the medium and the process takes place), and the filtration flow is considered as a certain background for the convective transfer of soluble substances (pollution), taking into account small diffusion phenomena.

CONCLUSIONS

1. The mathematical model of biological wastewater treatment has been developed, taking into account the interaction of bacteria, organic and biologically non-oxidizing substances under conditions of diffusion and mass exchange disturbances and the influence of temperature regimes.

2. The method and the algorithm for solving the corresponding nonlinearly perturbed problem "convection-diffusion-heat-mass-exchange" are offered.

3. The obtained results allow to forecast and automate technological processes of biological wastewater treatment with systems of energy utilization of these waters (for example, heat pump plants) in a more detailed and complex way.

REFERENCES

1. A. R. de Pauli, F. R. Espinoza-Quiñones, D. E. G. Trigueros, A. N. Módenes, A. R. C. de Souza, F. H. Borba, A. D. Kroumov, *Chem. Eng. J.*, **334**, 19 (2018).
2. F. Gao, J. Nan, S. Li, Y. Wang, *Chem. Eng. J.*, **332**, 671 (2018).
3. J. M. Ochando-Pulido, M. Stoller, A. Martinez-Ferez, *Separation and Purification Technology*, **193**, 147 (2018).
4. V. Adetola, D. Lehrer, M. Guay, *American Control Conference*, 31 (2011)
5. D. Dochain, *London: IWA Publishing*, 342 (2001).
6. M. Henze, W. Gujer, T. Matsuo, G. R. Marais, G. P. L. Grady Jr., *Scientific and Technical Report*, **9**, 122 (2000).
7. G. D. Knightes, C. A. Peters, *Biotechnol. Bioeng.*, **69**, 160 (2000).
8. Q. Ghai, Doctoral Thesis at Telemark University College, p.187 (2008).
9. A. Ya. Bomba, A. P. Safonik, *J. Eng. Phys. Thermophys.*, **91**, 318 (2018).
10. A. P. Safonyk, *International Journal of Mathematical Models and Methods in Applied Sciences*, **9**, 189 (2015).
11. V. N. Domanov, A. G. Kostin, E. I. Nikiforovich, Processes of heat and mass transfer of reservoirs-coolers with atmosphere . *Monograph*, p. 320 (2011).
12. A. P. Safonyk, *Int. J. Math. Models & Methods Appl. Scie.*, **12**, 67 (2018).
13. A. Ya. Bomba, A. P. Safonyk, E. A. Fursachik, *J. Autom. Inform. Sci.*, **45**, 16 (2013).
14. V. Orlov, A. Safonyk, S. Martynov, S. Kunytskyi, *Int. J. Pure Appl. Math.*, **90,** 87 (2016).
15. A. Ya. Bomba, Nonlinear problems such as filtration-convection-diffusion-mass transfer under incomplete data. *Monograph*, 276 (2011).

МАТЕМАТИЧНО МОДЕЛИРАНЕ НА ТОПЛО И МАСООБМЕННИ ПРОЦЕСИ В СИСТЕМИ ЗА ТРЕТИРАНЕ НА ОТПАДЪЧНИ ВОДИ

А.П. Сафоник *, О.О. Хрицина, В.А. Волошчук, В.В. Середа

Национален университет по водно и екологично инженерство, Ривне, Уктайна

Постъпила на 17 май, 2018 г.; приета на 27 юли, 2018 г.

(Резюме)

В настоящата работа е представен математичен модел за биологичното третиране на отпадъчни води, съдържащи многокомпонентни замърсители. Предложеният модел включва симулиране на избистрянето на водите в осветител, аеробното третиране в порьозна среда, асимптотична числена апроксимация за решаване на пространствената задача за аеробното третиране и симулиране на сингулярно смутения процес на конвективна дифузия с отчитане на топлообмена и компютърно моделиране на биологичните процеси в аериран танк с регенерация.

Идеята за теорията на пертурбациите е използвана за съставянето на модел на нелинейна задача (отчитат се нови фактори и ефекти чрез смущения на изхода, но без решаването на нови задачи).

Значимите процеси (като филтруване-конвективна дифузия, топло-и масообмен) са разгледани в непрекъсната среда (едно-свързана област, оградена от екви-потенциални и токови линии), която може да се деформира при някои характеристики на процесите. От своя страна това предопределя природата на процесите, т.е. налице е взаимна връзка на характеристиките на средата и на процеса. Филтруването се разглежда като основа за конвективния пренос на разтворимите вещества (замърсители) при слаби дифузионни ефекти.

На тази основа е съставен математичмия модел за аеробното третиране на отпадъчни води с отчитането на влиянието на бактериите, не-окисляемите органични и биологични компоненти в условията на смущения в дифузията, топло и масообмена и влиянието на температурата.

Bulgarian Chemical Communications, Volume 50, Special Issue K (pp. 76 – 82) 2018

Mathematical model of a plate heat exchanger for condensation of steam in the presence of non-condensing gas

L. L. Tovazhnyanskyy[1], P. O. Kapustenko[1], O. A. Vasilenko[2], S. K. Kusakov[2], O. P. Arsenyeva[1], P. Y. Arsenyev[1]

[1]National Technical University, Kharkiv Polytechnic Institute,, Dept. ITPA, Kharkiv, Ukraine;
[2]AO Spivdruzhnist-T LLC, Kharkiv, Ukraine.

Received March 15, 2018, Accepted June 26, 2018

The process of vapour condensation from its mixture with noncondensing gas is analysed and mathematical model for condensation in PHE channels is proposed. The model is developed with accounting for the variation of local parameters of heat and mass transfer processes along condensation surface and features of these processes intensification in PHEs channels. The model is accounting for the effects of plate corrugations geometry on process intensity. The system of ordinary differential equations with considerably nonlinear right parts is solved by the numerical method of finite differences. The solution is implemented with the software developed for personal computer. The model validation is performed by comparison with experimental data for condensation of steam from its mixture with air in a sample of PHE channel.

Keywords: Plate heat exchanger, condensation, noncondensing gas, heat and mass transfer, mathematical model, experiment.

INTRODUCTION

Big amounts of heat energy used in different industries are lost with streams outgoing to the environment. Considerable quantities of such wasted heat in a form of latent heat of different condensable vapours contained in a mixture of gases are leaving out from the processes of burning fuels, of drying different materials and other industrial processes [1]. The processes like volatile organic components recovery or condensation of ammonia from synthesis gas undergone catalytic conversion also contain heat wasted with cooling streams. The efficient recovery of the heat energy in such cases requires the use of heat exchangers capable to perform the condensation process effectively and in an economically viable way. It is possible with a plate heat exchanger (PHE), which is the modern efficient type of compact heat exchangers [2]. The PHE consists from a pack of corrugated plates, as shown in Fig. 1. The plates are stamped from a thin metal sheet and being assembled in the PHE are forming robust channels of complex geometry. The multiple contact points between the adjacent plates enable sufficient constructional strength of the PHE and its ability to withstand big pressure differences between heat exchanging streams. The considerable intensification of heat and mass transfer in such channels allows substantial reduction of heat transfer area, size and weight for the same processes as compared to traditional types of tubular heat exchangers.

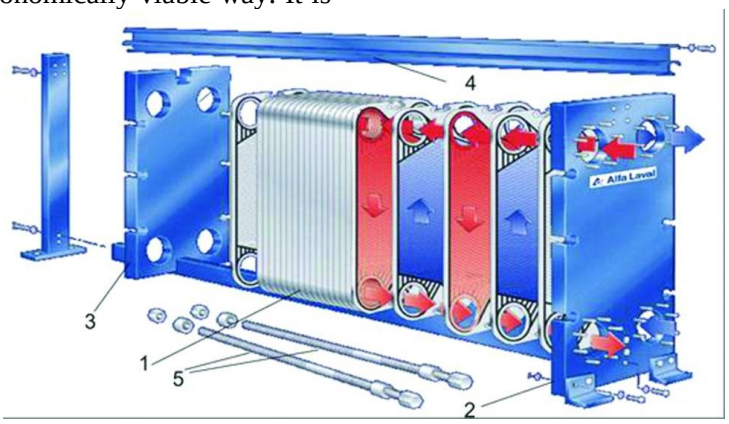

Fig. 1. The example of PHE drawing: 1 – heat transfer plate; 2 – fixed frame plate; 3 – moving frame plate; 4 – carrying bar; 5 – tightening bolts.

* To whom all correspondence should be sent:
E-mail: sodrut@gmail.com

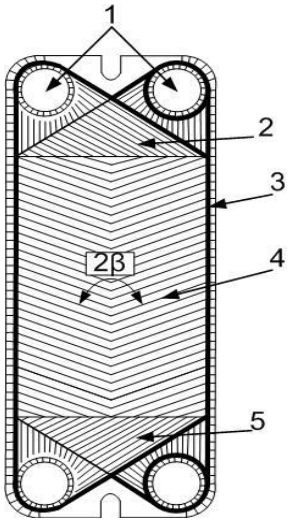

Fig. 2. Schematic drawing of a PHE plate: 1 – heat carriers inlet and outlet; 2,5 – zones for flow distribution; 3 – rubber gasket; 4 –main corrugated field.

For efficient and economically viable use of PHEs in the processes of both sensible and latent heat recovery from vapour - gas mixtures accurate enough methods for their design are required. Compared to heat transfer in single-phase conditions the condensation of vapour from its mixture with noncondensing gas is considerably complicated by the resistance to mass transfer of the condensing substance to the surface of plates, where condensed liquid film additionally creates thermal resistance for heat transfer to the cooling stream flowing in adjacent channels. The recent review of literature concerning the processes of heat and mass transfer in shell and tube condensers for condensation of vapour from its mixture with noncondensing gas is published by Huang *et al.* [3]. The substantial variation of all process parameters along the length of the heat exchanger channels necessitates utilization of mathematical models and software for adequate description of the condensing heat exchanger [4]. It requires results of experimental research of the process local parameters change in channels especially for the surfaces with enhanced heat and mass transfer [5]. In the channels of PHEs the hydrodynamics and heat and mass transfer are even more complicate because of intricate fluid flow distribution in the channels of complicated geometry. Compared to smooth tubes the effect of pressure drop on condensation in narrow channels is more important [6]. For PHEs, due to substantial differences in plate corrugations geometry, a number of different empirical correlations were developed which are adequate only for specific commercial plates in the limited experimental ranges of conditions [7].

The accurate modelling of vapour condensation in channels of PHEs must include accounting for local parameters variation along the channel length and use of reliable and accurate enough correlations for hydraulic resistance and heat and mass transfer [8]. Such mathematical model is presented in this paper with its validation according to experimental data for condensation of steam from its mixture with air in an experimental sample of PHE channel.

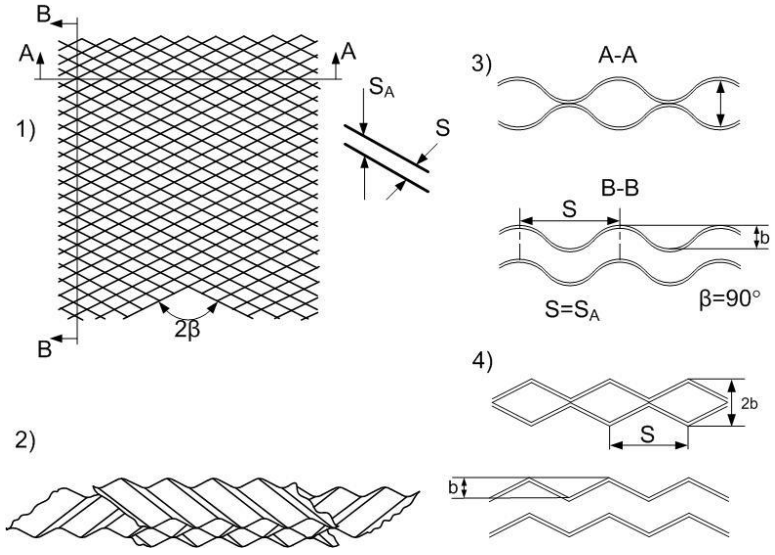

Fig. 3. Different corrugation forms: 1, 2 –intersection of the adjacent plates; 3 – channel cross-sections for the sinusoidal form of corrugations; 4 – channel cross-sections for the triangular form of corrugations.

MATHEMATICAL MODEL DEVELOPMENT

The development of a mathematical model for condensation of vapour from mixture with non-condensable gases in channels of PHE is based on the assumptions:

1. The parameters of hydrodynamic and heat –mass transfer processes on increments of the

channel are linked by the same relations as for any length of such channel with the same corrugation pattern.

2. For phase change in flow at the bulk of condensing stream equilibrium conditions of vapour are maintained and change of gaseous mixture temperature is happening due to convective heat transfer, which is also responsible for condensation in the flow core.

3. The film condensation occurs on the heat transfer surface of plates.

4. The ideal gas law is assumed for the gas-vapour mixture.

5. One-pass PHE is considered.

6. The process conditions at all PHE channels are changing in the same way and one channel surrounded by two adjacent channels with cooling media can be considered.

7. Heat losses are negligible.

The heat and material balances for the process of vapour condensation in the presence of noncondensing gas with counter-current flow of streams are written in the form of the following system of ordinary differential equations:

$$\frac{dG_v}{dx} = -\Pi \cdot j_v \tag{1}$$

$$\frac{dG_L}{dx} = \Pi \cdot j_v \tag{2}$$

$$\frac{dt_{cl}}{dx} = -\Pi \cdot q \cdot c_{cl}^{-1} \cdot G_{cl}^{-1} \tag{3}$$

$$\begin{aligned} &\frac{dt_L}{dx} \cdot c_L \cdot G_L + \\ &+\frac{dt_{mx}}{dx} \cdot c_{mx} \cdot \left(G_g + G_v\right) + \\ &+\Pi \cdot j_v \cdot r_v = \Pi \cdot q \end{aligned} \tag{4}$$

$$\begin{aligned} &\frac{dt_{mx}}{dx} \cdot c_{mx} \cdot \left(G_g + G_v\right) = \\ &= \Pi \cdot h_{cv} \cdot \left(t_{mx} - t_f\right) \end{aligned} \tag{5}$$

$$\begin{aligned} &\frac{dP_{mx}}{dx} = \frac{1}{d_e} \cdot \varsigma \cdot \frac{\rho_{mx} \cdot W_{mx}^2}{2} \cdot (1 + 2.9 \cdot X_{tt}^{0.46}) - \\ &-\frac{d}{dx}\left(\frac{\rho_{mx} \cdot W_{mx}^2}{2}\right) - \frac{d}{dx}\left(\frac{\rho_{mx} \cdot g \cdot x}{2}\right) \end{aligned} \tag{6}$$

where G_v, G_g, G_L and G_{cl} are mass flow rates of vapour, gas, condensed liquid and cooling megia in one channel, respectively, kg/s; t_{cl}, t_L, t_{mx} and t_f are cooling water, condensate, gaseous mixture and condensate film surface local temperatures, respectively, ºC; P_{mx} is the pressure of gaseous mixture, Pa; q is heat flux through the unit of plates surface, W/m^2; j_v is mass flux of vapour to the direction of heat transfer surface, kg/m^2; r_v is latent heat of vaporization, J/kg; h_{cv} is convective heat transfer film coefficient in gaseous phase, W/(m^{2}K); ρ_{mx} is density of gaseous mixture, kg/m^3; c_{cl}, c_L and c_{mx} are heat capacities of cooling media, liquid phase and gaseous mixture, respectively, J/(kg K); W_{mx} is flow velocity of gaseous mixture, m/s; Π is channel perimeter, m; x is longitudinal coordinate, m; d_e is channel equivalent diameter, m; X_{tt} is Lockhart-Martinelly parameter calculated by equation:

$$X_{tt} = \sqrt{\frac{dP_L}{dP_G}} \tag{7}$$

Here dP_L and dP_G are increments of pressure drops for liquid and gaseous phases flowing alone in a whole channel, calculated by turbulent single phase flow correlations. The system variables are also linked by algebraic equations. The relations between the saturation pressure Psat=Psat(t) and temperature t_{sat}=t_{sat}(P) are determined according to data available in literature.

The temperature of the liquid film outer surface is determined by equation:

$$t_f = t_{cl} + q \cdot \left(\frac{1}{h_{cl}} + R_f + \frac{\delta_{wl}}{\lambda_{wl}} + \frac{1}{h_L}\right), \tag{8}$$

where δ_{wl} is the thickness of plate metal, m; λ_{wl} is its thermal conductivity, W/(m K); R_f is thermal resistance of fouling, (m^2 K)/W; h_L is film heat transfer coefficient from condensate film to the channel surface, W/(m^{2}K). h_L is calculated according to the equation from paper [9]:

$$h_L = \frac{\lambda_L}{d_e} Nu^* \cdot \left[1 + x_{tp} \cdot \left(\frac{\rho_L}{\rho_{mx}}\right)\right]^{0.48}. \tag{9}$$

Here λ_L is thermal conductivity of condensate, W/(m K); ρ_L is condensate density, kg/m^3; x_{tp} is mass vapour quality; Nu^* is Nusselt number calculated for liquid phase with flow rate total for both phases.

The vapour partial pressure at film surface is calculated as saturation pressure:

$$P_{vf} = Psat(t_f) \tag{10}$$

The vapour mass fraction at liquid film outer surface is:

$$y_{vf} = \left(\frac{P_{mx} - P_{vf}}{P_{vf}} \cdot \frac{M_g}{M_v} + 1 \right)^{-1} \tag{11}$$

where M_v and M_g are molar masses of non-condensable gas and vapour, respectively, kg/kmol, (for water vapour M_v = 18.015 kg/kmol, for air M_g =28.96 kg/kmol).

The mass fraction of vapour at the flow core is:

$$y_{vb} = \frac{G_v}{G_v + G_g} \tag{12}$$

The vapour partial pressure at the flow core is:

$$P_{vb} = \frac{P_{mx}}{\frac{M_v}{M_g} \cdot \frac{G_g}{G_v} + 1}, \tag{13}$$

where G_g is mass flow rate of noncondensing gas, kg/s.

The saturation temperature at the flow core is:

$$t_{satb} = tsat(P_{vb}) \tag{14}$$

and with solution of equation (5) the following condition must be satisfied:

$$t_{mx} \geq t_{satb} \tag{15}$$

The mass flux to the condensation surface is:

$$j_v = \beta_D \cdot \left(y_{vb} \cdot \rho_{mx} - y_{vf} \cdot \rho_{mxf} \right) \tag{16}$$

The coefficients of heat transfer h_{cv} and mass transfer β_D are calculated according to heat and mass transfer analogy corrected for the influence of transverse mass flux [10]:

$$h_{cv} = \left(\lambda_{mx} / d_e \right) \cdot \Psi_H \cdot Nu_0 \tag{17}$$

$$\beta_D = \left(D_D / d_e \right) \cdot \Psi_D \cdot Nu_{D0}, \tag{18}$$

where λ_{mx} is the thermal conductivity of the gaseous mixture, W/(m K); D_D is diffusivity coefficient, m^2/s.

The relative factors of heat and mass transfer are:

$$\Psi_{H(D)} = 4 \cdot \left(1 + 0.85 \cdot b_{H(D)} \right) \cdot \left(1 + \sqrt{\frac{\rho_{mx}}{\rho_{mxf}}} \right)^{-2} \tag{19}$$

Here b_H and b_D are heat and diffusivity parameters:

$$b_H = \frac{c_{Pv}}{c_{Pmx}} \cdot \frac{j_v \cdot \mathrm{Re}_{mx} \cdot \mathrm{Pr}_{mx}}{\rho_{mx} \cdot W_{mx} \cdot Nu_0}$$
$$b_D = \frac{j_v \cdot \mathrm{Re}_{mx} \cdot \mathrm{Pr}_D}{\rho_{mx} \cdot W_{mx} \cdot Nu_{D0}} \tag{20}$$

The Nusselt numbers in a single phase flow are determined by correlation for the main corrugated field of the channels of PHEs presented in [11]:

$$Nu_{0(D)} = 0.065 \cdot \mathrm{Re}^{6/7} \cdot \left(\psi \cdot \zeta / F_x \right)^{3/7} \cdot \mathrm{Pr}_{(D)}^{0.4} \tag{21}$$

$$\psi = \left(\mathrm{Re} / A \right)^{-0.15 \cdot \sin(\beta)} \text{ at } Re > A;\ \psi = 1 \tag{22}$$

at $Re \leq A$ where $A = 380 / \left[tg(\beta) \right]^{1.75}$

The friction factor for the total hydraulic resistance is calculated by the following correlation from [12]:

$$\zeta = 8 \times \left[\left(\frac{12 + p2}{\mathrm{Re}} \right)^{12} + \frac{1}{(A + B)^{\frac{3}{2}}} \right]^{\frac{1}{12}} \tag{23}$$

$$A = \left[p4 \cdot \ln \left(\frac{p5}{\left(\frac{7 \cdot p3}{\mathrm{Re}} \right)^{0.9} + 0.27 \cdot 10^{-5}} \right) \right]^{16};$$

$$B = \left(\frac{37530 \cdot p1}{\mathrm{Re}} \right)^{16},$$

where p1, p2, p3, p4, p5 are empirical parameters calculated according to plates corrugations shape:

$$p1 = \exp(-0.157 \cdot \beta);\ p2 = \frac{\pi \cdot \beta \cdot \gamma^2}{3};\ p3 = \exp\left(-\pi \cdot \frac{\beta}{180} \cdot \frac{1}{\gamma^2} \right);\ p5 = 1 + \frac{\beta}{10};$$
$$p4 = \left(0.061 + \left(0.69 + tg\left(\beta \cdot \frac{\pi}{180} \right) \right)^{-2.63} \right) \cdot \left(1 + (1 - \gamma) \cdot 0.9 \cdot \beta^{0.01} \right) \tag{24}$$

where $\gamma = 2 \cdot b/S$ – the corrugation aspect ratio; β is angle of corrugations to the main flow direction, degrees; Re is Reynolds number determined with the equivalent diameter of the channel $de = 2b$; F_x is heat transfer area increase coefficient.

The equations (19)-(24) are also employed for determining heat transfer and pressure drop in the

flow of cooling fluid, and in equations (6) and (9). It makes possible accounting in mathematical model for the effects of plate corrugations geometrical parameters.

The equations (1)-(24) and correlations determining temperature and pressure effects on thermal and physical properties of substances together with geometrical relations for PHE channel are representing the system of ordinary differential equations. The right parts of the system equations are nonlinear that does not permit system analytical solution. The numerical solution by the finite difference method is implemented as software for PC using Mathcad.

EXPERIMENTAL PART

To validate the developed mathematical model experiments for condensation of a steam – air mixture in a sample of PHE channel were performed. For experimental study four corrugated plates were stamped from stainless steel AISI 304. The experimental model (Fig. 4) consisted of four plates welded together to form three inter-plate channels. The channel on the gas - steam side was formed by combination of two plates with a corrugation angle $\beta = 60°$.

The saturated steam-air mixture was directed and condensed in the central channel. It was cooled by a water flow in two periphery channels having thermal insulation on the outside. The temperatures of gaseous mixture and cooling media were measured by copper-constantan thermocouples with an accuracy of ±0.1 ºC. The temperature measuring points are situated at the inlet and exit of heat-exchanging streams and at seven points along the channel. The pressure of the gaseous stream is measured by pressure gauges at the inlet and exit of the channel with an accuracy of ±0.005 bar. The mass flow rate of the cooling water is determined with the use of orifice flow meter, accuracy ±1 %. The flow rate of incoming air is measured using a set or rotameters, with minimal accuracy of ±2 %. The volumetric flow rate of the water condensate created in the channel was measured by a set of measuring vessels with an accuracy of ±1 %. The steam flow rate is determined by summing the water condensate flow rate with the flow rate of not condensed steam exiting the channel with outgoing steam-air mixture at saturation conditions. The channel model is 1 meter long and its width is 0.225 m. The corrugation height is b = 5 mm, thickness of the plate is δ = 1 mm, corrugation angle β = 60º, aspect ratio γ = 0.556 and area increase coefficient Fx = 1.15. The experiments included 48 tests at different conditions of gas-steam mixture condensation. The absolute pressure was changed in the range from 2.93 to 1.025 bar; the air volume fraction in the entering channel mixture was in the range from 2.8 % to 70 %; the local velocity of gaseous stream was in the range from 46 to 4.1 m/s; the temperature of gaseous stream changed in the range from 88.2 to 115.1 ºC; the temperature of cooling media varied from 23.8 to 71.5 ºC.

MODEL VALIDATION AND DISCUSSION OF THE RESULTS

The simulations of the condensation process parameters are performed using computer software developed according to the presented mathematical model. The calculations are made based on conditions of the tests.

There are specified mass flow rates of steam, air, cooling water, temperatures and pressures of incoming gas-vapour mixture and of incoming cooling water. The simulated results are compared to the results of the experimental runs. The differences between calculated and experimental total heat loads are not bigger than ±2.8 % for all performed experiments.

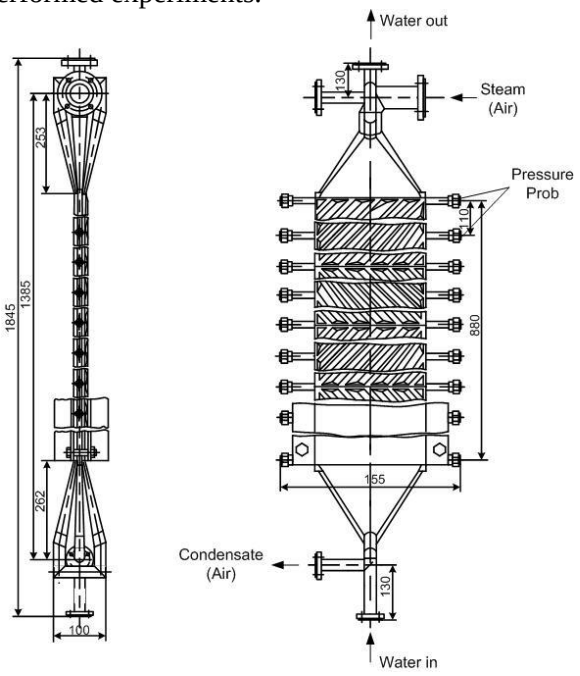

Fig. 4. Schematic drawing of the experimental sample of PHE channel.

The discrepancies in calculated and measured temperature of gas-vapour mixture at channel outlet were lower than ±2.5 ºC. Such accuracy can be regarded as acceptable for calculations of PHEs in industry for heat recovery and utilization of waste heat.

In Fig. 5 are shown the graphs of calculated local temperatures along the PHE channel for the test run with mass air content in the incoming mixture of 3%. The accuracy of predicting local

temperatures of gaseous stream is in the limits of ±3.1 ºC. The biggest errors are observed closer to the end of the channel, where allmost all the steam is condensed. It makes the relative error in prediction of remaining small quantities of gaseous steam more significant, than at the initial stages of condensation.

The temperature change is most significant at the end of the channel, while the temperature drop at the initial channel sections is rather small. It demonstrates the importance of modelling with accounting for change of the local process parameters and all its characteristics along the surface of condensation.

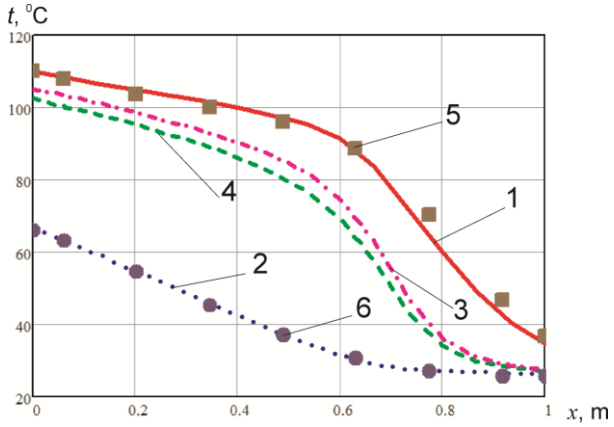

Fig. 5. Change of temperatures in a sample of PHE channel at air mass fraction of 3%. Calculated results are presented by solid curves, experimental data by dots. Calculated: 1 – gaseous stream; 2 - cooling water; 3 – liquid film; 4 - wall. Experimental: 5 – gaseous stream; 6 - cooling water.

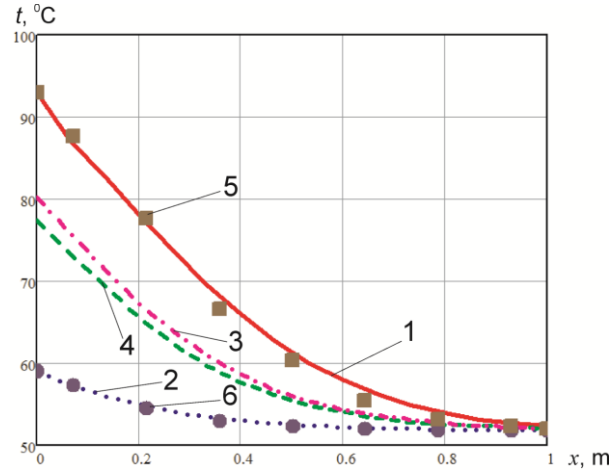

Fig. 6. Change of temperatures in a sample of PHE channel at air mass fraction of 55%.Calculated results are presented by solid curves, experimental data by dots. Calculated: 1 – gaseous stream; 2 - cooling water; 3 – liquid film; 4 - wall. Experimental: 5 – gaseous stream; 6 - cooling water.

With the increase of initial content of air in the mixture the character of process parameters distribution is changing, as it is shown in Fig. 6 for the test run with initial air mass fraction of 55%. Here the most changes in temperature are at the sections close to gaseous mixture inlet and prediction of the temperature at the channel exit is more accurate. Such cases are incountered with the use of PHEs for utilisation of waste heat from condensible gaseous streams and optimisation of their cost in cases like the case of drying process considered in paper [1], where the model presented here was used for PHE selection based on economical objectives. The accounting for the effect on heat transfer area and cost of PHE of plates corrugation parameters is also making the model a valuable tool when optimising PHEs plates geomery.

CONCLUSIONS

The accurate modelling of PHEs for utilisation of heat energy from condensing gaseous streams requires accounting for the variation of local parameters of heat and mass transfer processes along the length of condensation surface. The proposed mathematical model is based on a system of ordinary differential equations with strong nonlinearity of their right parts. For solution of this system the numerical method of finite differences is used, which is implemented on a PC. The validation and acceptable accuracy of the model is confirmed by comparison with data of experiments for condensation of steam from its mixture with air in a sample of PHE channel. The model is accounting for the effect of plate geometry on the process intensity and can be used for optimisation of PHE geometrical parameters for condensation processes, as well as for optimal selection of PHEs for waste heat utilisation from condensable gaseous streams in industry.

Acknowledgments: *Olga Arsenyeva is grateful to the Alexander von Humboldt Foundation for the financial support.*

REFERENCES

1. O. P. Arsenyeva, L. Čuček, L. L. Tovazhnyanskyy, P. O. Kapustenko, Y. A. Savchenko, S. K. Kusakov, O. I. Matsegora, *Front. Chem. Sci. Eng.*, **10**, 131 (2016).
2. J. J. Klemeš, O. Arsenyeva, P. Kapustenko, L. Tovazhnyanskyy, Compact Heat Exchangers for Energy Transfer Intensification: Low Grade Heat and Fouling Mitigation. CRC Press, Boca Raton, FL, USA, 2015.
3. J. Huang, J. Zhang, L. Wang, *Appl. Thermal Eng.*, **89**, 469 (2015).

4. C. R. Kharangate, I. Mudawar, Review of computational studies on boiling and condensation, *Int. J. Heat Mass Transfer*, **108**, 1164 (2017).
5. I. Z. Famileh, J.A. Esfahani, *Int. J. Heat Mass Transfer*, **108**, 1466 (2017).
6. L. K. Wang, B. Sunden, Q. S. Yang, *Heat Transfer Eng.*, **20**, 71 (1999).
7. R. Eldeeb, ,V. Aute, R. Radermacher, *Int. J. Refrigeration*, **65**, 12 (2016).
8. L. L. Tovazhnyanskyy, P. O. Kapustenko, O. G. Nagorna, O. Y. Perevertaylenko, *Heat Transfer Eng.*, **25**, 16 (2004).
9. O. Arsenyeva, L. Tovazhnyanskyy, P. Kapustenko, O. Perevertaylenko, G. Khavin, *Appl. Thermal Eng.*, **31**, 2146 (2011).
10. L. L. Tovazhnyanskyy, P. O. Kapustenko, *Chemical Industry (Khimicheskaya promyshlennost*) (In Russian), **8**, 17 (1989).
11. P. Kapustenko, O. Arsenyeva, O. Dolgonosova, *Chem. Eng. Trans.*, **25**, 357 (2011).
12. O. P. Arsenyeva, L. L. Tovazhnyanskyy, P. O. Kapustenko, , O. V. Demirskiy, *Theo. Found. Chem. Eng.*, **46**, 634 (2012).

МАТЕМАТИЧЕСКИ МОДЕЛ НА ПЛАСТИНЧАТ ТОПЛООБМЕННИК ЗА КОНДЕНЗАЦИЯ НА ВОДНА ПАРА В ПРИСЪСТВИЕ НА НЕКОНДЕНЗИРАЩ ГАЗ

Л. Л. Товажнянский[1], П. О. Капустенко[1], О. А. Василенко[2], С. К. Кусаков[2], О. П. Арсениева[1], П. Й. Арсениев[1]

[1] *Национален политехнически университет, Харковски политехнически институт, Департамент ITPA, Харков, Украйна*
[2]*АО Спивдружнист- T LLC, Харков, Украйна*

постъпила на 15 март, 2018 г.; приета на 26 юни, 2018 г.

(Резюме)

Анализиран е процесът на кондензация на пара от смес с неконденсиращ газ и е предложен математичен модел за кондензация в каналите на пластинчат топлообменник. Моделът е разработен с отчитане на промяната на локалните топлинни параметри и масопреносните процеси по протежение на кондензационната повърхност и характеристиките на интензифицирането на тези процеси в каналите на пластинчатия топлообменник. Методът отчита влиянието на геометрията на гофриране на пластините върху интензивността на процеса. Системата от обикновени диференциални уравнения със значително нелинейни десни части е решена по числовия метод на крайните разлики. Решението е осъществено със софтуер, разработен за персонален компютър. Моделът е валидиран чрез сравняване с експериментални данни за кондензация на водна пара от смес с въздух в канал на пластинчат топлообменник.

Bulgarian Chemical Communications, Volume 50, Special Issue K (pp. 83 – 89) 2018

Recovery of antioxidant phenolic compounds from avocado peels by solvent extraction

S. Boyadzhieva*, S. Georgieva, G. Angelov

Institute of Chemical Engineering, Bulgarian Academy of Sciences, Acad. St. Angelov str., Bl. 103, Sofia 1113, Bulgaria

Received July 20, 2018; Accepted September 10, 2018

The extraction of a vegetal waste (avocado peels) is studied aimed at quantification of polyphenolic content and antioxidant activity of the extracts. Ethanol-water mixtures are used as solvents for the reason that ethanol is the most common "green" solvent having high solubility power, and being completely biodegradable. The main task is to determine the optimal operational conditions, at which the extraction of antioxidant substances from avocado peels is maximized and correspondingly, extracts with higher antioxidant capacity are obtained. A simplified four-step experimental procedure is applied for optimization of the main process parameters, at which the yield of the target bioactive components (polyphenols) is maximized. The process kinetics is studied with the use of Peleg's equation, and model equilibrium concentration is calculated. The experimental concentration at equilibrium state fits well the model results (2.5 % difference).

Key words: Avocado peels, Extraction, Optimization, Antioxidants, Polyphenols

INTRODUCTION

There are two types of antioxidants used in the food, cosmetic and pharmaceutical industries: natural antioxidants obtained entirely from natural sources, and synthetic antioxidants created by chemical processes. In recent years, there is an increasing interest in natural (bio) antioxidant substances, because synthetic antioxidants are supposed to have toxic and mutagenic effects on the human body [1, 2]. Currently, the food industry is focused on replacing the use of synthetic by natural antioxidants [3].

The main source of natural antioxidants are plants such as fruits, vegetables, cereals, mushrooms, flowers, herbs and spices [4, 5]. Vitamins soluble in lipids and selenium also occur in food derived from animals (milk and fish lipids, eggs), but in smaller amounts, and in dependence on the kind of feed consumed (e. g. carotenoids content in milk lipids, eggs). For this reason, products derived from animals are not significant sources of antioxidants in human diet [5].

Due to considerable consumption and industrial processing of the edible parts of the plants, significant amount of biological waste is generated (such as citrus fruit skins, pineapple residues, avocado peels and seeds, sugarcane bagasse and other plant residues). One of the most beneficial approaches is to recover the bioactive constituents, especially the phenolic compounds, making full use of them in the food, pharmaceutical and cosmetics industry. Thus, utilization of fruit wastes as sources of bioactive compounds may be of considerable economic benefits and has become increasingly attractive [6-8].

With a global production exceeding 5.5 million tons in 2016, avocado has become a major agro-industrial commodity [9, 10]. The principal use of avocado fruit is for human consumption, although other applications related to the production of cosmetics, nutritional supplements and livestock feed have been reported [10, 11]. Only the avocado pulp is employed for commercial applications, while avocado peels and seeds are considered as waste [11, 12]. The antioxidant activity of avocado pulp and wastes has been evaluated in a number of studies [12-18]. It is reported that in view of higher polyphenolic content and antioxidant activity, the downward ranking is: peels, seeds, pulp [12, 15, 16].

A number of solvents have been used for recovery of polyphenols from avocado wastes: petroleum ether, water, methanol, 80% ethanol, acetone, ethyl acetate [12, 15-18]. Typically, the extraction has been made at selected constant conditions (solvent, solid-to solvent ratio, time and temperature) without variation of the process parameters, i.e. no attempts have been made to optimize the extraction process.

In this study, avocado peels, which are the richest part of avocado fruit, are examined as a source of antioxidant substances (polyphenols). The main task is to determine the optimal operational conditions at which their extraction from avocado peels is maximized and correspondingly, extracts with higher antioxidant capacity are obtained. Ethanol-water mixtures are used in our study for the reason that ethanol is the most common "green" bio-solvent

* To whom all correspondence should be sent:
E-mail: maleic@abv.bg

used on a large scale, because it is easily available, it has high solubility power, and is completely biodegradable [19].

EXPERIMENTAL

Raw material

Avocado fruits were purchased from the local market. The peels were separated from the fruits. After air drying they were ground to particle size not bigger than 1 mm by using a chopper. Finally, the dried and ground peels were stored in a dark place until use.

Chemicals and reagents

Standard Folin-Ciocalteu phenol reagent (2N), gallic acid, anhydrous Na_2CO_3, 2,2-diphenyl-1-picrylhydrazyl (DPPH) and methanol were obtained from Sigma. Ethanol-water solvents were prepared by using 96% ethanol obtained from Valerus.

Extraction procedure

In general, a sample of ground raw material (5 g) was mixed in a flask with a corresponding amount of solvent (depending on solvent-to-solid ratio). The extractions were carried out in a thermostatic water bath shaker (Gyrotory Water Bath Shaker, model G76, New Brunswick Scientific, USA) at 160 rpm. After extraction, the mixture was filtered, and the filtrate was stored in a refrigerator. Each extraction was repeated in duplicate or in triplicate in case of bigger difference between two analyses. Mean values were used.

Samples of liquid extracts were dried and weighed in order to obtain the quantity of extracted dry matter (de)

Analyses

Determination of total phenolic content. Total polyphenolic content (TPC) of the extracts was determined by the Folin-Ciocalteu method [20, 21] using UV-VIS spectrophotometer (UNICAM®-Helios β). The absorbance of the samples was measured at 765 nm. Calibration curve for gallic acid was made, and TPC was expressed as mg of gallic acid equivalent (GAE) per 1 gram of dry extract (mg GAE/g de).

In vitro antioxidant capacity (AOC). AOC was determined by the DPPH method [22, 23], based on a color reaction between the nitrogen atom (from DPPH) and the hydrogen atom of the hydroxyl group of the antioxidant compound. 1 ml of extract was mixed with 4 ml of DPPH solution in methanol (0.004%). After keeping the sample in dark at room temperature for 60 min, the absorbance was measured at 517 nm. AOC was expressed as IC50 (quantity of extract neutralizing 50% of DPPH amount).

Usually, AOC is expressed as extract concentration (mg/ml), which neutralizes 50% of a standard DPPH solution (IC50 value). In this presentation, a lower IC50 value means a higher AOC. In order to obtain a more logic presentation, we have recalculated and represented the values of IC50 as mg DPPH neutralized by 1 g of dry extract. In this case, a higher value refers to a higher AOC.

Statistical treatment

One-way Analysis-of-Variances software (ANOVA, Microsoft) with a significance level of 0.05 was applied to the treatment of experimental data in order to distinguish statistically equal mean results as opposed to statistically different ones.

RESULTS AND DISCUSSION

To simplify the experimental procedure in view of saving reagents and time, we have applied a four-step experimental approach for finding the operational conditions at which maximum bioactive components (polyphenols) are extracted.

Determination of appropriate solvent composition

The target substances might have different polarity, which plays on the selection of an appropriate solvent (polar or non-polar). In our case, as polyphenol compounds are mainly of polar type, they can be successfully extracted by polar solvents, such as water, methanol, ethanol, acetone, etc. [15]. As the extracts are intended for human applications, safe “green” solvents should be used. In this study, water (polarity 1.84 D) and ethanol (1.69 D) were chosen as being safe. The solvent polarity can be additionally tuned by mixing these solvents in different proportions.

At this initial stage, the optimal process parameters are not known, so it is convenient to proceed at conditions, which will ensure better solubility of the target substances resulting in a complete extraction. These are: high temperature, excessive amount of solvent (high solvent-to-solid ratio), long contact time, agitation.

The concentration of polyphenols in the extracts obtained by water, concentrated ethanol and different ethanol-in-water mixtures, is presented in Fig. 1a. Fig. 1b shows analogous results for the antioxidant capacity. The other constant process parameters are: temperature 70^{o}C (close to solvent boiling point), solvent-to-solid ratio 20, contact time 150 min under agitation.

According to Fig.1a, a clear maximum of extracted polyphenols is obtained with 48%

ethanolic solvent. The concentrated ethanol seems to be the worst solvent in our case study, which dissolves even less polyphenols than pure water.

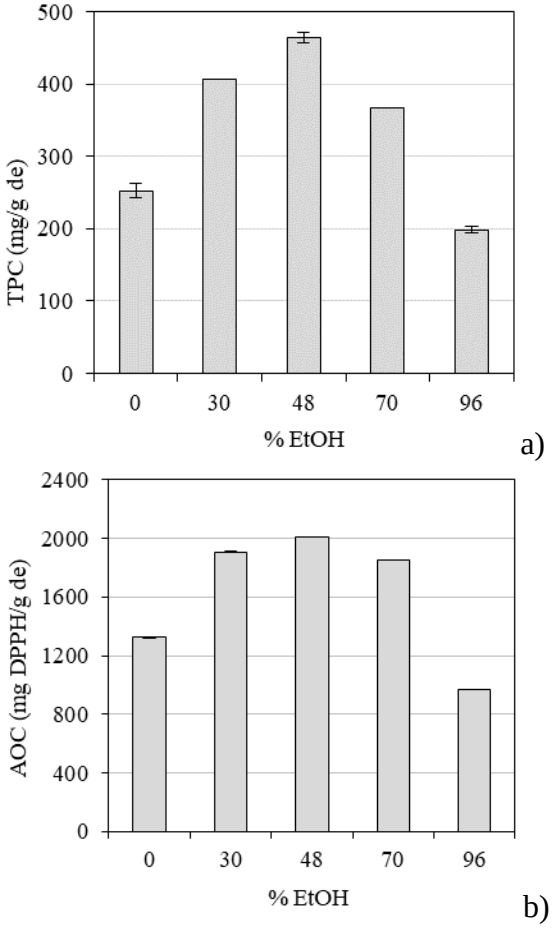

Fig. 1. Influence of ethanol concentration on: a) the concentration of polyphenols TPC); b) the antioxidant capacity (AOC) of the extracts

Similar is the situation with the antioxidant capacity (Fig. 1b) – maximum at 48% ethanol, lowest at 96% ethanol. Evident correlation exists between the amount of polyphenols and antioxidant capacity. A higher polyphenol concentration corresponds to a higher antioxidant capacity of the extracts.

Fig. 2 presents the amount of polyphenols (TPC) extracted from the raw material using different ethanol concentrations.

Again, best results were obtained with 48% ethanol. An interpolation of this graph for 80% ethanol (rectangular point) gives the value 66.77 mg/g rm. It is quite similar to the result 63.5 of Tremocoldi *et al.* [18] obtained with the same ethanolic concentration.

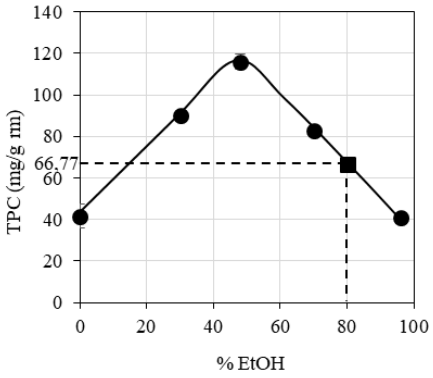

Fig. 2. Influence of ethanol concentration on TPC extracted from the raw material (rm)

With the optimal ethanol concentration 48%, both water-soluble and ethanol-soluble antioxidants were extracted at a maximum grade. Consequently, further experiments have to be carried out with this solvent composition.

Selecting a suitable temperature

Usually, the solubility of solids in a solvent is expected to be better at a higher temperature. From practical point of view, the influence of temperature should be studied in the range from room to solvent boiling point temperature (in our case about 70^0C). However, in case of thermally unstable substances, a high temperature can give rise to their destruction, and this possibility should be inspected. Figs. 3a and 3b illustrate the influence of temperature on the polyphenols content and on the antioxidant capacity of the extracts. The other process parameters keep constant values, namely 48% ethanolic solvent, solvent-to-solid ratio 20, contact time 150 min under agitation.

When the temperature is increased from 20 to 70°C, the polyphenol content shows a proportional rise, too. This fact can be interpreted as an evidence for better dissolution and for thermal stability of the active substances even in the upper temperature range. Similar observation is valid for antioxidant capacity (Fig.2b) – it grows with increasing temperature.

Based on the above results, the temperature selected for further experiments was 70^0C.

Influence of hydromodule on TPC and AOC

If the amount of solvent is insufficient, the target compounds cannot be fully dissolved. To avoid this situation, an excessive amount of solvent is often used in practice. Acting in this empirical way raises the expenses for the larger amount of solvent in use, more energy is spent for its regeneration and elimination from the extract, and reactors with larger volume are needed as well. There is some minimum

amount of solvent necessary for full dissolution of the target. It can be determined by making extractions with gradual increase of solvent-to-solid ratio, registering the minimum ratio at which the yield becomes constant and does not depend on further ratio increase.

Figs. 4a and 4b illustrate the impact of hydromodule on polyphenols concentration and AOC of the extracts. Some process parameters are kept at already optimized values, namely 48% ethanolic solvent and temperature 70°C. The solid-liquid system is agitated for a long time (150 min).

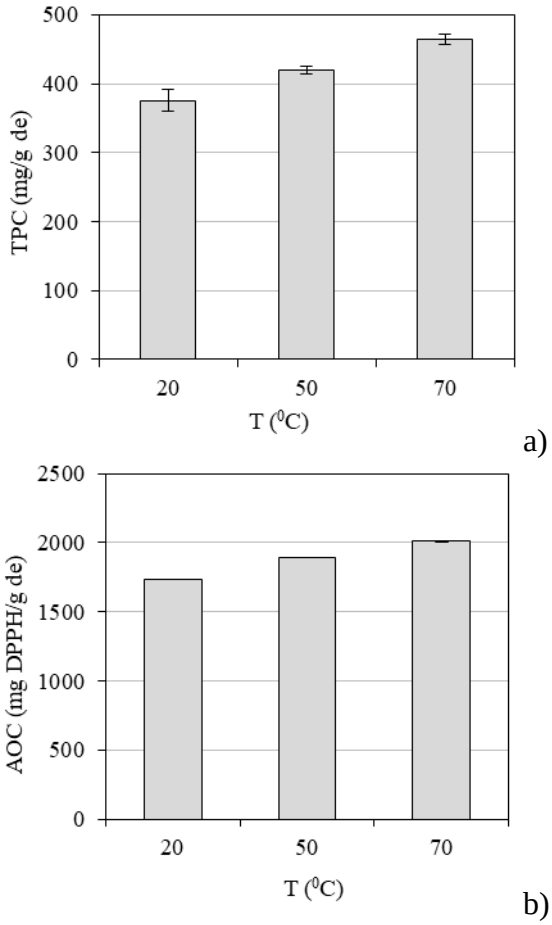

Fig. 3. Influence of temperature on TPC (a) and on AOC (b)

As can be seen from Fig. 4a, increasing the solvent amount from hydromodule 5 to 20 results in increased amount of extracted polyphenols. It is an indication that more solvent is necessary for complete dissolution of the target. Unlikely, at hydromodule 20 and more, the quantity of extracted polyphenols stays almost the same; i. e. further increase of hydromodule does not improve the extraction. So, a hydromodule of 20 can be selected as the minimum value of solvent-to-solid ratio required for complete recovery of the valuable components and for obtaining extracts with maximum AOC (Fig. 4b). ANOVA analysis confirms this observation by indicating statistically different values of TPC in the interval 5 – 20 and statistically similar results for hydromodule 20 and 25. It is worth mentioning that the relevant literature usually reports a solvent-to-solid ratio for extraction of avocado peels of 10, which seems insufficient in view of our results.

Process kinetics and determination of optimal contact time

Establishing the duration of phase contact required for achieving pseudo-equilibrium state is essential for optimizing the extraction process. The necessary contact time can be determined by tracking the process development in the course of time. The resulting kinetic curve has asymptotic shape, the plateau being an indication for no further extraction (pseudo-equilibrium state is attained). So, the optimized (minimum) processing time corresponds to the point where the plateau begins. In our case, pseudo-equilibrium state seems to be reached after 20 min (Fig. 5), as far as ANOVA test has shown statistically equal values of TPC in the interval 20 – 120 min.

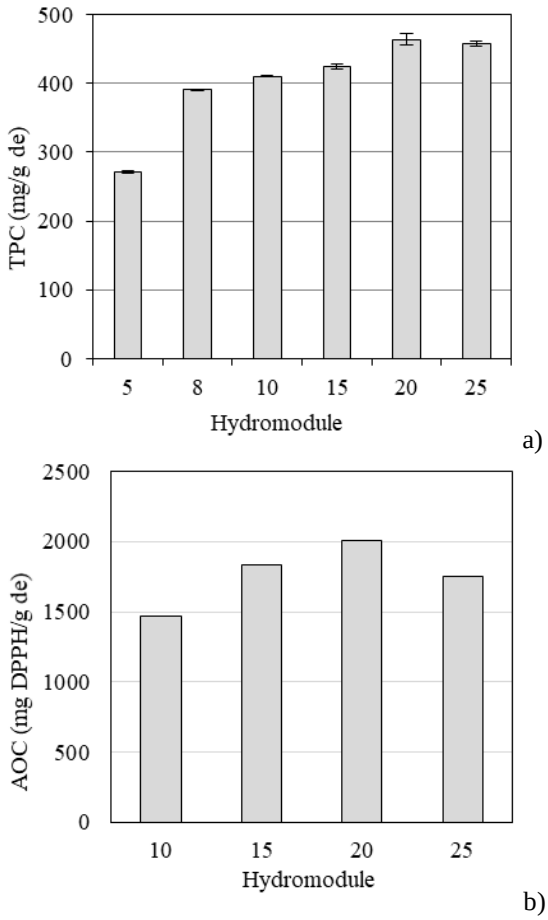

Fig. 4. Influence of hydromodule on TPC (a) and on AOC (b)

Modeling of extraction kinetics

Modeling was performed by using Peleg's equation. Although it is originally used to describe absorption kinetics [24], it can also be applied to the

extraction kinetic curves (extracted matter over time), because both curves have similar asymptotic shape.

The Peleg`s equation has the form:

$$C(t) = C_0 + \frac{t}{K_1 t + K_2} \quad (1)$$

In case of an extraction process, $C(t)$ is the concentration of extracted substance (mg/g de) at time t (min), C_0 is the concentration of extracted substance at the initial time t = 0, K_1 and K_2 are constants.

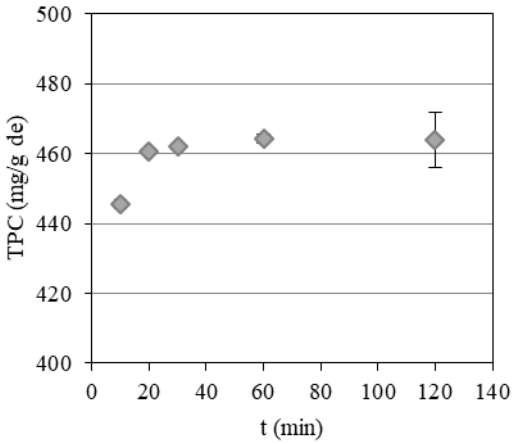

Fig. 5. Extraction kinetics of TPC of extracts obtained with 48 % ethanol, temperature 70°C, hydromodule 20

Since C_0 in all experimental runs is zero, Eq. (1) can be rewritten as:

$$C(t) = \frac{t}{K_1 t + K_2} \quad (2)$$

Eq. (2) can be rearranged in linear form:

$$\frac{t}{C(t)} = K_1 t + K_2 \quad (3)$$

Thus, K_1 and K_2 can be determined from the intercept and the slope of this straight line.

The extraction rate at time t can be obtained by differentiation of (2):

$$\frac{dC(t)}{dt} = \frac{K_2}{(K_1 t + K_2)^2} \quad (4)$$

At time t = 0, Eq. (4) takes the form:

$$\frac{dC(0)}{dt} = \frac{1}{K_2} = R_0 \quad (5)$$

So, the physical meaning of K_2 is related to the initial extraction rate R_0.

When $t \rightarrow \infty$, i.e. at equilibrium state, Eq. (2) becomes:

$$C(t)\,|_{t\rightarrow\infty} = C_e = \frac{1}{K_1} \quad (6)$$

Thus, the constant K_1 is related to the concentration at equilibrium state Ce.

Fig. 6 represents the linear form of Peleg's equation described by the expression:

$$y = 0.0021x + 0.0006 \quad (7)$$

The coefficients K_1=0.0021 and K_2=0.0006 serve to calculate the velocity and equilibrium constants, namely initial extraction rate R_0 = 1666.67 (mg GAE/g de min) and model equilibrium concentration C_e = 476.19 (mg GAE/g de).

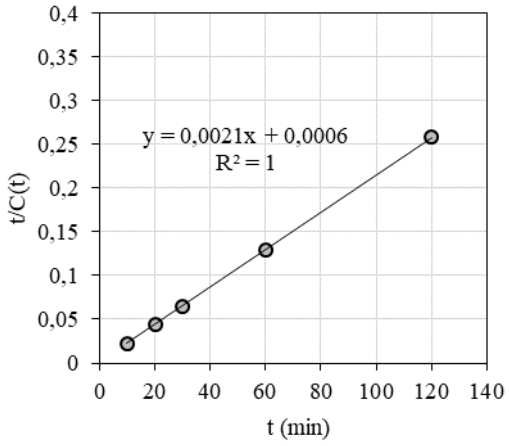

Fig. 6. Linear form of Peleg`s equation for TPC

Fig. 7 represents equation (2) (line) superimposed to real experimental data for the extraction kinetics of polyphenols (points). Good match is observed. Also, the values of calculated equilibrium concentration of polyphenols 476.19 (mg GAE/g de) and the experimentally determined equilibrium concentration from Fig. 5 (mean value 463,37) coincide rather well, the difference being only 2.5 %.

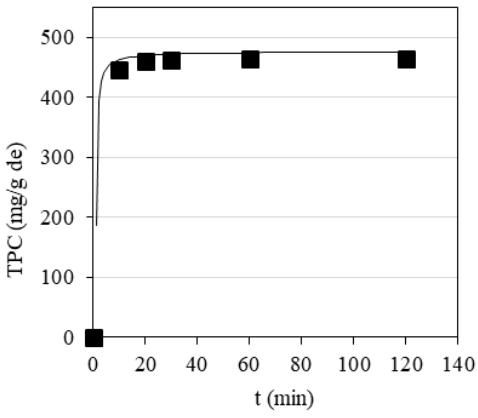

Fig. 7. Equation (7) confronted to real experimental data for extraction kinetics of polyphenols.

CONCLUSION

In view of valorization of food bio-wastes, the extraction of antioxidant phenolic substances from avocado peels with a "green" solvent (aqueous ethanol) was studied. Process optimization was

made using a simplified approach with a reduced number of experiments. It was found that the main process parameters, at which the yield and antioxidant activity of the extracts are maximized, are: extraction under agitation for 20 min with 48 % ethanol at temperature 70°C and solvent-to-solid ratio (v/w) 20.

The experimental data for process kinetics were treated by Peleg's equation, and model equilibrium concentration was determined. The experimental pseudo-equilibrium concentration matches closely the calculated equilibrium concentration (2.5 % difference).

In conclusion, an unused agricultural waste, avocado peels, was found to be rich of phenolic compounds. The results of this study specified the conditions for optimal processing in view of production of enriched extracts with higher antioxidant activity.

REFERENCES

1. G. Hocman, *Int. J. Biochem*., **20**, 639 (1988).
2. A. Pop, C. Berce , P. Bolfa, A. Nagy, C. Catoi , I. Dumitrescu , L. Silaghi-Dumitrescu , F. Loghin, *Farmacia*, , **61** (1), 202 (2013).
3. C. Caleia, L. Barros, A.L. Antonio, M.B. Oliveira, I.C. Ferreira, *Food Chem.*, **216**, 342 (2017).
4. D.P. Xu, Y. Li, X. Meng, T. Zhou, Y. Zhou, J. Zheng, J.-J. Zhang, H.-B. Li, *Int. J. Mol. Sci.*, **18**, 96 (2017).
5. E. Sikora, E. Cieślik, K. Topolska, *Acta Sci. Pol., Technol. Aliment*., **7**, 5 (2008).
6. G. F. Deng, C. Shen, X. R. Xu, R. D. Kuang, Y. J. Guo, L. S. Zeng, L. L. Gao, X. Lin, J. F. Xie, E. Q. Xia, S. Li, S. Wu, F. Chen, W. H. Ling, H. B. Li, *Int. J. Mol. Sci.*; **13**, 8308 (2012).
7. T. Varzakas, G. Zakynthinos, F. Verpoort, *Foods*, **5**, 88 (2016).
8. P. C. Widsten, D. Cristina, G. C. Fletcher, M. A. Pajak, T. K. McGhie, *J. Agr. Food Chem.*, **62**, 11146 (2014).
9. https://www.statista.com/statistics/577455/world-avocado-production/
10. P. F. Duarte, M. A. Chaves, C. D. Borges, C. R. B. Mendonça, *Food Technol*., **46**, 747 (2016).
11. M. P. Domínguez, K. Araus, P. Bonert, F. Sánchez, G. San Miguel, M. Toledo, in: Environment, Energy and Climate Change II. The Handbook of Environmental Chemistry, G. Lefebvre, E. Jiménez, B. Cabañas (eds.), vol. 34, Springer, Cham, 2014, p. 199.
12. J. G. Rodríguez-Carpena, D. Morcuende, M. J. Andrade, P. Kylli, M. Estévez, *J. Agr. Food Chem.*, **59**, 5625 (2011).
13. U. A. Prabath Pathirana, Y. Sekozawa, S. Sugaya, H. Gemma, *Int. Food Res. J.*, **20**, 1065 (2013)
14. A. F. Vinha, J. Moreira, S. V. P. Barreira, *J. Agr. Sci.*, **5**, 100 (2013).
15. A. Kosińska, M. Karamać, I. Estrella, T. Hernández, B. Bartolomé, G. A. Dykes, *J. Agric. Food Chem.*, **60**, 4613 (2012).
16. M. Calderón-Oliver, H. B. Escalona-Buendía, O. N. Medina-Campos, J. Pedraza-Chaverri, R. Pedroza-Islas, E. Ponce-Alquicira, *Food Sci. Tech.*, **65**, 46 (2016).
17. I. Antasionasti, S. Riyanto, A. Rohman, *Res. J. Med. Plants***, 11**, 55 (2017).
18. M. A. Tremocoldi, P. L. Rosalen, M. Franchin, A.P. Massarioli, C. Denny, E. R. Daiuto, *PLoSONE* **13,** (2018).
19. F. Chemat, M. A. Vian, G. Cravotto, *Int. J. Mol. Sci.*, **13**, 8615 (2012).
20. V. L. Singleton, R. Orthofer, R. M. Lamuela-Raventos, *Meth. Enzymol*., **299,** 152 (1999).
21. A. L. Waterhouse, *Curr. Protoc. Food Analyt. Chem.*, I1.1.1 (2001).
22. C. Sanchez-Moreno, *Food Sci. and Technol. Intern.*, **8**, 121 (2002)
23. J. Perez-Jimenez, S. Arranz, M. Tabernero, M. Diaz-Rubio, J. Serrano, I. Gono, F. Saura-Calixto, *Food Res. Int.*, **41**, 274 (2008).
24. M. Peleg, *J. Food Sci.*, **53**, 1216 (1988).

ИЗВЛИЧАНЕ НА АНТИОКСИДАНТНИ ФЕНОЛНИ СЪЕДИНЕНИЯ ОТ ОБЕЛКИ НА АВОКАДО ЧРЕЗ ТЕЧНА ЕКСТРАКЦИЯ

С. Бояджиева*, С. Георгиева, Г. Ангелов

Институт по инженерна химия, Българска академия на науките, ул. Акад. Ст. Ангелов, бл. 103, София 1113, България

Постъпила на 20 юли, 2018 г.; приета на 10 септември, 2018 г.

(Резюме)

Екстракцията на растителен отпадък (обелки от авокадо) е изучена с цел количествено определяне на съдържанието на полифеноли и антиоксидантната активност на екстракта. Водно-етанолни смеси са използвани като разтворител, тъй като етанолът е най-широко разпространеният „зелен" разтворител с висока разтваряща способност и е напълно биоразградим. Основната задача е да се определят оптималните условия на процедурата, при които екстракцията на антиоксидантни вещества от обелките на авокадо е максимална и се получава екстракт с максимален антиоксидантен капацитет. Четиристепенна експериментална процедура е използвана за оптимизиране на основните параметри на процеса, при които добивът на целевите биоактивни компоненти (полифеноли) е максимален. Кинетиката на процеса е изучена с помощта на уравнението на Peleg и е изчислена моделната равновесна концентрация. Експерименталната концентрация в равновесно състояние съвпада много добре с резултатите от модела (2.5 % разлика).

Bulgarian Chemical Communications, Volume 50, Special Issue K (pp. 90 – 99) 2018

ANN modeling of a two-stage industrial ATAD system for the needs of energy integration

E. G. Kirilova, N. Gr. Vaklieva-Bancheva

Institute of Chemical Engineering, Bulgarian Academy of Sciences, Akad. G. Bontchev, Str., Bl. 103, 1113 Sofia, Bulgaria

Received May 30, 2018; Accepted June 26, 2018

This study proposes an approach for Artificial Neural Network (ANN) modeling of a two-stage industrial Autothermal Thermophilic Aerobic Digestion (ATAD) system for wastewater treatment which can be incorporated in an energy-saving framework operating under uncertainties. For this purpose, ANN models with different architectures are developed for bioreactors from the first and second stages of the ATAD system. Then, they are connected in a common model of the two-stage ATAD system. Models are trained and validated using one-year records of data for a real ATAD system. Three different measures are used to assess their efficiency. The best models are used to create the model of the two-stage ATAD system which is validated with selected weekly data. The designed ATAD system model is able to capture the fluctuations in the parameters of the fresh sludge incoming into the system and to predict the expected target temperatures of the treated sludge at the end of each batch. The latter makes it suitable for use in energy-saving framework under uncertainties.

Keywords: Modeling, Artificial Neural Network, Two-stage ATAD bioreactor system, Uncertainties.

INTRODUCTION

Proper management and sustainability of water resources are some of the most important and talked about issues in the global water industry today. It concerns both improving the efficiency of wastewater disposal and the reduction of energy demands. An effective way to achieve these goals is implementation of Autothermal Thermophilic Aerobic Digestion (ATAD) processes for sludge treatment in urban wastewater treatment plant (WWTP) [1].

Autothermal Thermophilic Aerobic Digestion is a relatively novel technology for treatment of municipal wastewater in small towns and resorts with a population of 20000-30000, as well as of industrial wastewater mainly from dairy, food, poultry, swine facilities, etc. The end "product" is a biological sludge applied as a soil fertilizer, Class A biosolids [2]. The process is self-heating and has the ability to kill pathogens. Other ATAD advantages are its simplicity, high reaction rate and hence smaller sizes of bioreactors. Currently, numerous ATAD facilities work worldwide mainly in the USA, Canada and in the European Union – Austria, UK, Germany, Ireland, Poland, Spain, etc.

ATAD is carried out using thermophilic aerobic microorganisms which consume the biodegradable organic components of the sludge. As a result a high degree of stabilization is achieved due to the high level of degradation of volatile solids, 38% and more. This metabolic activity generates heat and elevates the temperature of the sludge. Retention of the heat in the system leads to high level of pathogen reduction.

Conventional ATAD processes are performed in a parallel series of two batch bioreactors where the wastewater is treated at different temperatures by aeration and mixing for 20-24 hours, Figure 1.

Once per day, part of the treated sludge from the last bioreactors is discharged to "product" storage tanks. Then, the partially treated wastewater from the previous stage is transferred to the next one and the system is fed with fresh sludge from the feed tanks. The required operating temperature for the bioreactors from the first stage is about 55°C, which is optimal for bacterial growth, while for the second one it is ~65°C which is the best for pasteurization. Nevertheless, both bioreactors typically operate below these temperatures.

Systematic observations of ATAD facilities have found that after filling the first stage bioreactors with fresh sludge, a sharp temperature drop occurs, which causes a thermal shock on the thermophilic microorganisms in the bioreactors and influenced the temperature conditions at both bioreactor stages due to the inability to reach the operating temperature [3]. Overcoming the thermal shock is associated with a delay in the operational time to restore the normal operating conditions in bioreactors and leads to increased air and electricity consumption for mixing and pumping. It results in increasing the total cost of energy and materials for the process.

* To whom all correspondence should be sent:
E-mail:eshopova@gmail.com

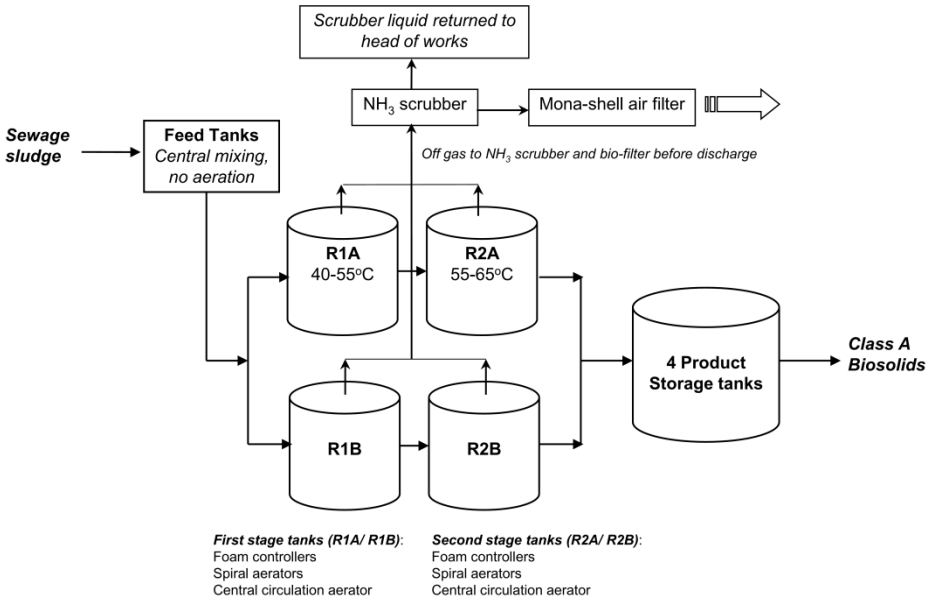

Fig. 1. Configuration of a conventional two-stage ATAD facility [3].

Given the wide use of ATAD systems, a number of experimental studies have been carried out to clarify and improve the process in terms of its duration and realization capabilities. Hayes *et al.* [4] have studied the microbial ecology of sludge, identifying novel bacterial strains responsible for the efficiency of the ATAD process. Liu *et al.* [5] have investigated the changes in volatile suspended solids depending on microbial diversity, conducting series of batch experiments on sewage sludge collected from a real-scale ATAD WWTP. Layden *et al.* [6] have gathered information from a number of sources and provided an insight into the actual application and experiences with a large-scale ATAD. Piterina *et al.* [7] have determined the main characteristics of the sludge, which are responsible for its poor dewatering and settleability. Piterina *et al.* [8] have investigated the bacterial community associated with ATAD treating sludge responsible for maintaining the elevated temperature at the later stages of the ATAD process.

Taking into account that the heat production and its retention in the ATAD process play a key role for its feasibility, many researchers have analyzed the opportunities to improve ATAD systems in terms of their energy efficiency. Earlier studies on ATAD systems from energy view point are focused mainly on heat balance modeling [9, 10, 11].

The latter, Gomez *et al.* [12] have presented a more detailed energy research where biodegradation and physicochemical reactions are related to the energy exchange realized in the ATAD bioreactors. Recently, Liu *et al.* [13, 14] have investigated the effect of temperature on sludge stabilization in one-stage ATAD systems and carried out a heat balance analysis that shows that the evaporation of water and discharging sludge under thermophilic conditions are the two main sources which contribute to the loss of heat.

Mathematical modeling has been used to investigate substantial aspects of the ATAD process. Many of the developed models are based on the Activated Sludge Models (ASMs), which include mass and energy balance equations for predicting either the biodegradation transformations [12] or the physico-chemical reactions and energy exchanges occurring in the ATAD bioreactors [15]. In order to minimize the energy requirement in the ATAD bioreactors, Rojas *et al.* [16] and Rojas and Zhelev [17] have created a dynamic model of ATAD and have shown that significant energy savings can be expected by appropriate altering the operating conditions while complying with the treatment objectives.

Earlier, Layden *et al.* [6] have shown that the recovery of released heat will limit the temperature fluctuations in the first bioreactor's stage. This idea is further developed by Zhelev *et al.* [18, 19]. They have proven that the energy potential of released heat from the second bioreactor's stage is sufficient to be re-used to preheat the raw sludge incoming into the first bioreactors stage. However, the heat integration process in a real industrial WWTP is complicated by the existence of many uncertainties in the parameters of the incoming raw sludge which affect the outgoing treated sludge. Therefore, in order to capture these uncertainties and to ensure effective heat recovery for the sustainable operation

of ATAD facilities, the heat integration problem should be included within a stochastic optimization framework.

For this reason, an appropriate mathematical model of the ATAD process is needed. The model should be able to predict the incoming raw sludge parameters, which are the most important ones from the point of view of energy integration, such as the maximum operating temperatures reached at the end of batches, the corresponding reduction in volatile solids and the expected thermal shock. On the other hand, it should be simple enough to be included in an optimization framework.

However, many of the models developed in the available literature include a large number of parameters, which complicates their including in the model of energy integration of the ATAD system operating under uncertainties. Given this fact, Artificial Neural Networks (ANNs) prove to be best suited to modeling the ATAD process.

The main aim of this study is to develop an ANN model of a two-stage industrial ATAD system, suitable for use in an energy-saving framework under uncertainties. The model should be able to capture the fluctuations of incoming raw sludge parameters and to predict the expected maximal temperature and reduction of volatile solids achieved at the end of each batch, as well as the resulting thermal shock.

The rest of the study is structured as follows: Section 2 provides a description of processes conducted in a two-stage industrial ATAD bioreactor system. Section 3 is devoted to developing the ANN models of bioreactors at each stage of the system and their connection in a series resulting in the design of the ANN model of the two-stage ATAD system. The results of models' validation are also shown. Finally, brief conclusions are presented.

Description of processes in a two-stage ATAD bioreactor system

The typical configuration of the ATAD facility, Figure 1, includes two sequentially connected bioreactors, called stages where the reduction of volatile solids in the sludge and the pasteurization of pathogens are carried out. Both bioreactors have the same volumes. Bioreactors R1A and R2A belong to the first series, while R1B and R2B to the second series. The temperature of the sludge in the first stage should be close to 55^0 C. The maximum disinfection is carried out in the second stage of the series where the temperature should be about 65^0 C. The ATAD bioreactors system operates within a 20-24 hours cycle. This sets up a batch operational mode of ATAD process.

For the purpose of energy integration, the operations of charging and discharging of bioreactors in the ATAD system are very important due to the fact that the integration will take place between incoming cold and outgoing hot flows. Therefore, a detailed description of these processes can be found below.

By maintaining a constant volume of the treated wastewater in the bioreactors, every day, Q_N % from the wastewater treated discharges from the second bioreactor R2 and the first bioreactor R1 feeds with the same amount of raw sludge from feed tanks, as the opening of the ATAD bioreactors system starts from the second bioreactor (R2). The discharged from R2 batch N has a temperature equal to the maximal operating temperature (Tmax2) reached inside the second bioreactor before its opening and the ratio of the volatile solids (VS2) is equal to the one at the end of the ATAD process in R2. However, both the operating temperature and the reduction of the volatile solids reached in R2 are results of implementation of the previous batch, N-1, what follows that produced in the beginning of cycle N outgoing from R2 flow has parameters (Q_N, $Tmax2_{N-1}$, $VS2_{N-1}$). Then, Q_N % from the treated raw sludge in the first bioreactor is transferred into the second bioreactor R2.

Likewise, the operating temperature and the composition of the wastewater treated in R1 measured before its opening is $Tmax1_{N-1}$, and $VS1_{N-1}$. They also are results of implementation of the previous batch N-1 and the outgoing from R1 to R2 flow has parameters Q_N, $Tmax1_{N-1}$, $VS1_{N-1}$. The raw sludge incoming to the first bioreactor R1 has inlet temperature TAD_N, and ratio of both, total solids and volatile solids TS_N and VS_N. However, due to destroying the bioreactors' insulations in the beginning of the cycle N, incoming and outgoing flows from and to R1 and R2 and mixing the inflows with the rested there wastewater, the temperatures in the bioreactors dramatically drop to the minimum ones, named $Tmin1_N$ and $Tmin2_N$, which causes the above mentioned thermal shock on the thermophilic microorganisms and takes time to restore the required operating temperatures.

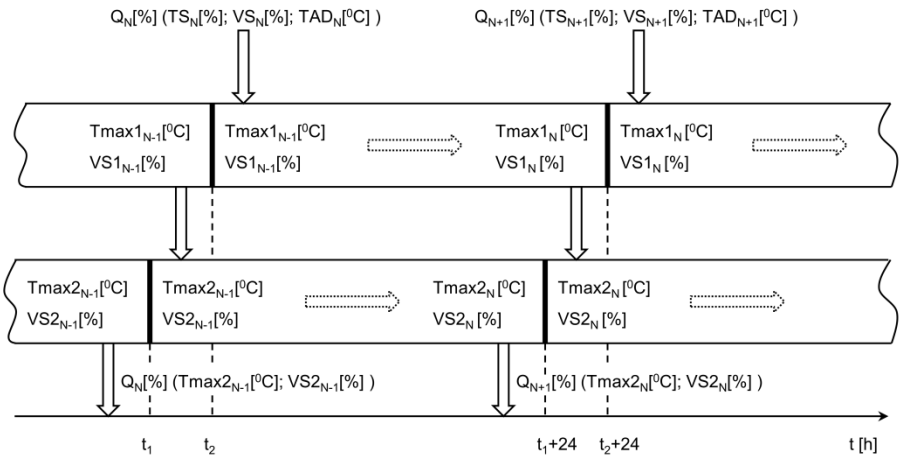

Fig. 2. Flow transfer between batches in a two-stage ATAD bioreactors system.

Then, the bioreactors are closed and isolated to conduct the ATAD process. The next day (at the end of cycle N) the bioreactors are opened and operating temperatures and the respective reduction of the volatile solids are measured which are $Tmax1_N$, and $Tmax2_N$ and $VS1_N$ and $VS2_N$, respectively. The provided brief description illustrates the interconnections in implementation of the consecutive batches that must be taken into account in modeling. It is represented in Fig.2.

Modeling of two-stage ATAD bioreactor system using artificial neural network

General Description of ANN models. Artificial Neural Networks are mathematical models inspired by the way biological neurons transmit and process information. They comprise a large number of highly interconnected artificial neurons which receive input data and process them so as to obtain output. They are applicable for modeling wide range phenomena in physics, computers science, biochemistry, mathematics, sociology, economics, telecommunications, bio-medical instrumentation and many other fields. They take into consideration only available data about the systems, developing conditional nonlinear functions based on the extraction of data.

Generally, a feed-forward ANN consists of *inputs* (like synapses through which natural neurons receive the signals from other ones), *outputs* and one or more *hidden layers* with multiple neurons in them. Connections between them are modified by *weights* (strength of the respective signals). In addition, each neuron has an extra input that is assumed to have a constant value of one. The weight that modifies this extra input is called the *bias*.

An illustration of ANN architecture, comprising several hidden layers with a different number of neurons in each one of them is shown in Fig. 3.

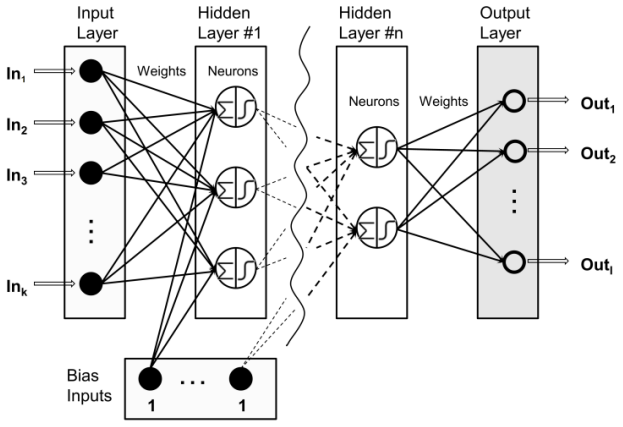

Fig. 3. Typical feed-forward ANN.

All data propagate along the connections in the direction from the network inputs to the network outputs, hence the term *feed-forward*.

Then, the neurons of hidden layers aggregate these weighted values to single values, as follows:

$$net_i = \sum_j w_{i,j} \cdot x_j + b \qquad (1)$$

$$\forall i, i \in k, \quad \forall j, j \in In,$$

where i are indices for the neurons; j are indices for the inputs; $w_{i,j}$ are the weighted coefficients of input-to-hidden connections and hidden-to-output connections; x_j are the inputs to the neurons for a given layer of the neural network; b are the bias inputs for each one of the neurons from the hidden layers;

Then, an *activation function* is applied to the aggregated weighted value to produce an individual *output* for the specific neuron (like activated natural neuron which emits a signal through the axon which might be sent to another synapse, and might activate other neurons). For the purpose of ATAD bioreactors modeling the following sigmoid function is used:

$$F(x)_i = \frac{1}{1+e^{-a \cdot net_i}}, \qquad (2)$$

where a is a coefficient which determines the slope of sigmoid function. In this case $a = 2$ is used.

Using *a least-square function* (LSF) as an optimization criterion, the weights of the artificial neurons are adjusted in a way so as the required outputs for specific inputs are thus obtained to minimize the optimization criteria. For this purpose a *powerful optimization tool* should be applied. This process is called *supervising***.**

Having in mind existing interconnections between the bioreactors and the batches described in Section 2, two models about the bioreactors from the first and second stages are designed. After that both models are connected creating the ANN model of the two-stage ATAD system through correct transfer of the calculated data from R1 to R2 and from batch to batch.

The performance of ANN is influenced substantially by the number of inputs and outputs for the model, as well as its architecture, i.e. the number of hidden layers and neurons in each hidden layer.

The purpose of ANN modeling of each bioreactor is to determine the expected temperature drop, maximal operating temperature reached at the end of batch and the respective reduction of volatile solids, as a function of the parameters of the flow incoming to the bioreactor. Thus, required inputs and outputs for modeling the bioreactors are selected and they are listed in Table 1.

The choice of ANN architecture is preceded by an analysis of the collected data, such as to clearly reveal the relations between inputs and outputs and to choose samplings for ANN learning and validation of designed models.

Table 1. Selected inputs and outputs for modelling.

	Bioreactor 1 (R1)		Bioreactor 2 (R2)	
	Inputs	Outputs	Inputs	Outputs
Feed amount, [%]	Q_N		Q_N	
Ratio of the total solids, [%]	TS_N		-	
Ratio of the volatile solids, [%]	VS_N		$VS1_{N-1}$	
Temperature of the feed, [˚C]	TAD_N		$Tmax1_{N-1}$	
Temperature inside the bioreactor before opening in a current day, [˚C]	$Tmax1_{N-1}$		$Tmax2_{N-1}$	
Volatile solids the next day, [%]		$VS1_N$		$VS2_N$
Temperature drop in the bioreactor, [˚C]		$Tmin1_N$		$Tmin2_N$
Temperature inside the bioreactor before opening the next day, [˚C]		$Tmax1_N$		$Tmax2_N$

Data analysis

For the purpose of ANN modeling one-year records of an industrial two-stage ATAD facility in Ireland were used. Beside the measured amounts, temperatures and compositions of the raw sludge fed in the first bioreactor, they also include records about the changes in operating conditions in both bioreactors such as temperatures drop, maximal temperatures reached after that and degradation rates of the volatile solids.

Given that charging and discharging operations in the considered ATAD system are carried out from Monday to Friday, while only temperature measurements are performed on Saturdays and Sundays, these temperature measurements are excluded from existing data sets.

By assuming a confidence interval of 95%, the upper and lower confidence limits for each set of measured data are determined:

$$\overline{X} \pm 1.96\frac{S}{\sqrt{n}}, \qquad (3)$$

where $\overline{X}$, S and n are average, standard deviation and size of the data set under consideration. In this way, only the data contained within the defined limits are used for modeling, the remainder is excluded from further consideration due to the presence of noise.

Then, full weekly data sets (Monday through Friday) are selected for six randomly selected weeks from different seasons for simulation and validation of the two-stage ATAD model. The remaining data set is used to determine the number of samplings for training and validation of the ANN models for the first and the second bioreactors stages.

The number of samplings for training is determined on the basis of a well-known empirical rule such as they should be at least twice as high as the number of weighting coefficients. Thus, for the validation of the designed ANN models for the first and second bioreactors stages, two sets of 27 and 26 samplings were determined.

ANN architecture

The number of available data allows us to investigate two architectures for each model with one (H1) and two (H2) hidden layers, which differ in the number of neurons in each layer.

The number of neurons selected for the chosen architectures is determined based on the following empiric rule:

$$NN \approx 2 \cdot \sqrt{In \cdot Out}\ , \qquad (4)$$

where In is the number of inputs; Out is the number of outputs.

According to that, for the first bioreactor R1 the acceptable number of neurons is 6-9, and for the second bioreactor R2 – 5-9.

Thus, the investigated architectures ((I,H1,O) and (I,H1,H2,O)) for modeling of R1 are (5,6,3); (5,7,3); (5,5,3,3) and (5,6,3,3), while for R2 they are (4,5,3); (4,6,3); (4,7,3); (4,5,3,3) and (4,6,3,3).

Training and validation of ANN models for both bioreactors

To design ANN with different architectures, an original software code was developed in MATHCAD environment, while for their training, BASIC genetic algorithm [20] was used to obtain the values of the weighting coefficients (models' parameters) at which the criterion LSF has a minimum value.

In order to assess the efficiency of ANN models and their ability for precise prediction three different measures to quantify the accuracy of the modeling: root mean square error (RMSE); mean absolute percentage error (MAPE); and linear correlation coefficient (R) were used.

The root mean square error (RMSE) represents the square root of the average of the summing square predicting errors and is defined as follows:

$$RMSE = \sqrt{\frac{1}{n}\sum_{i=1}^{n}\left(P_i - M_i\right)^2} \qquad (5)$$

Where P_i and M_i are calculated and measured values of Tmax; Tmin and VS, respectively, and n is the number of data samplings.

The second measure is the absolute percentage error (MAPE). It represents the percentage of the mean ratio of the error related to the measured data. MAPE is defined as:

$$MAPE = \frac{1}{n}\sum_{i=1}^{n}\left|\frac{P_i - M_i}{M_i}\right| \cdot 100 \qquad (6)$$

The lower values for RMSE and MAPE, the more accurate the prediction is.

The linear correlation coefficient *R* represents a measure of the strength of the straight-line or linear relationship between measured data and data calculated by the model. The best match between measured and calculated values corresponds to $R = \pm 1$. The linear correlation coefficient R is given by:

$$R = \frac{n \cdot \left(\sum_{i=1}^{n} P_i \cdot M_i\right) - \left(\sum_{i=1}^{n} P_i\right) \cdot \left(\sum_{i=1}^{n} M_i\right)}{\sqrt{\left[\left(n \cdot \sum_{i=1}^{n} M_i^2 - \left(\sum_{i=1}^{n} M_i\right)^2\right) \cdot \left(n \cdot \sum_{i=1}^{n} P_i^2 - \left(\sum_{i-1}^{n} P_i\right)^2\right)\right]}} \qquad (7)$$

The trained ANN models with selected architectures were validated by using the above measures. The values of RMSE, MAPE and R for the chosen models are listed in Table 2.

Concerning the models of bioreactors from the first stage, a very good consistency between different measures of ANN performance is seen for these with the architectures (5,6,3) and (5,7,3). The RMSE and MAPE values are almost equal and the values of the correlation coefficients tend to 1, indicating a very high correlation between measured and calculated data for Tmax, Tmin and VS.

However, the situation for the models with two hidden layers is quite different. There is a big

difference between the measures for the two studied architectures. It can be seen that for the architecture (5,5,3,3) the values of RMSE, MAPE and R are closer to the same measures for the models with one hidden layer, while for the architecture (5,6,3,3) RMSE and MAPE are 3-4 times higher and R shows a weak to modest correlation for Tmax, Tmin and VS. What follows, assuming a confidence level of 95% these correlation coefficients are compared with the critical value for R of 0.3809. It can be seen that R for VS is less than this, which means that this correlation coefficient is not significant. That is why the ANN model with the architecture (5,6,3,3) is excluded from further consideration, although R for Tmax and Tmin exceeds the critical value, they together with VS are outputs of the same model.

Table 2. Values of RMSE, MAPE and R for the considered ANN models.

ANN architectures for modeling of both bioreactors		*RMSE*			*MAPE*			*R*		
		Tmax	Tmin	VS	Tmax	Tmin	VS	Tmax	Tmin	VS
R1	(5,6,3)	2.072	1.242	0.144	2.757	2.046	4.019	0.972	0.987	0.953
	(5,7,3)	2.069	1.198	0.137	2.721	1.929	4.051	0.971	0.988	0.965
	(5,5,3,3)	1.728	1.334	0.355	2.202	2.268	12.77	0.976	0.972	0.753
	(5,6,3,3)	5.865	5.837	0.437	8.947	9.17	13.66	0.452	0.449	0.339
R2	(4,5,3)	1.614	0.915	0.082	2.393	1.200	2.495	0.875	0.903	0.690
	(4,6,3)	1.622	0.9186	0.0917	2.355	1.209	2.873	0.88	0.903	0.632
	(4,7,3)	1.597	0.898	0.078	2.362	1.171	2.365	0.877	0.907	0.731
	(4,5,3,3)	1.432	1.033	0.1412	2.047	1.348	4.923	0.885	0.875	0.454
	(4,6,3,3)	1.443	0.854	0.105	2.124	1.072	3.496	0.886	0.918	0.66

Note: The darkened data are excluded from further consideration.

Table 3. Values of the coefficient of determination for the second stage ANN models.

ANN architectures		$R^2.100\%$		
		Tmax	Tmin	VS
R2	(4,5,3)	76.56	81.54	47.61
	(4,6,3)	77.44	81.54	39.94
	(4,7,3)	76.91	82.26	53.43
	(4,5,3,3)	78.32	76.56	20.43
	(4,6,3,3)	78.49	84.27	43.56

Note: The darkened data are excluded from further consideration.

As far as the models for the second stage bioreactor are concerned, RMSE and MAPE have promising values. By analyzing the values of the correlation coefficients, it can be concluded that there is a large correlation between measured and calculated data for Tmax and Tmin. Whereas for VS the correlation can be assumed to be moderate to high without the model (4,5,3,3) where R for VS is 0.454. The latter is close to the critical value of 0.3882 within a confidence level of 95%. Therefore, for all models for the second stage bioreactor, the determination coefficients - R2.100% were calculated, which provides information about the percentage of the data closest to the line of best match between measured and calculated data, see Table 3. It can be seen that the coefficient of determination for VS for the model with the architecture (4,5,3,3) is very low - barely 20.43%. This is the reason, this model to be excluded from further consideration.

Figure 4 shows a comparison between the measured values for Tmax, Tmin, VS and the calculated values obtained in the architectures (5,7,3) for R1 and (4,6,3,3) for R2.

According to that, seven models that provide a very good match between measured and calculated values were chosen as the most prospective for modeling the two-stage ATAD system. Three of them, with architectures (5,6,3), (5,7,3) and (5,5,3,3) are related to the first stage, while the rest with architectures (4,5,3), (4,6,3), (4,7,3) and (4,6,3,3) – to the second stage.

Modeling of two-stage ATAD system

In order to model the two-stage ATAD system, the selected ANN models for R1 and R2 were connected in series. The transfer of data toward and between ANN models for the first and second stage bioreactors was organized according to the description of the real system flows given in Section 2. Thus, the organized models calculate $Tmin2_N$, $Tmax2_N$ and $VS2_N$ of outgoing flow from the second bioreactor at the end of each batch N. So, 12 possible models for the two-stage ATAD system were created.

Simulation of the performance of the two-stage ATAD system was carried out based on already selected data for six-week data from different seasons. During simulation, the Tmax, Tmin, and VS of the outgoing flows were tracked in each batch from both bioreactors stages, the calculated results to be verified with the measured values. Then, RMSE and R and also coefficients of determination - R^2.100% were calculated for Tmax, Tmin, and VS. The results for the best four models, including individual models with the following architectures R1(5,7,3)-R2(4,5,3); R1(5,7,3)-R2(4,6,3); R1(5,7,3)-R2(4,7,3) and R1(5,7,3)-R2(4,6,3,3) are summarized in Table 4.

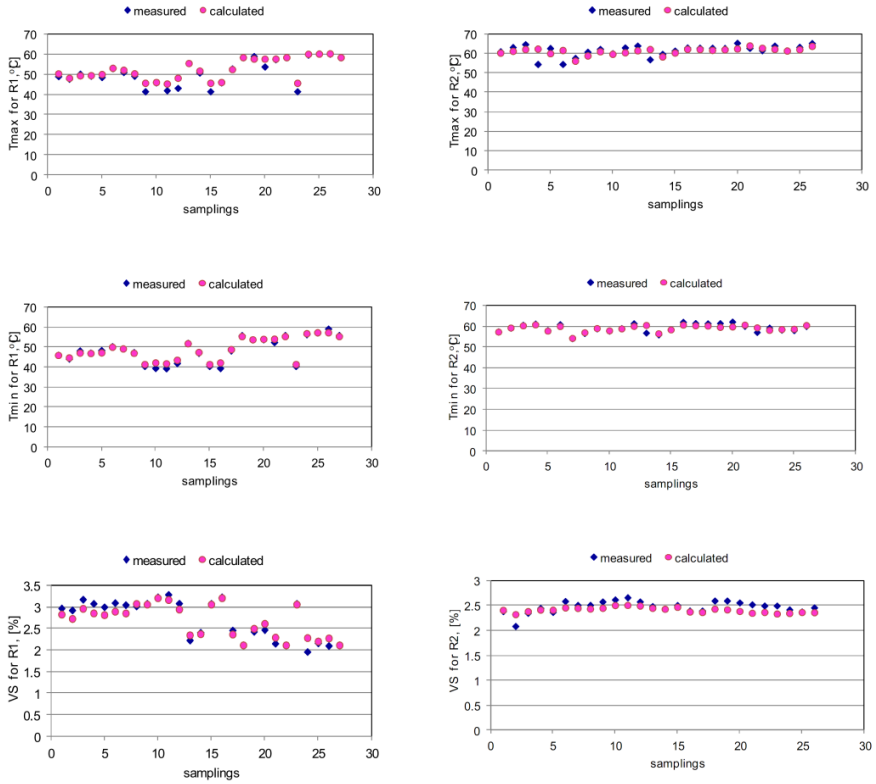

Fig. 4. Comparison between measured and calculated values for Tmax, Tmin and VS for R1 and R2.

Table 4. Values for RMSE, R and R^2 for the best ANN models of a two-stage ATAD system.

ANN models of a two-stage ATAD system	*RMSE*			*R*			*R^2.100%*		
	Tmax	Tmin	VS	Tmax	Tmin	VS	Tmax	Tmin	VS
R1 (5,7,3)	1.64	1.51	0.245	0.913	0.955	0.881	83.34	91.2	77.63
R2 (4,5,3)	2.74	2.27	0.195	0.619	0.482	0.616	38.34	23.26	38.02
R2 (4,6,3)	2.71	2.25	0.194	0.62	0.503	0.639	38.44	25.33	40.79
R2 (4,7,3)	2.17	1.91	0.192	0.639	0.534	0.656	40.79	28.57	43.06
R2 (4,6,3,3)	2.67	2.25	0.206	0.6538	0.5484	0.6526	42.75	30.07	42.57

Note: The darkened data are related to the selected ANN model R1(5,7,3)-R2(4,6,3,3).

Table 4 clearly shows the increase in RMSE values and the decrease in R values for $Tmax2_N$, $Tmin2_N$ and $VS2_N$. They go out of the created two-stage ATAD models compared to the same measures for the individual models of second stage bioreactors. The latter can be explained by the errors accumulated in the input data for the second bioreactor stage resulting from the simulation of the first stage. Correlation coefficients obtained show moderate correlations between measured and calculated data.

In this case, the coefficients of determination are an additional option to evaluate the results calculated by the models. It can be seen that the percentage of data closest to the line of best match between measured and calculated data is the most promising for the model R1(5,7,3)-R2(4,6,3,3). This is the reason for selecting the R1(5,7,3)-R2(4,6,3,3) model for incorporation in the ATAD energy integration framework. A comparison of measured and calculated values of R1(5,7,3)-R2(4,6,3,3) for $Tmax2_N$, $Tmin2_N$ and $VS2_N$ for one winter and one summer week is shown in Figure 5.

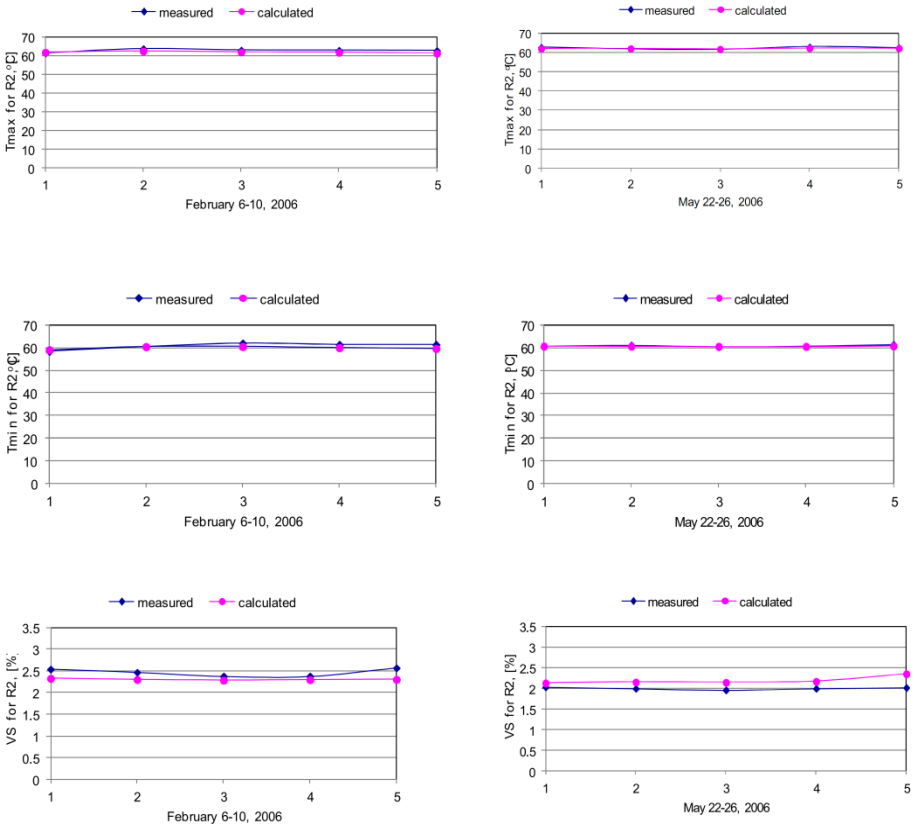

Fig. 5. Comparison between measured and calculated data by the model of two-stage ATAD system for one winter and one summer week.

CONCLUSIONS

This study presents a way to model a two-stage industrial ATAD system that can be included in an energy-saving working frame under uncertainties. Due to uncertainties in the incoming raw sludge parameters, Artificial Neural Networks are used for modeling ATAD bioreactors of each stage. Twelve different ANN architectures are investigated. One-year records of the environmental conditions and resulting operating conditions in ATAD bioreactors are used for training and validation of the ANN models. During validation of the ANN's architectures, three different measures such as root mean square error (RMSE), mean absolute percentage error (MAPE) and linear correlation coefficient (R) are used to assess their performances. The best models for the first and the second bioreactor in the ATAD system are selected based on the values obtained for the measures. Then, the selected models are connected in series by organizing the correct transfer of the calculated data between them. Thus, the constructed models of the two-stage ATAD bioreactor system are also validated with weekly data from different seasons, using the same performance measures. It was shown that there is a good consistency between the implementation measures not only for the two bioreactors models but also for the designed model of the two-stage ATAD system. The latter gives us reason to believe that the ANN model for a two-stage ATAD system is applicable to predict, with sufficient accuracy, the expected temperature drop, the maximal operating temperature reached at the end of batch and the respective reduction of volatile solids.

In future, the already developed ANN models of the two-stage ATAD bioreactors system will be included in analytical models of energy integration of the processes carried out in ATAD systems. The resulting hybrid model will be involved in an optimization framework under uncertainties.

Acknowledgements: *The study has been carried out by the financial support of National Science Fund, Ministry of Education and Science of the Republic of Bulgaria, Contract № ДН07-14/15.12.16. We also would like to thank our colleagues from the University of Limerick, Ireland and especially Prof. Toshko Zhelev† that provided us with real-scale data of an ATAD system.*

NOTATIONS

a – coefficient determining the slope of sigmoid function (activation function);
b – bias inputs for each neuron from the hidden layers;
F – activation function representing sigmoid function;
In – number of inputs;
M– measured values of Tmax, Tmin and VS;

MAPE– mean absolute percentage error, %;
N – number of data samplings;
net – function aggregating weighted values to a single one to each neuron in the hidden layer;
NN – number of neurons;
Out – number of outputs;
P – calculated values for Tmax, Tmin and VS;
Q – feed amount, %;
R – linear correlation coefficient;
R1 – first bioreactor in the series;
R2 – second bioreactor in the series;
S – standard deviation;
TAD – temperature of the feed, ^{0}C;
Tmax – temperature inside the bioreactor before opening in a current day, ^{0}C;
Tmax1 - temperature inside the bioreactor before opening the next day in R1, ^{0}C;
Tmax2 - temperature inside the bioreactor before opening the next day in R2, ^{0}C;
Tmin1 – temperature drop in the first bioreactor, ^{0}C;
Tmin2 – temperature drop in the second bioreactor, ^{0}C;
TS – ratio of total solids in the feed, %;
VS – ratio of volatile solids in the feed, %;
VS1 – ratio of volatile solids at the end of the process in the first bioreactor, %;
VS2 – ratio of volatile solids at the end of the process in the second bioreactor, %;
w - weighting coefficients of input-to-hidden connections and hidden-to-output connections;
x – inputs to the neurons for a given layer of the neural network;
$\overline{X}$ - mean deviation.

Subscripts

i – indices for neurons;
j – indices for inputs;
N – number of batches.

REFERENCES

1. H. G. Kelly, Proceedings of the 4th European Biosolids and Organic Residuals Conference, Chartered Institution of Water and Environmental Management, Wakefield, UK, 2011, p.1.
2. US Environmental Protection Agency, Environmental Regulations and Technology, Control of Pathogens and Vector Attraction in Sewage Sludge. Under 40 CFR Part 503. EPA Report, Cincinnati, OH 45268, 2003.
3. N. M. Layden, *J. Environ. Eng. Sci.*, **6**, 19 (2007).
4. D. Hayes, L. Izzard, R. Seviour, *Syst. Appl. Microbiol.*, **34**, 127 (2011).
5. S. Liu, F. Song, N. Zhu, H. Yuan, J. Cheng, *Bioresource Technol.*, **101**, 9438 (2010).
6. N. M. Layden, H. G. Kelly, D. S. Mavinic, R. Moles, J. Bartlett, *J. Environ. Eng. Sci.*, **6**, 679 (2007).
7. A. V. Piterina, J. Bartlett, T. Pembroke, *Wat. Res.*, **45**, 3427 (2011).
8. A. V. Piterina, J. Bartlett, T. Pembroke, *Wat. Res*., **46**, 2488 (2012).
9. R. Vismara, *Wat. Res.*, **19(4)**, 441 (1985).
10. J. R. Messenger, H. A. De Villiers, G. A. Ekama, *Wat. Sci. Technol.*, **22**, 217 (1990).
11. J. R. Messenger, H. A. De Villiers, G. A. Ekama, *Water SA*, **19**, 193 (1993).
12. J. Gomez, M. de Gracia, E. Ayesa, J. L. Garcia-Heras, *Wat. Res.*, **41**, 959 (2007).
13. S. Liu, N. Zhu, P. Ning, L. I. Li, X. Gong, *Chem. Eng. J.*, **197**, 223 (2012).
14. S. Liu, P. Ning, N. Zhu, *Fresenius Environ. Bull.*, **22**, 1913 (2013).
15. R. Kovács, Z. Csikor, F. Házi, P. Miháltz, *Wat. Environ. Res.*, **79**, 554 (2007).
16. J. Rojas, T. Zhelev, A. D. Bojarski, *Comput. Chem. Eng.*, **34**, 802 (2010).
17. J. Rojas, T. Zhelev, *Comput. Chem. Eng.*, **38**, 52 (2012).
18. T. Zhelev, N. Vaklieva-Bancheva, D. Jamniczky-Kaszás, *Computer Aided Chem. Eng.*, **25**, 1 (2008).
19. T. Zhelev, N. Vaklieva-Bancheva, J. Rojas-Hernandes, T. Pembroke, Proc. 10th Int. Symp. on Process Systems Engineering: Part A. Computer Aided Chemical Engineering, **27**, 933 (2009).
20. E. G. Shopova, N. G. Vaklieva-Bancheva, *Comput. Chem. Eng.*, **30**, 1293 (2006).

МОДЕЛИРАНЕ ПОСРЕДСТВОМ ИЗКУСТВЕНА НЕВРОННА МРЕЖА НА ДВУСТАДИЙНА ATAD СИСТЕМА ЗА НУЖДИТЕ НА ЕНЕРГИЙНАТА ИНТЕГРАЦИЯ

Е. Г. Кирилова, Н. Гр. Ваклиева-Банчева

Institute of Chemical Engineering, Bulgarian Academy of Sciences, 1113 Sofia, Bulgaria

Постъпила на 30 май, 2018 г.; приета на 26 юни, 2018 г.

(Резюме)

Предложен е подход за моделиране на двустадийна промишлена система за автотермално термофилно аеробно разграждане (ATAD) за обработка на отпадъчни води посредством изкуствена невронна мрежа (ANN), която да се включи в енергоспестяваща рамка, работеща в условията на несигурности. За целта са разработени ANN модели с различна архитектура за биореактори от първото и второто стъпало на ATAD системата, които впоследствие са свързани в общ модел на двустадийната ATAD система. Моделите са обучени и валидирани с данни за едногодишен период, получени от реална ATAD система. Използвани са три различни мерки за оценка на тяхната ефективност. Най-добрите модели са избрани за създаване на модел на двустадийната ATAD система, който е валидиран с избрани седмични данни. Създаденият модел на ATAD системата е в състояние да обхване флуктуациите на параметрите на суровата утайка, постъпваща в системата и да предскаже очакваните целеви температури на обработената утайка в края на всяка партида. Това го прави подходящ за използване в енергоспестяваща рамка, работеща в условията на несигурности.

Bulgarian Chemical Communications, Volume 50, Special Issue K (pp. 100 – 105) 2018

An approach for reduction of computational complexity of a two-stage stochastic optimization problem for capturing parameters uncertainty in an ATAD system

R.K. Vladova*, E.G. Kirilova, N.Gr. Vaklieva-Bancheva

Institute of Chemical Engineering, Bulgarian Academy of Sciences, Akad. G. Bontchev, Str., Bl. 103, 1113 Sofia, Bulgaria

Received May 30, 2018; Accepted June 26, 2018

An approach for reduction of the computational complexity of a two-stage stochastic optimization problem for capturing parameters uncertainty in a conventional ATAD system is proposed in this study. The main aim is to find the boundary values of the variables of the first stage of the approach which will result in solutions into the boundaries of the stochastic space. The boundaries of variation of the first stage variables determine the variation of the parameters of the main equipment (heat exchangers surfaces and operating volumes of heat storage tank) which are affected by the change in stochastic parameters. The computational complexity is reduced as in any scenario vertex in the stochastic space a deterministic optimization problem is formulated and solved. As an optimization criterion, the minimum capital costs for purchase of heat exchangers and heat storage tank are used. For the purpose of the study, data from measurements in a real ATAD system were used. As a result of the deterministic optimization problems solution, the values of the parameters of main equipment corresponding to the minimum capital costs are determined. Based on these values the lower and the upper boundaries of the variables of the first stage of the approach are determined.

Keywords: ATAD system, Stochasticoptimization, Uncertainties

INTRODUCTION

Optimization is the heart of the decision-making process in chemical engineering, and other fields of the economy and business. It provides the opportunity to formulate a wide range of problems in a concise manner, using the combination goals and constraints of the process. In some cases, there are uncertainties in the data or model parameters. In these cases, optimization problems are considered as stochastic optimization problems. In their solution the influence of the uncertain parameters should be taken into consideration. This influence can take the process out of the optimum operating conditions and to constraints violation. The most common approach to deal with uncertainties in chemical engineering problems is two-stage stochastic programming.

In general, the two-stage stochastic optimization problems, for each possible scenario include a separate set of second-stage variables. Thus, the problem can be presented as a multi-dimensional problem of deterministic mathematical programming.

Thus, the task can be presented as a multidimensional task of the determined mathematical programming. Assuming the independence of the scenarios, the coefficients of the constraints form a huge block-diagonal matrix in which each block describes the corresponding structures of the constraints with the specific to the given scenario parameters, Figure 1.

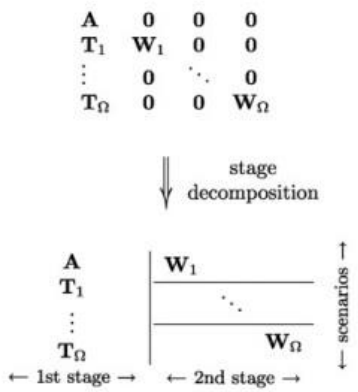

Fig. 1. Decomposition of the two-stage optimization problem [1].

The decomposition approach is the most widely used one to solve such optimization problems. The strategy of the process of obtaining the solution is the following: firstly, the values of the first stage parameters are determined, such as the probability objective function to be optimized. This stage of the process of obtaining the solution is called formulation of Master problem. The first stage variables represent the solutions which need to be taken into account before the uncertainty data are known (for example investment for equipment). While the second stage variables are solutions in which the uncertain parameters have already been found and additional solutions are obtained such as the constraints to be satisfied. The main aim of the

* To whom all correspondence should be sent:
E-mail:raika_vladova@abv.bg

optimization is to select these values of the first and the second stages variables (costs) so that their total amount to be minimal.

Assuming that the uncertainty parameters are with a certain probability, assign sets of known discrete values, postulate a final number of points (scenarios) in the stochastic space, then the two-stage stochastic optimization problem can be formulated as an equivalent deterministic multi-scenario optimization problem. The latter is well known as a multi-scenario model of the two-stage stochastic programming:

$$\min_{\bar{d},\bar{w}_s} Z = C'(\bar{d}) + \sum_s p_s C_s''(\bar{w}_s, \bar{\theta}_s),$$

Subject to:

$$h_{i,s}(\bar{d}, \bar{w}_s, \theta_s) = 0 \quad \forall i \in I,$$

$$g_{j,s}(\bar{d}, \bar{w}_s, \theta_s) \le 0 \quad \forall j \in J,$$

$$\bar{d} \in D, \ \bar{w}_s \in W, \ \theta_s \in \Theta, \ \forall s \in S.$$

$$\sum_{s=1}^{S} p_s = 1$$

where $\bar{d}$ is the vector of the first stage variables (design variables), and $\bar{w}_s$ is the vector of the second stage variables in scenario *s* (state variables). Θ_s is the vector of the uncertain parameters in scenario *s*, and p_s is the probability of the occurrence of scenario *s*. The scenarios number in the model is *S*. There are equality and inequality constraints for each scenario. In addition, the objective function, conditionally called cost function, includes the costs for the first stage (design variables) and the total amount of costs expected for the second stage $\sum_s p_s C_s''(\bar{w}_s, \bar{\theta}_s)$, calculated based on the costs for "system operation" for all scenarios with the respective probabilities p_s. The latter largely depend on the choice of the first-stage variables. However, the great number of scenarios leads to an increase in the computational complexity of the problem, even with the use of decomposition techniques. In order reasonable computational time to be reached it is necessary to determine the boundaries of the values of the first-stage variables that lead to solutions within the stochastic space.

The considered optimization approach is applied to a conventional Autothermal Thermophilic Aerobic Digestion (ATAD) system for municipal wastewater treatment operating under uncertainty. The ATAD process is conducted by the help of thermophilic microorganisms in two consecutively connected bioreactors operating in batch and semi-batch mode. As a final product Class A biosolidsare produced which are used as fertilizers in agriculture.

One of the main problems for the sustainable operation of the ATAD systems is the presence of uncertainty with regard to the main parameters of the ATAD systems such as temperature, quantity and composition of the raw sludge incoming into the ATAD system and the temperature of "product" flows outgoing from the ATAD system. This causes a lack of sustainability to the operating temperatures in the first-stage bioreactors and temperatures fluctuation in the whole system, as well as the presence of thermal shock on the thermophilic microorganisms resulting in prolongation of stabilization and pasteurization processes.

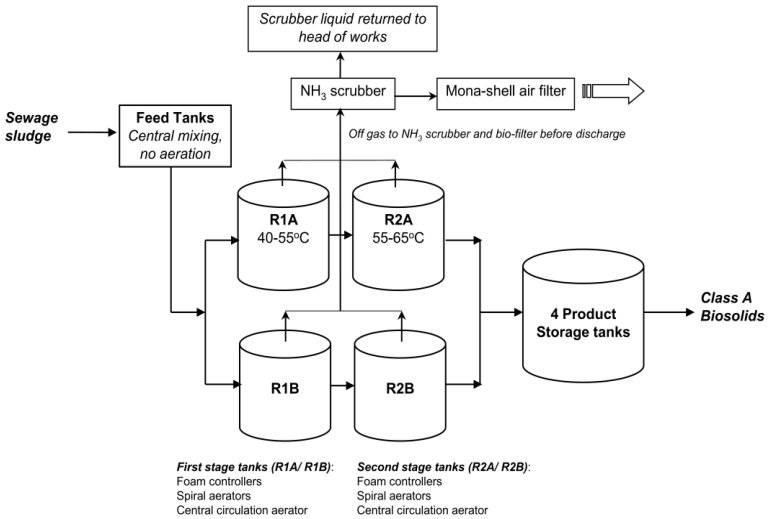

Fig. 2. Two-stage ATAD wastewater treatment system [2].

In order to increase the operating temperatures in the first bioreactor stages and to reduce the thermal shock on the thermophilic microorganisms, a mathematical model of heat integration with two heat exchangers (hot and cold) and one heat storage tank can be applied [3]. This model can be used as to utilize the waste heat from the second stage bioreactors for preheating of the sludge in the first-stage bioreactors, as well as to capture uncertain parameters of the flows incoming and outgoing from the ATAD system. For this purpose this model is modified in such a way to be involved in a two-stage stochastic optimization problem which involves variables of the first and the second stage [4]. However, the solution of this problem is hampered by the large stochastic space formed by the values of the uncertainty parameters.

This study proposes an approach for reduction of the stochastic space mentioned above by determination of reasonable boundary values of the variables of the first stage (design variables) of the two-stage stochastic optimization problem [4]. The latter leads to solutions obtained in the boundaries of the stochastic space, as well as to reduction of the needed calculation time for stochastic optimization problem solution.

In order to determine these boundaries, deterministic optimization problems should be formulated and solved in the boundaries of the stochastic space. The stochastic space can be conditionally interpreted as hyper-rectangular with vertices, determined from all possible combinations of lower and upper boundary values of the uncertainty parameters. Their number is equal to 2^N, where N in the number of the uncertainty parameters. The boundary values of the variables of the first stage should determine these regions of variation of the characteristics of the main equipment (heat exchangers surfaces and operating volume of the heat storage tank) which are affected by the change of the uncertainty parameters. For the ATAD system under consideration, the main uncertain parameters affecting the application of the heat integration model and their boundary values are as follows:

Volumes of loaded/treateddaily sludge: 12 [m^3] – 20 [m^3];

Temperatures of loaded sludge: 5.6 ^oC – 20.2 ^oC;

Temperatures of outgoing treated sludge: 54.5 ^oC – 68.1 ^oC.

For the purpose, for each scenario vertex in the stochastic space, a deterministic optimization problem is formulated. It results in formulation of 2^N deterministic optimization problems. They include the already used model of heat integration of the ATAD process [4], the constraints for feasibility of the heat exchange, as well as the constraints for efficiency of the heat integration.

Formulation of deterministic optimization problem

Data needed:

To formulate the deterministic optimization problem the following data should be known:

$M^c = V\rho$ - mass of the fluid subject to heating/cooling [kg];

cp^c - specific heat capacity of the fluid subject to heating [J/(kg.^{o}C)];

T^{c0} - temperature of the cold sludge subject to heating [^{o}C];

cp^h - specific heat capacity of the fluid subject to cooling [J/(kg.^{o}C)];

T^{h0} - temperature of the fluid subject to cooling [^{o}C];

U^c - heat transfer coefficient in heat exchanger *HE-c* [W/(m$^2{}^o$C)];

U^h - heat transfer coefficient in heat exchanger *HE-h* [W/(m$^2{}^o$C)].

$\Delta T^{\min}$ - admissible minimum temperature difference at the end of the heat exchangers [^{o}C];

cp^m - specific heat capacity of the fluid in the heat storage tank [J/(kg.^{o}C)];

T^{ef} - lower boundary of the efficiency of the heat integration scheme [^{o}C].

Control variables

The following independent control variables are introduced – heat exchangers surfaces A^c and A^h of the two heat exchangers *HE-c* and *HE-h*, the operating volume of the heat storage tank V^m, $M^m = V^m.\rho^m$, as well as the times τ^c and τ^h for heating and cooling fluids in the heat exchangers.

The independent variables are continuous variables which vary within the following boundaries:

$$A\min^c \le A^c \le A\max^c, \quad (1)$$

$$A\min^h \le A^h \le A\max^h, \quad (2)$$

$$V\min^m \le V^m \le V\max^m, \quad (3)$$

$$\tau\min^c \le \tau^c \le \tau\max^c, \quad (4)$$

$$\tau\min^h \le \tau^h \le \tau\max^h, \quad (5)$$

Mathematical description of the heat exchange

The mathematical description [3] includes equations determining the temperatures at the inputs and the outputs of both heat exchangers at the end of the heat integration of the processes in

the ATAD system. In addition, the model includes the equations determining initial temperatures in the heat storage tank, from which it begins to perform the functions of hot and cold respectively, as follows:

$$T^{c1}\left(\tau^{c}\right)=T^{c0}+\left[T^{mh}\left(\tau^{c}\right)-T^{c0}\right]R\Phi e^{c}, \quad (6)$$

$$T^{mh1}\left(\tau^{c}\right)=T^{mh}\left(\tau^{c}\right)-\left[T^{mh}\left(\tau^{c}\right)-T^{c0}\right]R\Phi e^{c}, \quad (7)$$

$$T^{mh}\left(\tau^{c}\right)=T^{c0}+\left(T^{mh0}-T^{c0}\right)\exp\left(-G^{mh}\Phi e^{c}\tau^{c}\right), \quad (8)$$

where: $R^{c}=\frac{w^{mh}.cp^{m}}{w^{c}.cp^{c}}$, $w^{c}=\frac{M}{\tau^{c}}$ [kg/s], $w^{mh}=\frac{M^{m}}{\tau^{c}}$ [kg/s], $G^{mh}=\frac{w^{mh}}{M^{m}}$ [s^{-1}],

$$\Phi e^{c}=\frac{1-\exp\left(-y^{c}.U^{c}.A^{c}\right)}{1-R^{c}.\exp\left(-y^{c}.U^{c}.A^{c}\right)}, \text{ and}$$

$$y^{c}=\frac{1}{w^{mh}.cp^{m}}-\frac{1}{w^{c}.cp^{c}};$$

$$T^{h1}\left(\tau^{h}\right)=T^{h0}-\left(T^{h0}-T^{mc}\left(\tau^{h}\right)\right)\Phi e^{h}, \quad (9)$$

$$T^{mc1}\left(\tau^{h}\right)=T^{mc}\left(\tau^{h}\right)+\left(T^{h0}-T^{mc}\left(\tau^{h}\right)\right)R^{h}\Phi e^{h}, \quad (10)$$

$$T^{mc}\left(\tau^{h}\right)=T^{h0}+\left(T^{mc0}-T^{h0}\right)\exp\left(-R^{h}\Phi e^{h}G^{mc}\tau^{h}\right), \quad (11)$$

where $R^{h}=\frac{w^{h}.cp^{h}}{w^{mc}.cp^{m}}$, $w^{h}=\frac{M}{\tau^{h}}$, [kg/s], $w^{mc}=\frac{M^{m}}{\tau^{h}}$ [kg/s],

$$\Phi e^{h}=\frac{1-\exp\left(-y^{h}.U^{h}.A^{h}\right)}{1-R^{h}.\exp\left(-y^{h}.U^{h}.A^{h}\right)}$$

$y^{h}=\frac{1}{w^{h}.cp^{h}}-\frac{1}{w^{mc}.cp^{m}}$ and $G^{mc}=\frac{w^{mc}}{M^{m}}$ [s^{-1}];

$$T^{mh0}=\frac{b^{22}+b^{12}b^{21}}{1-b^{11}b^{21}};\quad T^{mc0}=\frac{b^{12}-b^{11}b^{22}}{1-b^{11}b^{21}}, \quad (12)$$

where:

$b^{11}=\exp(-G^{mh}\Phi e^{c}\tau^{c});$ $b^{12}=\left[1-\exp\left(-G^{mh}\Phi e^{c}\tau^{c}\right)\right]T^{c0}$

$b^{21}=\exp(-R^{h}\Phi e^{h}G^{mc}\tau^{h});$ $b^{22}=\left[1-\exp\left(-R^{h}\Phi e^{h}G^{mc}\tau^{h}\right)\right]T^{h0}.$

Constraints

The model should be supplied with constraints for the feasibility of the heat exchange in the heat exchangers:

$$\Delta T^{c}\geq\Delta T^{\min} \quad (13)$$

$$\Delta T^{h}\geq\Delta T^{\min}, \quad (14)$$

where ΔT^{c} and ΔT^{h} are minimum temperature differences at the ends of the heat exchangers *HE-c* and *HE-h*. The values obtained of the temperatures allow ΔT^{c} and ΔT^{h} to be determined. They are equal to the smaller of the two temperature differences at the end of each of the heat exchangers:

$$\Delta T^{c}=\min\left\{\left(T^{mh1}\left(\tau^{c}\right)-T^{c0}\right),\left(T^{mh}\left(\tau^{c}\right)-T^{c1}\left(\tau^{c}\right)\right)\right\}, \quad (15)$$

$$\Delta T^{h}=\min\left\{\left(T^{h0}-T^{mc1}\left(\tau^{h}\right)\right),\left(T^{h1}\left(\tau^{h}\right)-T^{mc}\left(\tau^{h}\right)\right)\right\}, \quad (16)$$

In order the proposed model of heat integrated ATAD system to operate efficiently, the temperature of the pre-heated raw sludge incoming into the first bioreactors stage, should be higher or equal to T^{ef} [3].

$$T^{c1}\geq T^{ef} \quad (17)$$

Optimization criterion

The aim of each scenario vertex is to determine the minimum costs for the main equipment for the purpose of the heat integration:

$$Cost=\alpha_{HE}\left(A^{c}\right)^{\beta_{HE}}+\alpha_{HE}\left(A^{h}\right)^{\beta_{HE}}+\alpha_{HS}\left(V^{m}\right)^{\beta_{HS}},$$

$$\underset{A^{c},A^{h},V^{m}}{MIN}\left(Cost\right). \quad (18)$$

Determination of the boundaries of the first-stage variables. Results

Data used:

1. Characteristic data of the heating/cooling flows for the different scenario vertices, Table 1.
2. The specific heat capacity of the fluid in the heat storage tank. Water is used as an intermediate heating/cooling agent in the heat exchangers: cp^{m} = 4.186 [kJ/(kg. ^{o}C)].
3. Heat transfer coefficient in the heat exchanger U^{c} =657 [W/(m^{2o}C)] – heat transfer coefficient in the heatexchanger *HE-c*.
4. U^{h} =657 [W/(m^{2o}C)] - heat transfer coefficient in the heat exchanger *HE-h.*
5. Admissible minimum temperature difference at the end of the heatexchangers: ΔT^{min}= [^{o}C].
6. Lower boundary of the efficiency of the heat integration scheme: T^{ef}= 18[^{o}C].
7. Price correlation coefficients, [5] for the heat exchangers *HE-c* and *HE-h*: α_{HE} = 3.078.10^{3} [CU/m^{2}] and β_{HE} = *0.62*; for the heat storage tank α_{HS} = 3=247.10^{2} [CU/m^{3}] and β_{HS}=0.68.

Table 1. Data for each scenario vertex.

Number of hyper-rectangle vertices	V^c, V^h [m^3]	ρ^c, ρ^h [kg/m^3]	cp^c, cp^h [kJ/(kg °C)]	T^{c0} [°C]	T^{h0} [°C]
1	12	1025	4	5.6	54.5
2	12	1025	4	5.6	68.1
3	12	1025	4	20.2	54.5
4	12	1025	4	20.2	68.1
5	20	1025	4	5.6	54.5
6	20	1025	4	5.6	68.1
7	20	1025	4	20.2	54.5
8	20	1025	4	20.2	68.1

Table 2. Solutions obtained for the scenarios vertices.

Vertex No	1	2	3	4	5	6	7	8
Cost[CU]	16272.4	16968.0	11538.5	16604.0	19215.8	21453.2	15094.4	18877.4
A^c[m^2]	24.72	32.11	**13.64**	24.79	41.17	**53.77**	22.96	39.35
A^h[m^2]	51.88	64.19	**26.39**	57.99	82.42	**105.63**	45.61	76.34
V^m[m^3]	**75.39**	63.3	**31.02**	65.79	62.48	70.49	45.75	64.94
τ^c [s]	2640	2640	2640	2640	2640	2640	264	2640
τ^h [s]	1320	1320	1320	1320	1320	1320	1320	1320

The values used for the boundaries of the control variables in formulated deterministic optimization problem (1)-(18) are as follows:

$0 \le A^c \le 200;$

$0 \le A^h \le 250;$

$0.239 \le V^m \le 100;$

$900 \le \tau^c \le 2640;$

$900 \le \tau^h \le 1320.$

The obtained optimization problem solutions (1)-(18) for the scenarios vertices from 1 to 8 (Table 1) are listed in Table 2. As can be seen from Table 2, the capital costs for heat exchange equipment and heat storage tank range from 11538.5 [CU] to 21453.2 [CU]. They are defined by different values of the variables A^c, A^h, and V^m, while the times for heating/cooling the fluids in the respective heat exchangers have values defined by their upper limits.

Determining the minimum and maximum values with respect to A^c, A^h, and V^m for the scenarios vertices, the boundaries of the first stage variables are determined. They are presented in Table 3. The lower boundaries of the variables A^c, A^h, and V^m represent solutions of scenario vertex 3, while the mentioned above solutions correspond to scenario vertex 6.

Table 3. Boundaries of the first stage variables.

Heat exchanger*HE-c*,[m^2]*;*	Heat exchanger*HE-h*,[m^2]*;*	Heat storage tank -*HS*[m^3]*;*
$13.65 \le A^c \le 53.77$	$26.39 \le A^h \le 105.63$	$31.02 \le V^m \le 75.39$

CONCLUSION

The approach proposed in this study can be used to reduce the stochastic space for solutions of ATAD system operating under uncertainties. It is based on determination of the boundary values of the first-stage variables. It is realized through deterministic optimization problems formulation and solution in different combinations of the boundary values of the uncertain parameters which effect the sustainable operation of the ATAD system. Determination of the boundaries of the stochastic space allow to choose the size of the main equipment whereby the optimization problem has a solution and the capital costs for redesign of the ATAD system will be minimal. The combination of the boundary values reduces the solution space, decreasing the computational complexity of the two-stage stochastic optimization problem under consideration.

Acknowledgement: *The study was carried out by the financial support of National Science Fund, Ministry of Education and Science of the Republic of Bulgaria, Contract № ДН07-14/15.12.16.*

REFERENCES

1. T. Tometzki, S. Engell, *IEEE Trans. Evol. Computation*, **15**,196 (2011).
2. N. M. Layden, *J. Environ. Eng. Sci.*,**6**, 19 (2007).
3. N. Vaklieva-Bancheva, R. Vladova, E. Kirilova, *Proceedings of 56th Annual Science Conference of Ruse University "Industry 4.0.Business Environment. Quality of Life",* Reports Awarded with BEST PAPER Crystal Prize, Ruse, Bulgaria, 44 (2017).
4. N. Vaklieva-Bancheva, R. Vladova, E. Kirilova, *Proceedings of 17th International Symposium on Thermal Science and Engineering of Serbia "Energy-Ecology-Efficiency*, 851 (2015).
5. J. Douglas, Conceptual Design of Chemical Processes, Chemical Engineering Series, 1988.

ПОДХОД ЗА НАМАЛЯВАНЕ НА ИЗЧИСЛИТЕЛНАТА СЛОЖНОСТ НА ДВУСТАДИЙНА СТОХАСТИЧНА ОПТИМИЗАЦИОННА ЗАДАЧА ЗА ДЕФИНИРАНЕ НА НЕСИГУРНОСТИТЕ В ПАРАМЕТРИТЕ В ATAD СИСТЕМА

Р. К. Владова*, Е. Г. Кирилова, Н. Гр. Ваклиева-Банчева

Институт по инженерна химия, Българска академия на науките, ул. Акад. Г. Бончев, бл. 103, 1113 София, България

Постъпила на 30 май, 2018 г.; приета на 26 юни, 2018 г.

(Резюме)

В това изслеване се предлага подход, чрез който да бъде намалена изчислителната сложност на двустадийна стохастична оптимизационна задача, приложен за ограничаване въздействието на несигурните параметри върху конвенционална ATAD система. Методът цели да бъдат намерени границите на стойностите на променливите за първия стадий, които водят до решения в границите на стохастичното пространство. Границите, в които се изменят променливите на първия стадий определят изменението на характеристиките на основното оборудване (топлообменни повърхности и работен обем на топлинния резервоар), които се влияят от изменението на стохастичните параметри. Изчислителната сложност е намалена като за всеки сценариенвръх на стохастичното пространство, е формулирана и решена детерминирана оптимизационна задача. Използваният оптимизационен критерий са минималните капиталовите разходи за топлообменното оборудване и топлинния резервоар. За целите на изследването са използвани данни от измервания в реална ATAD система. В резултат на решаването на оптимизационните задачи са определени стойностите на основното оборудаване с най-ниски капиталови разходи. Въз основа на тези стойности саопределени и долната и горната граници, в които се изменят променливите на първия стадий.

Bulgarian Chemical Communications, Volume 50, Special Issue K (pp. 106 –111) 2018

Adopting environmental transportation practice in biodise lproduction as key factor for sustainable development: A Bulgarian case study

E. I. Ganev*, B. B. Ivanov, D. G. Dobrudzhaliev, Y. R. Dzhelil, D. Nikolova

Institute of Chemical Engineering, Bulgarian Academy of Sciences, Sofia, Bulgaria

Received March 20, 2018, Accepted June 26, 2018,

During the last decades the Bulgarian transport policy is directed mainly towards the construction of modern fast and safe road infrastructure. It corresponds to the geopolitical location of the state in Southeast Europe. Thus, reliable transport corridors will be provided to neighbour states and EU member states. The construction of transport corridors is directly related to the usage of internal combustion engine fuels, used for the vehicles in Bulgaria. The vehicles are based mainly on petrol and diesel engines as the entry of other engines goes at a slow pace. Diesel has become a fuel for trucks and agricultural machinery due to the low fuel consumption and the high efficiency of the diesel engines. On the other hand, the diesel exploitation inevitably reflects on the environment and its pollution because of the volume and the specificity of the waste gases emitted during combustion. Directive 2020 / EU provides the permanent increase of biofuels use. The developed toolbox consists of mathematical model and its optimization for production and use of biofuels, as follows: production and technological criteria, territorial distribution of logistic and production units and environmental pollution with waste gases, consisting mainly CO_2.The results of the toolbox implementation may be used for future effective transport policy for permanent and balanced development of Bulgaria in the next years.

Keywords: Biodiesel, Production technologies, Coordination, GHG emission.

INTRODUCTION

Over the last century, the planet has metaphorically contracted as transport has developed to meet the demands of the population. Global participation in this expansion has been disproportionate [1] as the driving force for transport demand is ultimately the economic growth, which in itself results in an increased need for travel. Although this link is gradually weakening [2], there are few signs of a full breakdown in the unsustainable relationship between increasing incomes and transport emissions [3]. Oil is the dominant fuel source for transportation (Fig. 1a) with road transport accounting for 81% of total energy use by the transport sector (Fig. 1b). This dependence on fossil fuels makes transport a major contributor of greenhouse gases and is one of the few industrial sectors where emissions are still growing [1]. The impact of transport on the global climate is not limited to vehicle emissions as the production and distribution of fuel from oil, a 'wells to wheels' approach, produces significant amounts of greenhouse gas in itself [6]. For example, consideration of total CO_2 emissions from an average car showed that 76% were from fuel usage whereas 9% was from manufacturing of the vehicle and a further 15% was from emissions and losses in the fuel supply system [7]. The reliance on transport appears to be causing long-term damage to the climate, and the ever-increasing consumption of fossil fuels means that peak production of petroleum is imminent **[**4] and world resources will come near exhaustion within 50 years [5]. Rapid decisions now need to be made so that the impacts of transport on the environment can be minimized and fossil fuel resources conserved.

Transport was one of the key sectors highlighted to be tackled by the 1997 Kyoto protocol. The aim was to reduce worldwide greenhouse gas emissions by 5.2% of 1990 levels by 2012. Therefore, since 1997, transport has featured heavily in the political agendas of the 38 developed countries who signed the agreement. Fig. 2a shows that the transport sector accounts for 26% of global CO_2 emissions [8], of which roughly two-thirds originate from the wealthier 10% of countries [9]. Road transport is the biggest producer of greenhouse gases in the transport sector, although the motor car is not solely responsible for all these emissions (Fig. 2b). Buses, taxis and inter-city coaches all play a significant role, but the major contributor is road freight which typically accounts for just under half of the road transport total. Away from road transport, the biggest contributor to climate change is aviation. Aviation is much more environmentally damaging than is indicated solely by CO_2 emission figures. This is due to other greenhouse gases being released directly into the upper atmosphere, where the localized effects can be more damaging than the effects of CO_2alone [10]. Although, the actual energy consumption and CO_2 emissions from

* To whom all correspondence should be sent:
E-mail: evgeniy_ganev@abv.bg

aviation appear relatively low when compared to the motor car (Fig. 2b, Table 1), it is the projected expansion in aviation which is the biggest concern. Air transport shows the highest growth amongst all transport modes and is predicted to be as high as 5% per annum for the next decade [11].

Liquid biofuels (biodiesel and bioethanol) can provide a much needed substitute for fossil fuels used in the transport sector. They can contribute to climate and other environmental goals, energy security, economic development, and offer opportunities for private companies to profit.

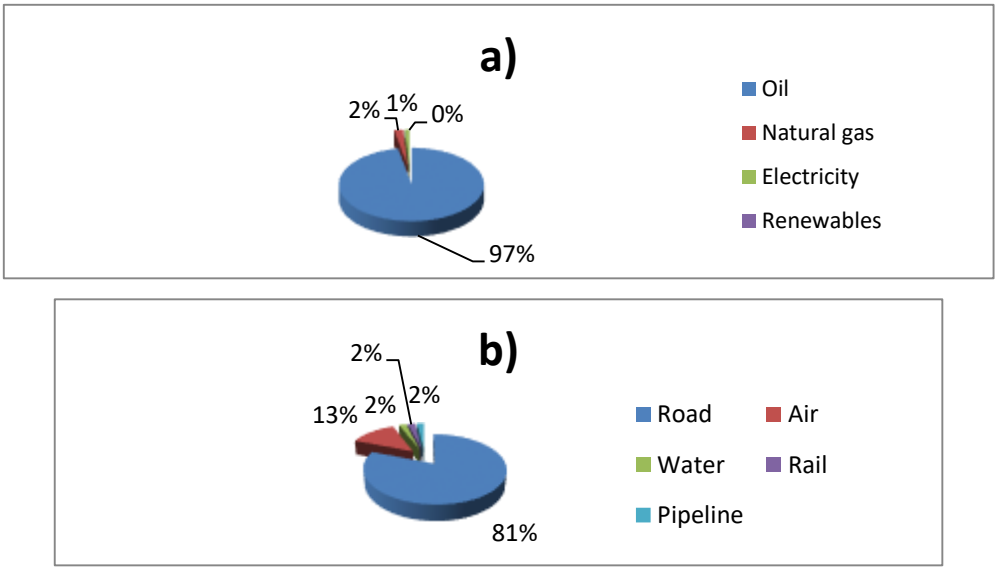

Fig. 1. (a) Fuel use in the transportation sector in OECD(Organisation for Economic Cooperation and Development) countries and(b) shares of transport modes in OECD countries. Source:IEA, 2002.

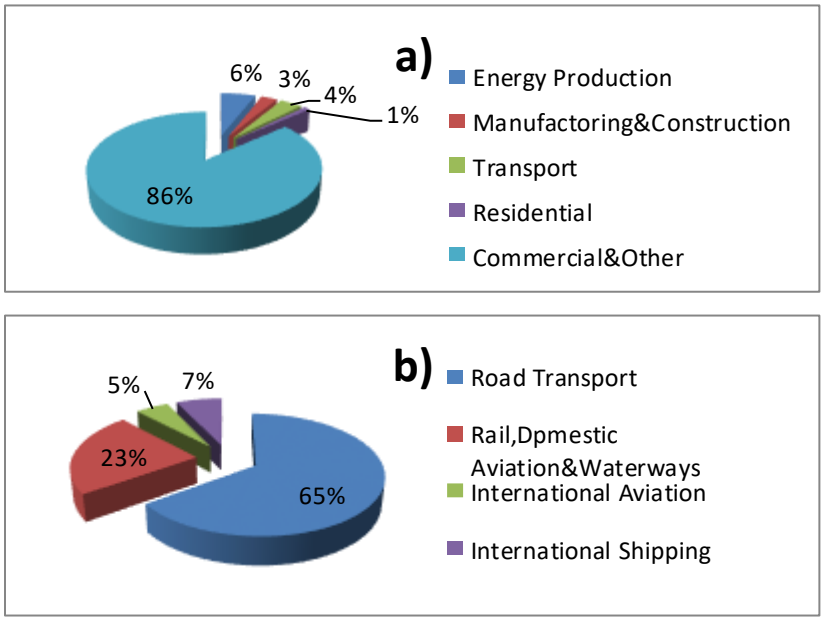

Fig. 2. (a) Carbon dioxide emissions per sector and (b) carbon dioxideemissions per transport sector.Source:IEA, 2000.

If not implemented with care, however, biofuel production can put upward pressure on food prices, increase greenhouse gas (GHG) emissions, exacerbate degradation of land, forests, water sources, and ecosystems, and jeopardize the livelihood security of individuals immediately dependent on the natural resource base.

To this goal we have designed an optimal supply chain (SC) that addresses the entire life cycle of biofuels, from the production of biomass to the combustion of biofuel produced, which should provide an optimal solution for the production of biofuels in order to make their use and production environmentally friendly and not affecting other areas.

METHODOLOGY

Life Cycle Assessment (LCA)has been chosen as the methodology to qualitatively evaluate the environmental loads of the studied fuels. Analysis of a system under LCA encompasses the extraction of raw materials and energy resources, the conversion of these resources into the desired product, the utilization of the product by the consumer, and finally the disposal, reuse or recycle of the product after its service life. The Society of Environmental Toxicology and Chemistry and the International Organization for Standardization **(ISO 14040, 1997; ISO 14041, 1998; ISO 14042, 2000a; ISO 14043,2000b)** developed in the 1990s the LCA methodology. The methodology used falls under the international standards of series ISO14040. The main stages in the aforementioned methodology include:

- Goal definition and scoping;
- Inventory analysis;
- Impact assessment;
- Interpretation.

The goal of this study is to evaluate the environmental performance of biodiesel, based on a life cycle perspective. The assessment includes the extraction of primary raw materials, as well as the combustion of the fuels in the car engine. The system boundaries do not include the production of capital goods, risks and human labor. Major operations within the boundary of the petroleum diesel system include:extract crude oil from the ground, transport crude oil to an oil refinery, refine crude oil to diesel fuel, transport diesel fuel to its point of use and use the fuel in the car engine.

Biodiesel production is achieved*via* different kinds of feedstocks. The nature of feedstock used is dependent on the geographical position and climate of the place. Singh and Singh [12] reported that the major feedstocks employed in producing biodiesel are cotton seed, palm oil, sunflower, soybean, canola, rapeseed, and Jatropha curcas. Additionally, Zhang *et al.* [13] remarked that employing feedstocks such as waste frying oils, nonedible oils, and animal fats, as feedstocks could be useful in producing biodiesel. We look at biomass (sunflower and rapeseed) as feedstock for biodiesel production because they are grown in Bulgaria. The biodiesel is produced by transesterification. Based on Fig. 3, which presents the life cycle of biodiesel and the fossil fuels, it is seen that the first stage in biodiesel chain refers to the cultivation of rapeseed and sunflower grains. After the growth and harvest of plants, the grains are dried and then oil is extracted in two steps, followed by an extraction with an organic solvent (hexane). The solvent is separated and recycled while a small quantity is lost (emission to air). Transesterification of the oil produces methyl esters (biodiesel) and glycerol, which is purified and then used in chemical industry.

Biodiesel can be blended and used in many different concentrations. The most common are B5 (up to 5% biodiesel) and B20 (6% to 20% biodiesel). B100 (pure biodiesel) is typically used as a blendstock to produce lower blends and is rarely used as a transportation fuel.

Low-level biodiesel blends, such as B5, can be used in any compression-ignition engine designed to be operated on petroleum diesel. This can include light-duty and heavy-duty diesel cars and trucks, tractors, boats, and electrical generators. B20 is popular because it represents a good balance of cost, emissions, cold-weather performance, materials compatibility, and ability to act as a solvent. B100 and other high-level biodiesel blends are less common than B20 and lower blends due to a lack of regulatory incentives and pricing. Biodiesel-compatible material for certain parts, such as hoses and gaskets, allow B100 to be used in some engines built since 1994. B100 has a solvent effect, and it can clean a vehicle's fuel system and release deposits accumulated from petroleum diesel use. The release of these deposits may initially clog filters and require frequent filter replacement in the first few tanks of high-level blends.

Comparison of CO_2emissions for biodiesel and petroleum diesel

Figure 4 and Table 1summarize CO_2 flows from the total life cycles of biodiesel and petroleum diesel and the total CO_2 released at the tailpipe for each fuel. The dominant source of CO_2 for both the petroleum diesel and the biodiesel life cycles is the combustion of fuel in the bus. For petroleum diesel, CO_2 emitted from the tailpipe represents 86.54% of the total CO_2 emitted across the entire life cycle of the fuel. Most remaining CO_2 comes from emissions at the oil refinery, which contribute 9.6% of the total CO2 emissions. For biodiesel, 84.43% of the CO_2 emissions occur at the tailpipe. The remaining CO_2 comes almost equally from biomass, biomasses crushing, and biomass oil conversion to biodiesel. Figure 5 shows the effect of biodiesel blend levels on CO_2 emissions

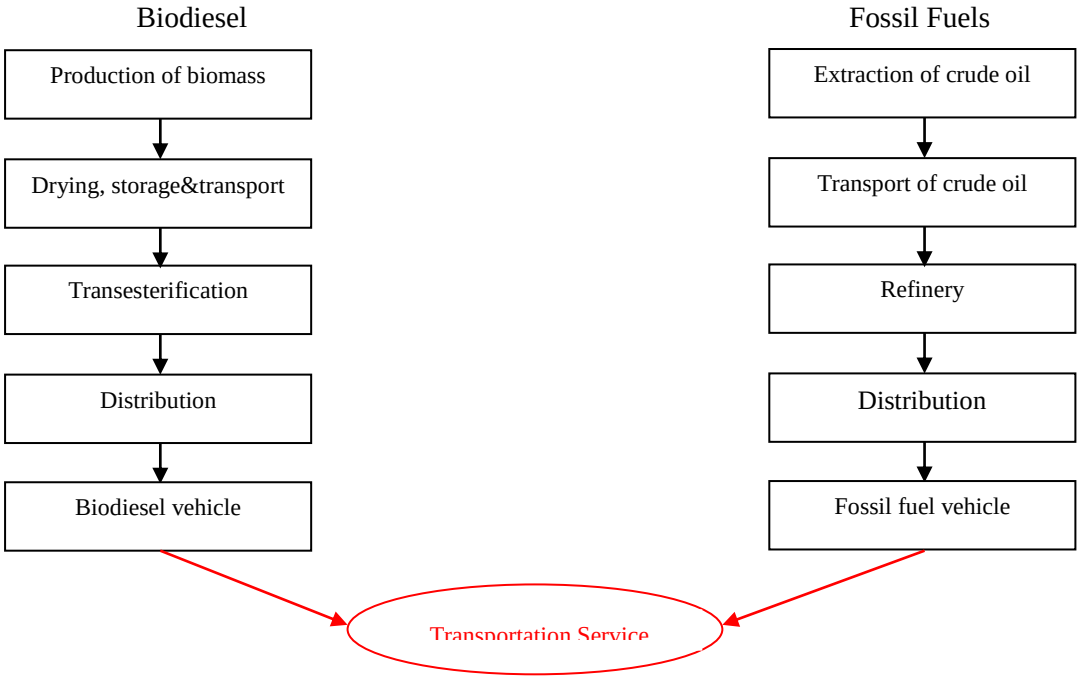

Fig. 3. Life cycle for biodiesel and fossil fuels.

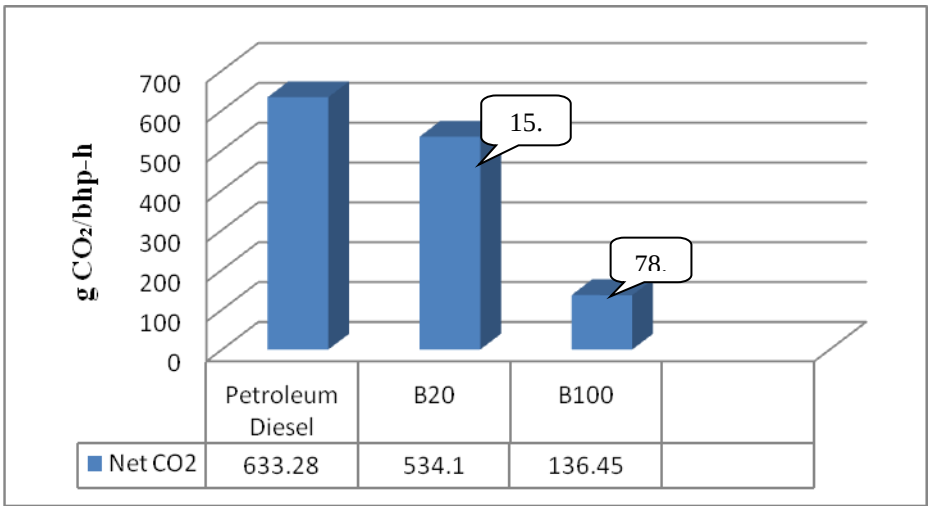

Fig.4. Comparison of net CO_2life cycle emissions forpetroleum diesel and biodiesel blends*.
*Net CO_2calculated by setting biomass CO_2emissions from the tailpipe to zero.

Table 1. Tailpipe contribution to total life cycle CO_2forpetroleum diesel and biodiesel(g CO_2/bhp-h)

Fuel	Total Life Cycle Fossil CO_2	Total Life Cycle Biomass CO_2	Total Life Cycle CO_2	Tailpipe Fossil CO_2	Tailpipe Biomass CO_2	Total Tailpipe CO_2	% of TotalCO_2fromTailpipe
Petroleum Diesel	633.28	0.00	633.28	548.02	0.00	548.02	86.54%
B100	136.45	543.34	679.78	30.62	543.34	573.96	84.43%

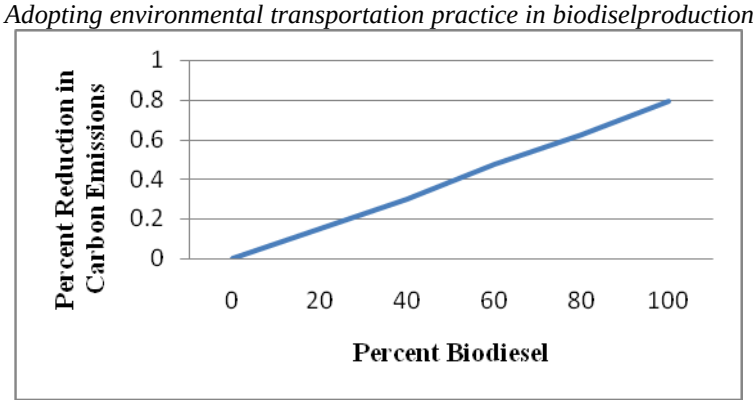

Fig.5. Effect of biodiesel blend level on CO_2emissions.

At the tailpipe, biodiesel (most of which is renewable) emits 4.7% more CO_2 than petroleum diesel. The nonrenewable portion comes from the methanol. Biodiesel generates 573.96 g/bhp-h compared to 548.02g/bhp-h for petroleum diesel. The higher CO_2 levels result from more complete combustion and the concomitant reductions in other carbon-containing tailpipe emissions. As Figure 8 shows, the overall life cycle emissions of CO_2 from B100 are by 78.45% lower than those of petroleum diesel. The reduction is a direct result of carbon recycling in rapeseed and sunflower plants. B20 reduces net CO_2 emissions by 15.66%.

Comparison of life cycle air emissions for biodiesel and petroleum diesel

Figure 6 summarizes the differences in life cycle air emissions for B100 and B20 *versus* petroleumdiesel fuel. Replacing petroleum diesel with biodiesel in an urban bus reduces life cycle air emissions forall but three of the pollutants we tracked. The largest reduction (34.5%) in air emissions that occurs whenB100 or B20 is used as a substitute for petroleum diesel is for CO. The effectiveness of B20 in reducinglife cycle emissions of CO drops proportionately with the blend level. Biodiesel could, therefore,effectively reduce CO emissions in CO non-attainment areas**.**

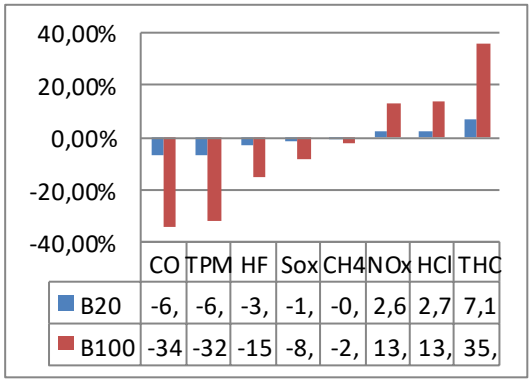

Fig. 6. Life cycle air emissions for B100 and B20compared to petroleum diesel life cycle air emissions.

DISCUSSION

The results of the present study can be used as an input to the strategic decision-making process for future transport energy policy and also to identify key areas of interest for further technology research and development of the Bulgarian transport system. Biofuels Life Cycle Analysis can be considered as a valuable tool, offering flexibility to the system parameterization and to the integrated evaluation of their environmental impacts and their performance in general. Furthermore, it can be a useful tool in the process of strategic and integrated transportation planning, since it takes into account environmental, technical and cost considerations. It is obvious that the use of LCA can result in a shift of the way planners make strategic and operational decisions, through being more effective in identifying improvement opportunities that may not have been previously obvious.

Taken into consideration the fact that the biodiesel is suitable for use in standard compression-ignition (diesel) engines designed to operate on petroleum-based diesel fuel, it is obvious that it can be easily used in existing diesel engines either in its pure form (B100) or in virtually any blend ratio with conventional diesel fuels. Additionally, biodiesel can be strongly promoted through captive and private fleets (bus, taxi, car driver, municipal fleets, etc.).

Acknowledgements: *The authors would like to thank theBulgarian NationalScience Fund forthe obtainedfinancial support under contract DN 07-14/15.12.2016.*

REFERENCES

1. H. Somerville, Transport energy and emissions: aviation,in: D.A. Hensher, K.J. Button (eds.), Handbooks in *Magazine*,**18**, 35 (2003).
2. M.A. Weiss, J.B.Heywood, E.M.Drake, A.Schafer, F.F.AuYeung, 2000. On the Road in 2020 – A life Cycle Analysis of New Automobile Technologies,

Energy Laboratory, Massachusetts Institute of Technology, October 2000.
3. S. Potter, Transport Energy and Emissions: Urban Public Transport. in: D.A. Hensher, K.J. Button (eds.), Handbooks in Transport 4: Handbook of Transport and the Environment. Elsevier, 2003, p. 247.
4. IEA, 2000. International Energy Agency. CO2 Emissions From Fuel Combustions 1971–1998. 2000 Edition, OECD, Paris.
5. M. Lenzen, C. Dey, C. Hamilton, Climate change,in: D.A.Hensher, K.J. Button (eds.), Handbooks in Transport 4: Handbook of Transport and the Environment, Elsevier, 2003, p. 37.
6. S. Cairns, C. Newson, Predict and decide. Aviation, Climate Change and UK Policy, Environmental Change Institute, 2006, p. 122.
7. Council for Sustainable Development. Mobility 2001: World Mobility at the End of the Twentieth Century and Its Sustainability, Published online: www.wbcsdmotability.org (accessed 30.01.06).
8. DfT, 2004a. The Future of Transport, A Network For 2030. UK Department for Transport, Crown Copyright, 2004, p. 140.
9. L.J. Schipper, L. Fulton, Carbon Dioxide Emissions from Transportation: Trends, Driving Forces and Forces for Change,in: D.A.Hensher, K.J. Button (eds.), Handbooks in Transport 4: Handbook of Transport and the Environment, Elsevier, 2003. p. 203.
10. R.C. Duncan, W.Youngquist, *Natural Resources Res.*,**8,** 219 (1999).
11. H. Oman, Energy sources for the world's post petroleum era. *IEEE Aerospace and Electronic Systems* Transport 4: Handbook of Transport and the Environment, Elsevier, 2003, p. 263.
12. S. Singh, D. Singh, *Renew. Sustain. Energ. Revs.*,**14,**200 (2010).
13. Y. Zhang, M.A. Dube´, D.D. McLean, M. Kates, *Bioresour. Technol.*,**89,**1 (2003).

ЕФЕКТИВНА И ЕКОЛОГОСЪОБРАЗНА ТРАНСПОРТНА ПОЛИТИКА ПРИ ПРОИЗВОДСТВОТО НА БИОДИЗЕЛ – КЛЮЧОВ ФАКТОР ЗА УСТОЙЧИВО И БАЛАНСИРАНО РАЗВИТИЕ В РАМКИТЕ НА БЪЛГАРИЯ.

Е. И.Ганев*,Б. Б. Иванов, Д. Г. Добруджалиев, Ю. Р.Джелил, Д. Николова

Институт по инженерна химия, Българска академия на науките, София, България

Постъпила на 20 март, 2018 г.;приета на26 юни, 2018 г.

(Резюме)

През последните десетилетия, транспортната политика на Република България, основно е насочена към изграждане на модерна и сигурна пътна инфраструктура. Това е в съответствие с геополитическото разположение на страната в Европа. Така ще се осигурят надеждни транспортни коридори към съседни нам страни от Европейския съюз. Това е в пряка връзка с използването на горива за двигателите с вътрешно горене, тъй като навлизането на други двигатели върви с бавни темпове. Дизелът, се е наложил като гориво при товарните автомобили и селскостопанската техника, поради високата ефективност, но от друга страна, поради обема на приложение и спецификата на вредните емисии, при изгаряне, експлоатацията на дизела неминуемо се отразава на екологичната обстановка и замърсяването на околната среда. Съгласно Директива 2020 на Европейския съюз е необходимо непрекъснато нарастване на използването на биогорива.

Разработеният инструментариум включва математичен модел и оптимизацията му за производство и използване на биогорива по: производствено-технологични критерии, териториално разпределение на логистични и производствени единици и замърсяването на околната среда с отпадъчни, горивни газове.

Резултатите от приложението на този инструментариум, могат да се използват за изграждане на ефективна транспортна политика за устойчиво и балансирано развитие на Република България през следвашите години.

Bulgarian Chemical Communications, Volume 50, Special Issue K (pp. 112 – 119) 2018

Reaction kinetics in chemical engineering

Christo Boyadjiev

Institute of Chemical Engineering, Bulgarian Academy of Sciences, 1113 Sofia, Bulgaria

Submitted July 31, 2018; Revised October 7, 2018

In the paper is presented a theoretical analysis of the role of the reaction kinetics in chemical engineering for the solution of the main problems in the chemical industry (biotechnology, heat energy), i.e. the optimal design of new devices and the optimal control of active processes. The thermodynamic and hydrodynamic approximations for the modeling of the industrial process rates are presented and analyzed. The relation between the Onsager's linearity coefficient and mass transfer coefficient is presented.

Keywords: reaction kinetics, optimal design, optimal control, thermodynamic approximation, hydrodynamic approximation.

INTRODUCTION

The main problems in the chemical industry (biotechnology, heat energy) are the optimal design of new devices and the optimal control of active processes, i.e. minimization of the investment and operating costs. These problems are solved by chemical engineering with modeling and simulation methods [1].

Mathematical models of processes in the chemical industry contain equations involving variables and parameters. Depending on the problem solved, variables can become parameters and vice versa. They are input mode variables (*X*), output mode variables (*Y*), and construction parameters (*A*):

$$F\left(X,Y,A\right)=0, \tag{1}$$

where *F* is a "vector", containing all the equations in the model, *X(Y)* are the vectors of the input (output) variables, that contain the flow rates and temperatures of the input (output) phase flows and the concentrations of their components, *A* is the vector of the constructive parameters, which contains the constructive parameters of the apparatuses.

The solutions to the optimal design problems of new apparatuses use algorithms, where input mode variables (*X*) and output mode variables (*Y*) are set (as parameters) and optimal construction parameters must be obtained (as variables):

$$A=F_1\left(X,Y\right). \tag{2}$$

The problems of optimal control of current processes use algorithms, where the output mode variables (*Y*) and constructive parameters *(A)* are set (as parameters) and the optimal input mode variables *A* are searched:

$$X=F_2\left(Y,A\right). \tag{3}$$

In the case of renovation (optimal reconstruction), part of the input mode variables and construction parameters are set.

Optimal design and control in the chemical industry is uniquely related to process rates, so all mathematical descriptions of processes are linked to algorithms to determine these rates.

THE PROCESSES RATES IN THE CHEMICAL ENGINEERING

The processes in the chemical industry (biotechnology, heat energy) are the result of the deviation of the systems from their thermodynamic equilibrium [2]. One system is not in a thermodynamic equilibrium when the concentrations of the components (substances) and the temperature at the individual points in the phase volumes are different. These differences are the result of reactions, i.e. of processes that create or consume substance and (or) heat.

The presented analysis shows that processes in the chemical industry are result of reactions that occur in the phase volume (homogeneous) or on the boundary between two phases (heterogeneous). Homogeneous reactions are generally chemical, while heterogeneous reactions are chemical, catalytic, physical and chemical adsorption, interphase mass transfer in gas-liquid and liquid-liquid systems (on the interphase surface the substance disappears from one phase and occurs in the other phase). The rates of these processes are determined by the reaction kinetics, which lies at the basis of modeling and simulation in chemical engineering, and solving the basic problems in the chemical industry (biotechnology, heat energy).

* Address for correspondence:
E-mail: chr.boyadjiev@gmail.com

MODELING AND SIMULATION

The basics of modeling and simulation in chemical engineering, as part of human knowledge and science, are related to the combination of intuition and logic that has different forms in individual sciences [3]. In the mathematics the intuition is the axiom (unconditional statements that cannot be proven), while the logic is the theorem (the logical consequences of the axiom), but logic prevails over intuition. In the natural sciences (physics, chemistry, biology), the "axioms" (principles, postulates, laws) are not always unconditional, but logic prevails over intuition too.

The processes in chemical engineering take place in the industrial apparatuses, where gas, liquid and solid phases move together or alone. They are described by variables, which are extensive or intensive. In the case of merging of two identical systems, the extensive variables are doubled, but the intensive variables are retained.

The processes in the chemical engineering are the result of a deviation from the thermodynamic equilibrium between two-phase volumes or the volume and phase boundaries of one phase and represent the pursuit of the systems to achieve the thermodynamic equilibrium. They are irreversible processes and their kinetics use mathematical structures derived from Onsager's principle of linearity [2]. According to him, the average values of the derivatives at the time of the extensive variables depend linearly on the mean deviations of the conjugated intensive variables from their equilibrium states. The principle is valid near equilibrium and the proportionality factors are the kinetic constants. When the process is done away from equilibrium (high intensity processes) kinetic constants become kinetic complexes, depending on the corresponding intensive variables.

MECHANISM OF INFLUENCE OF REACTION KINETICS

In the chemical industry (biotechnology, heat energy), processes take place in moving phases (gas, liquid, solid). Reactions (reaction processes) lead to different concentrations (and temperatures) in the phase volumes and the phase boundaries. As a result, hydrodynamic processes, diffusion mass transfer and heat conduction are joined to the reaction processes. Under these conditions there are various forms of mass transfer (heat transfer) that are convective (as a result of phase movements) and diffusion (as a result of concentration (temperature) gradients in the phases).

Convective mass transfer (heat transfer) can be laminar or turbulent (as a result of large-scale turbulent pulsations).Diffusion mass transfer (heat transfer) can be molecular or turbulent (as a result of small-scale turbulent pulsations).

Mathematical models of industrial processes aim at determining the concentration of substances (flow temperatures) in the phases. Mathematical models represent a material (thermal) balance in an elementary (small) phase volume that is equivalent to a mathematical point. Components in this balance are convective mass transfer (heat transfer), diffusion mass transfer (heat transfer) and homogeneous reactions (heat effect of reactions). Heterogeneous reactions take part in the boundary conditions of the equations in mass transfer (heat transfer) models. On this basis models of classical theory of mass transfer were created.

THEORY OF MASS TRANSFER

The modern theory of mass transfer is based on the theory of the diffusion boundary layer [4]. This approach replaces (physically justified) elliptic partial differential equations with parabolic partial differential equations, which facilitates their mathematical solution and offers a mathematical description of physical processes with free (not predetermined) ends. The theory of the diffusion boundary layer develops in the case of drops and bubbles [5], film currents [6], non-linear mass transfer and hydrodynamic stability [7, 8].

The modeling of chemical engineering processes has two levels of detail - thermodynamic and hydrodynamic approximation.

Thermodynamic approximation

The processes in chemical engineering are the result of a deviation from the thermodynamic equilibrium between two-phase volumes or the volume and phase boundaries of one phase and represent the pursuit of systems to achieve thermodynamic equilibrium. They are irreversible processes and their kinetics use mathematical structures derived from Onsager's principle of linearity. According to him, the average values of the derivatives at the time of the extensive variables

depend linearly on the mean deviations of the conjugated intensive variables from their equilibrium states. The principle is valid close to equilibrium, and the Onsager's linearity coefficients are kinetic constants. When the process is done away from equilibrium (high intensity processes) kinetic constants become kinetic complexes, depending on the corresponding intensive variables. The thermodynamic approximation models cover the entire volume of the phase or part of it.

Hydrodynamic approximations

The hydrodynamic level uses the approximations of the mechanics of continua, where the mathematical point is equivalent to an elementary physical volume, which is sufficiently small with respect to the apparatus volume, but at the same time sufficiently large with respect to the intermolecular volumes in the medium. In this level the molecules are not visible, as is done in the next level of detail of Boltzmann.

The models of the hydrodynamic approximations are possible to be created on the basis of the mass (heat) transfer theory, whose models are created by the models of the hydrodynamics, diffusion, thermal diffusion and reaction kinetics, using the logical structures of three main "axioms", related with the impulse, mass and heat transfer:

1. The postulate of Stokes for the linear relationship between the stress and deformation rate, which is the basis of the Newtonian fluid dynamics models;
2. The first law of Fick for the linear relationship between the mass flow and the concentration gradient, which is the basis of the linear theory of the mass transfer;
3. The first law of Fourier for the linear relationship between the heat flux and the temperature gradient, which is the basis of the linear theories of the heat transfer.

These are the laws of the impulse, mass and energy transfer.

In Boltzmann's kinetic theory of the ideal gas, these are three "theorems" that derive from the axiom of the "elastic shock" (in a shock between two molecules the direction and the velocity of the movement change, but the sum of their kinetic energies is retained, i.e. there is no loss of kinetic energy) and the rate coefficients are theoretically determined by the average velocity and the average free run of the molecules.

Rate of thermodynamic processes

In the chemical engineering, the Onsager's linearity principle is used to determine the mass transfer rate in one phase or between two phases, where the mass of the transferred substance is an extensive quantity, but its concentration is an intensive quantity. The mass m [kg-mol] of a substance, dissolved in the phase volume, and its derivative at the time (its rate of change over time) $J_0 = dm/dt$ [kg-mol.s^{-1}] depends linearly on the mean deviation from the thermodynamic equilibrium $\left(c_0 - c^*\right)/\delta > 0$ [kg-mol.m^{-4}], where c_0 [kg-mol.m^{-3}] is the concentration of the dissolved substance in a point in the phase, c^* is its equilibrium concentration on the phase boundary, δ [m] is the distance between this point and the phase boundary, i.e.

$$J_0 = k_0 \frac{c - c^*}{\delta}. \tag{4}$$

is the mass flow through the surface s [m^2], where k_0 [m^4.s^{-1}] is the Onsager's linearity coefficient.

The mass flow per unit surface $J = J_0/s$ [kg-mol.m^{-2}.s^{-1}] is obtained directly

$$J = k\left(c_0 - c^*\right), \tag{5}$$

where $k = \frac{k_0}{s\delta}$ [m.s^{-1}] is the mass transfer rate coefficient.

This is a fundamental result, representing the relationship between the thermodynamic kinetics (the Onsager's linearity principle) and the mass transfer kinetics, where the mass transfer coefficient is proportional to the Onsager's linearity coefficient.

In a two-phase system (gas-liquid, liquid-liquid), the concentrations in phase volumes are $c_i, i = 1,2$, and at the phase boundary there is always a thermodynamic equilibrium of the dissolved substance in the two phases $c_1^* = \chi c_2^*$, where $c_i^*, i = 1,2$ are the equilibrium concentrations of the dissolved substance. This is the law of Henry and χ is the number of Henry (in liquid-liquid systems this is the distribution coefficient). In this case the reaching rate of the thermodynamic equilibrium (Onsager's linearity principle) is

$$J_0 = k_{01} \frac{c_{10} - c_1^*}{\delta_1} = k_{02} \frac{c_2^* - c_{20}}{\delta_2} > 0. \tag{6}$$

The mass flow in this case is

$$J = k_1\left(c_{10} - c_1^*\right) = k_2\left(c_2^* - c_{20}\right), \qquad (7)$$

where $k_i = \dfrac{k_{0i}}{s\delta_i}, i = 1,2$ [m.s^{-1}] are the mass transfer rate coefficients.

Similarly, the velocity of the interphase mass transfer can be expressed:

$$J = K_1\left(c_{10} - \chi c_{20}\right) = K_2\left(\frac{c_{10}}{\chi} - c_{20}\right), \qquad (8)$$

where $K_i, i = 1,2$ [m.s^{-1}] are the interphase mass transfer rate coefficients:

$$K_1^{-1} = k_1^{-1} + \chi k_2^{-1}, \quad K_2^{-1} = \chi^{-1}k_1^{-1} + k_2^{-1}. \qquad (9)$$

An analogous result can also be obtained in the case of heat conduction in the presence of temperature differences.

The Onsager's principle of linearity is the thermodynamic approximation of the mathematical description of the kinetics of the complex irreversible processes, but it does not show the way to achieve the equilibrium (the mechanism of the process) an as a result the velocity coefficients are unknown. Obviously, this "thermodynamic level" does not allow for a real quantitative description of the reaction kinetics of irreversible processes in chemical engineering, and the use of the next level of description detail, the so-called "hydrodynamic level", is required.

Relationship between thermodynamic and hydrodynamic approximation

The presence of concentration differences in phase volumes (as a result of the reactions) leads to molecular diffusion and the diffusion mass transfer flow I [kg-mol.m^{-2}.s^{-1}] is determined by the first law of Fick:

$$I = -D\,\mathrm{grad}\,c. \qquad (10)$$

where D [m^2.s^{-1}] is the molecular diffusion coefficient.

In the case of one-dimensional diffusion

$$I = -D\frac{dc}{dx}, \qquad (11)$$

where c is the solution of the equation:

$$\frac{d^2c}{dx^2} = 0; \quad x = 0, \quad c = c^*; \quad x = \delta, \quad c = c_0. \qquad (12)$$

As a result is obtained

$$c = c^* + \frac{c_0 - c^*}{\delta}x, \quad \frac{dc}{dx} = \frac{c_0 - c^*}{\delta}, \quad I = -D\frac{c_0 - c^*}{\delta} < 0, \quad I = -D\frac{c_0 - c^*}{\delta} < 0. \qquad (13)$$

The condition $I = -J$ makes it possible to determine the diffusion mass transfer coefficient $k = D/\delta$. This is a fundamental result that links the thermodynamic and hydrodynamic approximation in determining the read of the industrial processes, i.e. the relationship between Onsager's linearity principle and Fick's first law, where Fick's first law is a consequence of Onsager's principle of linearity in diffusion processes. An analogous connection can also be obtained with the first Fourier law.

This approach will be illustrated in the cases of mass transfer in flowing liquid films and one-phase and two-phase diffusion boundary layers.

Liquid film flows

Let's considers the absorption of slightly soluble gas in a laminar liquid film flow on a vertical flat surface $(y = 0)$. The equation of convection-diffusion has the form [1].

$$\frac{g}{2\nu}\left(2h_0y - y^2\right)\frac{\partial c}{\partial x} = D\left(\frac{\partial^2 c}{\partial x^2} + \frac{\partial^2 c}{\partial y^2}\right);$$
$$x = 0, \quad c = c_0; \quad x \to \infty, \quad c = c^*; \quad y = 0, \quad \frac{\partial c}{\partial y} = 0; \quad y = h_0, \quad c = c^*. \qquad (14)$$

There is a thermodynamic equilibrium at the surface $(y = h_0)$ of the film and c^* is the equilibrium concentration. The solid surface $(y = h_0)$ is impermeable to the diffusion substance, whose concentration at the inlet is $c_0 < c^*$ (absorption). A film with length l will be considered. The thickness of the diffusion boundary layer δ is less than the thickness of the liquid film h_0, which allows the diffusion boundary layer approximation to be used. As a consequence of this approach, the following generalized variables can be introduced:

$$x = lX, \quad y = h_0 - \delta Y, \quad c = c_0 + (c^* - c_0)C, \qquad (15)$$

where $\delta << h_0$ and $h_0 << l$.

The introduction of the generalized variables leads to

$$\left(1+\frac{\delta^2}{h_0^2}Y^2\right)\frac{\partial C}{\partial X}=\frac{Dl}{u_{av}\delta^2}\left(\frac{\delta^2}{l^2}\frac{\partial^2 C}{\partial X^2}+\frac{\partial^2 C}{\partial Y^2}\right), \quad (16)$$

where

$$u_{av}=\frac{gh_0^2}{3\nu}, \quad \delta=\sqrt{\frac{Dl}{u_{av}}}, \quad \frac{\delta^2}{h_0^2}=\frac{Dl}{u_{av}h_0^2}=Fo<10^{-1}, \quad \frac{\delta^2}{l^2}=\frac{D}{u_{av}l}=Pe^{-1}<10^{-2}. \quad (17)$$

In these equations u_{av} is the film average velocity, Fo - Fourier number), Pe - Peclet number. In these conditions the problem must be solved in diffusion boundary layer approximation ($10^{-2}>Pe^{-1}=0$), i.e.

$$\left(1+FoY^2\right)\frac{\partial C}{\partial X}=\frac{\partial^2 C}{\partial Y^2}; \quad X=0, \quad C=0; \quad Y=0, \quad C=1; \quad Y\to\infty, \quad C=0. \quad (18)$$

The mass transfer rate in a film of length l is the average value of the local mass flux through the film surface ($y=h_0$). It can also be represented by the mass transfer coefficient k , i.e.

$$J=\frac{D}{l}\int_0^l\left(\frac{\partial c}{\partial y}\right)_{y=h_0}dx=k(c^*-c_0). \quad (19)$$

The resulting expression allows the determination of the Onsager's linearity coefficient after solving the convection-diffusion equation (18).

The introduction of the generalized variables leads to:

$$Sh=\frac{kl}{D}=-\sqrt{Pe}\int_0^1\left(\frac{\partial C}{\partial Y}\right)_{Y=0}dX. \quad (20)$$

In (18) Fo is a small parameter and the perturbation method must be used. As a result is obtained:

$$Sh=\sqrt{\frac{6Pe}{\pi}}\left(1-\frac{Fo}{6}-\frac{19Fo^2}{120}\right), \quad (21)$$

where Sh is the Sherwood number and represent the dimensionless form of the mass transfer coefficient.

The thickness of the diffusion boundary layer varies along the film length, and as a result, the Onsager's linearity principle has the form:

$$J_0(x)=k_0\frac{\left(c_0-c^*\right)}{\delta_0(x)}, \quad \delta_0(x)=\sqrt{\frac{Dx}{u_{av}}}, \quad J(x)=\frac{k_0}{s}\left(c_0-c^*\right)\sqrt{\frac{u_{av}}{Dx}}. \quad (22)$$

As a result, the average value of the mass flux through the film surface is:

$$\bar{J}(x)=\frac{1}{l}\int_0^l J(x)dx=\frac{2k_0}{s}\left(c_0-c^*\right)\sqrt{\frac{u_{av}}{Dl}}=k\left(c_0-c^*\right), \quad (23)$$

from where the relation between of the Onsager's linearity coefficient and the mass transfer coefficient is obtained:

$$k_0=\frac{ks}{2}\sqrt{\frac{Dl}{u_{av}}}. \quad (24)$$

One-phase diffusion boundary layers

The interphase mass transfer in the gas (liquid) – solid systems is realized at a fixed phase boundary. The flow on a smooth semi-infinite plate of a potential flow with a constant velocity u_0, will be considered. The substance of the solid phase proceeds with a concentration c_0, and on the solid surface y = 0 its equilibrium concentration is c^*. Depending on the sign of the concentration difference (c^* - c_0) there is a process of deposition (crystallization) or dissolution. In this case, the velocity and the concentration satisfy the equations of the laminar boundary layer and the diffusion boundary layer [1]:

$$u\frac{\partial u}{\partial x}+v\frac{\partial u}{\partial y}=\nu\frac{\partial^2 u}{\partial y^2}, \quad \frac{\partial u}{\partial x}+\frac{\partial v}{\partial y}=0, \quad u\frac{\partial c}{\partial x}+v\frac{\partial c}{\partial y}=D\frac{\partial^2 c}{\partial y^2}; \quad (25)$$

$$x=0, \quad u=u_0, \quad c=c_0; \quad y=0, \quad u=0, \quad v=0, \quad c=c^*; \quad y\to\infty, \quad u=u_0, \quad c=c_0.$$

The mass transfer rate in a diffusion boundary layer of length l is the average value of the local mass flux through the solid surface ($y=0$). It can also be represented by the mass transfer coefficient k , i.e.

$$J=\frac{D}{l}\int_0^l\left(\frac{\partial c}{\partial y}\right)_{y=0}dx=k(c^*-c_0). \quad (26)$$

The solution of (25) permits to be obtained the Sherwood number:

$$Sh=\frac{kl}{D}=-Pe^{0,5}\psi'(0)\approx\frac{2}{3}\sqrt{\mathrm{Re}}\sqrt[3]{Sc}, \quad (27)$$

where $\psi'(0)$ is a solution of:Eqs.(28):

$$\varphi'''+\varepsilon^{-1}\varphi\varphi''=0, \quad \psi''+\varepsilon\varphi\psi'=0;$$
$$\varphi(0)=0), \quad \varphi'(0)=0), \quad \psi(0)=1, \quad \psi'(\infty)=2\varepsilon^{-1}, \quad \psi(\infty)=0. \quad (28)$$

The thickness of the diffusion boundary layer varies along the solid surface, and as a result, the Onsager's linearity principle has the form:

$$J_0(x)=k_0\frac{(c_0-c^*)}{\delta_0(x)}, \quad \delta_0(x)=\sqrt{\frac{Dx}{u_0}}, \quad J(x)=\frac{k_0}{s}(c_0-c^*)\sqrt{\frac{u_0}{Dx}}. \quad (29)$$

As a result, the average value of the mass flux through the solid surface is:

$$\bar{J}(x)=\frac{1}{l}\int_0^l J(x)dx=\frac{2k_0}{s}(c_0-c^*)\sqrt{\frac{u_0}{Dl}}=k(c_0-c^*), \quad (30)$$

from where the relation between of the Onsager's linearity coefficient and the mass transfer coefficient is obtained:

$$k_0=\frac{ks}{2}\sqrt{\frac{Dl}{u_0}}. \quad (31)$$

Two-phase diffusion boundary layers

The interphase mass transfer into the gas-liquid and liquid-liquid systems is realized at a moving interphase boundary. In the approximations of the boundary layer theory the processes are described by the following set of Equation [1]:

$$u_j\frac{\partial u_j}{\partial x}+v_j\frac{\partial u_j}{\partial y}=\nu_j\frac{\partial^2 u_j}{\partial y^2}, \quad \frac{\partial u_j}{\partial x}+\frac{\partial v_j}{\partial y}=0, \quad u_j\frac{\partial c_j}{\partial x}+v_j\frac{\partial c_j}{\partial y}=D_j\frac{\partial^2 c_j}{\partial y^2}.$$
$$x=0, \quad u_j=u_{j0}, \quad c_j=c_{j0}; \quad y=0, \quad u_1=u_2, \quad \mu_1\frac{\partial u_1}{\partial y}=\mu_2\frac{\partial u_2}{\partial y}, \quad (32)$$
$$c_1=\chi c_2, \quad D_1\frac{\partial c_1}{\partial y}=D_2\frac{\partial c_2}{\partial y}, \quad v_j=0, \quad j=1,2;$$
$$y\to\infty, \quad u_1=u_{10}, \quad c_1=c_{10}; \quad y\to-\infty, \quad u_2=u_{20}, \quad c_2=c_{20}.$$

The index for the first phase $(j=1)$ is for gas or liquid, and for the second phase $(j=2)$ is for liquid. At the phase boundary there is thermodynamic equilibrium and χ is the Henry's number (in liquid-liquid systems is the distribution coefficient).

The average rate of the interphase mass transfer through a phase boundary with a length l is similarly determined:

$$J=K_1(c_{10}-\chi c_{20})=\frac{1}{l}\int_0^l I_1dx=k_1(c_{10}-c_1^*)=$$
$$=K_2\left(\frac{c_{10}}{\chi}-c_{20}\right)=\frac{1}{l}\int_0^l I_2dx=k_2(c_2^*-c_{20}), \quad c_1^*=\chi c_2^*, \quad (33)$$

where $K_j, j=1,2$ are the interphase mass transfer coefficient and $k_j, j=1,2$ are mass transfer coefficient in the phases.

The local mass fluxes are

$$I_j=-D_j\left(\frac{\partial c_j}{\partial y}\right)_{y=0}, \quad j=1,2 \quad (34)$$

and the Sherwood numbers are:

$$Sh_j=\frac{K_jl}{D_j}=\frac{\chi^{j-1}}{c_{10}-\chi c_{20}}\int_0^l\left(\frac{\partial c_j}{\partial y}\right)_{y=0}dx, \quad j=1,2. \quad (35)$$

From (33) and (35) is possible to be obtained:

$$K_1^{-1}=k_1^{-1}+\chi k_2^{-1}; \quad \chi=0, \quad K_1=k_1; \quad K_2^{-1}=(\chi k_1)^{-1}+k_2^{-1}; \quad \chi\to\infty, \quad K_2=k_2. \quad (36)$$

At the end for the Sherwood numbers is obtained:

$$Sh_j=-\sqrt{Pe_j}\psi_j'(0), \quad Pe_j=\frac{u_{j0}l}{D_j}, \quad j=1,2, \quad (37)$$

where $\psi_j'(0),\ j=1,2$ is the solution of the equations set:

$$\varphi_j''' + j\varepsilon_j^{-1}\varphi_j\varphi_j'' = 0, \quad \psi_j'' + j\varepsilon_j\varphi_j\psi_j' = 0;$$

$$\varphi_j(0) = 0, \quad \varphi_j'(\infty) = \frac{2}{j\varepsilon_j}, \quad \psi_j(\infty) = 0, \quad j = 1,2;$$

$$\varphi_1'(0) = 2\theta_1\frac{\varepsilon_2}{\varepsilon_1}\varphi_2'(0), \quad \varphi_2''(0) = -0{,}5\theta_2\left(\frac{\varepsilon_1}{\varepsilon_2}\right)^2\varphi_1''(0),$$

$$\psi_1'(0) = \frac{\chi}{\varepsilon_0}\psi_2'(0), \quad \psi_1(0) + \psi_2(0) = 1. \tag{38}$$

The thickness of the diffusion boundary layers changes along the interphase surface, and as a result, the Onsager's linearity principle has the form:

$$J_0(x) = k_{0j}\frac{\left(c_{j0} - c_j^*\right)}{\delta_{0j}(x)}, \quad \delta_{0j}(x) = \sqrt{\frac{D_j x}{u_{0j}}}, \quad J(x) = \frac{k_{0j}}{s}\left(c_{j0} - c_j^*\right)\sqrt{\frac{u_{0j}}{D_j x}}, \quad j = 1,2. \tag{39}$$

As a result, the average values of the mass fluxes through the interphase surfaces are:

$$\bar{J}(x) = \frac{1}{l}\int_0^l J(x)\,dx = \frac{2k_{0j}}{s}\left(c_{j0} - c_j^*\right)\sqrt{\frac{u_{0j}}{D_j l}} = k_j\left(c_{j0} - c_0^*\right), \quad j = 1,2, \tag{40}$$

from where the relation between of the Onsager's linearity coefficients and the mass transfer coefficients are obtained:

$$k_{0j} = \frac{k_j s}{2}\sqrt{\frac{D_j l}{u_{0j}}}, \quad j = 1,2. \tag{41}$$

CONCLUSION

The main problems in the chemical industry (biotechnology, heat energy) are the optimal design and optimal control of the industrial processes, using the laws of the reaction kinetics.

Industrial processes are the result of reactions, i.e. creation or disappearance of a substance and (or) heat as a result of chemical and (or) physical processes and their rate is determined by the reaction kinetics.

The reactions deviate the systems from the thermodynamic equilibrium and as a result processes arise, who are trying to restore that equilibrium. The rate of these processes can be determined by Onsager's "linearity principle", where the rate of the process depends linearly on the deviation from the thermodynamic equilibrium.

The Onsager's linearity coefficient can be determined after solving the hydrodynamics, mass transfer and heat transfer equations, where it is proportional to the mass transfer (heat transfer) coefficient.

The dimensionless form of the mass transfer coefficient is the Sherwood number.

REFERENCES

1. Chr. Boyadjiev, Theoretical Chemical Engineering. Modeling and simulation, Springer-Verlag, Berlin Heidelberg, 2010.
2. J. Keizer, Statistical Thermodynamics of Nonequilibrium Processes, Springer-Verlag, New York, 1987.
3. Chr. Boyadjiev, *Open Access Library Journal*, №6, 1 (2014).
4. L.D. Landau, E.M. Lifshitz, Fluid Mechanics, Pergamon, Oxford, 1989.
5. V.G. Levich, Physicochemical Hydrodynamics, Prentice Hall, New York, 1962.
6 .Chr. Boyadjiev, V. Beschkov, Mass Transfer in Liquid Film Flows, Publ. House Bulg. Acad. Sci., Sofia, 1984.
7. V.S. Krylov, Chr. Boyadjiev, Non-linear Mass Transfer (in Russian), Edition of the Institute of Thermophysics, Siberian Branch of the Russian Academy of Sciences, Novosibirsk, 1996.
8. Chr.B. Boyadjiev, V.N. Babak, Non-Linear Mass Transfer and Hydrodynamic Stability, Elsevier, New York, 2000.

РЕАКЦИОННАТА КИНЕТИКА В ХИМИЧНОТО ИНЖЕНЕРСТВО

Христо Бояджиев

Институт по инженерна химия, Българска академия на науките, 1113 София

Постъпила на 31 юли, 2018 г.; Коригирана на 7 октомври, 2018 г.

(Резюме)

В работата е представен теоретичен анализ на ролята на реакционната кинетика в химичното инженерство за решаване на основните проблеми в химичната промишленост (биотехнологиите, топлоенергетиката), т.е. оптимално проектиране на ново оборудване и оптимално управление на действащи процеси. Представен е анализ на термодинамичното и хидродинамичното приближение при моделирането на скоростта на промишлените процеси. Представена е връзката между коефициента в принципа на линейността на Онзагер и коефициента на масопренасяне.

Ключови думи: реакционна кинетика, оптимално проектиране, оптимално управление, термодинамично приближение, хидродинамично приближение

Instructions about Preparation of Manuscripts

General remarks: Manuscripts are submitted in English by e-mail The text must be typed on A4 format paper using Times New Roman font size 11, normal character spacing. The manuscript should not exceed 15 pages (about 3500 words), including photographs, tables, drawings, formulae, etc. Authors are requested to use margins of 2 cm on all sides

Manuscripts should be subdivided into labelled sections, e.g. **Introduction, Experimental, Results and Discussion**, *etc*. **The title page** comprises headline, author's names and affiliations, abstract and key words. Attention is drawn to the following:

a) **The title** of the manuscript should reflect concisely the purpose and findings of the work. Abbreviations, symbols, chemical formulas, references and footnotes should be avoided. If indispensable, abbreviations and formulas should be givenin parentheses immediately after the respective full form.

b) **The author**'s first and middle name initials and family name in full should be given, followedby the address (or addresses) of the contributing laboratory (laboratories). **The affiliation** of the author(s) should be listed in detail by numers (no abbreviations!). The author to whom correspondence and/or inquiries should be sent should be indicated by asterisk (*) with e-mail address.

The abstract should be self-explanatory and intelligible without any references to the text andcontaining not more than 250 words. It should be followed by key words (not more than six).

References should be numbered sequentially in the order, in which they are cited in the text. The numbers in the text should be enclosed in brackets [2], [5, 6], [9–12], etc., set on the text line. References are to be listed in numerical order on a separate sheet. All references are to be given in Latin letters. The names of the authors are given without inversion. Titles of journals must be abbreviated according to Chemical Abstracts and given in italics, the volume is typed in bold, the initial page is given and the year in parentheses. Attention is drawn to the following conventions:a) The names of all authors of a certainpublications should be given. The use of "*et al*." inthe list of references is not acceptable.b) Only the initials of the first and middle names should be given. In the manuscripts, the reference to author(s) of cited works should be made without giving initials, e.g. "Bush and Smith [7] pioneered...". If the reference carries the names of three or more authors it should be quoted as "Bush *et al*. [7]", if Bush is the first author, or as "Bush and co-workers [7]", if Bush is the senior author.

Footnotes should be reduced to a minimum. Each footnote should be typed double-spaced at thebottom of the page, on which its subject is first mentioned.**Tables** are numbered with Arabic numerals on the left-hand top. Each table should be referred to inthe text. Column headings should be as short as possible but they must define units unambiguously.The units are to be separated from the preceding symbols by a comma or brackets. Note: The following format should be used when figures, equations, *etc*. are referred to the text (followed by the respective numbers): Fig., Eqns., Table, Scheme.

Schemes and figures. Each manuscript should contain or be accompanied by the respective illustrative material as well as by the respective figure captions in a separate file (sheet).As far as presentation of units is concerned, SI units are to be used. However, some non-SI units are also acceptable, such as °C, ml, l, etc.The author(s) name(s), the title of the manuscript, the number of drawings, photographs, diagrams, etc., should be written in black pencil on the back of the illustrative material (hard copies) inaccordance with the list enclosed. Avoid using more than 6 (12 for reviews, respectively) figures in the manuscript. Since most of the illustrative materials are to be presented as 8-cm wide pictures, attention should be paid that all axis titles, numerals, legend(s) and texts are legible.

The authors are required to submit the text with a list of three individuals and their e-mail addresses that can be considered by the Editors as potential reviewers. Please, note that the reviewers should be outside the authors' own institution or organization. The Editorial Board of the journal is not obliged to accept these proposals.

The authors are asked to submit **the final text** (after the manuscript has been accepted for publication) in electronic form by e-mail. The main text, list of references, tables and figure captions should be saved in separate files (as *.rtf or *.doc) with clearly identifiable file names. It is essential that the name and version of the word-processing program and the format of the text files is clearly indicated. It is recommended that the pictures are presented in *.tif, *.jpg, *.cdr or *.bmp format.

The equations are written using “Equation Editor” and chemical reaction schemes are written using ISIS Draw or ChemDraw programme.

EXAMPLES FOR PRESENTATION OF REFERENCES

REFERENCES

1. D. S. Newsome, *Catal. Rev.–Sci. Eng*., **21**, 275 (1980).
2. C.-H. Lin, C.-Y. Hsu, *J. Chem. Soc. Chem. Commun*., 1479 (1992).
3. R. G. Parr, W. Yang, Density Functional Theory of Atoms and Molecules, Oxford Univ. Press, New York, 1989.
4. V. Ponec, G. C. Bond, Catalysis by Metals and Alloys (Stud. Surf. Sci. Catal., vol. 95), Elsevier, Amsterdam, 1995.
5. G. Kadinov, S. Todorova, A. Palazov, in: New Frontiers in Catalysis (Proc. 10th Int. Congr. Catal., Budapest,(1992), L. Guczi, F. Solymosi, P. Tetenyi (eds.), Akademiai Kiado, Budapest, 1993, Part C, p. 2817.
6. G. L. C. Maire, F. Garin, in: Catalysis. Science and Technology, J. R. Anderson, M. Boudart (eds), vol. 6, SpringerVerlag, Berlin, 1984, p. 161.
7. D. Pocknell, *GB Patent* 2 207 355 (1949).
8. G. Angelov, PhD Thesis, UCTM, Sofia, 2001, pp. 121-126.
9 JCPDS International Center for Diffraction Data, Power Diffraction File, Swarthmore, PA, 1991.
10. CA **127**, 184 762q (1998).
11. P. Hou, H. Wise, *J. Catal.*, in press.
12. M. Sinev, private communication.
13. http://www.chemweb.com/alchem/articles/1051611477211.html.

Texts with references which do not match these requirements will not be considered for publication!!!

CONTENTS

СЪДЪРЖАНИЕ